Catechol-Functionalized TiO_2 Nanoparticles: From Fundamental Surface Chemistry to Promising Applications

Dissertation

zur Erlangung des Grades

„Doktor der Naturwissenschaften“ (Dr. rer. nat.)

im Promotionsfach Chemie

am Fachbereich Chemie, Pharmazie, Geographie und Geowissenschaften

der Johannes Gutenberg–Universität Mainz

Eugen Schechtel

geboren in Stschutschinsk, Kasachstan

Mainz, 2020

Dekan: [redacted]

Erster Berichterstatter: [redacted]

Zweiter Berichterstatter: [redacted]

Tag der mündlichen Prüfung: 11.12.2020

Erklärung

Die vorliegende Arbeit wurde in der Zeit von September 2013 bis August 2019 unter Betreuung von Herrn Prof. Dr. Wolfgang Tremel am Department Chemie der Johannes Gutenberg–Universität Mainz angefertigt.

Ich erkläre hiermit, dass ich die vorliegende Arbeit selbstständig und ohne fremde Hilfe verfasst habe. Alle verwendeten Quellen und Hilfsmittel sind vollständig angegeben.

Mainz, August 2020

Danksagung

Contents

Abstract

Titanium dioxide (TiO_2) is an abundant, non-toxic material that has found numerous applications in diverse research fields over the last few decades. To enhance its surface functionality, TiO_2 nanoparticles (NPs) are frequently modified with catechol anchor molecules, which incorporate the benefits of a high binding strength and an extended spectral response. However, this strategy is often pursued with minimal knowledge of the underlying surface chemistry, thus making accurate assessments very difficult.

Therefore, the goal of this thesis is to investigate the fundamental surface processes taking place when hydrophobic TiO_2 NPs are reacted with catecholic molecules and to utilize thus-functionalized TiO_2 NPs in applications of photocatalysis and nanocomposites.

The first part of the thesis lays a solid foundation for the surface chemistry during catechol ligand adsorption on hydrophobic, oleate-stabilized TiO_2 NPs. Using a broad set of NMR techniques (1D and 2D, ^{1}H and ^{13}C, solution and solid state), the surface coverage of the incoming catechol and the displacement of the native oleate were precisely monitored. Contrary to the prevailing view, catechol was not able to substitute the entirety of the native ligand shell. Instead, a mixed ligand shell was formed after displacement of only a minor fraction (~20%) of the native ligand shell. Starting at a value of 2.3 nm^{-2} for the native oleate ligand shell, the total ligand density more than doubled to 4.8 nm^{-2} for the mixed ligand shell at maximum catechol loading. This surprising behavior can be rationalized by the assumption that the incoming catechol ligand preferably adsorbs to unoccupied Ti surface sites rather than displacing native oleate ligands.

The second part of the thesis shows a promising application of a specially designed catecholic anchor as a visible-light sensitizer for TiO_2 NPs in a photocatalytic oxidative cyanation reaction. The sensitizer molecule, 6,7-dihydroxy-2-methylisoquinolinium chloride (DHMIQ), was designed in such a way that it incorporates the structural features of a number of powerful homogeneous organic photocatalysts such as the 2,7-diazapyrenium dication. When attached to TiO_2 NPs, DHMIQ al-

lows for a panchromatic sensitization over the whole visible range and even extending into the near-infrared (NIR) region. The extended spectral response of the TiO_2–DHMIQ photocatalyst was exploited in aerobic photocyanation reactions of tertiary amines with visible and NIR light. When irradiated with light of different wavelengths, the photocatalyst achieved remarkable catalytic performance not only for energetic blue light of 462 nm, but also for low-energy NIR light of 730 nm.

The third part of the thesis deals with 4-allylcatechol-functionalized TiO_2 NPs, which were covalently embedded into thiol–ene (TE) polymer matrices through their terminal double bonds. Thus, hybrid nanocomposites with varying inorganic filler fractions were fabricated in order to study the effect of the inorganic filler on the material's mechanical and thermal properties. To access these properties, the sound velocity (and thus elastic modulus) and the thermal conductivity of the TE/TiO_2 nanocomposites were measured by Brillouin light scattering spectroscopy (BLS) and by the 3ω method, respectively. Both properties increased with increasing TiO_2 NP filler fraction: The effective elastic modulus increased from 6.2 GPa at 0 wt% of TiO_2 NPs to 37.5 GPa at 90 wt% of TiO_2 NPs (by a factor of 6), while the effective thermal conductivity increased even more significantly, from 0.04 to 0.76 W/m·K (by a factor of 18). The increase of the effective elastic modulus was attributed to the covalent cross-linking of the nanocomposite constituents. The pronounced enhancement of the effective thermal conductivity was ascribed to the addition of a high-conductivity filler in the form of nanoparticulate TiO_2 and the associated formation of conductive channels at high TiO_2 NP fractions.

Kurzzusammenfassung

Titandioxid (TiO_2) ist ein reichlich vorkommendes, unbedenkliches Material, das in den letzten Jahrzehnten zahlreiche Anwendungen in den unterschiedlichsten Forschungsgebieten gefunden hat. Um seine Oberflächenfunktionalität zu verbessern, wird TiO_2 häufig in Form von Nanopartikeln (NP) mit Catechol-Ankermolekülen modifiziert, die die Vorteile einer hohen Bindungsstärke und einer erweiterten Lichtabsorption in sich vereinen. Diese Strategie wird in der Praxis jedoch oft mit unzureichender Kenntnis der zugrundeliegenden Oberflächenchemie verfolgt, was eine genaue Beurteilung der durchgeführten Oberflächenreaktionen sehr schwierig macht.

Ziel dieser Dissertation ist es daher, die grundlegenden Oberflächenprozesse bei der Modifizierung hydrophober TiO_2-NP mit Catechol-Ankern zu untersuchen und derart funktionalisierte TiO_2-NP in Anwendungen der Photokatalyse und in Nanokompositen zu nutzen.

Der erste Teil der Arbeit legt eine solide Grundlage für die Oberflächenprozesse während der Catechol-Ligandenadsorption an hydrophoben, Oleat-stabilisierten TiO_2-NP. Unter Einsatz einer ganzen Bandbreite von NMR-Techniken (1D und 2D, ^{1}H und ^{13}C, Lösung und Festkörper) wurden die Oberflächenbedeckung des adsorbierten Catechols und die Verdrängung des nativen Oleats präzise quantifiziert. Entgegen der vorherrschenden Literaturmeinung war das Catechol nicht in der Lage, die gesamte native Ligandenhülle zu ersetzen. Stattdessen wurde nur ein kleiner Teil (~20%) der nativen Ligandenhülle verdrängt und es bildete sich eine gemischte Ligandensphäre aus. Ausgehend von einem Wert von 2.3 nm^{-2} für die native Oleat-Ligandenhülle hat sich die Gesamtligandendichte bei maximaler Catechol-Beladung auf 4.8 nm^{-2} für die gemischte Ligandensphäre mehr als verdoppelt. Dieses überraschende Verhalten kann durch die Annahme erklärt werden, dass der ankommende Catechol-Ligand vorzugsweise an unbesetzten Ti-Oberflächenstellen adsorbiert, anstatt die nativen Oleat-Liganden zu verdrängen.

Der zweite Teil der Arbeit zeigt eine vielversprechende Anwendung eines speziell konzipierten Catechol-Ankers zur Photosensibilisierung von TiO_2-NP im sichtbaren Spektralbereich für den Einsatz in einer photokatalytischen oxidativen Cyanierungsre-

aktion. Das Sensibilisatormolekül, 6,7-Dihydroxy-2-methylisochinoliniumchlorid (DHMIQ), wurde so konzipiert, dass es die strukturellen Merkmale einer Gruppe von leistungsstarken homogenen organischen Photokatalysatoren, wie z.B. dem 2,7-Diazapyrenium-Dikation, in sich vereint. Die Anbindung von DHMIQ an TiO_2-NP ermöglicht eine panchromatische Sensibilisierung über den gesamten sichtbaren Bereich und sogar bis in den Nahinfrarotbereich (NIR). Die erweiterte spektrale Empfindlichkeit des TiO_2−DHMIQ-Photokatalysators wurde bei aeroben Photocyanierungsreaktionen von tertiären Aminen mit sichtbarem und mit NIR-Licht ausgenutzt. Bei Bestrahlung mit Licht unterschiedlicher Wellenlängen erreichte der Photokatalysator eine bemerkenswerte katalytische Umsetzung nicht nur für energiereiches blaues Licht von 462 nm, sondern auch für niederenergetisches NIR-Licht von 730 nm.

Der dritte Teil der Arbeit beschäftigt sich mit 4-Allylcatechol-funktionalisierten TiO_2-NP, die über ihre terminalen Doppelbindungen kovalent in Thiol−En (TE)-Polymermatrizen eingebettet wurden. Auf diese Weise wurden hybride Nanokomposite mit variablen Anteilen eines anorganischen Füllstoffs hergestellt, um den Einfluss des anorganischen Füllstoffs auf die mechanischen und thermischen Eigenschaften des Materials zu untersuchen. Um auf diese Eigenschaften zugreifen zu können, wurden die Schallgeschwindigkeit (und damit der Elastizitätsmodul) sowie die Wärmeleitfähigkeit der TE/TiO_2-Nanokomposite mittels Brillouin-Lichtstreu-Spektroskopie (BLS) und 3ω-Methode gemessen. Beide Eigenschaften nahmen mit zunehmendem TiO_2-NP-Anteil zu: Der effektive Elastizitätsmodul stieg von 6.2 GPa bei 0 Gew% TiO_2-NP auf 37.5 GPa bei 90 Gew% TiO_2-NP (um den Faktor 6), während die effektive Wärmeleitfähigkeit noch signifikanter zunahm, von 0.04 auf 0.76 W/m·K (um den Faktor 18). Der Anstieg des effektiven Elastizitätsmoduls wurde auf die kovalente Vernetzung zwischen TiO_2-NP und TE-Polymermatrix zurückgeführt. Die ausgeprägte Steigerung der effektiven Wärmeleitfähigkeit wurde der Zunahme des anorganischen Füllstoffs mit höherer Wärmeleitfähigkeit und der damit verbundenen Bildung von leitfähigen Kanälen bei hohen TiO_2-NP-Anteilen zugeschrieben.

1

Theoretical Background

1.1 General Introduction to Nanoparticles

Inorganic structures are referred to as nanoparticles (NPs) when they have a spatial extent in the range from 1 to 100 nm in at least one of the three dimensions.[1–3] Compared to their bulk parent materials, NPs often show altered physical and chemical properties, which also vary with their size. The size-dependent physical properties are all related to spatial confinement effects that occur as a consequence of the limited NP dimensions.[3] The most studied physical phenomena are quantum confinement effects in semiconductor NPs,[4,5] localized surface plasmon resonance in noble metal NPs,[6,7] and superparamagnetism in magnetic NPs.[8] The enhanced chemical properties of NPs originate from their high surface-to-volume ratio, which increases with decreasing NP size. Thus, for very small sizes, the fraction of surface atoms becomes extraordinarily large (e.g., from 10% for a 20 nm particle to 50% for a 3 nm particle)[9] and surface-relevant chemical processes are boosted. One very impressive example of this phenomenon is the self-ignition of pyrophoric iron.[10] In addition to this, synthetic conditions and the high curvature of NP surfaces may introduce surface sites with enhanced chemical reactivity.[11] All of these properties make NPs very attractive for an extremely broad range of potential applications,[2,12] including biomedicine,[13–15] catalysis,[16–18] electronics,[19–21] and energy-related fields.[22–24]

1.1.1 Nanoparticle Synthesis

There are two principal methods to produce nanoparticulate materials (Figure 1.1):[3] (i) The top-down approach exploits physical methods, such as lithography and high-energy ball milling, to remove large fractions of a bulk material in a controlled manner or to break down the bulk material altogether into nanoscale particles, respectively. (ii) The bottom-up approach utilizes mostly chemical methods to assemble the nanomaterials from molecular building blocks. Apart from vapour phase deposition techniques, which employ the thermal decomposition of gas phase precursors at high temperatures, liquid phase methods involve the growth (and precipitation) of NPs within a liquid phase.

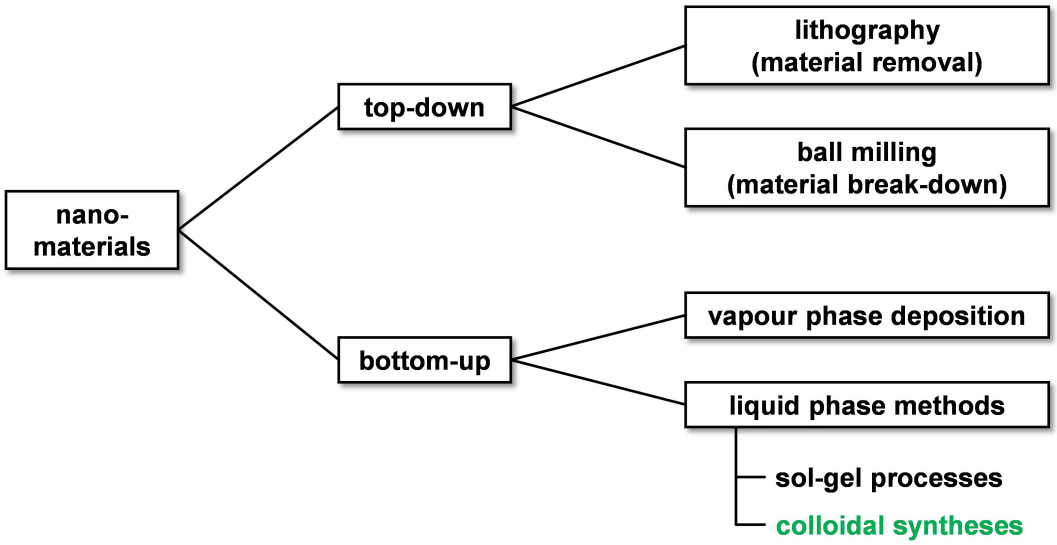

Figure 1.1. Simplified overview of synthetic methods for nanomaterials.

These methods can further be divided into sol-gel processes (mainly for metal oxides) and colloidal syntheses. During the sol-gel process, metal precursors (typically metal alkoxides) are hydrolyzed to form a colloidal sol that subsequently undergoes condensation to transform into a cross-linked gel, which finally needs to be heat-treated.[25] Sol-gel processes usually yield fine powders of aggregated nanoparticles with broad size distribution and poor dispersibility in liquid media.[26] However, colloidal stability is a prerequisite for solution-based processing[27] of NPs for numerous applications like superconductive films,[28] thermoelectric[24] and electronic devices.[21] Thus, in order to obtain colloidally stable nanoparticles, researchers have developed several synthetic protocols that are summarized as colloidal syntheses in Figure 1.1. The colloidal meth-

ods are highly versatile and applicable to a wide range of compositions,[29] such as metallic NPs,[30] semiconductors,[31,32] or metal oxides.[33,34] All of these techniques offer a high degree of synthetic control over composition, size, and shape of the NPs, while ensuring perfect colloidal stability through the use of stabilizing ligands.

Some of the synthetic protocols for colloidal NPs will be discussed in more detail in the context of TiO_2 NPs in section 1.2.2.

1.1.2 Nanoparticle Constituents

Consisting of an inorganic core that is surrounded by a shell of organic ligands, colloidal NPs can be viewed as organic-inorganic hybrid nanomaterials (Figure 1.2). The hybrid nature of colloidal NPs allows for a flexible engineering of their physical and chemical properties since both components can be manipulated independently. Furthermore, the interaction of the inorganic core with its organic surroundings can also have a significant effect on the resulting NP properties.[35]

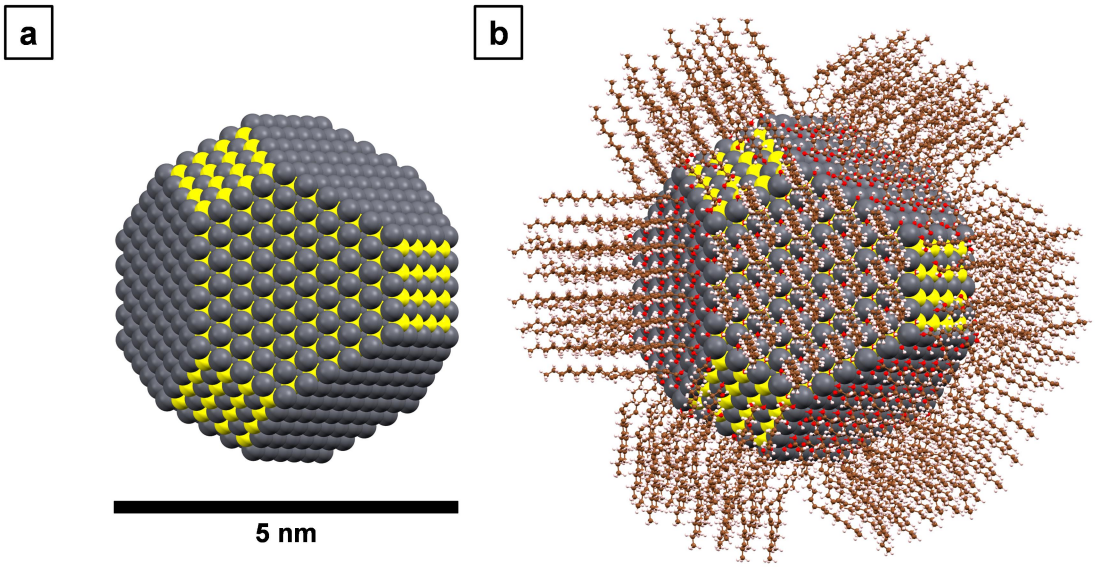

Figure 1.2. Calculated atomistic model of a faceted colloidal lead sulfide (PbS) NP passivated with oleic acid (OA). (a) Space-filling representation of the inorganic PbS NP core. (b) Complete NP model with the organic OA ligand shell visualized in ball-and-stick style. Color code: Pb, gray; S, yellow; O, red; C, brown; H, light pink. The structure was replotted from the atomic coordinates provided by Zherebetskyy et al.,[36] using the Mercury 4.1.0 software[37] for visualization.

1.1.2.1 The Inorganic Core

The inorganic core defines the intrinsic physical properties of the NP, such as magnetic or optoeletronic properties. These properties are dictated by the NP core's composition, but also depend on its size and shape and can even be influenced by the surface ligands.[38]

Due to nanoscale effects and the larger surface contribution, the inorganic core may exhibit crystal structures that are metastable for the bulk material (e.g., γ-Al_2O_3 instead of α-Al_2O_3 (corundum) or anatase and brookite instead of rutile TiO_2).[39] Thus, the stabilization of the desired phase is of crucial importance, since the crystal structure defines the NP's electronic structure, which, in turn, dictates its physical properties. Phase control can be achieved by establishing the proper reaction conditions (such as pH value), as will be discussed in more detail for TiO_2 NPs in section 1.2.2. The NP's electronic structure can further be modified via doping[40,41] or substitution[42,43] chemistry where the secondary metal ions are introduced through molecular precursors during the synthesis. Similarly, the electronic structure can also be altered by postsynthetic cation or anion exchange to tune the magnetic properties of metal oxide NPs[44] or the optical properties of metal halide perovskite NPs.[45]

Synthetic procedures were optimized to ensure precise control over NP size and size distribution.[46] Such control is achieved by adjusting the reaction parameters, such as the precursor concentration,[47] the heating rate,[48] and the surfactant ratio.[49]

In addition to the size control, significant efforts have been devoted to the control over NP shape.[30,50,51] This goal is usually achieved by using two surfactants in the synthesis with different affinities to certain crystal facets, thus accelerating the growth rates on the less passivated facets. The most widely used surfactant duo to accomplish shape control is the acid/base combination of oleic acid (OA) and oleylamine (OM)[52] that have shown shape-directing properties for many different NPs.[49,53–58]

The NP core can also be composed of different nanosized domains with common interfaces.[35,59–61] Such multicomponent or hybrid NPs thus combine different functionalities in a single system, such as plasmonic and magnetic functionalities in Au−Fe_3O_4 dumbbell NPs.[62]

1.1.2.2 The Organic Ligand Sphere

While the inorganic core bears the NP's intrinsic physical properties, the organic ligand shell serves as a barrier and mediator to its chemical surroundings. The ligands (or surfactants) perform two essential roles in different stages: (i) During the synthesis, they influence the nucleation and growth of the NP core, thus allowing control over size and shape (*vide supra*). (ii) After the synthesis, the ligands define the NP's behavior in liquid media and decide upon the accessibility of the NP surface.

Typically, the ligand is an amphiphilic molecule that consists of a polar head group and a non-polar tail. The polar head group acts as an anchoring group to the metal ions/atoms at the core's surface, while the hydrocarbon tail shields the NP core from the surrounding medium and ensures colloidal stability (cf. Figure 1.2b). The attachment of the ligand to the NP surface involves coordination chemistry between electron-donating atoms (especially N, O, P, S) in the anchoring groups and eletron-accepting metal atoms and ions at the NP surface. Thus, the surface complexation can be viewed as a Lewis acid−base interaction, whose binding strength can be rationalized in terms of Pearson's concept of hard and soft acids and bases (HSAB).[63,64] According to Pearson's HSAB concept, Lewis acid−base interactions are especially strong when both components are either hard (small size, high charge, low polarizability) or soft (large size, low charge, high polarizability). This is why thiols (soft bases) are excellent anchoring groups for gold atoms (soft acids), while carboxylates (hard bases) are a better choice for the metal ions in transition metal oxides (hard acids, such as Ti^{4+} or Zn^{2+}).

To account for the diversity of NP core compositions (*vide supra*), there is also a wide range of possible surface ligands.[65] Table 1.1 gives a rough overview of common combinations with some selected examples of frequently employed ligands.

Besides the appropriate acid−base pairing, the NP−ligand binding strength also dependes on the number of coordinating donor atoms, i.e., the denticity of the ligand. In general, the binding strength increases with the denticity (i.e., monodentate < bidentate < tridentate). Accordingly, a metal oxide NP should exhibit increasing NP−ligand interactions in the order $R{-}NH_2 < R_3P{=}O < R{-}SH < R{-}COOH < R{-}PO(OH)_2$.

Table 1.1. Common combinations of NPs and native surface ligands.[a]

NP class and examples	anchoring group	commonly employed ligands
(noble) metal		
Au, Ag	thiol (−SH)	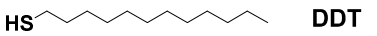 DDT
Pt, Pd	amine ($-NH_2$)	
Fe, Co	carboxyl (−COOH)	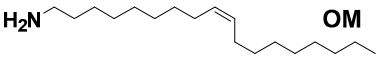 OM
		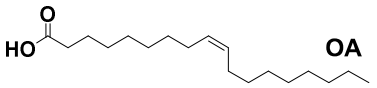 OA
metal chalcogenide		
PbS, CdSe	phosphine oxide ($R_3P=O$)	
	thiol (−SH)	
	carboxyl (−COOH)	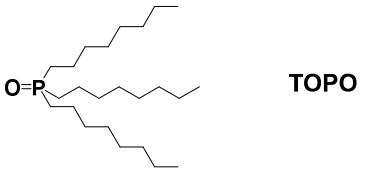 TOPO
(transition) metal oxide		
TiO_2	amine ($-NH_2$)	
Fe_3O_4	hydroxyl (−OH)	
ZnO	carboxyl (−COOH)	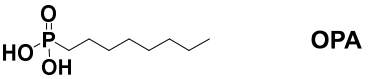 OPA
	phosphonate ($-PO(OH)_2$)	

[a]DDT, dodecanethiol; OM, oleylamine; OA, oleic acid; TOPO, trioctylphosphine oxide; OPA, octylphosphonic acid.

1.1.3 The Organic–Inorganic Interface

The organic–inorganic interface is of fundamental importance for almost every NP-based application because it defines the surface chemistry of the NP,[38,66,67] thus influencing surface-related processes such as accessibility of catalytically active surface sites, ligand exchange efficiencies, and electron transfer dynamics. To investigate these phenomena, the surface coordination of the anchoring group has to be revealed. However, due to the curved nature and intrinsic heterogeneity of NP surfaces, an exact characterization of the surface coordination is extremely challenging and the binding motifs are usually deduced from the well-characterized structures of low-molecular-weight metal complexes or self-assembled monolayers (SAMs) on flat surfaces.

A more realistic picture of the actual surface coordination chemistry of NPs was obtained with the advent of atomically precise colloidal nanoclusters (with sizes of up to 2 nm),[68] whose total crystal structures were successfully resolved by X-ray diffraction (XRD) techniques. The crystal structures revealed that even seemingly simple systems, such as the gold–thiolate (Au–SR) combination, exhibit unexpectedly complex surface coordinations. One of the first total structure determinations was reported in 2007 by Jadzinsky et al.[69] for the thiolated Au nanocluster $Au_{102}(SR)_{44}$ (Figure 1.3a). This

nanocluster showed surface coordination geometries that deviated strongly from the assumed standard binding model of thiols in SAMs on flat Au surfaces.[70,71] The characteristic feature is a so-called staple motif where exposed surface Au atoms (light green sphere in Figure 1.3b) are stapled to the kernel structure through bridging thiolate ligands on opposite sides. Apart from the monomeric staple motif (−RS−Au−SR−, Figure 1.3b), the $Au_{102}(SR)_{44}$ nanocluster also features dimeric staple motifs (−RS(−Au−SR)$_2$−, Figure 1.3c) and even longer oligomeric staple motifs have been reported for smaller Au nanoclusters.[72]

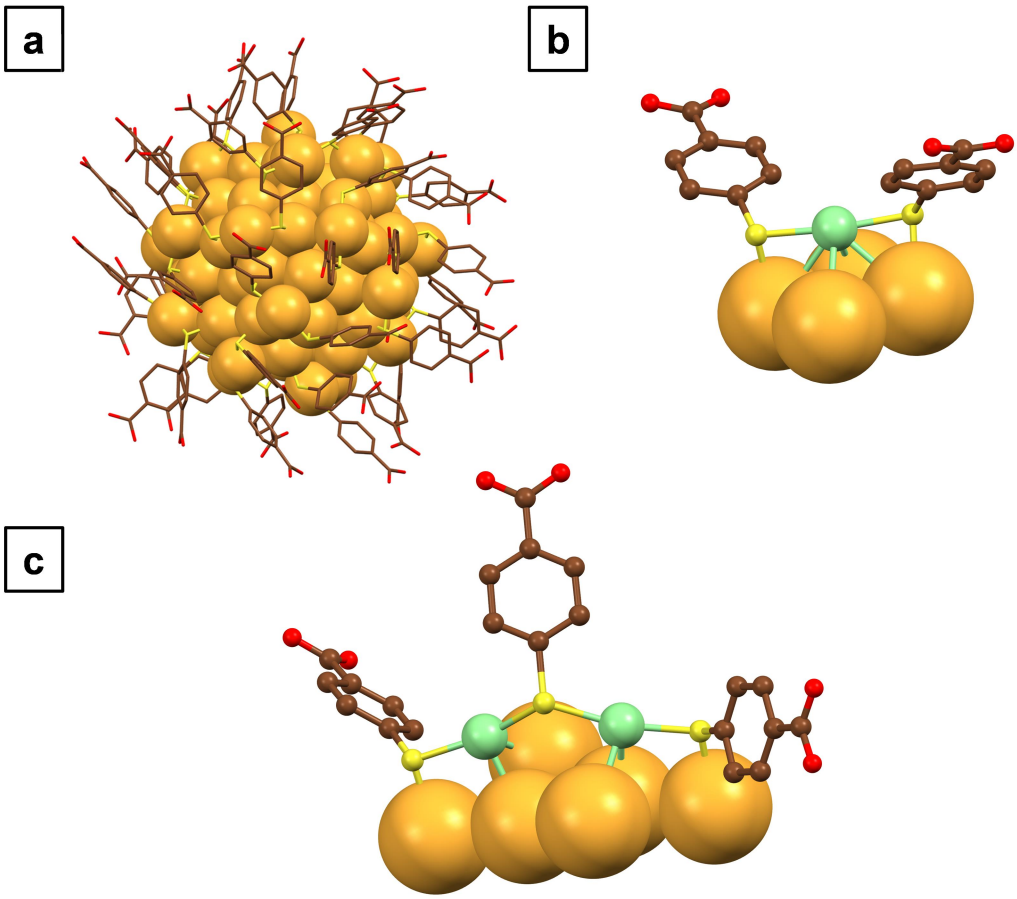

Figure 1.3. Surface coordination chemistry of a thiol monolayer-protected gold nanocluster.[69] (a) Total structure of $Au_{102}(pMBA)_{44}$ (pMBA: *p*-mercaptobenzoic acid; core diameter: ~1.5 nm). (b) Monomeric (−RS−Au−SR−) and (c) dimeric (−RS(−Au−SR)$_2$−) staple motifs on the Au nanocluster surface. Au core atoms are shown as space-filling orange spheres, while the surface-exposed Au staple atoms are represented as smaller, light green spheres for clarification. Color code: Au, orange & light green; S, yellow; O, red; C, brown. The structures were plotted with the Mercury 4.1.0 software,[37] on the basis of the crystallographic information file (CIF) that was retrieved from the Cambridge Crystallographic Data Centre (CCDC),[73] deposition number: CCDC 714255.

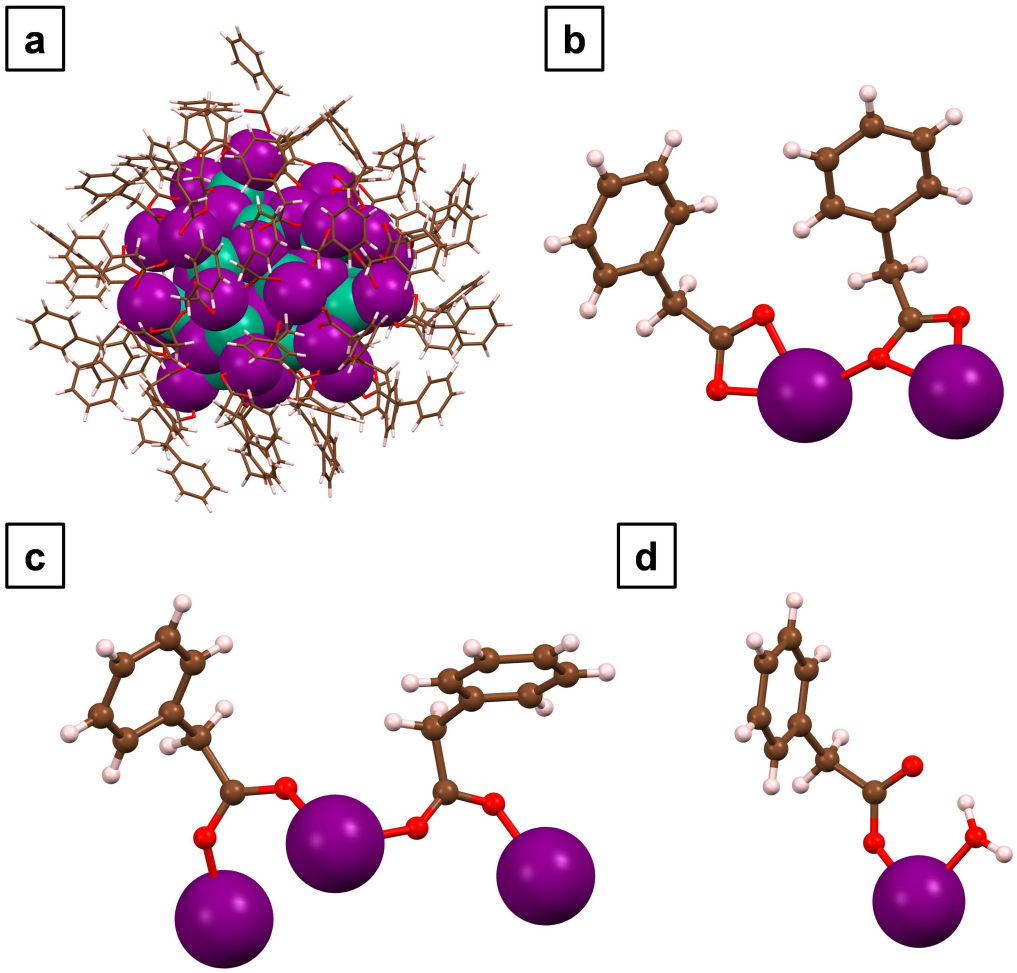

Figure 1.4. Surface coordination chemistry of a carboxylate-ligated indium phosphide nanocluster.[74] (a) Total structure of $In_{37}P_{20}(O_2CCH_2Ph)_{51}(H_2O)$ (core diameter: ~1.3 nm). (b) Bidentate chelating binding modes in normal configuration (left) and with dative contribution to a neighboring In atom (right). (c) Bidentate bridging binding modes in symmetric (left) and asymmetric (right) manifestations. (d) Monodentate binding mode with coadsorbed water. Color code: In, purple; P, green; O, red; C, brown; H, light pink. The structures were plotted from the CIF[74] (CCDC 1417966) using the Mercury 4.1.0 software[37] for visualization.

Another impressive example, showing that the real binding situations can deviate strongly from the ideal, symmetric textbook representations,[75] is the recently reported carboxylate-ligated indium phosphide nanocluster $In_{37}P_{20}(O_2CR)_{51}(H_2O)$ (Figure 1.4a).[74] Interestingly, this small cluster (core diameter: ~1.3 nm) exhibits a broad variability in surface coordination, covering almost all of the known carboxylate binding modes: (i) bidentate chelating binding modes in normal configuration and with dative contribution to a neighboring In atom (Figure 1.4b), (ii) bidentate bridging binding modes in symmetric and asymmetric manifestations (Figure 1.4c), and (iii) monodentate

binding mode with coadsorbed water (Figure 1.4d). The monodentate binding mode is an especially interesting feature as it forms from a water-free precursor cluster upon exposure to moist air, thus indicating the possibility of site-specific ligand chemistry.[74]

As an intermediate entity between molecular complexes and NPs, atomically precise nanoclusters provide the best approximation of the versatile surface coordination chemistry taking place at the organic–inorganic interface of NPs.

1.1.4 Colloidal Stabilization

For many applications, NPs need to be processed in the liquid state,[27] which requires colloidal stabilization. There are two fundamentally different mechanisms to keep the NPs in the dispersed state, thus preventing aggregation of their cores: (i) Steric stabilization in nonpolar media through long-chain ligands and (ii) electrostatic stabilization in polar media by surface-bound charged species.[38,76]

Steric stabilization is a key element in all colloidal syntheses that make use of long-chain, nonpolar surfactants (see section 1.1.2.2). It is based on the fact that chain–solvent interactions are favored over chain–chain interactions, when the NPs are dispersed in a suitable, lipophilic solvent (e.g., *n*-hexane for oleate chains). As a result, the ligand spheres are swollen with solvent molecules and repell each other upon contact to avoid unfavorable ligand–ligand interactions (Figure 1.5a, top). Addition of a polar solvent (e.g., ethanol) destabilizes the system in such a way that the corresponding chain–solvent interactions become highly unfavorable and interdigitation of the ligand chains is preferred (Figure 1.5a, bottom), thus causing the NPs to precipitate. Similarly, when the lipophilic solvent is gradually evaporated, the effective interparticle interaction eventually changes from repulsive to attractive and highly ordered NP superlattices may be obtained.[76] Unsaturated hydrocarbon chains (e.g., oleate) are usually preferred over their saturated counterparts (e.g., stearate) because they enhance steric stabilization due to their weaker chain–chain interactions, which is already evident from their melting points (oleic acid: 14 °C, stearic acid: 69 °C).[77]

Electrostatic stabilization can be realized through ligand exchange of hydrocarbon chains or by direct synthesis of NPs in polar solvents with charged, surface-active species. In both cases, the NP surface is covered with charges, which are surrounded by a diffuse layer of oppositely charged counterions. Such NPs are colloidally stabilized by polar solvents with high dielectric constants (e.g., water, $\varepsilon = 80$ or formamide,

$\varepsilon = 111$)[77] because the solvent molecules effectively screen the opposite charges from electrostatic attraction, forming an electrical double layer (Figure 1.5b, top). As a result, the charged coronas of individual NPs experience electrostatic repulsion as they closely approach each other. Addition of a less polar solvent (e.g., tetrahydrofuran, $\varepsilon = 7.5$)[77] reduces the dielectric screening of the charges and causes the diffuse counterion corona to collapse. The attraction of the opposite charges now enables the NPs to closely approach each other (Figure 1.5b, bottom), resulting in agglomeration and flocculation.

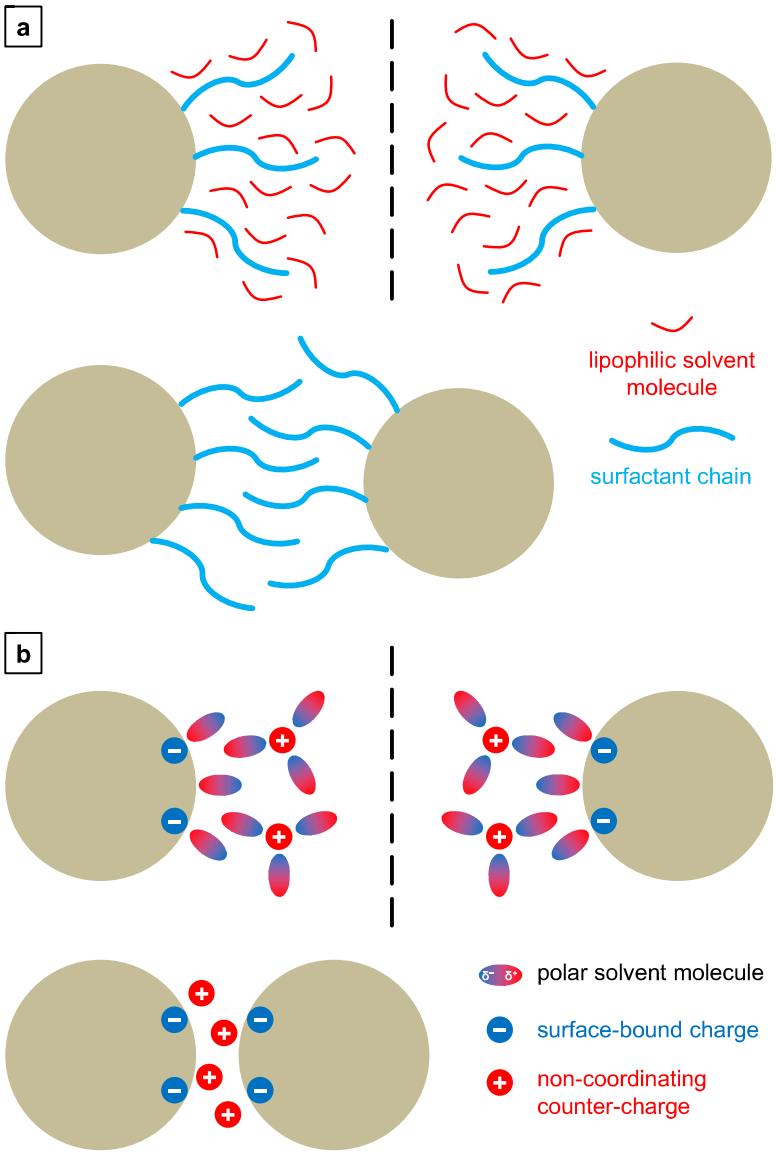

Figure 1.5. Mechanisms of colloidal stabilization. (a) Steric stabilization in nonpolar media through long-chain ligands. (b) Electrostatic stabilization in polar media by surface-bound charges. The upper part of each panel depicts the NPs in their colloidaly stable states, while the lower part shows the destabilized (or dry) states. For the sake of a better overview only a fraction of the complete NP corona is shown in each case.

1.2 Titania Nanoparticles

1.2.1 TiO_2 Polymorphs

Titania (titanium dioxide, TiO_2) occurs naturally as a mineral in the three modifications rutile, anatase, and brookite, all of which can also be obtained synthetically. All three polymorphs have the same coordination chemistry: Each titanium ion is surrounded by 6 oxygen ions in a more or less distorted octahedral configuration (TiO_6), while each oxygen ion is in correspondingly distorted trigonal planar coordination of 3 titanium ions (OTi_3).[78] The different polymorphs result from different linking patterns of the TiO_6 octahedra through edge- and corner-sharing under fulfillment of the above coordination criteria (Table 1.2).[79,80] In rutile, the TiO_6 octahedra share two opposite edges with adjacent octahedra, thus forming linear chains along the **c** axis that are interconnected through shared corners (Figure 1.6a). In anatase, each TiO_6 octahedron shares four edges with neighboring octahedra to form pseudotetrahedral building units that generate a sponge-like three-dimensional structure (Figure 1.6b). Brookite and anatase share the common feature of zigzag octahedral chains (in contrast to rutile's linear chains), but differ in the way these chains are interconnected: While in anatase, each octahedron in the chain connects to two other chains via two shared edges (4 shared edges in total), in brookite, the connection to the other chains is made through one shared edge (3 shared edges in total) and one shared corner (Figure 1.6c).

An alternative to the description of the TiO_2 polymorphs in terms of connected octahedra is to examine the packing motifs of the oxygen sublattices of the three phases. All three phases exhibit more or less distorted types of close-packed oxygen ions, with the titanium ions occupying one half of the octahedral sites.[81] The different polymorphs arise from different layer sequences of the close-packed oxygen sublattice and different distributions of the titanium ions over the octahedral voids. In rutile, the arrangement of the oxygen ions approximates hexagonal close-packing (hcp, layer sequence ABAB),[82] while the structure of anatase is built on a strongly distorted cubic close-packing (ccp, layer sequence ABCABC).[83] Brookite, on the other hand, exhibits a double hexagonal close-packing (dhcp, layer sequence ABACABAC) of the oxygen ions.[79] The octahedral sites are filled with titanium ions in such a way that the TiO_6 octahedra are connected according to the linking patterns described above.

Table 1.2. Linking patterns and packing motifs of the TiO_2 polymorphs.

TiO_2 phase	number of contacted octahedra			close-packing[a] (layer sequence)
	total	edge-shared	corner-shared	
rutile	10	2	8	hcp (ABAB)
anatase	8	4	4	ccp (ABCABC)
brookite	9	3	6	dhcp (ABACABAC)

[a]hcp, hexagonal close-packing; ccp, cubic close-packing; dhcp, double hexagonal close-packing.

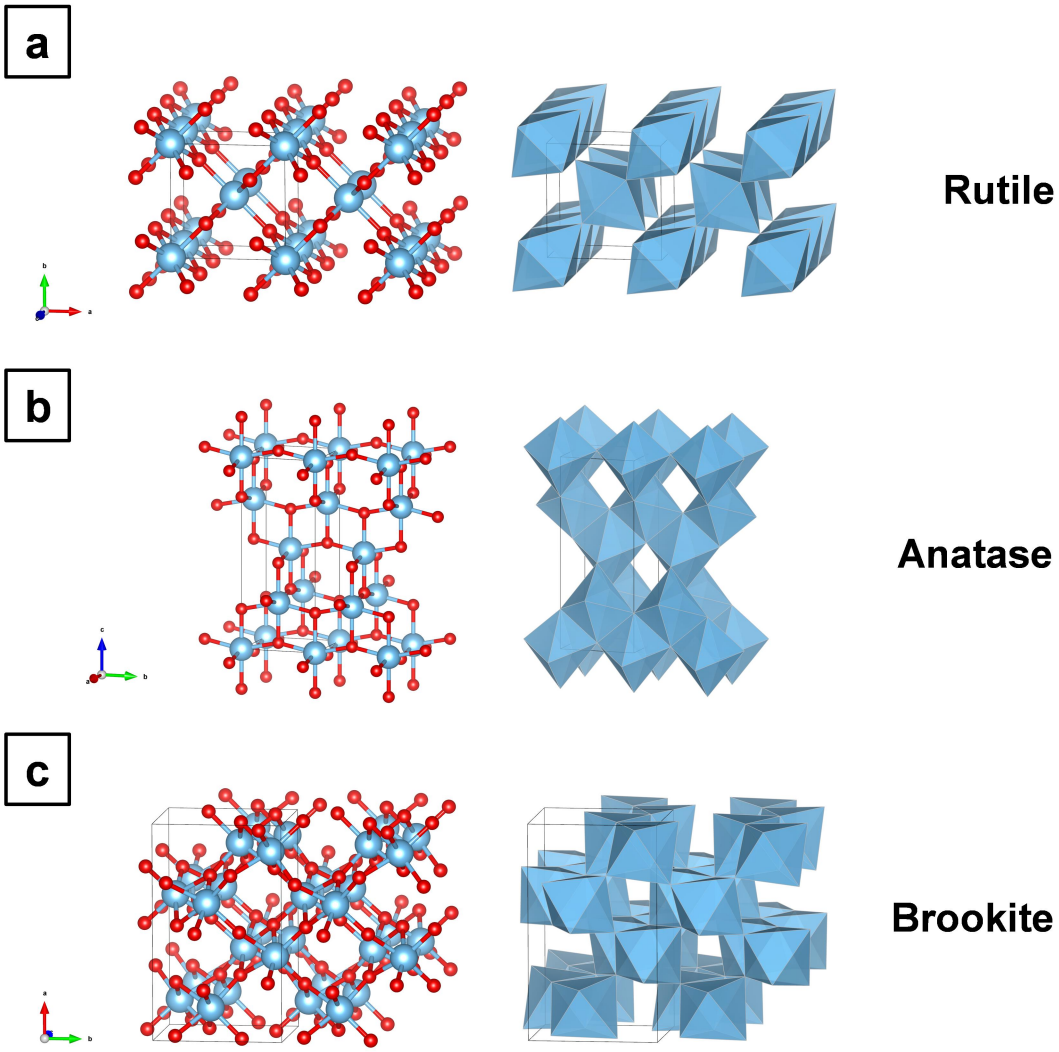

Figure 1.6. Crystal structures of the main TiO_2 polymorphs (a) rutile, (b) anatase, and (c) brookite, each visualized in the ball-and-stick (left) and the polyhedral style (right), using the VESTA 3.4.3 software.[84] Color code: Ti, blue spheres; O, red spheres; [TiO_6], blue octahedra. The CIF data were retrieved from the American Mineralogist Crystal Structure Database (AMCSD)[85] under the depository numbers 0009404 for rutile,[86] 0010735 for anatase,[87] and 0005160 for brookite.[88]

Rutile is the most stable form of TiO_2 under normal conditions, while anatase and brookite are metastable phases that transform irreversibly to rutile at high temperatures.[78,89] For the macrocrystalline materials, the thermodynamic phase stability decreases in the order rutile > brookite > anatase.[90] However, the differences are rather small and so for nanocrystalline materials, the relative phase stability is reversed due to favorable surface-energy effects at the nanoscale. Accordingly, anatase was found to be the most stable phase for crystallite sizes <11 nm, while brookite is dominant in the size range from 11 to 35 nm, and rutile is most stable at sizes >35 nm.[91] It must be noted, though, that these (purely) thermodynamic considerations are insufficient in predicting the resulting TiO_2 polymorph during NP synthesis in solution phase. Instead, the chemical environment during nucleation and growth of TiO_2 NPs has a much more pronounced effect on the resulting polymorph.[92] For instance, it was recently shown, that small rutile NPs (<10 nm) can form prior to the formation of anatase NPs.[93]

1.2.2 Synthetic Methods

Tremendous synthetic efforts have been devoted to the solution-phase preparation of TiO_2 NPs with controlled phase, size, and morphology.[26,94] The synthetic procedures can roughly be devided into aqueous methods (primarily sol−gel and hydrothermal processes), and non-aqueous methods (including solvothermal and ambient-pressure, surfactant-assisted techniques).[26] The subcategory of the ambient-pressure, surfactant-assisted techniques is often categorized under the rather historical term of non-aqueous (or even non-hydrolytic) sol−gel methods in order to highlight the analogy of similar mechanistic pathways in both aqueous and non-aqueous sol−gel chemistries.[25,95] Alternatively, this class of reactions has also been summarized under the term “sol method”,[94] while other reviews refer to it as “heat-up synthses”, following the standard classification of many other colloidal NPs (e.g., CdSe, FePt, or Fe_3O_4) synthesized under similar conditions.[96] Going one step further, Niederberger et al. subdivided the non-aqueous sol−gel methods into surfactant-directed and solvent-controlled approaches[33] to account for their “benzyl alcohol route“, which produces fine TiO_2 NPs without additional surfactants.[97,98] Beside the various classification approaches, it is sometimes difficult to clearly categorize a certain synthetic procedure due to the merging of different techniques. One such example is the surfactant-assisted hydro/solvothermal synthesis of TiO_2 NPs in a two-phase mixture of water/toluene.[99]

Historically, aqueous sol−gel methods were the first synthetic procedures for the preparation of nanoparticulate titania. While these syntheses are simple, scalable, and provide high yields, they allow little control over size and shape and the as-prepared solids usually exhibit poor crystallinity and insufficient dispersibility in liquid media.[26] Some of these drawbacks were overcome with the development of hydrothermal processes, which are performed with aqueous media in closed reaction vessels (i.e., autoclaves) at elevated temperatures and autogenous pressures.[100] The greatest advantage of the hydrothermal method is the strongly enhanced crystallinity of the obtained solids. Furthermore, a fairly good control over the titania phase can be achieved through the addition of suitable carboxylate salts and even the shape can be tuned through the addition of fluoride or sulfate anions, which bind to specific facets of the anatase crystal.[101] Another example for hydrothermal synthesis reported the preparation of size-controlled TiO_2 NPs, which even showed moderate colloidal stability through electrostatic stabilization in acidic environment.[102]

To obtain better control over size, morphology and especially colloidal stability of TiO_2 NPs, the hydrothermal approach was further advanced to the solvothermal approach, which uses organic solvents instead of aqueus media. Compared to the high hydrolysis rates of aqueous procedures, the non-aqueous environment of solvothermal syntheses drastically decreases the reaction rates of the titanium precursors with oxygen-containing organic molecules. Consequently, the growth of TiO_2 NPs proceeds at a lower rate, thus allowing a better control over their size and size distribution. Additionally, organic surfactants can be employed that serve two purposes: (i) They direct the shape evolution of a growing NP through their preferential binding to specific facets. (ii) They impart colloidal stability to the NPs in non-polar media via steric stabilization (cf. section 1.1.4).

Utilizing the solvothermal approach, Kim et al.[103] synthesized colloidal TiO_2 anatase NPs in toluene with oleic acid as surfactant and they were able to change the morphology from quasi-spherical NPs to elongated nanorods by increasing the precursor concentration in solution. Another interesting approach is to to combine the benefits of the solvothermal procedure with the fast hydrolysis rates of hydrothermal synthesis to obtain an even better control over NP morphology. This was done by Dinh et al.[56] by placing a water source in a separated compartment of the reaction vessel, so the only way for the water to hydrolyze the organic titanium precursor was through the vapor

phase. Thus, using water vapor as the hydrolysis agent and adjusting the ratio of the two surfactants OA and OM, they were able to achieve an impressive control over NP morphology, ranging from quasi-spherical, over rhombic, to dog-bone shapes.[56] Although OA and OM are the shape-directing additives, it is the fast hydrolysis through water vapor that enables the facet-specific growth of the NPs in the first place.

The most versatile and advanced category of TiO_2 NP syntheses are the non-aqueous, surfactant-assisted methods that are typically performed in conventional reaction flasks at elevated temperatures and ambient pressure using standard Schlenk line techniques. An early example was the synthesis of colloidally stable TiO_2 NPs via non-hydrolytic condensation reactions between the two precursors titanium halide and titanium alkoxide in the presence of TOPO as surfactant.[104] Using only titanium alkoxide as precursor in combination with OA and OM as surfactants, Zhang et al.[105] synthesized colloidal TiO_2 nanodots (of 2.3 nm diameter) and nanorods with tunable aspect ratio and narrow size distribution.

A more elaborate synthesis for TiO_2 nanorods with tunable length was achieved by Buonsanti et al.[106] through a seed-mediated growth approach. This is a two-step process, where first, small TiO_2 anatase seeds were prepared from the reaction of $TiCl_4$ with OA and OM, which were then reacted with defined amounts of additional $TiCl_4$ precursor to produce TiO_2 nanorods of specific length. Interestingly enough, the authors observed a phase transition from the anatase to the brookite structure for nanorods longer than 30 nm.[106] Extending this seed-mediated growth approach to additional titanium precursors and co-surfactants, Gordon et al.[107] achieved an unprecedented level of shape control with narrow size distributions. Here, both titanium halides $TiCl_4$ and TiF_4 were used as precursors, in conjunction with either oleyl amine or octadecanol as co-surfactants. These combinations allowed the authors to precisely engineer the ratio of {001} and {101} facets on the correspondingly shaped TiO_2 anatase NPs. The expectionally narrow size distributions achieved in this seed-mediated growth approach are attributed to the temporal separation of the nucleation (seed formation from initial precursor) and growth (conversion of additional precursor) stages during the synthesis.[106,108]

1.2.3 Mechanistic Considerations

In most of the synthetic methods introduced in section 1.2.2, tetravalent titanium precursors are used as starting materials for TiO_2 preparation, mainly titanium halides and alkoxides, such as titanium tetrachloride $TiCl_4$ and titanium tetraisopropoxide $Ti(O^iPr)_4$. All of these precursors have highly Lewis-acidic Ti(IV) centers that are sensitive to nuclephilic attack by water and other oxygen-containing molecules. As a result of the nucleophilic attack, the coordination geometry expands from tetrahedral (with coordination number 4) to octahedral (with coordination number 6), thus saturating the precursor's electron deficiency.

The high reactivity is reflected in a fast hydrolysis of titanium alkoxide precursors in aqueous environment, yielding a white precipitate of an amorphous, hydrated titania phase.[109,110] The first steps of this conversion involve the actual hydrolysis of titanium alkoxide (eq 1.1), followed by condensation reactions through oxolation (eq 1.2) and alkoxolation (eq 1.3), thus forming oxo bridges between individual Ti(IV) centers.[25,111]

$$\equiv Ti{-}OR + H_2O \rightarrow \equiv Ti{-}OH + ROH \quad (1.1)$$

$$\equiv Ti{-}OH + HO{-}Ti\equiv \rightarrow \equiv Ti{-}O{-}Ti\equiv + H_2O \quad (1.2)$$

$$\equiv Ti{-}OR + HO{-}Ti\equiv \rightarrow \equiv Ti{-}O{-}Ti\equiv + ROH \quad (1.3)$$

Upon further condensation and concomitant expansion of the coordination sphere, a polymeric network of hydrated, connected $[TiO_6]$ octahedra is formed. These polymeric structures have no long-range order, which is the reason for the poor crystallinity of sol−gel-derived oxides.

Due to the high reaction rates of the hydrolysis step (eq 1.1), the active monomeric species in titania NP formation are often postulated to be octahedral hydroxo−aquo complexes, which are expected to condense in a more or less linear fashion.[112–115] However, extensive studies in the field of titanium oxo clusters (TOCs), also known as polyoxotitanates (POTs),[116–118] have disclosed a plethora of stable, polynuclear titanium compounds, ranging from low-molecular-weight Ti_3 complexes[119] to large, elongated Ti_{52}−oxo nanoclusters with a length of 3.6 nm.[120] These studies suggest that TiO_2 NP formation does not proceed through a continuous step-by-step growth via addition of isolated octahedral building units, but rather through a staged process, where first, poly-

nuclear TOCs are formed as active monomeric species, which then condense to generate bigger structures.[121]

This picture is further supported by the fact that TOCs are usually prepared under synthetic conditions that are very similar to those of NP syntheses. Table 1.3 provides a comparative representation of NP and cluster syntheses based on the two Ti precursors $TiCl_4$ and $Ti(O^iPr)_4$ under both, aqueous and non-aqueous reaction conditions. It becomes evident that most of the NP synthesis methods from section 1.2.2 are suitable to produce TOCs when the reaction conditions are adapted accordingly, i.e., lower temperatures, longer reaction durations, and controlled amounts of added water. Consequently, many authors regard TOCs as prenucleation clusters or snapshots of intermediate structures during TiO_2 NP formation.[119,122–125]

The notion of polyoxometalate clusters as intermediates in NP formation is not limited to TiO_2, but has also been expressed for other transition metal oxides, such as Zr,[126] Hf,[127] and Fe[128] oxides. This picture is further supported by the observation that polyoxometalate clusters increase in size when reaction temperatures are increased, thus achieving higher degrees of condensation.[126,129]

Interestingly, some of the higher-nuclearity clusters have been reported to exhibit structural units that strongly resemble the crystal structures of the TiO_2 polymorphs rutile,[122,130] anatase,[122,124] and brookite[131,132] (cf. section 1.2.1). Some authors have even claimed that the structure of the titanium precursor complex can influence the resulting TiO_2 phase.[112,131] However, this is generally not the case, as many studies have shown that the chemical environment has a much more pronounced effect on the phase composition, resulting from a complex interplay of several factors, such as pH, temperature and presence of counterions or additives.[92,115,133,134] Furthermore, phase transitions can also occur during the growth of NPs, a process that is completely decoupled from the precursor's structure.[106,135]

Table 1.3. Parallels between NP and cluster syntheses.[a,b]

RM	SP	Ti precursor: $TiCl_4$	Ti precursor: $Ti(O^iPr)_4$
aqueous	NP	$TiCl_4$ in HCl(aq);[113] 90 °C, air atmosphere, 6 h; anatase crystallites, 10 nm	$Ti(O^iPr)_4$ in isopropanol + H_2O;[136] 250 °C, hydrothermal, 20 min; anatase crystallites, 5 nm
	cluster	$TiCl_4$ in H_2O + TBAC;[124] ambient conditions, few days; $[Ti_6O_8(OH_2)_{20}]^{8+}$ 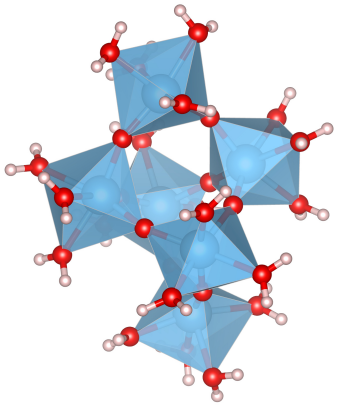 (CCDC 1418040)	$Ti(O^iPr)_4$ in isopropanol + 1 equiv. H_2O;[137] 100 °C, ambient pressure, 3 d; $Ti_{12}O_{16}(O^iPr)_{16}$ 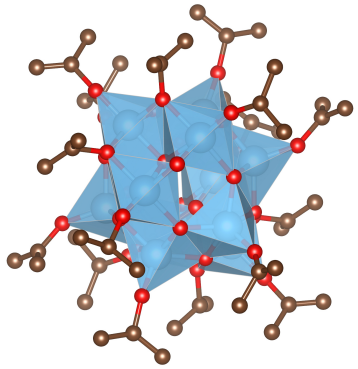 (CCDC 1300021)
non-aqueous	NP	OM & OA in ODE + $TiCl_4$ in ODE;[106,107] 290 °C, ambient pressure, 30 min; brookite nanorods, 50 nm	$Ti(O^iPr)_4$ in OA;[138] 270 °C, ambient pressure, 2.5 h; anatase nanorods, 40 nm
	cluster	propanoic acid in CCl_4 + $TiCl_4$;[139] 70 °C, ambient pressure, 0.5 h; $Ti_3O_2Cl_3(O_2CEt)_5$ 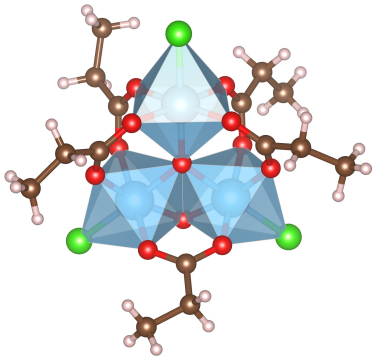 (CCDC 225068)	$Ti(O^iPr)_4$ in toluene + formic acid;[140] room temperature, inert atmosphere, 12 h; $Ti_6O_6(O^iPr)_6(O_2CH)_6$ 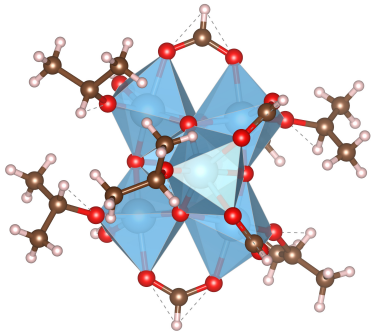 (CCDC 1169959)

[a]Abbreviations: RM, reaction medium; SP, synthetic product; TBAC, tetrabutylammonium chloride; ODE, 1-octadecene. [b]Color code: Ti, blue; O, red; Cl, green; C, brown; H, light pink. Structures were plotted with VESTA 3.4.3.[84]

1.2.4 TiO_2 Surface Chemistry

For most applications of TiO_2 NPs the surface structure and its interaction with organic molecules is of utmost importance. Among the three polymorphs of TiO_2 (cf. section 1.2.1), anatase is the the most frequently employed representative, especially with regard to its photoreactivity (section 1.2.5). Using a Wulff construction, the equilibrium shape of an anatase crystal was calculated to be a slightly truncated tetragonal bipyramid (Figure 1.7a), limited by a majority of {101} facets (94% of the crystal surface) and a minority of {001} facets (6%).[141] This shape corresponds well to the shape of naturally occuring anatase minerals[142,143] and has been reproduced in many TiO_2 NP syntheses.[56,107,144] The ideal atomic structure of the (001) anatase surface (Figure 1.7b, top) is characterized by five-fold coordinated Ti surface sites (Ti_{5c}) and two- and three-fold coordinated O sites (O_{2c}, O_{3c}), whereas the ideal (101) surface layer (Figure 1.7b, bottom) is composed of both saturated Ti_{6c} and O_{3c} sites and undercoordinated Ti_{5c} and O_{2c} surface sites.[145,146] Due to their low surface energy, the {101} facets are thermodynamically the most stable among all TiO_2 anatase facets, while the {001} high energy facets are significantly more reactive in most surface-related processes.[147,148]

All facets interact with organic and inorganic molecules in their specific manners and reactivities, thus altering their catalytic activities. Many studies have investigated the adsorption behavior of inorganic anions onto TiO_2 anatase surfaces, including carbonate (CO_3^{2-}),[149] sulfate (SO_4^{2-}),[150] and phosphate (PO_4^{3-})[151,152] ions. Most of these studies focus on how the adsorption of inorganic anions affects the NPs' photocatalytic acitivy.[149,153] Apart from catalytic performance, inorganic anions also play a crucial role in the synthesis of TiO_2 NPs as their adsorption characteristics can dramatically influence the size, shape, and phase of the resulting titania.[26,101] This is especially true for halide ions, which have been used for shape tuning of anatase NPs.[107,154] In particular, fluoride (F^-) ions were found to selectively bind to {001} high energy facets, thus directing the NP morphology towards platelet shape with astonishingly high percentages of fluorine-terminated {001} facets.[155–157] To retrieve the reactive nature of fluorine-passivated {001} facets, the NPs are simply treated with aqueous NaOH solution, whereupon fluoride is exchanged with hydroxide.[107,158,159]

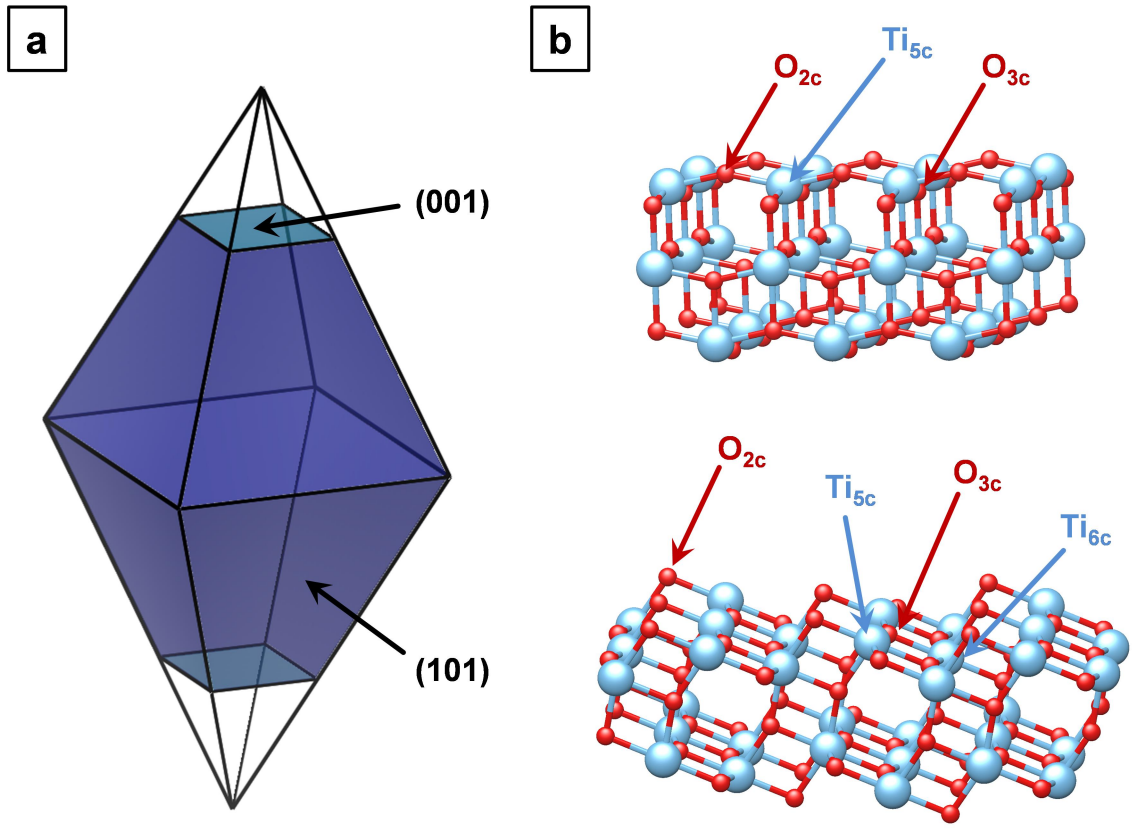

Figure 1.7. Surface structure of anatase TiO_2. (a) Slightly truncated tetragonal bipyramid as the equilibrium shape of an anatase crystal with the main facets {001} and {101}. (b) Ideal atomic structures of the (001) (top) and (101) (bottom) anatase surfaces. Two- and three-fold coordinated O atoms and five- and six-fold coordinated Ti atoms are denoted by O_{2c}, O_{3c}, Ti_{5c} and Ti_{6c}, respectively. Color code: Ti, blue; O, red. Structures visualized with VESTA 3.4.3.[84]

In analogy to the oxygen-containing inorganic ions, TiO_2 anatase surfaces have also been subjected to organic molecules with carboxylate ($-CO_2^-$),[160] sulfonate ($-SO_3^-$),[161] and phosphonate ($-PO_3^{2-}$)[162] binding groups. Most of those studies seek to optimize the optoelectronic coupling at the TiO_2–molecule interface[161] or to enhance dispersibility of TiO_2 NPs in various solvents.[163,164] Phosphonate was found to exhibit the highest binding affinity among the three anchoring groups.[161,165,166]

Numerous density functional theory (DFT) calculations revealed a higher reactivity of {001} facets towards chemisorption of organic molecules,[148] such as trifluoroacetic acid[167] or the nerve agent sarin.[168] The difference in adsorption behavior of various TiO_2 facets can be exploited to differentiate Ti surface states by means of nuclear magnetic resonance (NMR) spectroscopy. Here, a phosphor-containing surface probe (tri-

methylphosphine, TMP) produces distinctive signals in ^{31}P NMR spectra that can be attributed to specific surface adsorption sites on the {001} and {101} facets.[169,170]

Multiple studies have shown that adsorption onto TiO_2 NPs usually follows some Langmuir-type adsorption model,[171] both for inorganic[149,153] and for organic adsorbates.[158,172]

1.2.4.1 Catechol Functionalization

Apart from the organic adsorbates described above, another anchoring group has become very popular over the last 20 years: the catechol (1,2-dihydroxybenzene) group, which is well-known for its versatile chemistry in mussel adhesive proteins.[173] The catechol moiety has three major advantages as an anchoring group for metal oxides in general: (i) It allows for virtually irreversible surface binding due to its bidentate binding geometry and remarkably high binding constants,[174,175] which have their origin in an enhanced orbital overlap between metal d-orbitals and ligand valence orbitals as compared to carboxylate complexes.[176,177] (ii) Catechol derivatives are redox-active compounds that facilitate electron transfer processes across the ligand−metal interface.[178–180] This property is crucial for catalytic processes, such as in the fields of bioinorganic[181] and of synthetic organic chemistry.[182] (iii) The catechol moiety can be easily modified through ring substituents with desired chemical functionalities and can thus be incorporated into the sidechains of a polymer backbone.[183]

Similar to other adsorbates (*vide supra*), numerous studies of catechol chemisorption on TiO_2 NPs revealed Langmuirian adsorption behavior.[11,180,184–186] All of these studies investigated catechol chemisorption on hydrophilic colloidal TiO_2 in aqueous media, but the Langmuirian adsorption model also holds true for chemisorption on hydrophobic TiO_2 NPs in non-aqueous, organic media, as will be described in Chapter 2.

Due to the nanoscale nature of NP surfaces with their high curvatures and intrinsic heterogeneities, it is extremely challenging to determine the exact binding modes of chemisorbed catechol molecules. However, the true picture of the organic−inorganic interface can be approximated by two different approaches that provide complementary views on NP surface complexation: (i) Adsorption studies on extended, flat TiO_2 surfaces, such as the (001) and (101) anatase surfaces shown in Figure 1.7b, allow to describe the binding modes on pronounced crystal facets. (ii) Atomically precise X-ray structures of catechol-containing TOCs can serve as model systems to describe the more

complex binding situations on the edges and vertices of the NP, where crystal facets meet, and on irregular surface sites in general.

The investigation of catechol adsorption on flat TiO_2 surfaces is usually performed through a combination of several characterization techniques, most notably scanning tunneling microscopy (STM),[187,188] photoelectron spectroscopy (PES),[189] and near-edge X-ray absorption fine structure (NEXAFS) spectroscopy,[190] routinely supported by DFT calculations.[191] These studies have revealed that catechol binds onto TiO_2 surfaces (both rutile and anatase) predominantly in a bridging bidentate configuration, with the aromatic rings usually tilted by ~30° with respect to the surface normal,[190] as represented in Figure 1.8 for catechol chemisorption onto the TiO_2 anatase (101) surface. Furthermore, it was found that only bidentately bound catechol generates energy states in the band gap of TiO_2, thus boosting the potential for extended light absorption and enhanced photoreactivity (cf. section 1.2.5.2).[189]

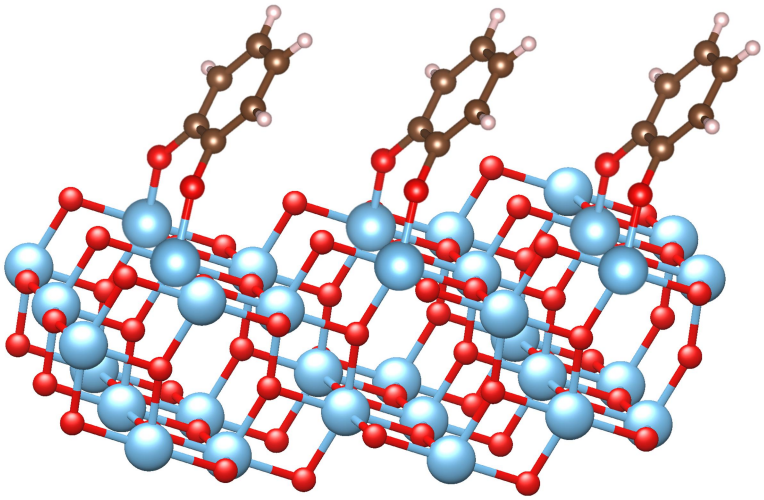

Figure 1.8. Atomistic model of bridging bidentate catechol adsorption on (101) TiO_2 anatase surfaces. Color code: Ti, blue; O, red; C, brown; H, light pink. Structures visualized with VESTA 3.4.3.[84]

Similar to the description of the organic–inorganic interface in section 1.1.3, polynuclear, catechol-containing TOCs can give an approximate picture of the true binding situations of catechol at irregular surface sites, such as the edges and corners of TiO_2 NPs. Over the last two decades, a large variety of catechol-containing TOCs have been synthesized.[118,132,192,193] Apart from the commonly discussed catechol binding modes

(bridging bidentate vs. chelate bidentate),[75,173] the great structural diversity of catechol-containing TOCs allows for further, partly exotic binding modes (Table 1.4).

When titanium alkoxide precursors are reacted with an excess of catechol (molar ratio catechol/Ti = 3),[132,194] very small TOCs with Ti_2 core and catechol in monodentate coordination mode are obtained (Table 1.4, entry 1). Monodentate catechol coordination has also been discussed for the adsorption onto TiO_2 at high catechol surface coverages.[173,189] For reduced molar ratios, a variety of chelate binding modes is found (Table 1.4, entries 2+3). A molar ratio catechol/Ti of 2 still yields very small TOCs (with Ti_2 or Ti_3 core),[195,196] but with bidentate chelate binding mode, where both oxygens bind simultaneously to the same Ti site (Table 1.4, entry 2). Further reduction of the molar ratio towards 1 increases the cluster nuclearity (with Ti_6 or Ti_{10} cores)[132,192] and promotes the formation of singly and doubly bridging chelate binding motifs, where one catecholato ligand bridges two or even three Ti ions (Table 1.4, entry 3).

Although the bridging bidentate motif is the most accepted adsorption mode for catechol on flat TiO_2 surfaces (cf. Figure 1.8), there are only few reports of catechol-containing TOCs featuring this binding motif. One such rare example is the $Ti_{10}O_{12}(cat)_8(py)_8$ (py = pyridine)[197] cluster depicted in Table 1.4 (entry 4), which is the condensation product of the catechol-containing precursor complex $Ti_2(cat)_4(DMA)_2$ (DMA = dimethylacetamide)[198] in hot pyridine. The fact that this binding motif has only been observed on a high-nuclearity cluster so far might be an indication that it preferentially forms on extended structures, including flat surfaces and NP facets.

The chelate bidentate mode usually occurs on low-nuclearity clusters at terminal positions (cf. Table 1.4, entry 2). However, this binding motif has also been observed on the vertices of a high-nuclearity cluster with Ti_{17} core (Table 1.4, entry 5)[132] after catechol ligand exchange of the preformed $Ti_{17}O_{24}(O^iPr)_{20}$ cluster.[129] Strikingly, the ligand exchange only took place at undercoordinated Ti_{5c} sites, which were transformed into saturated six-fold coordinated Ti_{6c} upon chelate bidentate binding of catecholate. This adsorption behavior is also highly conceivable for catechol functionalization of TiO_2 NPs.

Table 1.4. Catechol-containing TOCs and binding motifs.[a,b]

entry	CLN	molecular structure (CCDC)	catechol binding motif[c]
1	2	$Ti_2(cat)_2(cat\text{-}H)_2(OMe)_2(HOMe)_2$ (1489373)[194] 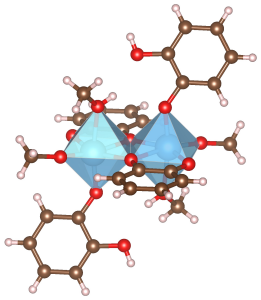	monodentate μ_1-(O) 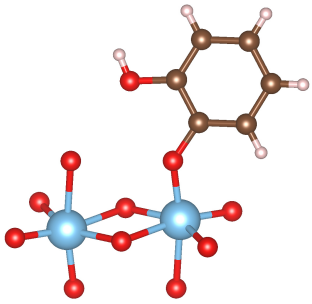
2	2	$Ti_2(cat)_4(HO^iPr)_2$ (284457)[196] 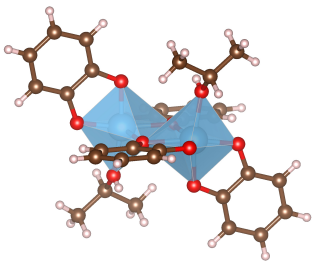	chelate bidentate μ_1-(O,O′) 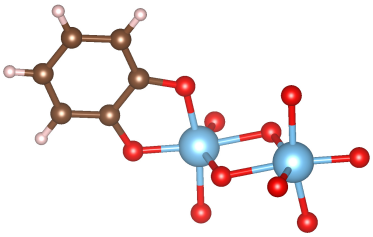
3	6	$Ti_6O(cat)_6(O^iPr)_{10}$ (779643)[132] 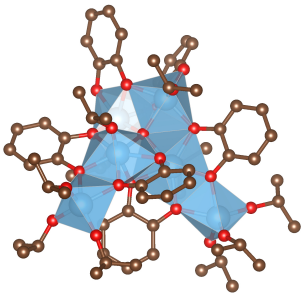	singly bridging chelate μ_2-(O,O′,O′) 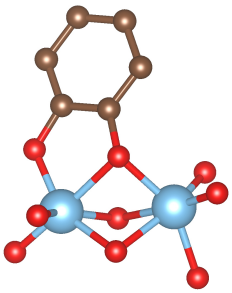
			doubly bridging chelate μ_3-(O,O,O′,O′) 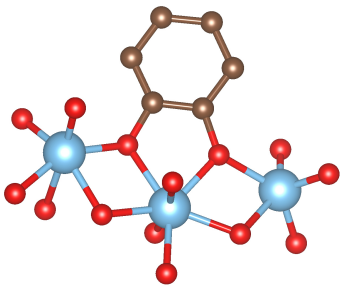

Table 1.4. Continued.

entry	CLN	molecular structure (CCDC)	catechol binding motif[c]
4	10	$Ti_{10}O_{12}(cat)_8(py)_8$ (953666)[197] 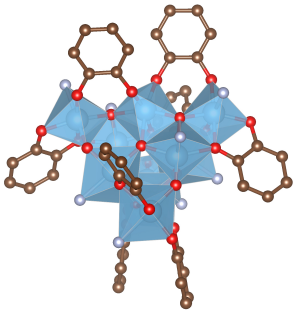	bridging bidentate μ_2-(O,O′) 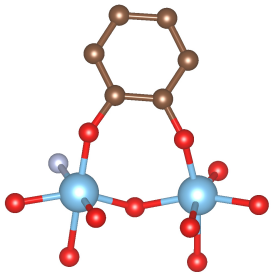
5	17	$Ti_{17}O_{24}(cat)_4(O^iPr)_{16}$ (779644)[132] 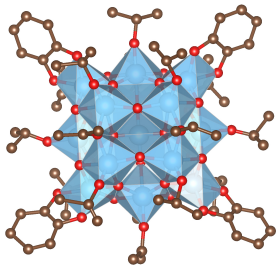	chelate bidentate μ_1-(O,O′) 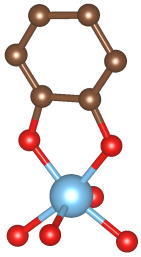

[a]Abbreviations: CLN, cluster nuclearity; cat, catecholate dianion $(C_6H_4O_2)^{2-}$; cat-H, catecholate monoanion $(C_6H_5O_2)^-$; py, pyridine. [b]Color code: Ti, blue; O, red; N, grey; C, brown; H, light pink. Structures were plotted with VESTA 3.4.3[84] from the corresponding CIF data. H atoms are omitted for clarity in the cases of the higher-nuclearity clusters. [c]Notations according to references 192,199.

Considering the variety of binding sites on a NP surface, which is mainly governed by its facets and the interfacing edges and vertices, it appears more than likely that several of the described binding motifs coexist at varying proportions on the same TiO_2 NP. For instance, it is very plausible to assume that catechol functionalization yields bridging bidentate binding on anatase (101) surfaces (cf. Figure 1.8), whereas the vertices are coordinated in chelate bidentate mode (Table 1.4, entry 5). Furthermore, increased ligand concentrations may also lead to monodentate catechol binding (Table 1.4, entry 1) in competition to the bidentate modes.

1.2.5 Photoreactivity

1.2.5.1 Principles

TiO_2 is a semiconductor with a wide band gap separating the occupied energy states in the valence band (VB) from the vacant states in the conduction band (CB). The photoreactivity of TiO_2 is based on the fact that electrons can overcome the band gap by absorption of UV radiation, thereby generating a quasiparticle with positive charge, also known as a hole, in the VB (Figure 1.9). Both constituents of the generated electron−hole pair can move independently throughout the particle and to its surfaces before finishing their lifetimes in one of several possible pathways of de-excitation (cf. Figure 1.9).[80,200] The most preferred options in terms of photocatalysis are pathways ❶ and ❷, where the charge carriers are taking part in redox reactions on the NP surface: Here, the electrons reduce an acceptor molecule A (pathway ❶), while the holes oxidize a donor species D (pathway ❷). The undesired decay pathways are electron−hole recombinations within the NP volume (pathway ❸) or at its surfaces (pathway ❹). These fundamental processes are summarized by the following equations:

electron−hole pair formation	$TiO_2 + \text{photon}\ (h\nu) \rightarrow e^-_{CB} + h^+_{VB}$	(1.4)
reduction	$e^-_{CB} + A \rightarrow A^-$	(1.5)
oxidation	$h^+_{VB} + D \rightarrow D^+$	(1.6)
electron−hole recombination	$e^-_{CB} + h^+_{VB} \rightarrow \text{photon/phonon}$	(1.7)

The valence band of TiO_2 is composed of overlapping 2p orbitals of the oxygen atoms, whereas the lower section of the conduction band results from overlapping 3d orbitals of the titanium atoms.[200,201] Due to their different crystal structures (cf. section 1.2.1), the three TiO_2 polymorphs rutile, anatase, and brookite differ significantly in their electronic band structures, thus exhibiting different band gaps: 3.0 eV in rutile, 3.2 eV in anatase, and 3.4 eV in brookite.[202,203] Among these three polymorphs, anatase has been found to show the highest activity in many photocatalytic reactions due to lower recombination rates of electron−hole pairs.[204] To overcome its band gap of 3.2 eV, anatase particles have to be irradiated with UV light of wavelength $\lambda <$ 387 nm.[201]

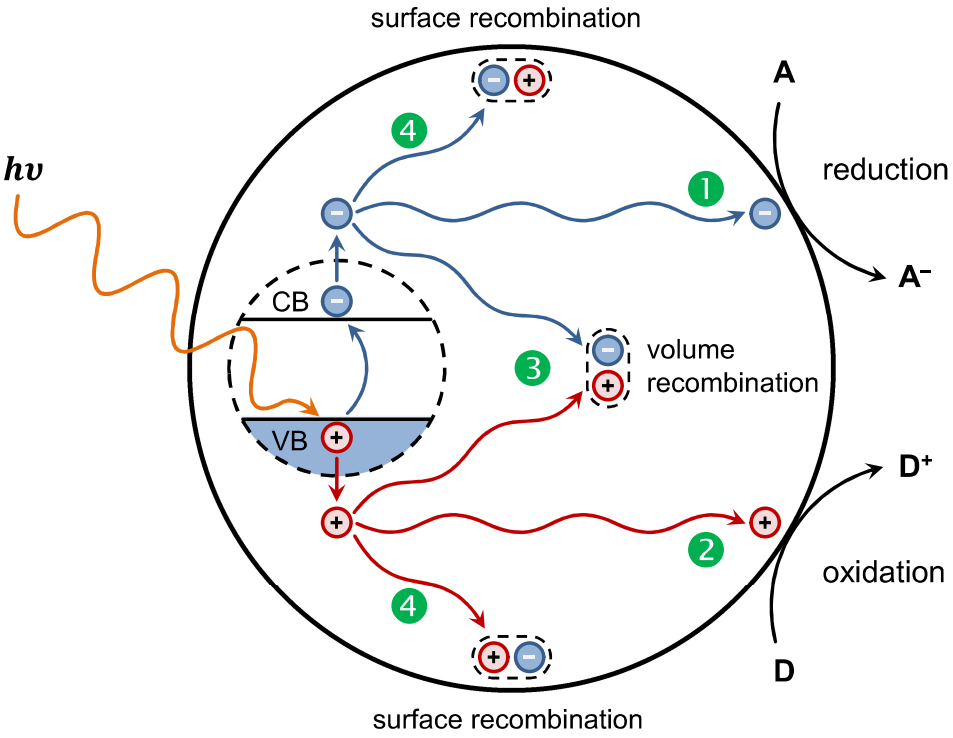

Figure 1.9. Electron–hole pair formation after photoexcitation in a semiconductor NP and subsequent de-excitation pathways. (−), electron; (+), hole; *hν*, photon; CB, conduction band; VB, valence band; A, electron acceptor; D, electron donor. Adapted from reference 80.

The reductive and oxidative power of photogenerated electrons and holes in a semiconductor NP is determined by its band edge positions. Oxide semiconductor surfaces in contact with aqueous solutions typically exhibit Nernstian pH dependence of their band edge positions, just like any other pH-dependent redox couple.[205,206] Accordingly, the band edges at the surface shift to more cathodic, i.e. more negative potentials with increasing pH value, with 59 mV per pH unit at 298 K (eq 1.8).

$$E^0 = E^0(\text{pH } 0) - 0.059\ \text{V} \cdot \text{pH} \tag{1.8}$$

For TiO_2 anatase in neutral aqueous solution, the conduction band minimum (CBM) is at −0.55 V against the normal hydrogen electrode (NHE), while the valence band maximum (VBM) lies at +2.65 V vs. NHE (Figure 1.10, left).[207] For the reduction process (eq 1.5) to occur at the NP surface, the CBM has to be more negative than the reduction potential of the acceptor, while on the other side, the VBM has to be more positive than the reduction potential of the donor to cause its oxidation (eq 1.6). Due to the wide band gap of the TiO_2 anatase modification and its favorable band edge posi-

tions, photoexcited anatase is able to support a variety of redox processes (Figure 1.10, right). Its CBM is sufficiently negative to reduce protons to hydrogen ($E^0(H^+/H_2)$ = −0.41 V vs. NHE at pH 7) and its VBM has enough oxidative potential to generate O_2 from water ($E^0(O_2/H_2O)$ = +0.81 V), thus making anatase a promising material for photocatalytic water splitting.[208–210]

Furthermore, in aerated solutions, the photoexcited electron can be transferred to an oxygen molecule to generate the superoxide radical anion $^{\bullet}O_2^-$ ($E^0(O_2/^{\bullet}O_2^-)$ = −0.33 V), while hole oxidation of adsorbed water promotes the formation of the hydroxyl radical $^{\bullet}OH$ ($E^0(^{\bullet}OH/H_2O)$ = +2.32 V). Both radicals are well-known reactive oxygen species (ROS)[211,212] that are important reactants in the photocatalytic degradation of pollutants, with many applications in environmental remediation.[213–215]

Another heavily investigated application is the photocatalytic reduction of CO_2 into solar fuels such as methane or methanol.[200,216] Apart from these traditional applications, the redox properties of photoexcited TiO_2 can also be used for selective organic transformations,[217–220] including reduction,[221,222] oxidation[223–225] (cf. Chapter 3), and coupling reactions.[226,227]

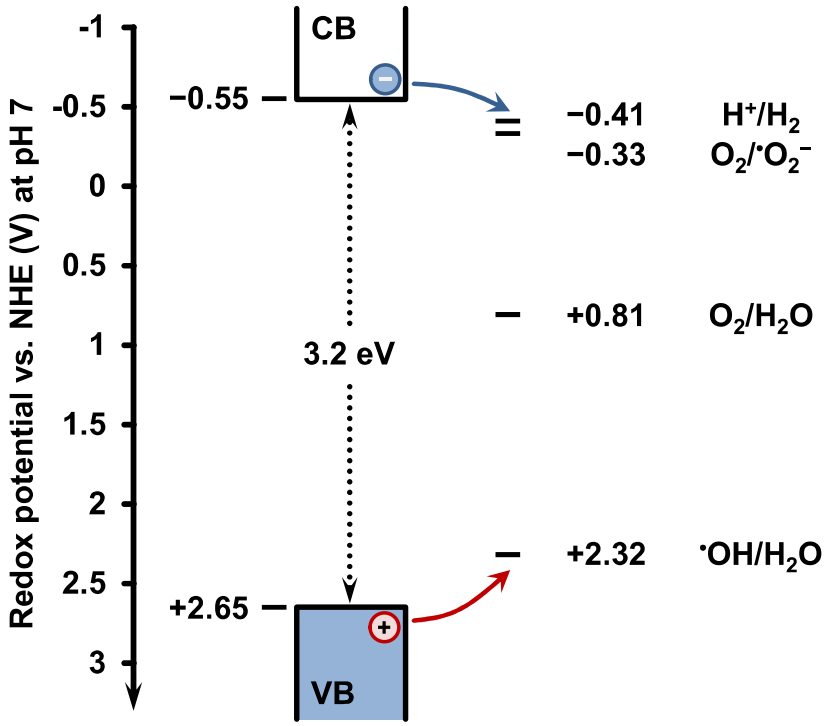

Figure 1.10. Band edge positions of anatase TiO_2 and reduction potentials of common species in aqueous photocatalysis. The redox potentials are presented relative to the normal hydrogen electrode (NHE) at pH 7 and were calculated according to eq 1.8 from the corresponding values at pH 0 from refs 207,228,229.

1.2.5.2 Surface Sensitization

Despite its superior properties in terms of photocatalytic activity and chemical stability, one of the biggest drawbacks of TiO_2 is its wide band gap that only allows high-energy excitation with UV light (cf. section 1.2.5.1). In order to extend the light absorption of TiO_2 into the visible range of the solar spectrum, thus increasing its impact for sustainable applications, two major approaches have been intensively pursued: (i) band gap engineering via doping with other elements and (ii) surface sensitization through visible-light-responsive adsorbates.[209] The latter strategy has become particularly popular with the introduction of dye-sensitized solar cells (DSSCs) by O'Regan and Grätzel in 1991.[230] Here, TiO_2 NPs are decorated with dye molecules, typically Ru-containing complexes, that absorb light in the visible range.[231] The sensitization principle of DSSCs is depicted in Figure 1.11a: Upon light absorption, an electron is excited from the highest occupied molecular orbital (HOMO) to the lowest unoccupied molecular orbital (LUMO) within the dye molecule (step ❶). Due to the close proximity of the semiconductor surface, the photoexcited electron can then be transferred to the TiO_2 NP through injection into higher states of the CB (step ❷). Eventually, the electron reaches the CBM after relaxation via electron−phonon interactions (step ❸).[232] This two-step photoinjection scheme is often referred to as type I sensitization.[233]

If the electronic coupling between the organic adsorbate and the TiO_2 CB is particularly strong, the electron dynamics change dramatically and the photoinjection occurs directly from the adsorbate's HOMO into the semiconductor's CB edge (Figure 1.11b, step ❹). This one-step process is a direct consequence of ligand-to-metal charge transfer (LMCT) and is usually classified as type II photosensitization.[232,234] The catechol molecule (cf. section 1.2.4.1) is the most heavily investigated representative of this class, as it is very strongly coupled to the TiO_2 CB, thus producing a pronounced LMCT band in absorption spectra.[235,236] Interestingly, despite bearing a catechol moiety, the anthraquinone dye alizarin does not exhibit the direct photoinjection characteristics of a strongly coupled adsorbate, but is rather a type I sensitizer with indirect electron injection.[232,237,238]

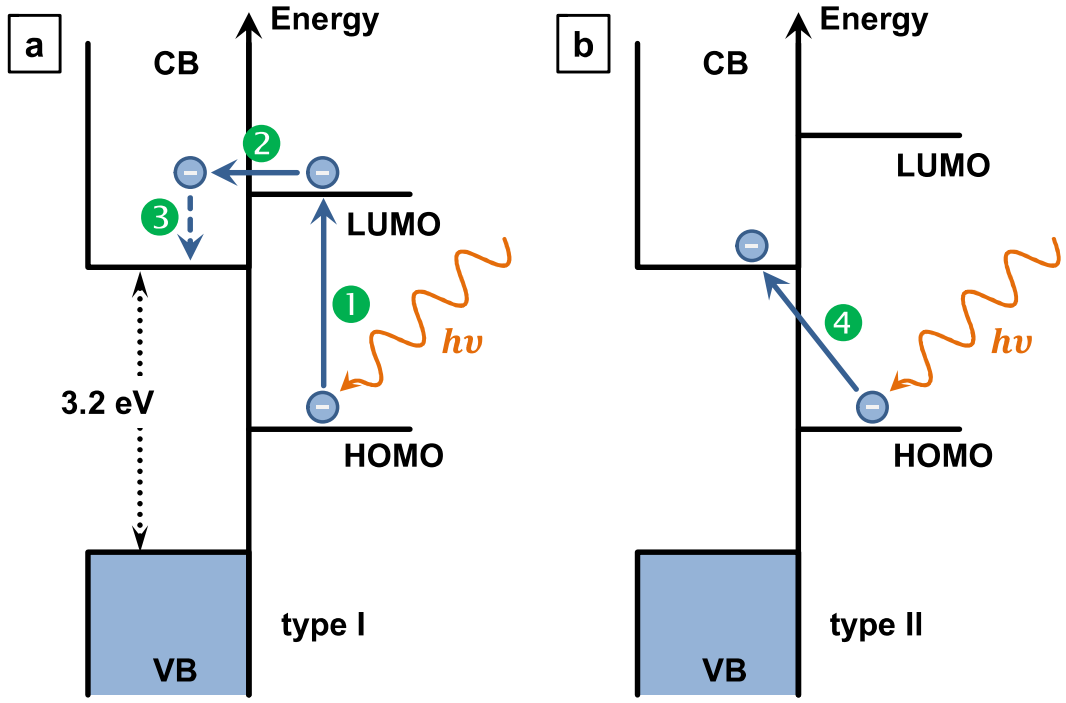

Figure 1.11. Types of surface sensitization of TiO_2 NPs. (a) Type I sensitization through indirect photoinjection from weakly coupled dye molecules. (b) Type II sensititzation with direct photoinjection from strongly coupled organic adsorbates. Numbered steps: ❶, photoexcitation; ❷, electron injection; ❸, relaxation; ❹, direct photoinjection via LMCT. Abbreviations: HOMO, highest occupied molecular orbital; LUMO, lowest unoccupied molecular orbital; LMCT, ligand-to-metal charge transfer.

Catechol-derived type II sensitizers have found little application in sensitized solar cells because of their high recombination rates and correspondingly poor photoconversion efficiencies as compared to their popular type I counterparts containing Ru complexes.[234,239] However, LMCT-mediated activation of titania is being increasingly employed for visible light-driven photocatalysis,[236,239] with special focus on organic transformations.[240–242]

2

Mixed Ligand Shell Formation upon Catechol Ligand Adsorption on Hydrophobic TiO_2 Nanoparticles

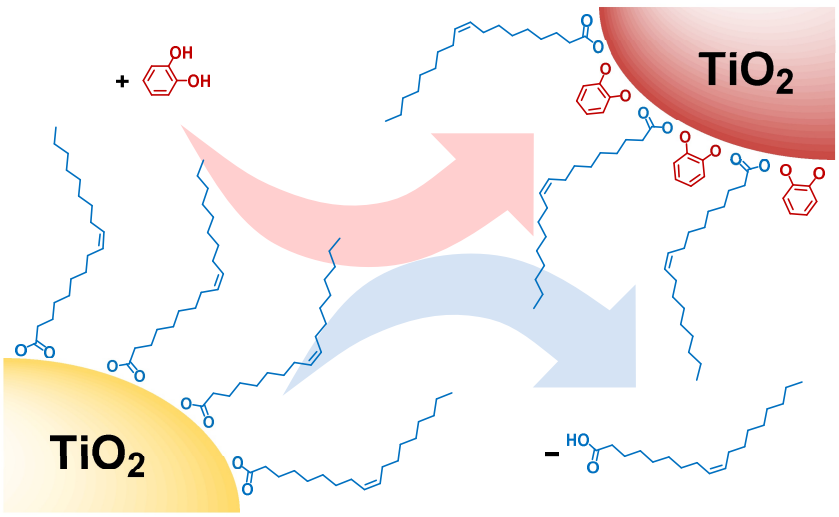

This chapter contains an adapted reproduction of *Langmuir* **2019**, *35*, 12518–12531, reprinted with permission of the American Chemical Society (© 2019).

Authorship Contributions

Study conception and design	E. Schechtel R. Dören W. Tremel
Acquisition of data	E. Schechtel R. Dören M. Mondeshki
Analysis and interpretation of data	E. Schechtel R. Dören
Drafting of manuscript	E. Schechtel
Critical revision	E. Schechtel R. Dören H. Frerichs M. Panthöfer M. Mondeshki W. Tremel

2.1 Abstract

Modifying the surfaces of metal oxide nanoparticles (NPs) with monolayers of ligands provides a simple and direct method to generate multifunctional coatings by altering their surface properties. This works best if the composition of the monolayers can be controlled. Mussel-inspired, non-innocent catecholates stand out from other ligands like carboxylates and amines, because they are redox-active and allow for highly efficient surface binding and enhanced electron transfer to the surface. However, a comprehensive understanding of their surface chemistry, including surface coverage and displacement of the native ligand, is still lacking. Here, we unravel the displacement of oleate (OA) ligands on hydrophobic, OA-stabilized TiO_2 NPs by catecholate ligands using a combination of one- and two-dimensional nuclear magnetic resonance (NMR) spectroscopy techniques. Conclusive pictures of the ligand shells before and after surface modification with catecholate were obtained by ^{1}H and ^{13}C NMR spectroscopy (the ^{13}C chemical shift being more sensitive and with a broader range). The data could be explained using a Langmuir-type approach. Gradual formation of a mixed ligand shell was observed, and the surface processes of catecholate adsorption and OA desorption were quantified. Contrary to the prevailing view, catecholate displaces only a minor fraction (~20%) of the native OA ligand shell. At the same time, the total ligand density more than doubled from 2.3 nm^{-2} at native oleate coverage to 4.8 nm^{-2} at maximum catecholate loading. We conclude that the catecholate ligand adsorbs preferably to unoccupied Ti surface sites rather than replacing native OA ligands. This unexpected behavior, reminiscent of the Vroman effect for protein corona formation, appears to be a fundamental feature in the widely used surface modification of hydrophobic metal oxide NPs with catecholate ligands. Moreover, our findings show that ligand displacement on OA-capped TiO_2 NPs is not suited for a full ligand shell refunctionalization because it produces only mixed ligand shells. Therefore, our results contribute to a better understanding and performance of photocatalytic applications based on catecholate ligand-sensitized TiO_2 NPs.

2.2 Introduction

Metal oxide nanoparticles (NPs) are a subject of rapidly growing interest due to their wide range of potential applications.[12] What makes metal oxide NPs superior over their bulk counterparts is their small size associated with excellent dispersibility in different solvents. Colloidal stability is a key requirement for the solution-based processing of NPs for applications like superconductive films,[28] thermoelectric devices,[24] photovoltaics,[243] and hybrid organic−inorganic nanocomposites with tailored mechanical properties.[244,245]

There are two principal methods to ensure colloidal stability of NPs in solution: (i) Steric stabilization by attaching long chain ligands to the NP surface with favorable chain−solvent interactions in a given solvent (e.g., oleic acid in *n*-hexane). (ii) Alternatively, NPs can be stabilized electrostatically by introducing surface charges, which are effectively screened by a solvent of high dielectric constant (e.g., water or formamide).[38,76] Steric stabilization in hydrophobic media has proven to be the more effective option in the synthesis of well-defined NPs because surface-active ligands allow good control over facet growth. However, native ligands are usually lacking the chemical functionalities needed for water solubility[246] and bioconjugation[13] for medical applications.[247]

Therefore, the hydrophobic NP surfaces must be modified in a suitable fashion. One concept for metal oxide functionalization with surface ligands[75] has become particularly popular in the past few years: Inspired by the versatile chemistry of mussel adhesive proteins, the catechol (1,2-dihydroxybenzene) group has found widespread application as a surface ligand.[173] The bidentate binding geometry and the extraordinarily high binding constants of catechol with transition metal ions[174,175,248] allow for virtually irreversible surface binding to metal oxides[249] like zinc oxide,[250,251] iron oxide,[252–254] or titanium dioxide (titania, TiO_2).[11,186,255,256]

Apart from its superior binding affinity, the catechol moiety has another intriguing property: Catecholate anchors are redox-active ligands that behave “non-innocently” in transition-metal complexes;[257,258] i.e., they change their oxidation state easily because the frontier orbitals of the redox-active ligands and metal ions have similar energies.[178,179] This non-innocent behavior enables efficient electron transfer at the ligand−metal interface, thereby facilitating catalytic processes, both in a biochemical con-

text[181] and in synthetic organic chemistry.[182,259] In previous work we have demonstrated the non-innocent behavior of catecholate anchors on iron oxide[260] and TiO_2 NPs.[261]

Besides its importance as an industrial mass product, TiO_2 has become a heavily investigated material for a wide range of emerging applications, all of which rely on its semiconductor properties and the associated photoreactivity.[262,263] The potential applications include biomedical,[264] environmental,[265] and energy-related technologies,[209,266–268] as well as selective organic synthesis.[218] To make these applications more efficient and environmentally benign at the same time, much effort has been invested in the sensitization of TiO_2 in order to extend its solar light harvesting capabilities from the ultraviolet (UV) into the visible range.[269] A promising approach is the surface modification of TiO_2 with catecholic molecules, which produce a red-shifted absorption band upon binding.[270] This band is caused by ligand-to-metal charge transfer (LMCT) due to the strong electronic coupling between catechol anchor and surface Ti sites.[239]

In order to assess the efficiency of photocatalytic applications, it is crucial to understand the catechol adsorption process on TiO_2 NPs. Catechol adsorption on colloidal TiO_2 has been studied experimentally[11,180,184,185] and theoretically.[191,235] All studies so far focused on "naked" hydrophilic TiO_2 surfaces, where refunctionalization is not needed. We present a comprehensive study of catechol surface modification on TiO_2 NPs, which are stabilized sterically by hydrophobic oleate ligands. The catechol−TiO_2 combination was chosen as a prototypical model system that represents a wide range of catecholic ligands used for surface modification of hydrophobic metal oxide NPs. Nuclear magnetic resonance (NMR) spectroscopy was employed as a powerful tool for elucidating the NP surface chemistry.[271–275] This model system is suited perfectly for an NMR study of the surface chemistry because (i) TiO_2 is a well-defined, stable, nonmagnetic, and therefore NMR-compatible material. (ii) The hydrophobic TiO_2 NPs exhibit outstanding colloidal stability, thus enabling direct observation of particle-bound ligands using solution NMR. (iii) OA and catechol have very different NMR signatures, which facilitates their differentiation and reliable quantification.

The NMR toolbox approach enabled us to thoroughly characterize the organic ligand sphere of oleate-capped hydrophobic TiO_2 NPs before and after catechol adsorption. We performed systematic studies to quantify the extent of catechol adsorption and concomitant OA desorption, thus gaining insight into the mechanism of these fundamental surface processes. Catechol adsorption could be rationalized with the Langmuir

adsorption model, while OA desorption followed an Arrhenius-type behavior. A mixed ligand shell was formed in the first step, but different from the prevailing model, catecholate displaces only a small fraction (20%) of the native oleate ligand shell. At the same time, the total ligand density more than doubled from 2.3 nm^{-2} for native OA coverage to 4.8 nm^{-2} at maximum catecholate loading. This shows that the catecholate ligand adsorbs preferably to empty Ti surface sites rather than replacing native oleate ligands. This unexpected behavior, reminiscent of the Vroman effect for protein corona formation,[276,277] is likely to be a fundamental feature in the widely used surface modification of hydrophobic metal oxide NPs with catecholate ligands. Our findings might have important implications for the design of photocatalytic applications with ligand-sensitized TiO_2 NPs, because ligand displacement on OA-capped TiO_2 NPs produces mixed ligand shells, but is not suited for a full ligand shell refunctionalization. Finally, the acquired knowledge has fundamental validity and may also apply to the catechol modification of other hydrophobic metal oxide NPs, such as manganese[278] or iron oxide.[253]

2.3 Experimental Section

Materials. All chemicals and solvents were obtained from commercial suppliers and used without further purification unless stated otherwise. Oleic acid (OA, technical grade, 90%), catechol (Cat, ≥99%), and nitromethane (≥98.5%) were purchased from Sigma-Aldrich. Titanium(IV) *n*-butoxide (99%) and 4-*tert*-butylcatechol (tBuCat, 99%) were obtained from Acros Organics. Oleylamine (>50.0% (GC)) and 2,3-dihydroxynaphthalene (DHN, >97%) were acquired from TCI. The deuterated solvents chloroform-*d* ($CDCl_3$, 99.8 atom% D), acetone-d_6 (99.8 atom% D), and methanol-d_4 (CD_3OD, 99.8 atom% D) were obtained from Deutero GmbH.

General Considerations. In order to obtain reliable NMR spectra of NP and supernatant solutions, it is of utmost importance to minimize contact of analyte solutions with plastic surfaces, as there is a danger of contamination from numerous plastic additives, which either obscure the low-intensity signals of NP-bound ligands or lead to incorrect results in the quantification of unbound ligands. Therefore, all laboratory techniques described here were performed with non-plastic labware whenever possible. In particular, screw top amber glass vials were used instead of plastic (micro)centrifuge

tubes for the purification, handling, and storage of NP solutions. Also, liquids were transferred with glass Pasteur pipettes and Hamilton syringes instead of their plastic counterparts. Further details on the identification of contaminants from plastic labware are provided in section 2.6.2 of the Supporting Information.

NMR tubes were cleaned thoroughly by manual scrubbing with soap water, soaking in Piranha solution (3:1 (v/v) conc. H_2SO_4/35 wt% H_2O_2) for 1 h, multiple rinsing with deionized water, and drying at moderate temperatures (<70 °C). Heavily soiled NMR tubes with strongly adhering NP residues were presoaked in Piranha solution prior to the standard cleaning procedure. NMR tubes were always sealed with new, unused caps.

Synthesis of Oleate-Stabilized Titania Nanoparticles (TiO_2−OA NPs). TiO_2−OA NPs were prepared by solvothermal synthesis, following a previously reported procedure,[56] with slight modifications as described before.[245,261] In brief, titanium(IV) butoxide was hydrolyzed in the presence of oleic acid and oleylamine as surface-active reactants. Following the standard purification procedure of repeated cycles of precipitation and dissolution (EtOH/*n*-hexane),[261] one part of the NPs (200 mg) was purified further with deuterated solvents (acetone-d_6/$CDCl_3$) to obtain a sample suitable for NMR characterization (cf. Figure 2.3a, *vide infra*). ^{1}H NMR (400 MHz, $CDCl_3$): δ [ppm] = 5.7−5.0 (m, −CH=CH−), 2.4−0.6 (m, $-CH_2-$ & $-CH_3$).

Bipyramidal TiO_2−OA NPs were obtained following the same synthetic procedure, but using an oleic acid/oleylamine ratio of 4:6 instead of 6:4.[56]

Surface Modification of Titania Nanoparticles with Catechol (TiO_2−Cat NPs), 4-*tert*-Butylcatechol (TiO_2−tBuCat NPs), and 2,3-Dihydroxynaphthalene (TiO_2−DHN NPs). In a typical catechol functionalization reaction, an aliquot of the TiO_2−OA stock solution in chloroform, corresponding to a NP amount of 200 mg, was precipitated with excess CD_3OD, centrifuged (9000 rpm, 10 min), and re-dissolved in $CDCl_3$ (0.8 mL). In a 15 mL glass centrifuge tube with screw top, the catechol derivative (0.91 mmol; 100 mg catechol or 151 mg 4-*tert*-butylcatechol or 146 mg 2,3-dihydroxynaphthalene) was dissolved in CD_3OD (0.1 mL), the NP solution was added, and the reaction mixture was sonicated at 40 °C for 1 h. After precipitation with CD_3OD (2.0 mL), the NPs were separated by centrifugation (9000 rpm, 10 min), and the yellow supernatant was discarded. The brownish-red pellet was re-dissolved in $CDCl_3$ (0.5 mL) by vortexing and sonication, precipitated with CD_3OD (1.5 mL), separated by centrifu-

gation (9000 rpm, 10 min), and dried in rough vacuum (30 mbar, 5 min). The catecholate-functionalized TiO_2 NPs were further purified by repeated cycles of dissolution, precipitation, and drying as described above (4 iterations in total). Finally, the purified and dried TiO_2 NPs were re-dissolved in $CDCl_3$ (0.6 mL) to obtain a highly concentrated sample for ^{1}H NMR spectroscopy (cf. Figure 2.3b and 2.7a, *vide infra*). ^{1}H NMR (400 MHz, $CDCl_3$): **TiO_2−Cat NPs.** δ [ppm] = 8.0−5.0 (br m, Ar−H), 5.8−5.0 (m, −CH=CH−), 2.5−0.4 (m, $-CH_2-$ & $-CH_3$). **TiO_2−tBuCat NPs.** δ [ppm] = 7.6−4.9 (br m, Ar−H), 5.7−4.9 (m, −CH=CH−), 2.4−0.2 (m, $-CH_2-$, $-CH_3$, $-C(CH_3)_3$). **TiO_2−DHN NPs.** δ [ppm] = 8.5−4.8 (br m, Ar−H), 5.8−4.9 (m, −CH=CH−), 2.5−0.0 (m, $-CH_2-$ & $-CH_3$).

Systematic Surface Modification Studies. In a typical surface modification reaction, a 200 µL aliquot of the titania stock solution, corresponding to a NP amount of 100 mg, was transferred into a 1.5 mL amber glass vial with screw top. An appropriate amount of the catechol stock solution (cf. Table 2.1) was added to the NP solution, and the reaction mixture was filled up with additional solvent to obtain a total acetone-d_6 volume of 600 µL. After sonication at 40 °C for 1 h, the reaction mixture was centrifuged (9000 rpm, 10 min), and the supernatant was decanted into a separate vial and set aside for later NMR characterization. The centrifugation residue was re-dissolved in 0.2 mL of $CDCl_3$, precipitated with 0.6 mL of acetone-d_6, and the supernatant was retained in a separate vial. This procedure was repeated until a set of 7 consecutive supernatant solutions was obtained. For quantitative ^{1}H NMR characterization, an internal standard of 5 µL nitromethane was added to each of the samples.

Table 2.1. Compositions of reaction mixtures for surface modification studies.[a]

	reaction no.					
	1	2	3	4	5	6
targeted catechol mass (mg)	2	5	10	20	50	100
volume catechol solution (µL)[b]	10	25	50	100	250	500
additional volume acetone-d_6 (µL)	590	575	550	500	350	100
catechol concentration (mol L^{-1})	0.02	0.06	0.11	0.23	0.57	1.14

[a]Amount of TiO_2−OA NPs employed in each reaction: 100 mg, added in 200 µL of a highly concentrated NP stock solution (500 mg/mL in $CDCl_3$). [b]Catechol stock solution concentration: 200 mg/mL in acetone-d_6.

Additional surface modification studies with 4-*tert*-butylcatechol, catechol, and 2,3-dihydroxynaphthalene were performed on a second batch of TiO_2−OA NPs (cf. Figure S2.15 and Table S2.3), using the same reaction conditions as for reaction no. 4 in Table 2.1, i.e., at a ligand concentration of 0.2 mol L^{-1}. Due to this low concentration (as compared to the maximum catechol loading investigated in Table 2.1), 4 cycles of purification by precipitation (instead of 7) were sufficient to retrieve a substantial portion of the free ligands.

Characterization. *Transmission Electron Microscopy (TEM).* TEM images for determining the size and morphology were acquired on a FEI Tecnai G2 Spirit microscope operating at 120 kV (LaB_6 filament), equipped with a Gatan US1000 CCD-camera (16-bit, 2048 × 2048 pixels), using the Gatan Digital Micrograph software. Samples for TEM were prepared by placing one drop (10 µL) of a diluted NP solution in chloroform (0.1 mg mL^{-1}) on a carbon-coated copper grid and letting it dry at room temperature. Size evaluation of individual nanoparticles on the TEM images was performed with ImageJ.

Thermogravimetric Analysis (TGA). TGA was performed on a Perkin Elmer Pyris 6 instrument under oxygen atmosphere. A typical heat program was (i) to equilibrate at 30 °C for 10 min, (ii) to heat from 30 °C to 750 °C at 5 °C min^{-1}, and (iii) to hold at 750 °C for 10 min. Prior to the TGA, the samples were ground in a mortar and dried in a vacuum drying chamber at 60 °C for several hours. The typical amount of sample for the TGA analysis was in the range from 2 to 4 mg.

Powder X-Ray Diffraction (PXRD). PXRD patterns were obtained on a STOE Stadi P diffractometer, equipped with a Dectris Mythen 1k detector in transmission mode, using Mo Kα_1 radiation (λ = 0.7093 Å). The X-ray diffractograms were recorded in the 2θ range from 2° to 45° with a step size of 0.015°. The samples were dried thoroughly and ground before being applied as a thin layer between two stripes of 3M Scotch® tape for X-ray measurement. Crystalline phases were identified according to the Crystallography Open Database (COD) using the Match! software from Crystal Impact.

UV−Vis Spectroscopy. Ultraviolet−visible (UV−vis) absorbance spectra ranging from 250 to 800 nm were collected on a Cary 5G UV−vis−NIR spectrophotometer, using quartz cuvettes with a path length of 1 cm. Typically, the analyte solutions (NPs or reference molecules) were used at concentrations of 50 µg mL^{-1} in THF.

Nuclear Magnetic Resonance (NMR) Spectroscopy. All solution NMR spectra were recorded at 295 K on a Bruker Avance DRX 400 spectrometer (Bruker Biospin GmbH, Rheinstetten, Germany) operating at frequencies of 400.31 MHz for ^{1}H and 100.67 MHz for ^{13}C. NP-containing samples were measured at concentrations in the range from 100 to 200 mg mL^{-1} to obtain well-defined signal shapes in high enough intensity of the particle-bound ligands, with the spectral width extended to 24 ppm to capture the signals in their entire width. For quantitative ^{1}H NMR measurements, nitromethane was used as an internal standard. All 1D NMR spectra were processed with the MestReNova or TopSpin software packages. NMR spectra used for quantifications were all processed in the same way with manual phase correction and automatic baseline correction using the ablative method. For nuclear Overhauser effect spectroscopy (NOESY), the mixing time was set to 400 ms, and a recycle delay of 2 s was used. Solid-state ^{13}C magic angle spinning (MAS) NMR spectra were acquired on a Bruker Avance DSX 400 spectrometer (100.55 MHz ^{13}C frequency, 10 kHz spinning frequency).

2.4 Results and Discussion

Highly soluble, hydrophobic anatase TiO_2 NPs were synthesized by controlled hydrolysis of titanium butoxide with water vapor in a solvothermal reaction, using oleic acid and oleyl amine as capping agents.[56] In order to obtain reliable information on the surface chemistry of the NPs, it was crucial to thoroughly purify the crude NPs. This was done by repeated cycles of dissolution and precipitation (with *n*-hexane and EtOH) to remove excess capping agents, of which oleic acid is the more surface-active compound because of its carboxylate functionality. The as-synthesized, oleate-stabilized TiO_2 NPs are of spherical to elongated shape (Figure 2.1a+b) and can be described, on average, as prolate spheroids with a major axis of 10.4 ± 2.4 nm and a minor axis of 7.4 ± 1.1 nm (Figure 2.1c). PXRD confirmed the anatase modification of TiO_2 (Figure S2.1), and TGA yielded an organic fraction of 17.4 wt% (Figure 2.1d). Combining the organic fraction with the dimensions of the NPs, the native ligand density is calculated as 2.3 ± 1.1 molecules oleic acid per nm^2 of NP surface, adding up to 509 ± 194 molecules per NP (Table 2.2). This value is lower than most of the ligand densities reported in the literature for other oleate-capped NPs.[279,280] However, it has also been shown that

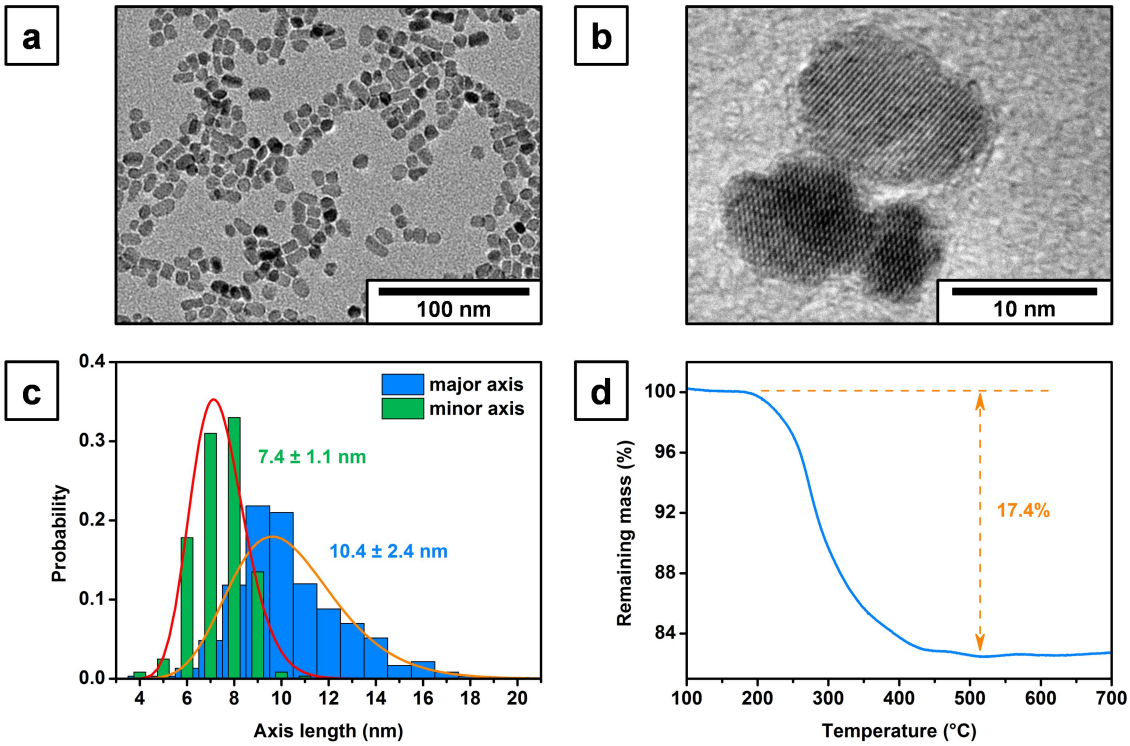

Figure 2.1. Characterization of as-synthesized, OA-stabilized TiO_2 NPs. (a) Typical TEM overview image, revealing spherical to elongated morphology. (b) High resolution TEM image of individual NPs, exhibiting continuous crystallinity and oval shape. (c) Size histogram over 600 individual particles, fitted as ellipses with major and minor axes, confirms the elongated shape of the TiO_2 NPs. The solid lines (red and orange) were obtained by fitting the size distribution histograms to the log-normal distribution. The values given are the mean values of the corresponding histograms. (d) TGA profile of thoroughly washed and dried TiO_2–OA NPs. The indicated difference represents the mass fraction of the native ligand shell.

Table 2.2. Characteristics of as-synthesized TiO_2–OA NPs.

quantity	value
major axis (nm)[a]	10.4 ± 2.4
minor axis (nm)[a]	7.4 ± 1.1
volume (nm^3)[b]	298 ± 112
surface area (nm^2)[b]	220 ± 56
specific surface area ($m^2\ g^{-1}$)	160 ± 73
organic fraction (%)	17.4 ± 1.0
ligands per particle	509 ± 194
ligand density (nm^{-2})	2.3 ± 1.1

[a]Mean values from TEM size evaluation after fitting individual particles as ellipses. [b]Values calculated according to the formulae for prolate (elongated) spheroids.

thorough purification of NPs with suitable solvents can drastically lower the organic fraction obtained by TGA.[281] Thus, the rather low ligand density of 2.3 nm^{-2} indicates a successful purification procedure. To put this value in the context of a molecular perspective, the maximum packing densities at the ligand−NP interface must be considered. Typically, the maximum packing density of alkyl chains in a self-assembled monolayer is limited to about 5 chains per nm^2.[282] On the other side of the ligand−NP interface, the theoretical surface density of Ti sites exposed on the three most common anatase crystal faces (101), (001), and (100) ranges from 5.1 to 6.9 nm^{-2}.[145] In comparison, the native ligand density of TiO_2−OA NPs is less than half of the possible maximum ligand density, both from the surface site and the ligand packing point of view.

In order to obtain a first qualitative picture of the surface modification with catechol, hydrophobic TiO_2−OA NPs were reacted with a sevenfold excess of catechol with respect to the amount of bound OA (Figure 2.2a). Performing this reaction in solution, catechol adsorption onto the TiO_2 surface was immediately indicated by an intense red coloration of the initially yellow solution (see digital photographs in Figure 2.2b). Although the initial yellow color is also caused by a LMCT from OA to TiO_2, catecholate complexation of surface Ti atoms has a much more significant impact on the absorption spectrum due to much stronger LMCT transitions between catecholate and TiO_2.[11] Indeed, UV−vis spectroscopy revealed a broad LMCT band above 350 nm, where neither the as-synthesized TiO_2−OA NPs nor the pure catechol reference show significant absorptions (Figure 2.2b).

Although catechol modification is widely used to impart functionality to NP surfaces through ligand exchange,[253] the efficiency of such surface reactions is only poorly studied and understood. While UV−vis spectroscopy is an easy and quick qualitative evidence of catechol adsorption, it cannot provide quantitative information concerning the binding of the remaining oleate ligands. Here, nuclear magnetic resonance (NMR) spectroscopy is a more suitable technique. Due to their small size and outstanding solubility, TiO_2 NPs can be studied by solution NMR in order to analyze the ligand sphere of the TiO_2 NPs. Figure 2.3a shows the ^1H NMR spectrum of as-synthesized, oleate-stabilized TiO_2 NPs in $CDCl_3$.

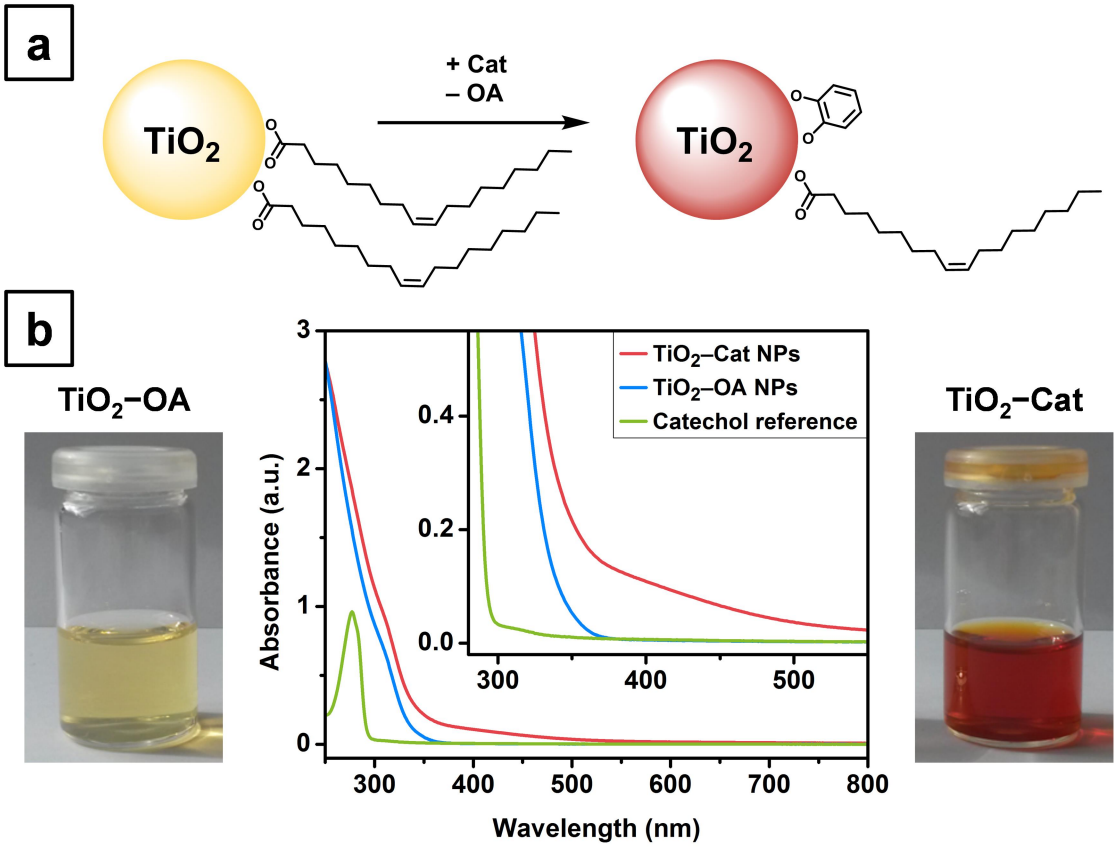

Figure 2.2. (a) Schematic representation of catechol adsorption on hydrophobic TiO_2 nanoparticles. (b) Digital image of as-synthesized TiO_2–OA NPs (left) and modified TiO_2–Cat NPs (right) in solution (50 mg/mL in THF, respectively) and corresponding UV–vis absorbance spectra (middle) of a pure catechol reference (green line), TiO_2–OA NPs (blue line), and TiO_2–Cat NPs (red line). The inset shows an enlarged view of the spectral range where the charge transfer in TiO_2–Cat NPs takes place. For UV–vis spectroscopy, solutions of 50 µg/mL analyte in THF were used.

The most apparent features of this spectrum are the greatly broadened signals of particle-bound oleate. This resonance broadening is due to the fact that the ligands are strongly restricted in their rotational mobility when bound to the NP's surface.[274] A valuable advantage of solution NMR for NP analysis is the possibility to easily identify impurities that are not associated with the NP as they produce much sharper signals. The fact that the spectrum displays no sharp signals other than those of residual solvent molecules confirms the successful purification of the NPs, with strongly bound oleic acid as the only relevant species found in the NP solution. To obtain this grade of purity, the NPs had to go through at least five purification cycles (cf. Figure S2.2).

The olefinic protons (Figure 2.3a, signal **e**) of surface-bound OA give rise to a broad signal in the range 5.7−5.0 ppm, which is clearly separated from other signals and therefore perfectly suited to monitor any ligand displacement from the NP surface. The aliphatic protons are all cluttered in the range 2.4−0.6 ppm, with pronounced overlapping of signals. Nevertheless, some groups can be assigned more precisely by comparison with the reference of free oleic acid in solution: The terminal methyl group (**f**) appears at 0.8 ppm, the methylene protons (**d**) adjacent to the double bond appear at 1.9 ppm, while the bulk of the methylene groups (**c**) produce the very intense signal around 1.2 ppm.

The ^{1}H NMR spectrum of TiO_2−OA NPs displayed in Figure 2.3a is very similar to the spectra of other OA-capped NPs reported in the literature, such as PbSe,[271] CdSe,[280,283] or HfO_2.[284,285] One striking feature has not been observed so far: All signals of TiO_2-bound OA exhibit distinct shoulders, indicating that every signal contains two overlapping components. The ^{13}C solution NMR spectrum of as-synthesized TiO_2−OA NPs (Figure S2.3) shows very similar shoulders, albeit not quite as pronounced. A ^{1}H–^{13}C heteronuclear single quantum correlation (HSQC) experiment was performed to unravel the cluttered aliphatic signals of bound OA. As shown in Figure 2.4, every single visible signal has a pronounced shoulder. We assume this to be the result of two different packing motifs of OA on two major crystal facets of the pseudo-spherical TiO_2 NPs. Indeed, anatase NPs of such morphology are usually described in the literature as highly truncated tetragonal bipyramids, dominated by the {001} and {101} facets (cf. Figure S2.4a for illustration).[143,169,286] The surface densities for five-fold coordinated Ti atoms (which act as binding sites for OA) are reported to be 6.9 nm^{-2} for the (001) and 5.1 nm^{-2} for the (101) anatase crystal surfaces.[145] Correlating the surface densities with the two-component signals of bound oleate as shown in Figures 2.3 and 2.4, it is plausible to attribute the lower-intensity, lower-field shoulder to the oleate species bound to the {001} facets. These facets allow for a higher packing density of the oleate ligands, which translates into a lower chain mobility and therefore a broader NMR resonance, shifted to lower field. On the other hand, the less densely packed oleate species on the {101} facets gives rise to a higher chain mobility with narrower, high-field shifted NMR signals.

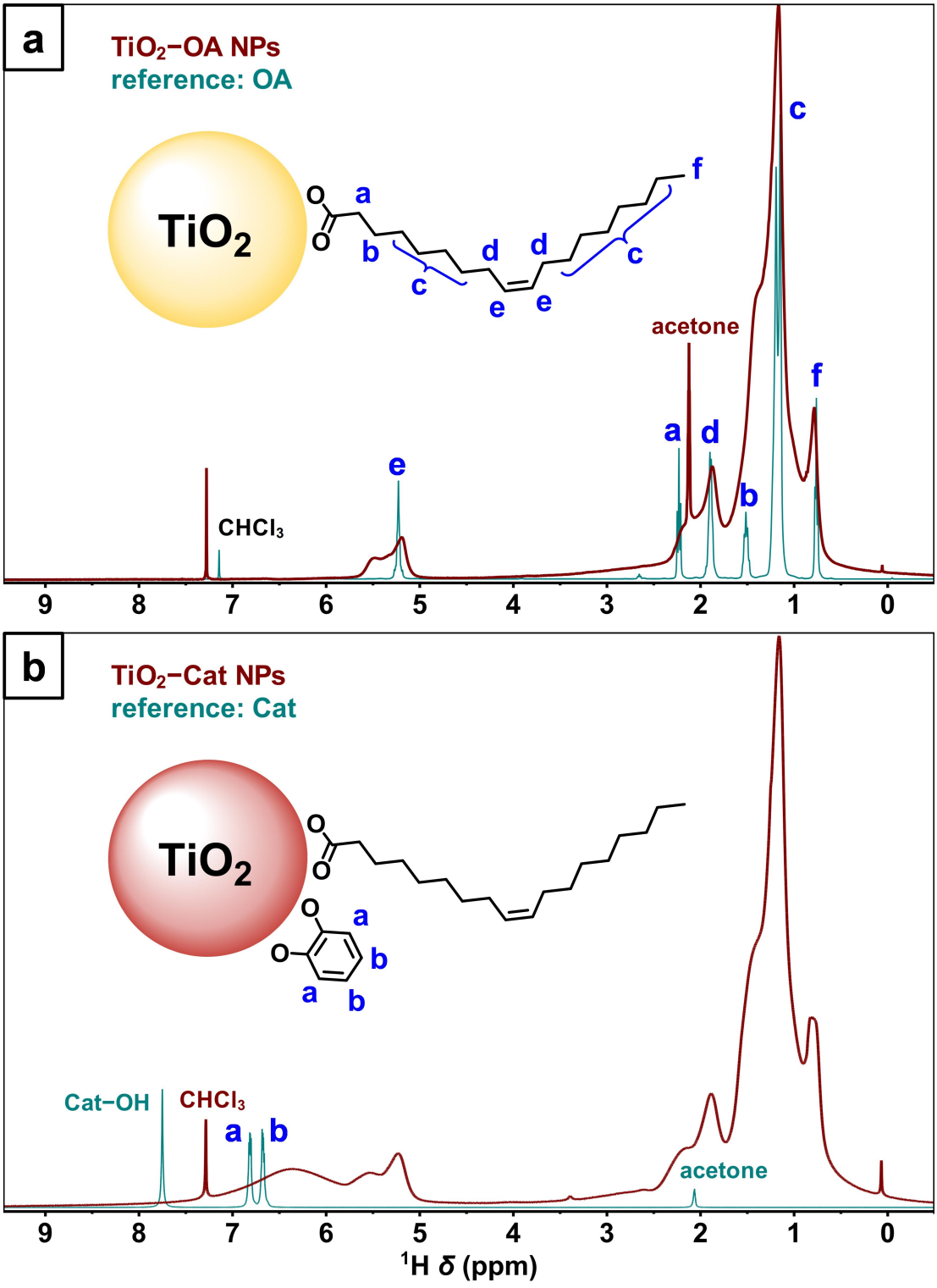

Figure 2.3. ^{1}H solution NMR spectra (400 MHz, $CDCl_3$) of (a) as-synthesized TiO_2–OA NPs and (b) catechol-modified TiO_2–Cat NPs, with corresponding reference spectra and assignment of signals. Spectra of particle-bound ligands are drawn in brown, while the reference spectra of free ligands are shown in teal. The reference spectrum of OA was shifted to higher field to account for a better alignment with the NP spectrum.

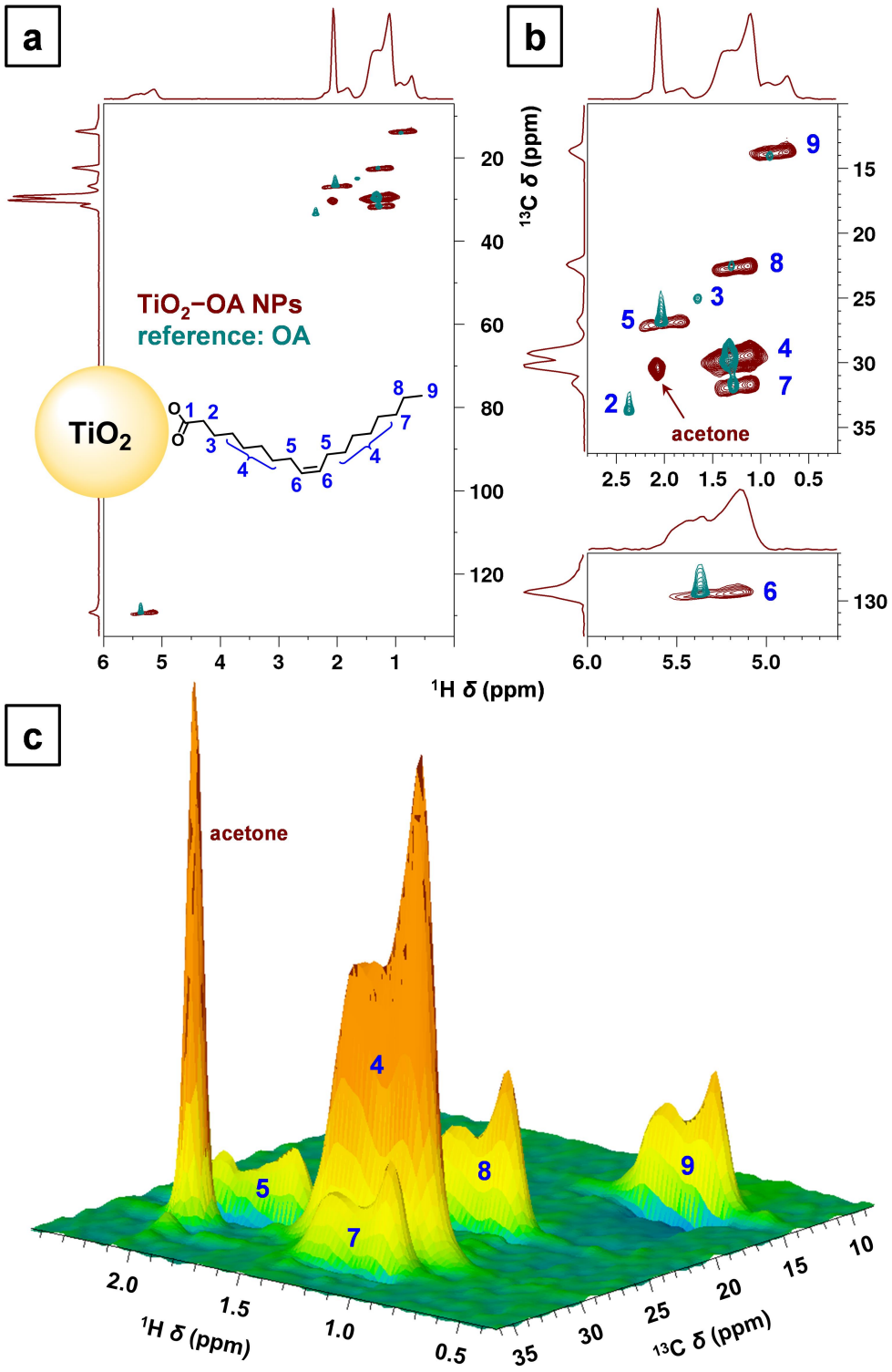

Figure 2.4. $^{1}H-^{13}C$ HSQC spectra of as-synthesized TiO_2–OA NPs (brown) and OA reference (teal). (a) Overview spectrum of all relevant resonances. (b) Enlarged views of the aliphatic (upper panel) and the olefinic (lower panel) correlations with corresponding assignment of signals. The superimposed correlations of free OA reveal that the methylene groups closest to the NP surface (signals **2**+**3**) are not detectable in solution NMR (cf. Figure S2.3). (c) Three-dimensional view of the aliphatic correlations to illustrate the composite structure of all visible signals.

To support the hypothesis of different crystal facets producing different NMR resonances, we synthesized TiO_2 anatase NPs with only one major facet, namely the {101} facets of slightly truncated bipyramids (cf. Figure S2.4b for illustration). Exploiting the shape-controlled synthetic procedure by Dinh et al.,[56] bipyramidal TiO_2 NPs were obtained by using an oleic acid/oleylamine ratio of 4:6 instead of 6:4. TEM analysis confirmed the bipyramidal morphology of the TiO_2 NPs and yielded a major axis length in the range from 10 to 30 nm (Figure S2.5). The ^{1}H NMR spectrum (Figure S2.6) shows no such pronounced signal shoulders as observed in Figure 2.3, thus confirming that the signal shoulder arises from a second crystal facet with different Ti surface density.

To obtain a ^{1}H NMR spectrum as shown in Figure 2.3a, two essential requirements must be met: (i) The NMR sample must contain very large quantities of analyte to account for sufficient intensities of the extremely broadened signals of particle-bound ligands. In this case, 200 mg of TiO_2−OA NPs were employed, whereas for usual ^{1}H NMR experiments of free molecules in solution only 1% of this concentration is sufficient to obtain reliable results. (ii) Due to the very low signal intensities, it is important to carefully remove excess ligands and solvents by repeated purification cycles (as shown in Figure S2.2), since impurities can also be introduced from external sources (contaminated or inappropriate labware). The risk of contamination is particularly high when working with disposable plastic labware, which is, unfortunately, part of the standard equipment for NP synthesis, purification, handling, and modification. Plastic centrifuge tubes, which are usually used for purification purposes, are mostly made from polypropylene (PP), a material that is not recommended by commercial suppliers to be used in combination with most organic solvents, including chloroform.[287] Chloroform in contact with PP tends to swell the polymer, thereby extracting a variety of polymer additives[288] that contaminate the NP sample. Additionally, common laboratory techniques, especially sonication and heating, have been shown to greatly intensify the leaching of polymer additives.[289] We observed that some of these contaminants can accumulate to such an extent that the low-intensity signals of NP-bound ligands are obscured completely. Furthermore, some additives have almost identical NMR signatures as oleic acid, which impedes a quantification of the native ligand. Further details on the identification of these contaminants are provided in section 2.6.2 of the Supporting Information (Figures S2.7−S2.9 and Table S2.1). The contamination problems were cir-

cumvented by avoiding laboratory plasticware and using non-plastic labware instead. In this way, the contact of the analyte solutions with plastic surfaces was kept as short as possible. In the field of biosciences, researchers have developed an increased awareness of this issue over the last 10 years, after reports emerged that bioactive leachates from plastic labware may compromise the results of bioassays,[290–292] but such concerns appear to be less common among nanoscientists who use NMR in their characterization portfolio. Table S2.2 in the Supporting Information provides a critical examination of NMR results published recently.

Despite the high quality of the ^{1}H NMR spectrum shown in Figure 2.3a, we did not use the signals of particle-bound ligands for ligand quantification, because we could (i) not rule out the possibility of contaminations giving rise to higher integrals (*vide supra*) and (ii) not ensure that the signals exhibit their full intensities due to the reduced mobility of particle-bound ligands. Although there are examples of successful ligand quantification by integration of the olefinic resonance,[271,283] a recent study uncovered a significant disproportion between the integrals of the olefinic and methyl signals,[293] confirming our reservations. Therefore, the native ligand density of TiO_2−OA NPs was determined gravimetrically from TGA data (Figure 2.1d).

After surface modification with catechol, the NPs remained perfectly soluble in nonpolar solvents (Figure 2.2b), allowing NMR characterization. Figure 2.3b shows the corresponding ^{1}H NMR spectrum of TiO_2 NPs with catecholate surface ligands in $CDCl_3$. Surprisingly, the spectrum did not change significantly: The prominent signals of surface-bound oleate are still very present, while the catechol ligands add an extremely broad signal of low intensity, representing the aromatic protons, in the 8.0−5.0 ppm range. The observed smearing of the catecholate signal appears to be related to the close proximity of the NP surface,[274] coupled with strongly hampered mobility due to the rigidity of the bidentate coordination geometry. For the same reasons, it was not possible to detect the aromatic carbon atoms through ^{13}C solution NMR experiments (Figure S2.10). However, magic angle spinning (MAS) solid state NMR spectroscopy retrieved every single carbon signal, regardless of the groups' proximity to the NP surface (Figure 2.5). Additionally, the pronounced down-field shift of catecholate's α-carbons implies a strong binding to the TiO_2 surface.

Nuclear Overhauser effect spectroscopy (NOESY) was applied to study the interactions between both constituents of the mixed ligand shell.[274] The NOESY spectrum

(Figure S2.11) exhibits only negative cross-peaks, thus confirming the strong attachment of both ligands.[283,294] Moreover, the pronounced cross-peaks between the aromatic and the aliphatic resonances reveal a close proximity of catecholate and oleate species on the NP surface, i.e., catechol ligands are randomly distributed between the native oleate ligands during adsorption.

A semi-quantitative evaluation of the ^{1}H (Figure 2.3b) and ^{13}C spectra (Figure 2.5) indicated that the ligand exchange reaction did not proceed to completion. In contrast to the prevailing assumption that catecholates replace carboxylate groups quantitatively simply because of their higher binding constant,[253] the NMR spectrum revealed that substantial amounts of residual oleate remained attached to the NPs after surface modification. Despite the wide-spread use of catechol anchors for surface modification, there are only few reports[295–297] addressing incomplete ligand exchange reactions on hydrophobic, oleate-stabilized NPs. However, none of them provided direct and obvious evidence of a mixed ligand shell as shown in Figures 2.3b and 2.5.

Given the significance of catechol functionalization, we next set out to accurately quantify the composition of the mixed ligand shell and to elucidate the surface processes. Because of the extreme broadening of the aromatic signals, the shortcomings discussed above become even more significant, and integration of the signals in Figure 2.3b would not lead to reliable results. Thus, we followed an *ex situ* approach to quantify the adsorbed catechol and the desorbed oleic acid from the supernatant of the reaction mixture. For a thorough investigation of the surface processes, a systematic series of surface modifications with increasing amounts of catechol was carried out. For each reaction, the amount of TiO_2−OA NPs was set to 100 mg, while the amount of catechol was varied from 2 to 100 mg. The reactions were carried out in deuterated solvents. This allowed all purification steps to be monitored and quantified by ^{1}H NMR spectroscopy. Due to the poor solubility of catechol in $CDCl_3$, a solvent mixture of $CDCl_3$ and acetone-d_6 (1:3) was employed as reaction medium. To ensure consistent reaction conditions throughout the series, stock solutions of the reactants were prepared in well-defined concentrations (TiO_2−OA: 500 mg/mL in $CDCl_3$, Cat: 200 mg/mL in acetone-d_6). The reactions mixtures were prepared by combining appropriate volumes of the reactants' stock solutions, along with further addition of acetone-d_6 to keep the NP concentrations constant throughout the reactions. The exact compositions of the reaction mixtures are compiled in Table 2.1.

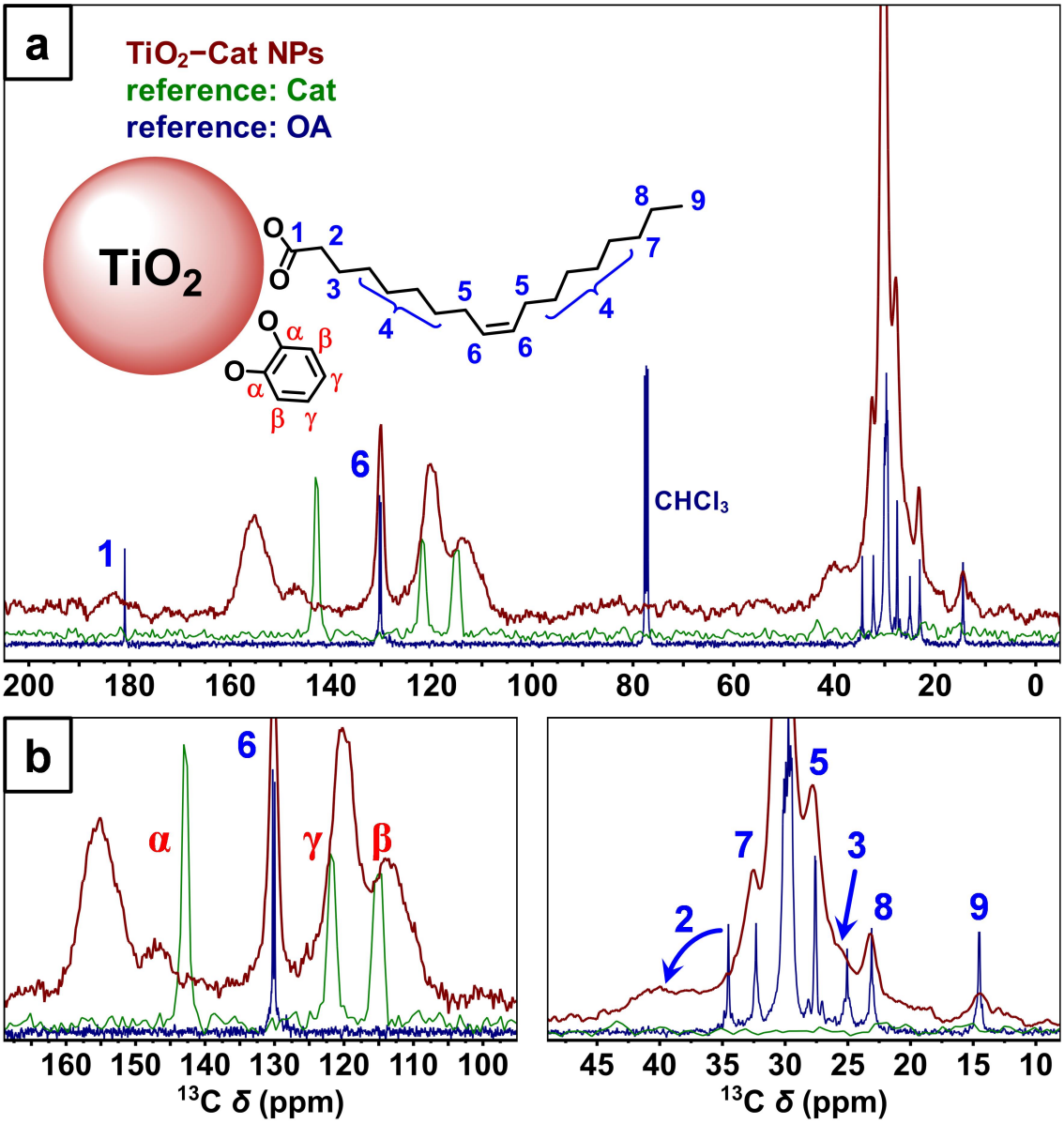

Figure 2.5. ^{13}C solid state MAS-NMR spectra of catechol-modified TiO_2–Cat NPs (brown), catechol reference (green), and OA reference (blue). (a) Spectrum overview of all relevant resonances. (b) Enlarged views of the aromatic (left panel) and the aliphatic (right panel) resonances with corresponding assignments of signals.

The catecholate-coated TiO_2 NPs were separated from the respective reaction mixtures by centrifugation. The supernatant was examined by ^1H NMR spectroscopy to determine the amount of excess catechol and free oleic acid after surface modification. As free ligands could be trapped between precipitated NPs, six additional re-dissolution–precipitation cycles were performed for every reaction to ensure complete recovery of unbound surface ligands. Examination of the supernatant solutions showed the necessity of repeated purification cycles to retrieve a substantial portion of the total

amount of free catechol (Figure S2.12a). The extraction of unbound catechol followed Nernst's distribution law (Figure S2.13),[298] which usually describes the distribution of a solute between two phases during a liquid−liquid extraction. Furthermore, the examined supernatant solutions confirmed the identity of the desorbed species as (protonated) oleic acid (Figure S2.12b).

Once the total amount of catechol from the supernatant solutions was determined, the amount of adsorbed catechol was calculated from the difference between starting and recovered amounts of catechol. The amount of desorbed OA is simply the total amount from the supernatant solutions. Performing this quantification for a reaction series where the starting amount of catechol was increased, the processes of catechol adsorption and OA desorption could be described as a function of catechol concentration (Figure 2.6a).

As has been shown for the binding of catechol on naked (i.e., non-functionalized), hydrophilic TiO_2 surfaces,[180,184] this process can be described in terms of a Langmuir adsorption isotherm,[299] which is characterized by a steep increase of adsorbed species for low ligand concentrations and a saturation in surface coverage for high concentrations (Figure 2.6a and Table 2.3). TiO_2 surface complexation with catechol universally shows a Langmuir behavior, regardless of the adsorbent's macroscopic surface polarity. We found a maximum adsorbate surface concentration of $\Gamma_{max} = 4.9 \times 10^{-6}$ mol m^{-2}, which is significantly higher than the values reported for hydrophilic TiO_2 ($1.0-1.25 \times 10^{-6}$ mol m^{-2}).[180,184] This increased value is probably due to the higher ligand concentration employed in our study.

While catechol adsorption follows a Langmuir behavior, the desorption of oleic acid can be described by an Arrhenius-type function,[300] which starts with low desorption for low catechol concentrations, but also converges to a saturation level for high concentrations (Figure 2.6a and Table 2.3). When dealing with desorption processes, the Arrhenius term is frequently encountered, as it is also a central part of the Polanyi−Wigner equation,[301] which is used for describing thermal desorption processes.[302]

The desorption curve in Figure 2.6a allows some fundamental conclusions to be drawn about the catechol adsorption process: (i) For very low catechol concentrations, virtually no oleic acid is desorbed while almost the entire amount of catechol is adsorbed to the surface. Consequently, catechol adsorption must first occur at empty surface sites that are not occupied by native oleate ligands. Given the fact that the native

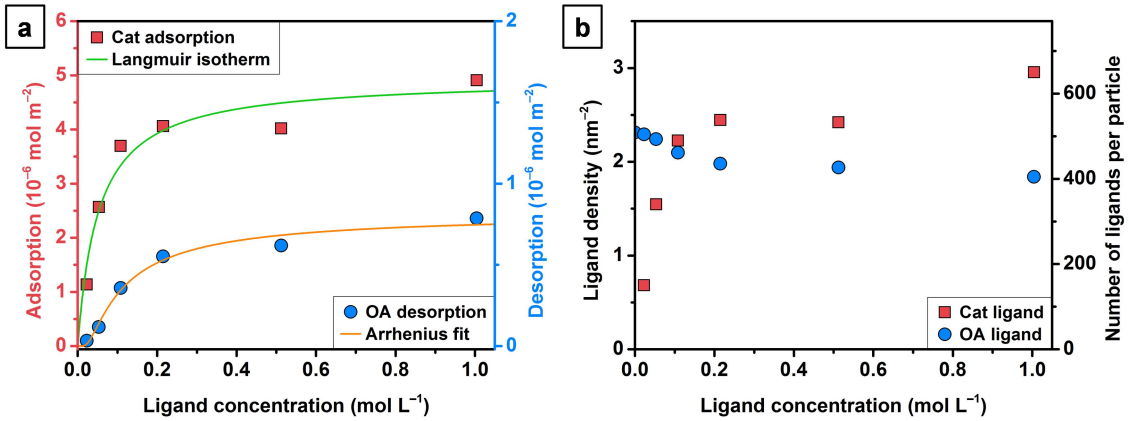

Figure 2.6. Quantification of surface processes on hydrophobic TiO_2–OA NPs. (a) Adsorption of catechol (red squares, left ordinate) onto the TiO_2 NP surface and desorption of oleic acid (blue circles, right ordinate) from the NP surface as a function of catechol concentration in solution. The adsorption process was fitted with a Langmuir isotherm (green line), while the desorption process was described by an Arrhenius-type function (orange line). (b) Absolute surface coverage of TiO_2–OA NPs with catechol (red squares) and oleic acid (blue circles) as a function of catechol concentration. The surface coverage is given in quantities of ligand density (left ordinate) and ligand number per particle (right ordinate). The starting value for the native surface coverage of as-synthesized TiO_2–OA NPs was adopted from Table 2.2.

Table 2.3. Fit functions for the theoretical description of the surface processes.

	surface process	
	adsorption	desorption
type of ligand	catechol	oleic acid
fit function	$y = a \cdot \frac{bx}{1+bx}$	$y = a \cdot \exp\left(\frac{b}{x}\right)$
values for a	4.95	0.82
values for b	19.17	−0.09
associated equations	Langmuir[299] (isothermal adsorption)	Arrhenius,[300] Polanyi–Wigner[301] (thermal desorption)

ligand density of TiO_2–OA NPs was found to be less than half of the maximum ligand density, this assumption appears very plausible. (ii) Our study yielded a maximum OA desorption value of only 0.8×10^{-6} mol m^{-2}, while more than the 6-fold amount of catechol is adsorbed. This finding reveals that the assumed ligand exchange process is far away from a 1:1 substitution stoichiometry, as typically suggested in the literature.

This picture becomes even more conclusive, when adsorption and desorption data are translated into ligand densities (Figure 2.6b), where the native ligand density of TiO_2–OA NPs is adopted from the TGA results. In absolute values, it is possible to ad-

sorb as much as 3.0 catechol ligands per nm^2 of TiO_2 surface, while at the same time the OA ligand density decreases from 2.3 nm^{-2} to no less than 1.8 nm^{-2}. This comparison reveals that the actual ligand substitution at OA-coordinated surface sites plays only a minor role because most of the native ligand density (~80%) is preserved during catechol adsorption. Rather than replacing native OA ligands, catechol strongly prefers to adsorb to empty surface sites. Altogether, the total ligand density increases from 2.3 nm^{-2} at a native OA coverage to 4.8 nm^{-2} at maximum catechol loading or, in other terms, from 510 molecules of OA per nanoparticle to 1050 molecules of a mixed ligand shell (1:1.6 OA/catechol). While the as-synthesized TiO_2–OA NPs exhibited less than half of the maximum ligand density possible (*vide supra*), the surface-modified TiO_2–Cat NPs approached the maximum level. The obtained grafting density of catechol is consistent with values for other catecholic ligands reported in the literature.[297]

The catechol appears to preferentially displace oleate from the {101} facets, as is evidenced by the declining intensity of the narrower, higher-field signal with increasing catechol concentration (Figure S2.14). This is probably due to the lower oleate chain density on this facet (*vide supra*). Therefore, catechol can penetrate more easily through the ligand shell and adsorb to the NP surface.

In order to explore the scope and general validity of the recent findings, the surface modification was performed with two other catechol derivatives, 4-*tert*-butylcatechol (tBuCat) and 2,3-dihydroxynaphthalene (DHN) (Table 2.4). These derivatives share the common feature of an apolar backbone to ensure consistent NP behavior in solution, i.e., dissolution in chloroform and precipitation with acetone or methanol. However, they differ distinctly from the unsubstituted parent compound in two respects: (i) 4-*tert*-butylcatechol is a sterically much more demanding catechol ligand due to its bulky *tert*-butyl group. (ii) 2,3-Dihydroxynaphthalene displays an altered electronic structure as a result of its extended π-conjugated aromatic system.

Furthermore, in order to examine the dependence of the surface processes on the TiO_2 NP batch (cf. Figure 2.1), the reaction was performed on a second batch of TiO_2–OA NPs with comparable dimensions (Figure S2.15 and Table S2.3). Surface modification on nanoparticles may be complicated by the polydispersity of particle size. Furthermore, the metal centers at the nanoparticle surface are not equivalent. Therefore, the dynamics of the surface processes are dictated by the arrangement of the ligands on the NP surface, in particular by the nature and accessibility of the metal sites, which can

Table 2.4. Employed catechol ligands and corresponding pK_a values.[303,304]

ligand	abbreviation	molecular structure	pK_{a1}	pK_{a2}	ref
4-*tert*-butyl-catechol	tBuCat	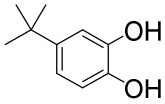	9.5	14.0	303
catechol	Cat	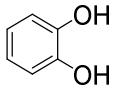	9.4	13.7	303
2,3-dihydroxy-naphthalene	DHN	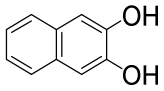	8.7	12.5	304

vary significantly from batch to batch. To allow for a consistent comparison of the batches, the functionalization with the unsubstituted catechol was repeated as control. Rather than examining the surface processes throughout the entire ligand concentration range (as done for Figure 2.6), the additional ligands were investigated only at one medium concentration of 0.2 mol L^{-1} (corresponding to reaction no. 4 in Table 2.1) by way of example. This concentration is high enough to yield significant amounts of adsorbed and desorbed species and also small enough to retrieve all unbound catechol ligands within four cycles of precipitation.

The ^{1}H NMR spectra of the corresponding surface-modified TiO_2 NPs (Figure 2.7a) are in line with the semi-quantitative picture that was derived from the study using the unsubstituted catechol parent ligand (cf. Figure 2.3b): Independent of the catechol derivative, the spectra reveal substantial amounts of residual oleate remaining attached to the TiO_2 NPs, while the adsorption of catecholic ligands is indicated by the typical broad resonances in the aromatic regime. The quantitative study revealed slight, but still significant differences in the adsorption and desorption processes (Figure 2.7b): Both processes yielded increasing values in the order tBuCat < Cat < DHN. This trend can be rationalized by an increasingly facilitated proton transfer from the catecholic ligand to the oleate. This property is in turn reflected in the pK_a values of the ligands (Table 2.4), which decrease in the same order as the amounts of adsorbed and desorbed ligands increase.

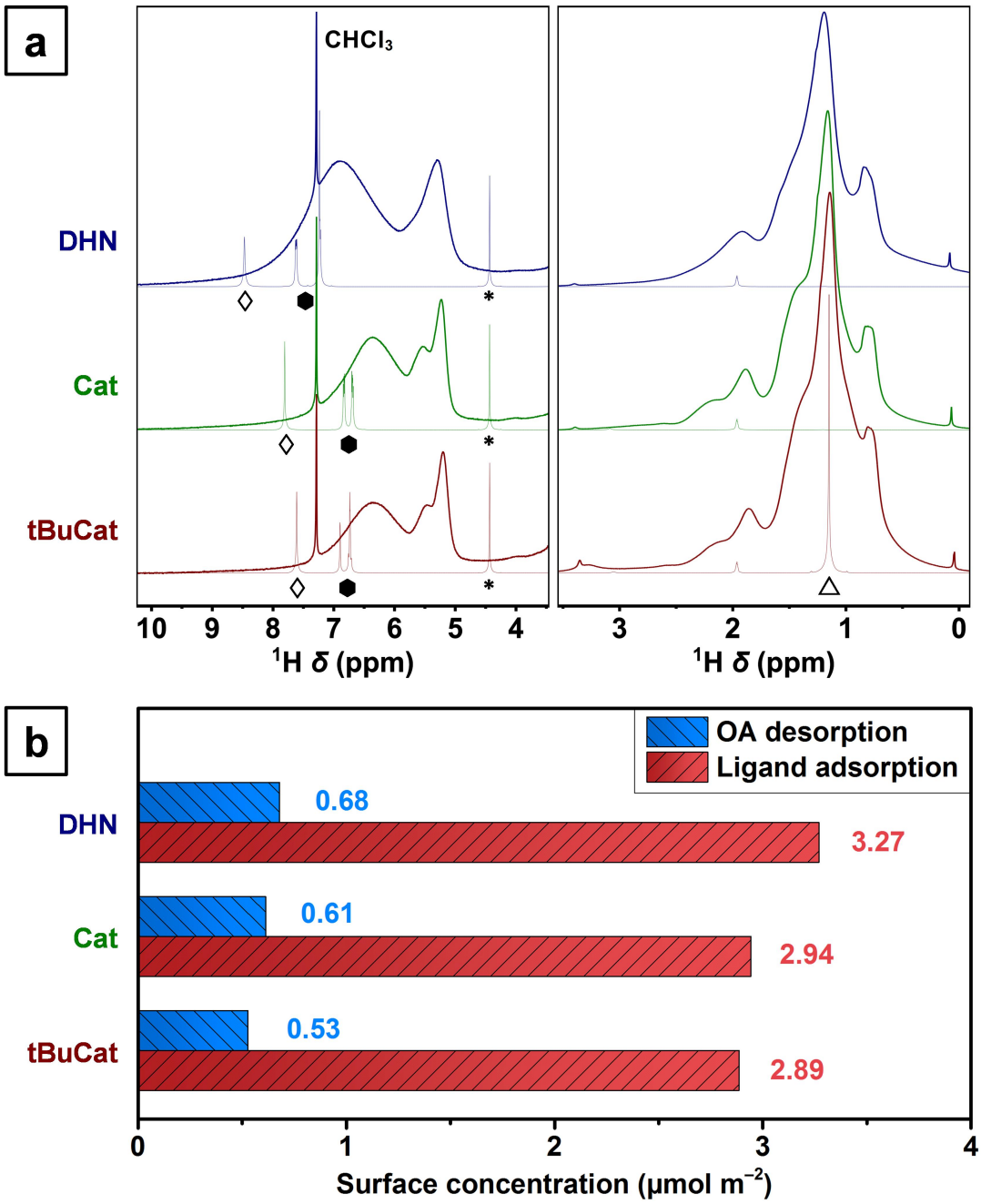

Figure 2.7. Surface modification of hydrophobic TiO_2–OA NPs with the three different ligands 4-*tert*-butylcatechol (tBuCat), (unsubstituted) catechol (Cat), and 2,3-dihydroxynaphthalene (DHN). (a) ^{1}H solution NMR spectra (400 MHz) of the surface-modified TiO_2 NPs in $CDCl_3$ and the corresponding reference spectra of the free ligands in acetone-d_6. The left panel shows the low-field regime of the aromatic and olefinic signals, while the right panel displays the high-field region of the aliphatic groups. For better comparison, the two domains were scaled differently (cf. Figure 2.3b). Assignment of signals: open diamonds (◊), hydroxyl protons; filled hexagons (⬢), aromatic protons; open triangle (△), aliphatic protons; asterisks (*), nitromethane standard. (b) Quantification of ligands after surface modification with tBuCat, Cat, and DHN at a ligand concentration of 0.2 mol L^{-1}.

Small deviations of the binding of unsubstituted catechol (Figure 2.6a vs 2.7b) can be related to the specific properties of individual TiO_2−OA NP batches. Small variations in particle size, morphology, and aspect ratio (Figure S2.15 and Table S2.3) translate into slight changes of the surface chemistry. The general finding is that catechol derivatives with apolar backbones display a similar adsorption behavior on hydrophobic TiO_2 NPs. Small differences in their behavior are primarily governed by their proton-donating ability (i.e., Brønsted acidity), expressed through their pK_a values.

The processes of catecholate adsorption and OA desorption are most probably accompanied by proton transfer[283] from catechol to surface-bound hydroxyl groups or oleate to induce the cleavage of water and/or oleic acid (cf. Figure S2.12b). The exact mechanism limiting the oleate displacement to 20% remains to be elaborated. We assume the desorption of OA to be restricted to some species that are less strongly attached to the NP surface, such as electrostatically associated or monodentately bonded oleate.[75] In both cases proton transfer from the catechol to the oleate and subsequent OA desorption should be facilitated as compared to the more stable bidentate binding mode of oleate. Additionally, the most easily displaced ligand species may be situated at particularly exposed binding sites, such as facet edges and vertices, which are easily accessed by the incoming ligands.[305]

Ligand displacement on NP surfaces can be compared with ligand substitution reactions in metal complexes, whose mechanisms with a classification as associative (A), dissociative (D), and interchange (I) mechanisms are well understood.[306] The dissociative and associative mechanisms are characterized by the formation of reaction intermediates where the leaving ligands are dissociated, or where both, entering and leaving ligands are coordinated, at the same time. The interchange mechanism I is a concerted, one-step process without detectable intermediate. This classification is reminiscent of – but not equivalent to – the S_N2/S_N1 mechanisms in organic chemistry.

The surface ligand displacement of OA by catechol-type ligands on TiO_2 NPs follows an associative mechanism characterized by the binding of the entering ligand. A discrete, detectable intermediate with mixed ligand shell is formed. The subsequent proton transfer from the catechol to the oleate is the rate-determining step, which culminates in the desorption of OA.

Associative mechanisms have also been suggested for thiol ligand exchange reactions in monolayer protected gold nanoclusters (Au NCs).[305,307,308] Both surface reac-

tions, catechols on TiO_2 NPs and thiols on Au NCs, have in common that only a limited fraction of the native ligands is replaced by the incoming ligands. This behavior is attributed to heterogeneities in the binding sites (e.g., facet edges and vertices) on the NP surface[305] and has recently been described for CdSe NPs as well.[309,310] Interestingly, polyoxotitanate nanoclusters, composed of 17 or 22 Ti atoms[123,132] and stabilized by isopropoxide groups (O^iPr), were found to exhibit similar limited ligand displacement upon catechol functionalization. Indeed, in the case of the former cluster $[Ti_{17}O_{24}(O^iPr)_{20}]$, catechol functionalization resulted in the displacement of only 4 HO^iPr units.[132] This accounts for 20% of the native ligand shell and coincides surprisingly well with our findings. Furthermore, crystallographic characterization of these clusters revealed that the ligand exchange took place only at the five-fold coordinated Ti surface sites, thus restoring the preferred six-fold coordination after bidentate binding of catecholate.[132]

2.5 Conclusion

Using the catechol−TiO_2 combination as a model system for the surface modification of hydrophobic metal oxide NPs, we have thoroughly investigated the surface chemistry of oleate-stabilized TiO_2 NPs upon catechol ligand adsorption. In order to gain direct insight into the ligand sphere, we utilized an NMR toolbox approach, comprising 1D and 2D, ^1H and ^{13}C, solution and solid state (MAS) NMR experiments. This provided comprehensive pictures of the native ligand shell before and the mixed ligand shell after catechol adsorption. The native ligand density was calculated to be 2.3 nm^{-2}, whereas the mixed ligand density increased more than twice to 4.8 nm^{-2} at maximum catechol loading. Surprisingly, catechol displaced only 20% of the native OA ligand shell. As a consequence, incoming catechol must predominantly adsorb to unoccupied Ti surface sites. Therefore, we do not consider this process a ligand exchange, substitution, or replacement, but simply a surface modification. The adsorption process appears to be irreversible due to the strong binding of the catechol ligand. Furthermore, we could show that all catecholic ligands with apolar backbones display this kind of surface chemistry, with only marginal differences that are governed by their Brønsted acidity.

In conclusion, catechol modification of hydrophobic TiO_2 NPs is a convenient method to produce mixed ligand shells. However, it is not suited for a complete ligand

shell refunctionalization. To achieve a complete ligand exchange, a two-step approach would rather be needed: (i) First, the native ligands would have to be removed by reactive stripping agents to yield cationic naked NPs.[311–313] (ii) Then, the surface would be refunctionalized with the catecholic ligand.[311,312]

The model derived here bears resemblance to the Vroman effect postulated for the formation of protein layers,[276] where highly abundant proteins adsorb only weakly during the early state. These proteins are replaced subsequently by less abundant proteins, which, however, bind with a higher affinity. This leads to a complex series of adsorption and displacement steps[314] and to the concept of a dynamic protein corona evolution.[277,315]

Our study contributes to the fundamental understanding of the formation of a layer of low molecular ligands. The unsubstituted catechol employed in this study is a valid prototype molecule to elucidate the fundamental surface chemistry of hydrophobic TiO_2 NPs. Here, "abundant" but less strongly bound OA ligands are displaced by catechol ligands binding strongly on metal oxide NP surfaces. Because of their non-innocent behavior catechol-sensitized TiO_2 NPs are of great interest for potential applications involving electron transfer reactions, such as photocatalysis.[261]

Further work is currently under way to investigate the effect of polar ring substituents on the oleate displacement efficiency. A recent study revealed that the ligand binding enthalpies of catechol derivatives depend on the electronic contributions of their substituents.[251] Similarly, we observed in an earlier study that a cationic catecholic anchor with an extended aromatic system is much more effective in the displacement of native oleate ligands, while exhibiting a similar catechol ligand coverage.[261]

2.6 Supporting Information

2.6.1 Additional Characterization of As-Synthesized TiO_2–OA NPs

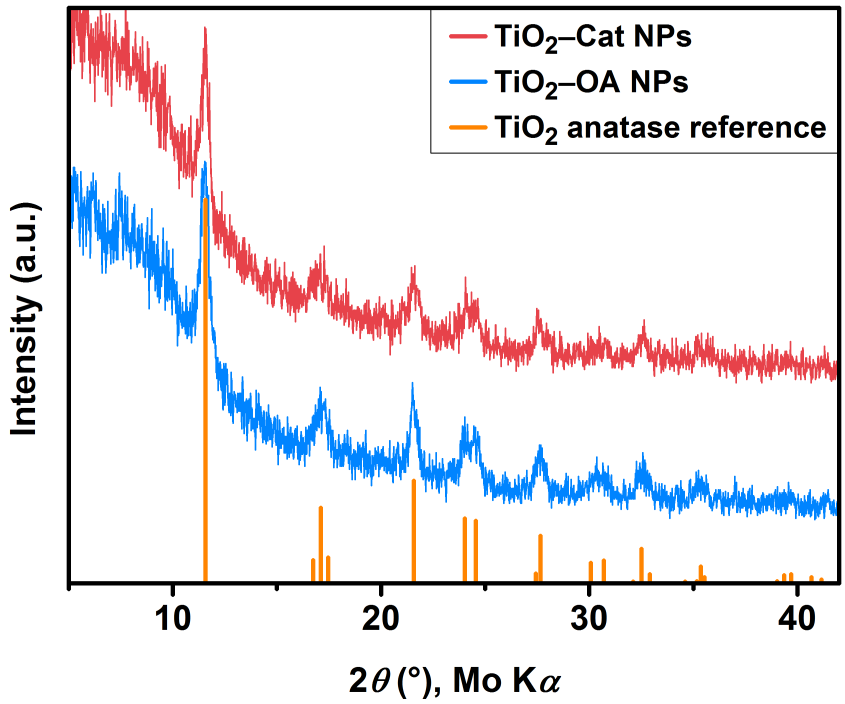

Figure S2.1. Powder X-ray diffractograms of TiO_2 NPs before (blue curve, TiO_2–OA NPs) and after catechol modification (red curve, TiO_2–Cat NPs), both matching the bulk anatase TiO_2 reference pattern (in orange, COD 96-500-0224).

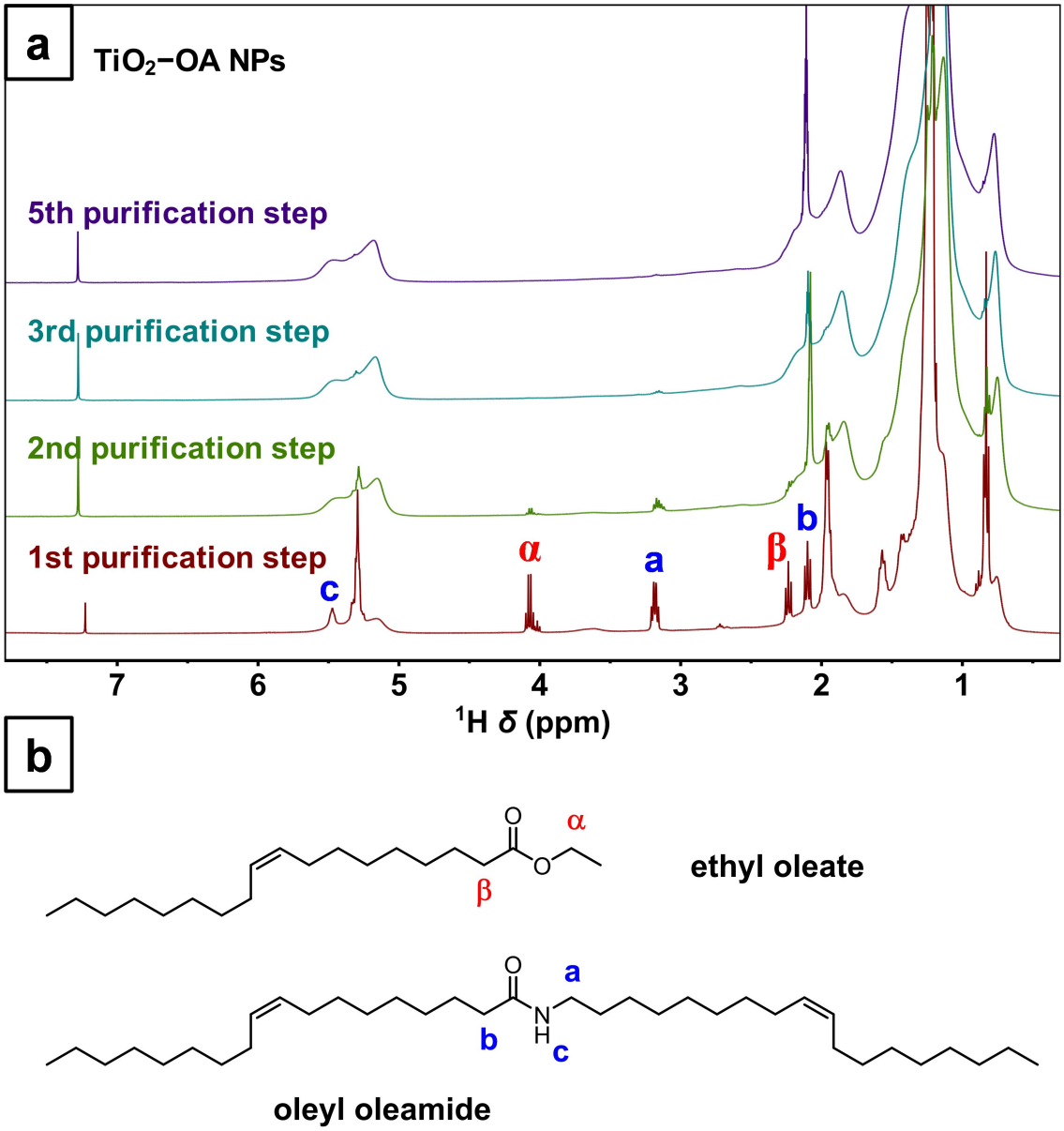

Figure S2.2. Purification of as-synthesized TiO_2–OA NPs. (a) ^1H solution NMR spectra (400 MHz, $CDCl_3$) after several precipitation–dissolution cycles. To remove residual solvents and reactants, the NPs had to go through at least five purification cycles. (b) Molecular structures of ethyl oleate and oleyl oleamide, the two major condensation byproducts formed under the high-temperature (solvothermal) conditions necessary for NP formation.[316–318]

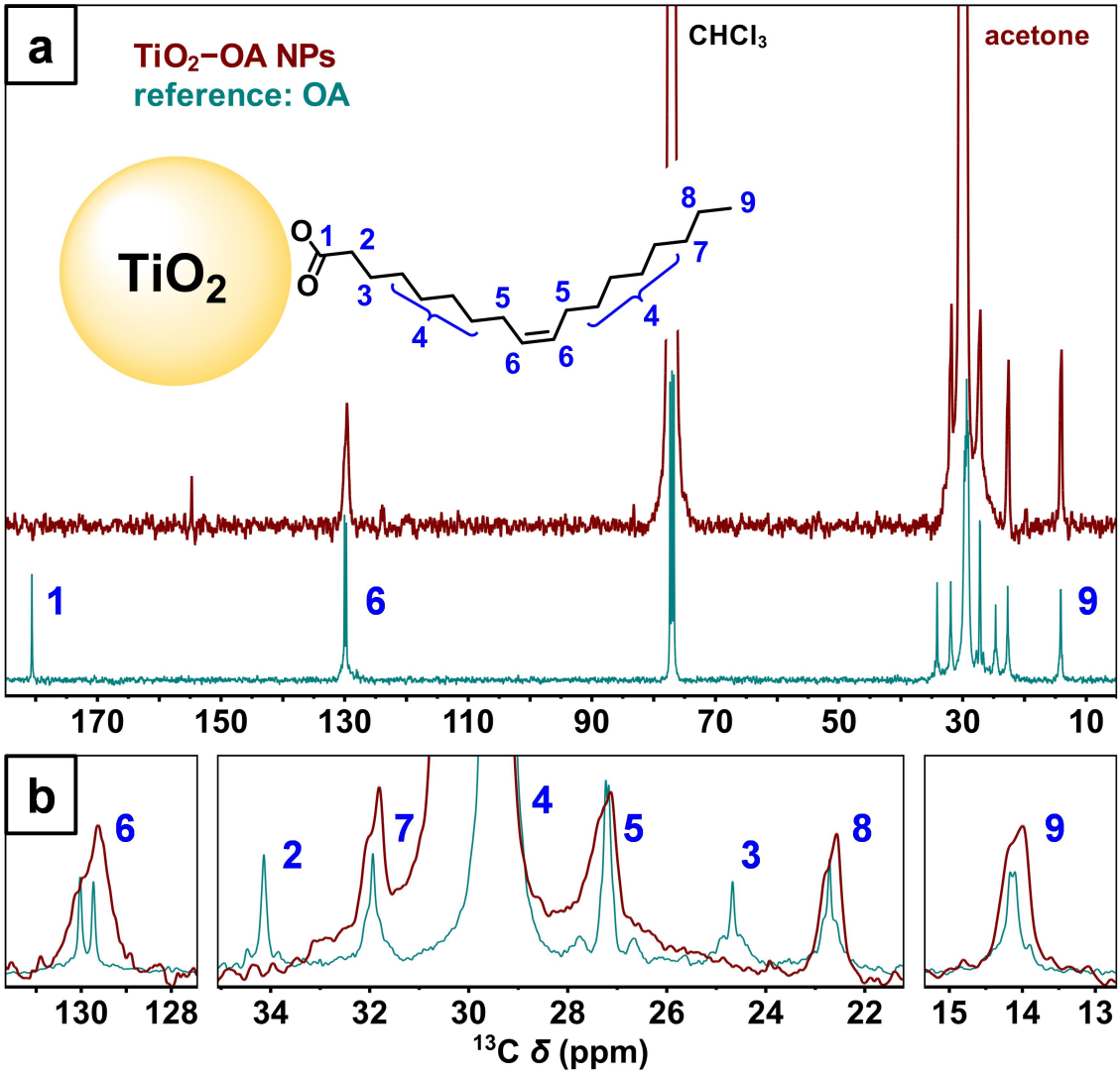

Figure S2.3. (a) ^{13}C solution NMR spectra (100 MHz, $CDCl_3$) of as-synthesized TiO_2–OA NPs (brown) and OA reference (teal). (b) Enlarged views of the relevant resonances. The three carbon atoms **1**, **2**, and **3** nearest to the NP surface are not detectable in solution NMR due to their highly restricted mobilities. All of the visible signals exhibit similar shoulders as observed for the ^{1}H resonances in Figure 2.3a.

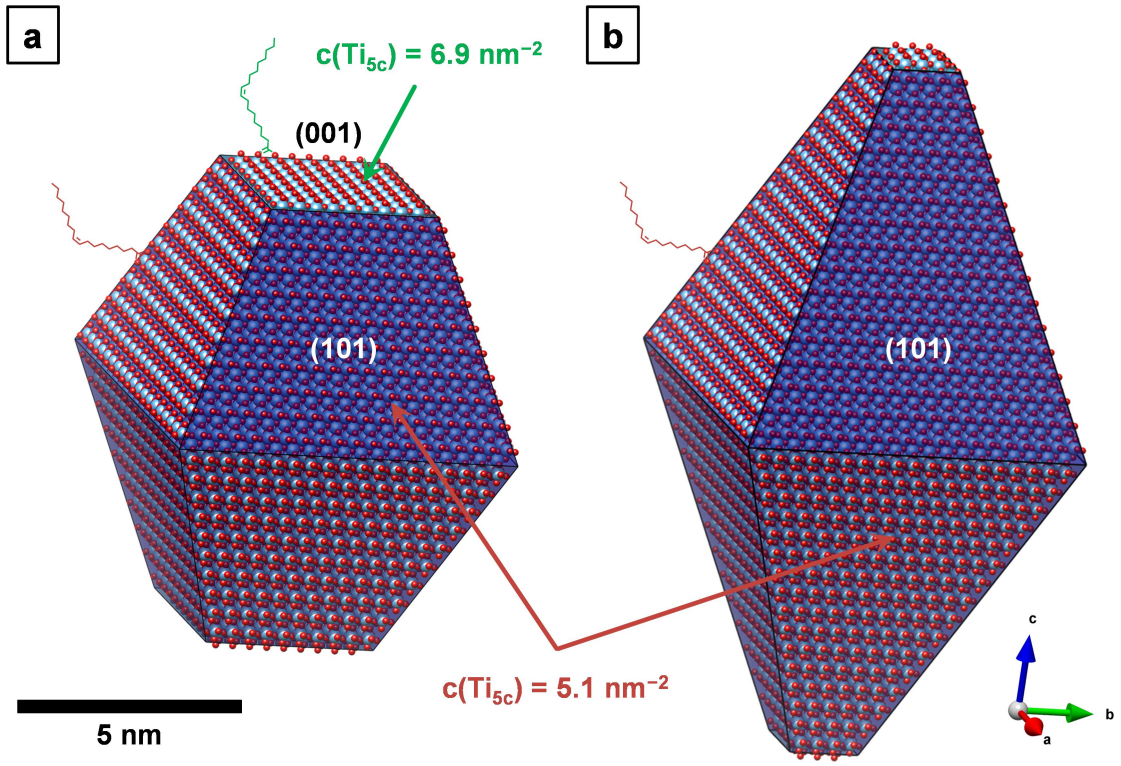

Figure S2.4. Three-dimensional representations of the differently shaped TiO_2 NPs as (a) highly and (b) slightly truncated bipyramids (red spheres: oxygen; blue spheres: titanium). The surface densities for five-fold coordinated Ti sites (Ti_{5c}) exposed on the two most common anatase crystal faces (101) and (001) are given as 5.1 nm^{-2} and 6.9 nm^{-2}, respectively. The oleate species bound to the {001} facets (drawn in green) is assumed to give rise to the broader, lower-intensity, lower-field shoulder signal due to the higher theoretical packing density of oleate chains. Consequently, the narrower, higher-intensity, higher-field signal is attributed to the oleate species bound to the {101} facets (shown in red), which allow for higher chain mobility due to the lower packing density of oleate chains.

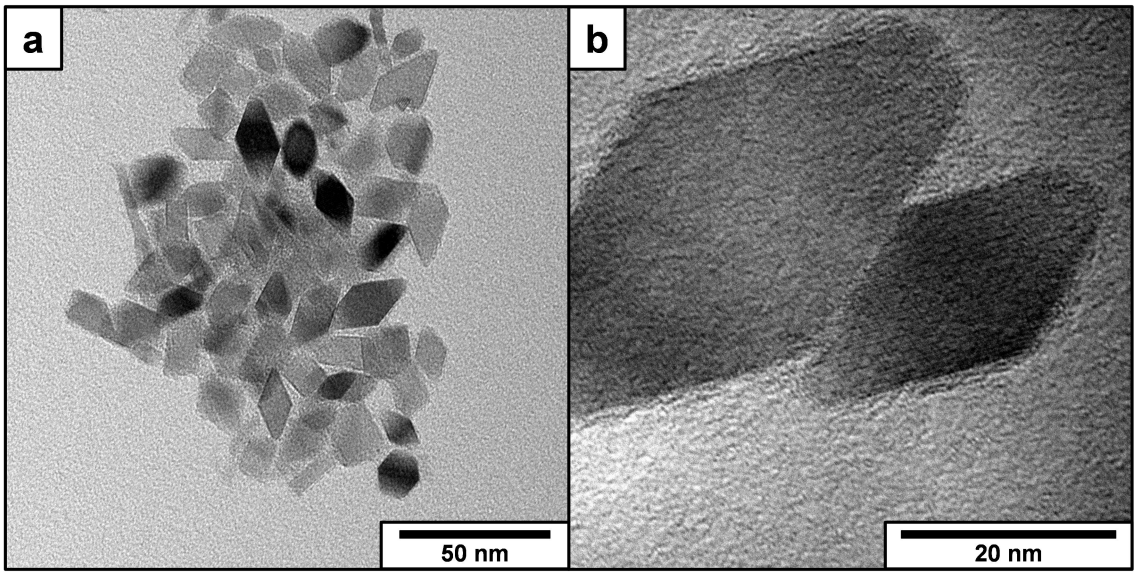

Figure S2.5. TEM characterization of slightly truncated bipyramidal TiO_2−OA NPs synthesized with an oleic acid/oleylamine ratio of 4:6. (a) Overview image of a NP ensemble. (b) High resolution TEM image of individual NPs. The major axis length of the NPs ranges from 10 to 30 nm.

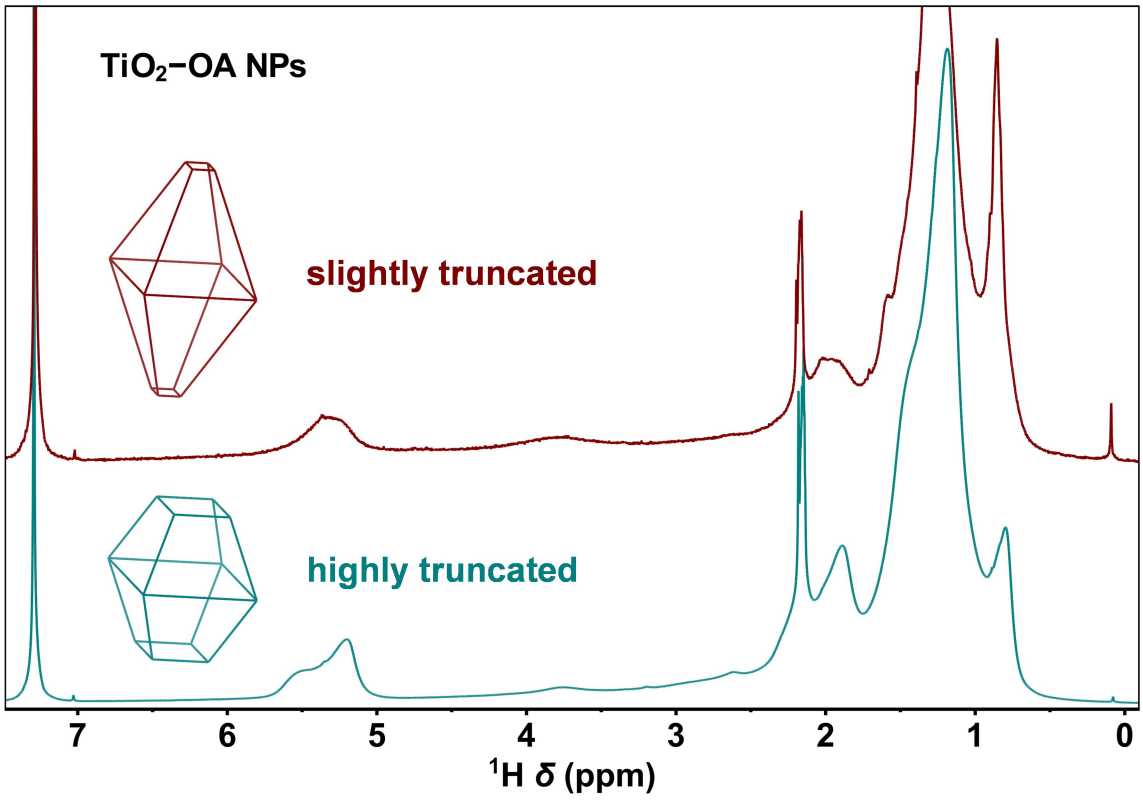

Figure S2.6. ^1H solution NMR spectra (400 MHz, $CDCl_3$) of slightly truncated (brown curve) and highly truncated (teal curve) TiO_2−OA NPs, synthesized with an oleic acid/oleylamine ratio of 4:6 and 6:4, respectively. The slightly truncated TiO_2−OA NPs with only one major crystal facet show no pronounced signal shoulder (cf. olefinic signal in the range 5.5−5.0 ppm) as is the case for the highly truncated, pseudo-spherical NPs.

2.6.2 Identification and Discussion of Plastic Labware Contaminations

In order to identify some of the most prominent contaminations from common laboratory plasticware made from polypropylene (PP), the plastic containers were exposed to $CDCl_3$ for several hours to allow for sufficient accumulation of contaminants to be analyzed by NMR spectroscopy.

Figure S2.7a displays the NMR spectra of $CDCl_3$ extracts from a disposable syringe and a centrifuge tube. Both PP materials were found to leach considerable amounts of contaminants with partly matching signals. In the context of this work, two components were found to be the most hazardous for the NMR investigation of oleate-stabilized nanoparticles: (i) The most pronounced contamination is a very intense set of aliphatic signals in the range 1.8−0.7 ppm, where they can easily obscure the low-intensity signals of NP-bound ligands. (ii) A contamination, which is only found in the PP material of disposable syringes, exhibits a pronounced signal at 5.4 ppm, which is identical to the olefinic resonance of oleic acid used for the quantification of the native ligand.

Due to their high significance, efforts were made to identify the nature of these major contaminations. The olefinic contamination from the syringe material was found to arise from oleamide or its higher homologue erucamide (Figure S2.7b). These fatty acid amides are commonly employed slip agents that reduce the friction between the plunger and the barrel components of the syringe. They are usually added to the polypropylene composition before injection moulding of the polymer.[319,320]

To gain further information about the contaminations shown in Figure S2.7a, a diffusion-ordered spectroscopy (DOSY) experiment was carried out on the $CDCl_3$ extract from the PP centrifuge tube. The resulting DOSY spectrum (Figure S2.8) reveals a broad mixture of species with various diffusion coefficients. Based on their diffusion behavior, the contaminants are divided into three groups: (i) Fast-diffusing, low-molecular-weight additives featuring signals over the entire chemical shift range, with signatures typical for aromatic, olefinic, and aliphatic groups. These contaminations are caused by a multitude of polymer additives, such as antioxidants, light stabilizers, antistatic or nucleating agents.[288,321] (ii) Some polymeric, aliphatic additives with a slightly lower diffusion coefficient, giving rise to the most intense ^1H NMR signals of all contaminations (cf. Figure S2.7a). (iii) A high-molecular-weight species with a significant-

ly lower diffusion coefficient, caused by a resonance signal in the high-field region (0.07 ppm) typical for organosilicon compounds. This contamination is a silicone oil based on polydimethylsiloxane (PDMS) and used as a lubricant or mold-release agent in the plastic manufacturing process.[288,322]

To identify the polymeric additive responsible for the immense signals in the aliphatic region of the ^{1}H NMR spectrum (cf. Figure S2.7a), a ^{1}H–^{13}C heteronuclear single quantum correlation (HSQC) experiment was performed on the $CDCl_3$ extract from the PP centrifuge tube. The corresponding HSQC spectrum (Figure S2.9) displays a complex set of correlations in the aliphatic region. Besides the broad ^{1}H and ^{13}C resonance signals that are indicative of the polymeric species, the spectra also show a superimposed subset of sharp signals (marked with asterisks in Figure S2.9a), which arise from the low-molecular-weight additives.

The most intense signal of the polymeric species (δ_H = 0.85 ppm) suggests that this contamination is very rich in methyl groups. An obvious assumption would be the presence of dissolved polypropylene, especially since both the ^{1}H and ^{13}C NMR spectra show some striking similarity to the corresponding spectra of atactic polypropylene.[323–325] However, polypropylene alone cannot account for all of the polymeric correlations in the HSQC spectrum in Figure S2.9a. An in-depth literature research allowed a more thorough identification of the polymeric compound, which was found to be an ethylene–propylene copolymer.[323,326] Thus, the additional correlations in the HSQC spectrum are attributed to various ethylene–propylene sequence placements and inverted propylene structures (Figure S2.9b).[326,327] Comparing the ^{1}H and ^{13}C NMR spectra of the polymeric contamination with those reported in the literature for some ethylene-propylene copolymers,[323,326,328] it is safe to assume an approximate ethylene content of 10–20 mol%.

This rather unexpected additive is a usual constituent of so-called impact polypropylene, which is the most common grade of industrial polypropylene.[329] Impact polypropylene is produced in a two-stage polymerization process, where first the polypropylene homopolymer is synthesized and then the ethylene–propylene copolymer is polymerized within the same batch, using a mixed monomer feed of ethylene and propylene.[321,330] The resulting product is a blend of the homopolymer with the rubber-like ethylene–propylene copolymer, which exists as a segregated phase of discrete droplets in a continuous matrix of the homopolymer. This composite structure leads to enhanced

impact strength of the otherwise brittle polypropylene homopolymer with inherently low impact strength.[321,329,331] However, due to its discrete nature and lower molecular weight compared to the homopolymer, the rubber-like ethylene–propylene copolymer is easily extracted from the PP matrix with nonpolar solvents, such as xylene, hexane, or $CHCl_3$.[321,329] As a result, this polymeric material tends to accumulate in NMR samples that were subjected to PP surfaces, giving rise to the immense aliphatic signals shown in Figure S2.7a.

To emphasize the risk of contaminations from plastic labware, Table S2.1 provides an overview of the polymer additives identified in this study. With this knowledge in mind, we reviewed some NMR spectra from the recent literature where plastic contaminations might have compromised the reported NMR results. Table S2.2 gives some examples.

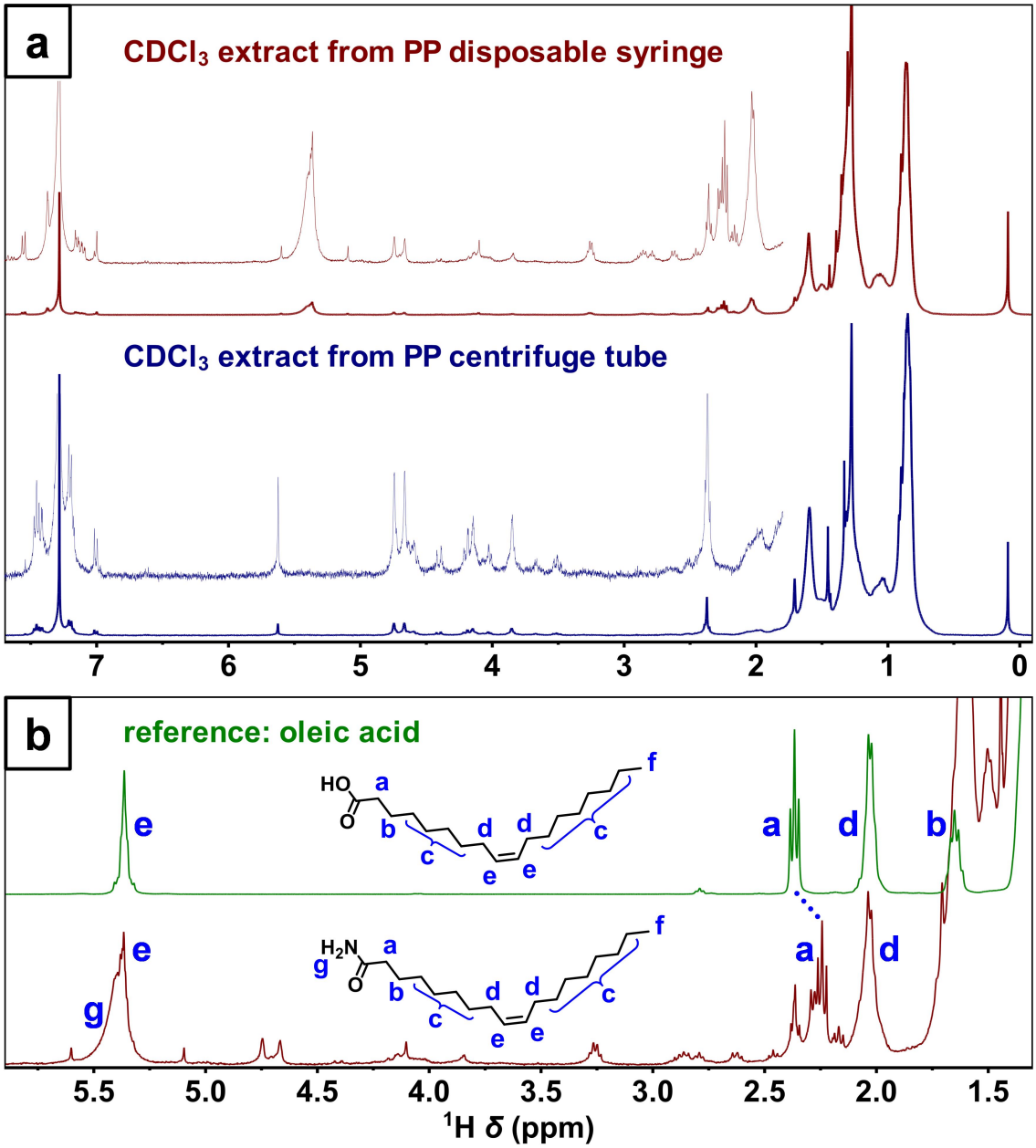

Figure S2.7. ^{1}H NMR spectra of contaminants extracted from polypropylene (PP) laboratory consumables. (a) $CDCl_3$ extracts from a disposable 1 mL-syringe (brown curves in upper panel) and a 50 mL-centrifuge tube (blue curves in lower panel). Enlarged views in the range 7.7−1.8 ppm are given as stacked spectra. (b) Reference spectrum of free oleic acid (green curve in upper panel) in comparison with the $CDCl_3$ extract from the syringe material (brown curve in lower panel). The comparison reveals that the major syringe contaminant must be a compound closely related to oleic acid. Indeed, the signals can be clearly assigned to oleamide, the amide derivative of oleic acid.

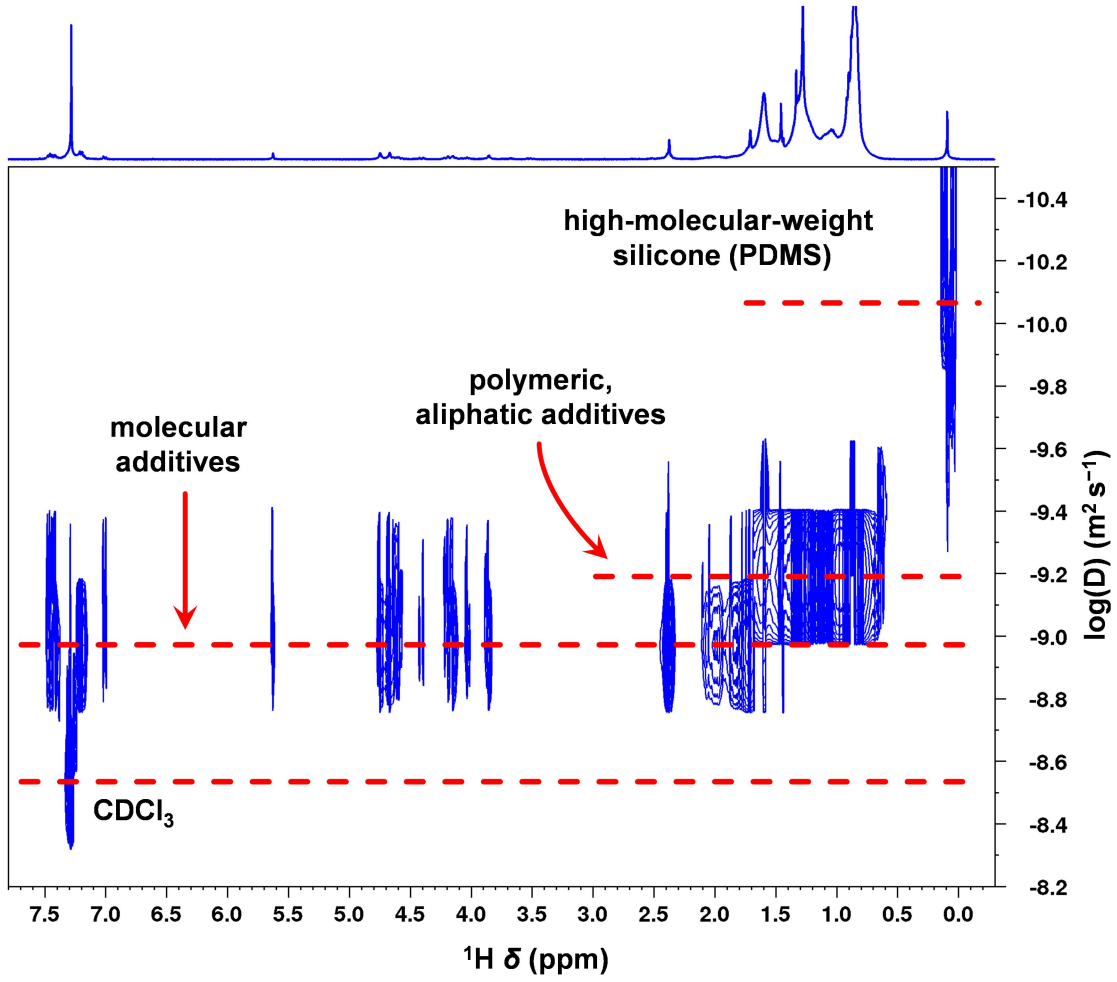

Figure S2.8. DOSY spectrum of the $CDCl_3$ extract from the PP centrifuge tube. Apart from the quickly diffusing solvent molecules, the contaminants are divided into three groups with significantly different diffusion behaviors: (i) fast-diffusing, low-molecular-weight species caused by a multitude of polymer additives, (ii) a polymeric, aliphatic species with a slightly lower diffusion coefficient, and (iii) a high-molecular-weight silicone oil based on polydimethylsiloxane (PDMS) with a significantly lower diffusion coefficient.

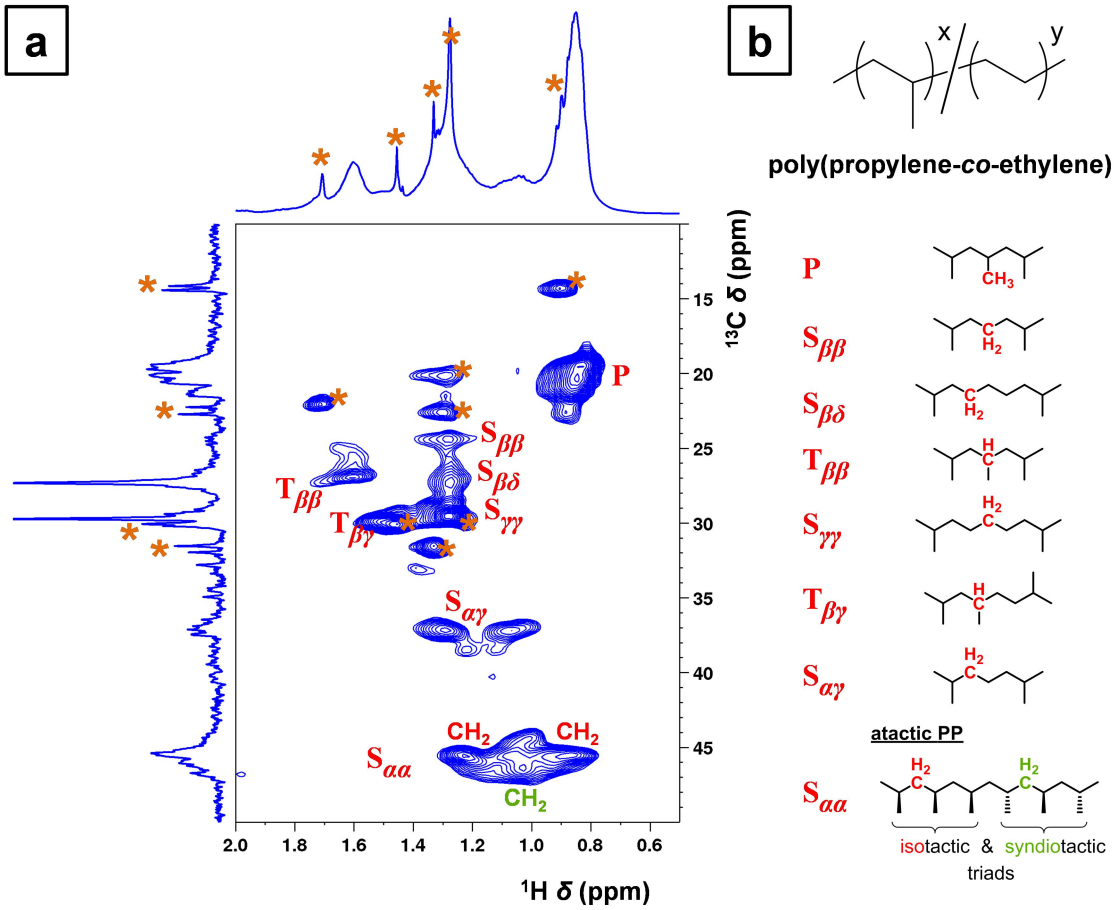

Figure S2.9. Identification of the polymeric, aliphatic additive extracted from the PP centrifuge tube. (a) HSQC spectrum of the aliphatic region, displaying a complex set of correlations among the polymeric signals. On top of those signals is a subset of sharp signals (marked with orange asterisks) that arise from the low-molecular-weight additives. (b) The polymeric correlations can be assigned reliably to different monomer sequences in the ethylene–propylene copolymer. The assignments were carried out according to Cheng et al.,[326,327] using the nomenclature of Carman et al.:[332] **P**, **S**, and **T** refer to primary (methyl), secondary (methylene), and tertiary (methine) carbons, respectively; the Greek subscripts indicate the carbon's position relative to the nearest tertiary carbons in both directions along the polymer chain (e.g., $\mathbf{T}_{\beta\gamma}$ denotes a methine group whose nearest tertiary carbon neighbors are two bonds to the left and three bonds to the right). The propylene sequences of the copolymer exhibit features of both isotactic and syndiotactic triads, thus rendering the polymer atactic.

Table S2.1. Summary of the most promiment contaminations from PP labware.

kind of additive	identity	δ_H (ppm)	log(D) ($m^2 s^{-1}$)
stabilizing additives (antioxidants, light stabilizers, etc.)	several non-identified species, featuring aromatic, olefinic, and aliphatic signatures	7.5−0.9	−9.0
nucleating/clarifying agent	1,3:2,4-bis(3,4-dimethylbenzylidene)-D-sorbitol (DMDBS)[333,334] 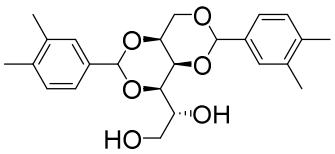	7.5−7.2, 5.6, 4.4−3.8, 2.4	(−9.0)
slip agent	oleamide 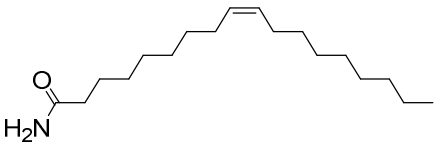 (or erucamide)	5.4−0.9	(−9.0)
impact modifier	poly(propylene-*co*-ethylene) 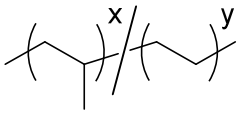 x ≈ 0.8, y ≈ 0.2	1.8−0.7	−9.2
	with vinylidene end group[335–337] 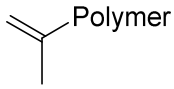	4.8−4.6, 1.7	
lubricant, mold-release agent	polydimethylsiloxane (PDMS) 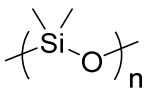	0.07	−10.1

Table S2.2. Examples of recent literature with potentially compromised NMR results.

publication year and ref#	kind of NPs and NMR measurements	potentially compromised results
2008 ref 338	oleate-capped iron oxide NPs + ligand exchange; high-resolution magic-angle spinning (HRMAS)	^{1}H (MAS) NMR spectra of supposedly NP-bound ligands (oleate and other carboxylates) showed pronounced aliphatic signals with a methyl-rich component strongly resembling the NMR signature of the ethylene−propylene copolymer. In accordance with the non-polar nature of the copolymer, these signals were only observed, when benzene was used as a solvent. Sharp signals of (presumably residual) ligands were only obtained whenever polar solvents, such as DMSO or MeOH, were employed. Also, the authors were not able to retrieve the olefinic oleate signal in non-polar solution, which is unusual for NMR spectra of oleate-capped NPs (cf. main text of the manuscript). Note: De Roo et al.[339] have already expressed concerns about the validity of the reported methods.
2015 ref 281	oleate-capped $NaYF_4$ NPs; ^{1}H NMR	No detectable signal from the olefinic protons (*vide supra*); questionable integration of overlapping methyl signal.
2015 ref 317	oleate-capped iron oxide and TiO_2 NPs; ^{1}H NMR	^{1}H NMR spectrum of TiO_2 NPs with sharp signals of residual oleyl oleamide (cf. Figure S2.2), which was erroneously interpreted as the only capping agent. Most probably the NP amount was too small to reveal the low-intensity signals of bound oleate ligands (see main text) lying below the impurity signals of oleyl oleamide.
2017 ref 340 (SI)	$Eu_2(CO_3)_3$ clusters coated with PCDA; ^{1}H NMR	^{1}H NMR spectrum of $Eu_2(CO_3)_3$ clusters coated with 10,12-pentacosadiynoic acid (PCDA) essentially displaying the ethylene−propylene copolymer.
2018 ref 341	oleyl amine-capped Au NPs + ligand exchange with octadecanethiol (ODT); ^{1}H NMR, DOSY	Previous work from our group with NMR spectra showing contaminant signals from the ethylene−propylene copolymer that was mistaken for the signals of NP-bound ODT ligands.

2.6.3 Additional Characterization of Catechol-Modified TiO_2–Cat NPs

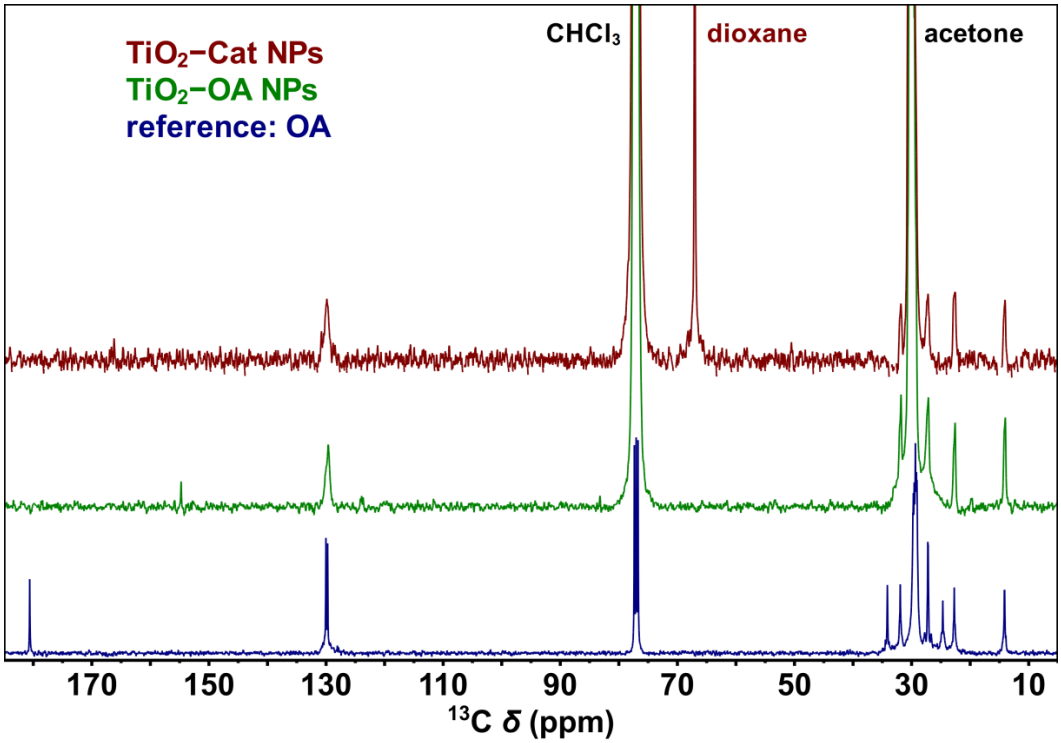

Figure S2.10. ^{13}C solution NMR spectra (100 MHz, $CDCl_3$) of catechol-modified TiO_2–Cat NPs (brown), as-synthesized TiO_2–OA NPs (green), and OA reference (blue). Catechol carbons are not detectable in ^{13}C solution NMR experiments.

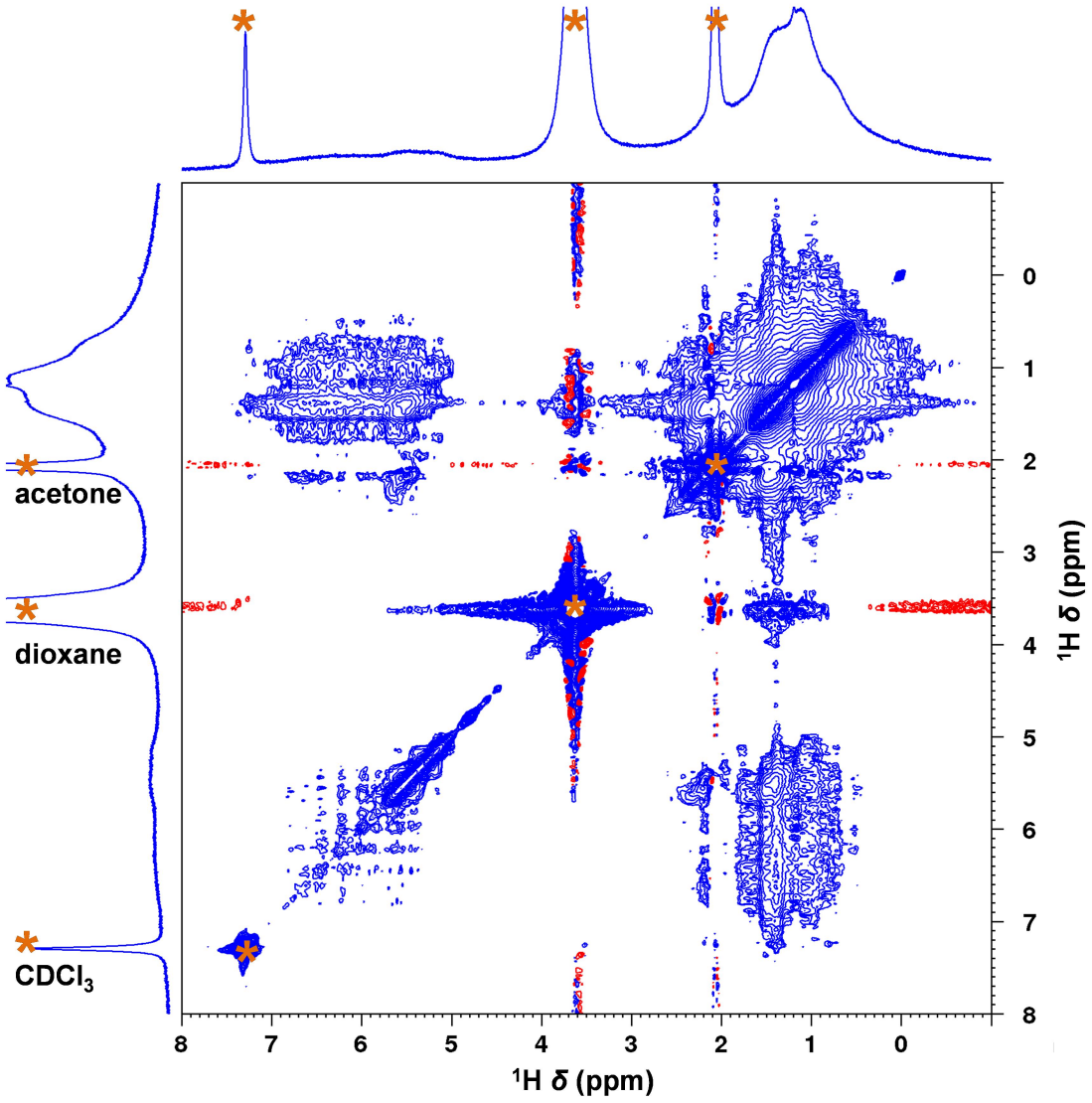

Figure S2.11. 2D NOESY spectrum (400 ms mixing time) of catechol-modified TiO_2−Cat NPs in $CDCl_3$. The pronounced negative cross-peaks between the aromatic and the aliphatic resonances reveal the close proximity of catecholate and oleate ligands on the NP surface. The cross-shaped disturbances are caused by solvent signals of acetone, dioxane, and $CDCl_3$ (marked with orange asterisks).

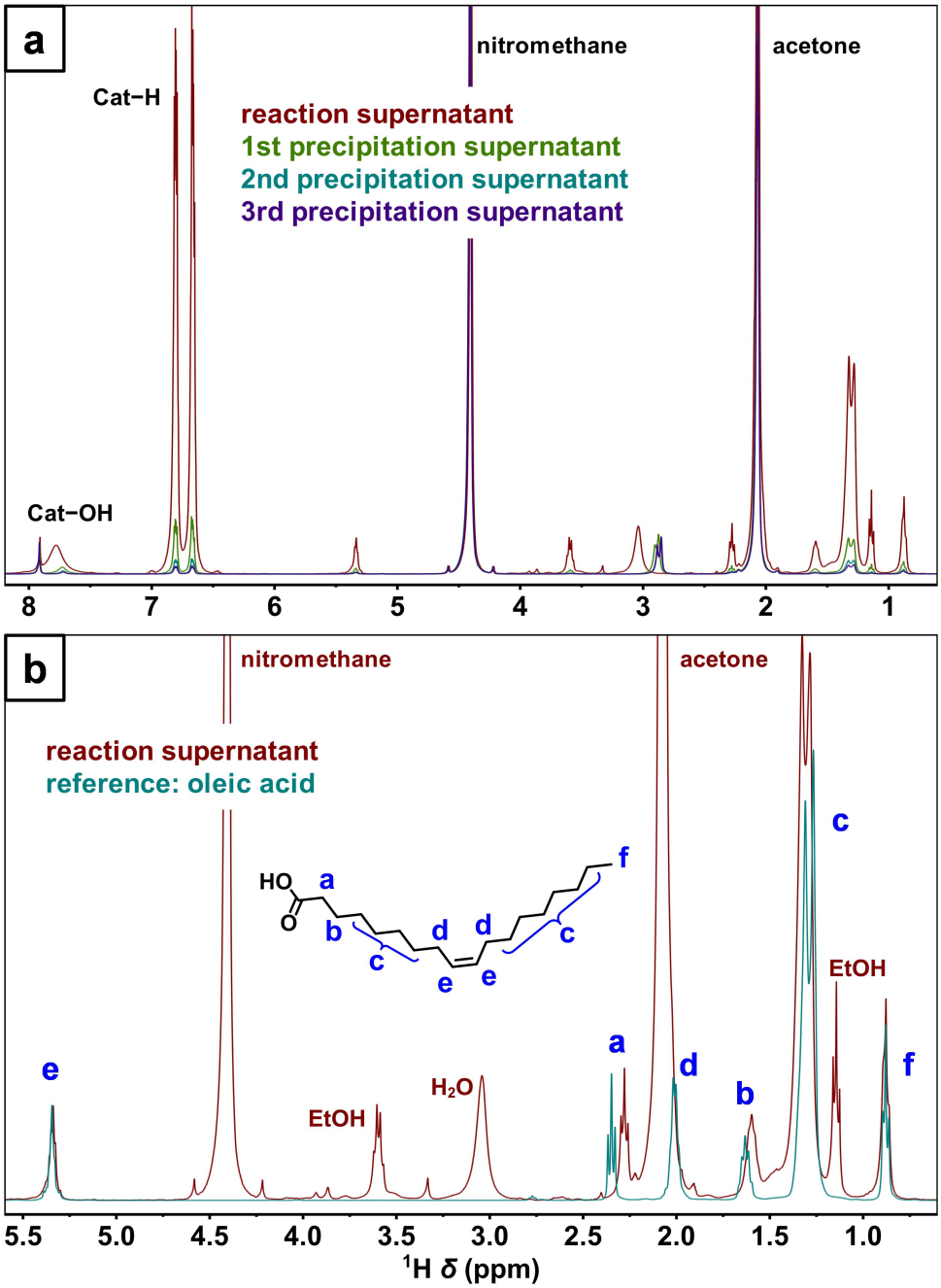

Figure S2.12. ^{1}H solution NMR spectra (400 MHz, acetone-d_6) of the supernatant solutions collected during the NP purification process after surface modification with a nominal catechol mass of 20 mg (reaction no. 4 in Table 2.1). (a) Superposition of the reaction supernatant and the first 3 precipitation supernatants, confirming the necessity of repeated precipitation cycles to remove excess catechol and desorbed OA. In addition, the spectra confirm that catechol remains in its reduced form during surface modification. The spectra were adjusted to the same resonance integral of the internal standard nitromethane. (b) Comparison of the reaction supernatant (brown curve) with a reference of oleic acid in $CDCl_3$ (teal curve) to confirm the desorbed species' identity as (protonated) oleic acid. The resonances **a** and **b** nearest to the carboxyl group are shifted slightly towards higher field due to the more polar nature of acetone-d_6 as compared to $CDCl_3$.

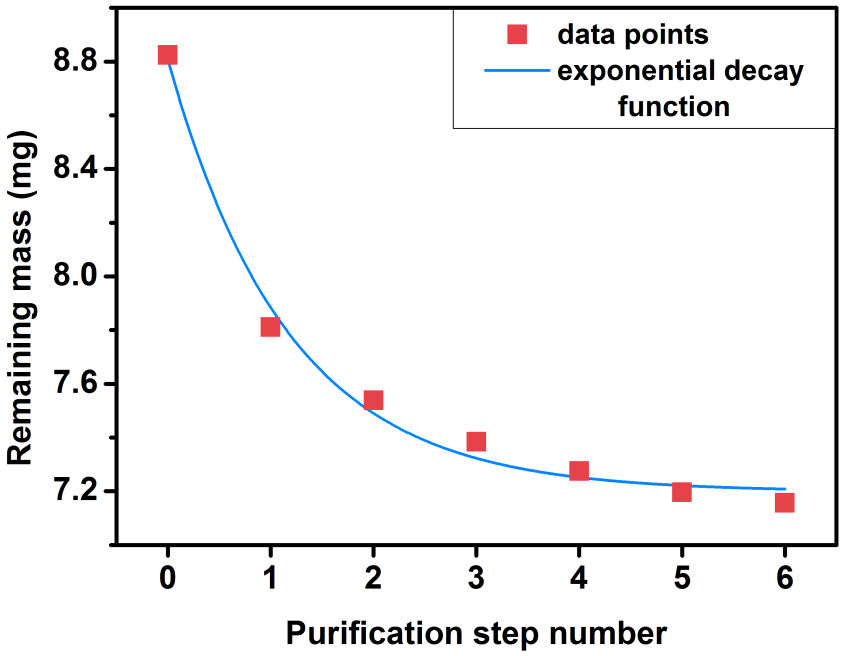

Figure S2.13. Remaining amount of catechol retained within the precipitated NP residue after several consecutive purification steps. The data was obtained from surface modification with a nominal catechol mass of 20 mg (cf. Table 2.1). The first data point corresponds to the amount of catechol retained within the NP residue after centrifugation of the reaction mixture, including both irreversibly adsorbed and reversibly absorbed species of catechol. The subsequent purification steps serve to remove the reversibly absorbed catechol molecules that are trapped between the NPs. This process is comparable to the method of liquid–liquid extraction where the solute concentrations in the two immiscible phases are governed by Nernst's distribution law.[298] Indeed, the declining amount of remaining catechol with increasing number of purification steps can be described with a Nernst-type exponential decay function of the form

$$\frac{m}{\text{mg}} = a \cdot b^x + c$$

where

m = remaining mass (in mg),
x = number of purification steps,
a = 1.608,
b = 0.426,
c = 7.199.

This type of function incorporates two important values for the employed purification process in accordance with Nernst's distribution law: (i) Setting the purification step number to $x = 0$ returns the starting amount as $m_0 = a+c$. (ii) For high values of x, *i.e.*, many purification cycles, the function converges to the boundary value $m_\infty = c$. Conveniently, this value corresponds to the amount of catechol that is irreversibly adsorbed to the NP's surface.

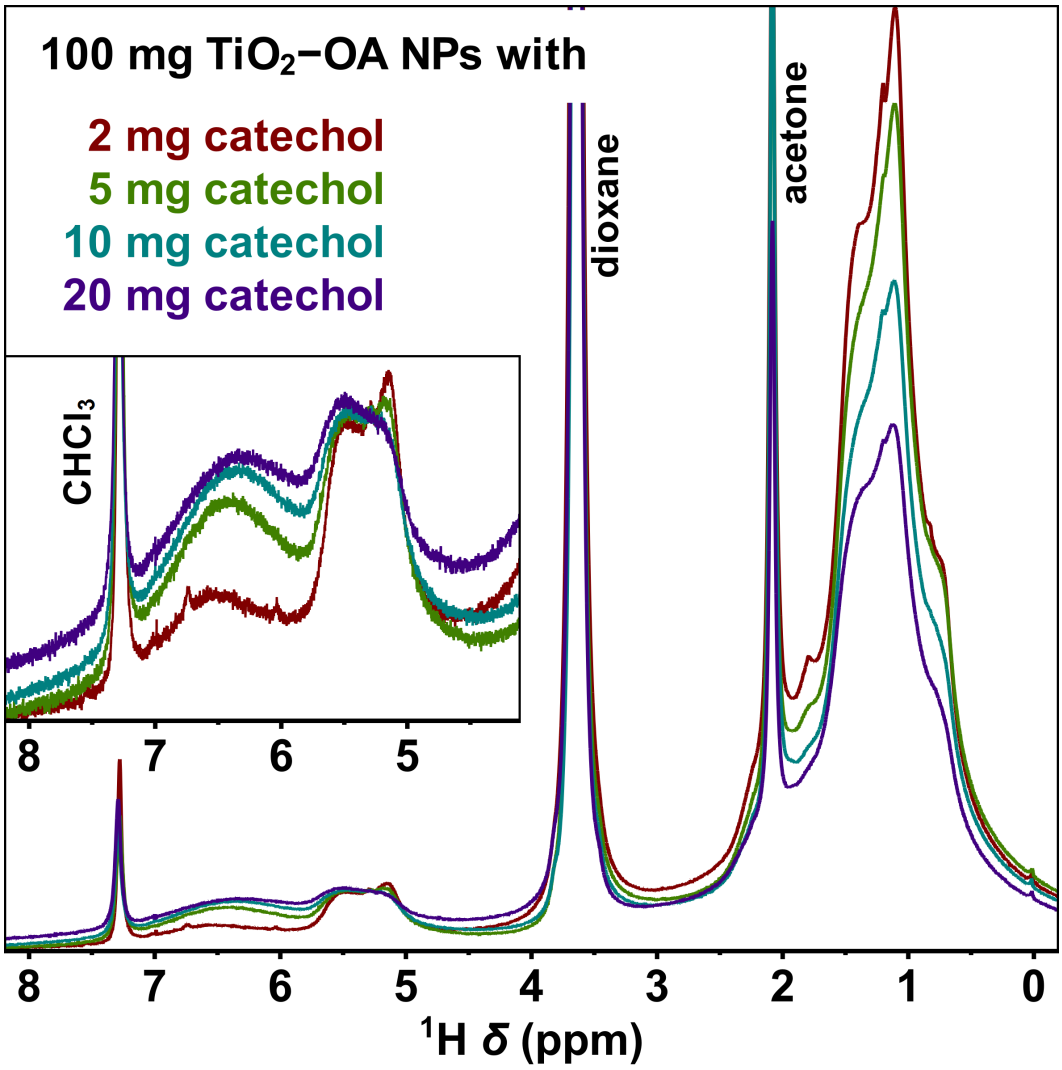

Figure S2.14. ^1H solution NMR spectra (400 MHz, $CDCl_3$) of catechol-functionalized TiO_2−Cat NPs with increasing amounts of catechol. The higher-field components of the oleate signals decrease more pronouncedly than their lower-field counterparts as the amount of adsorbed catechol and the corresponding aromatic resonance increase. Dioxane serves as an internal standard to align the spectra. These spectra exhibit less sharp signals than the spectrum of TiO_2−Cat NPs in Figure 2.3a due to the excessive washings performed in this reaction series to retrieve as much unbound ligands as possible.

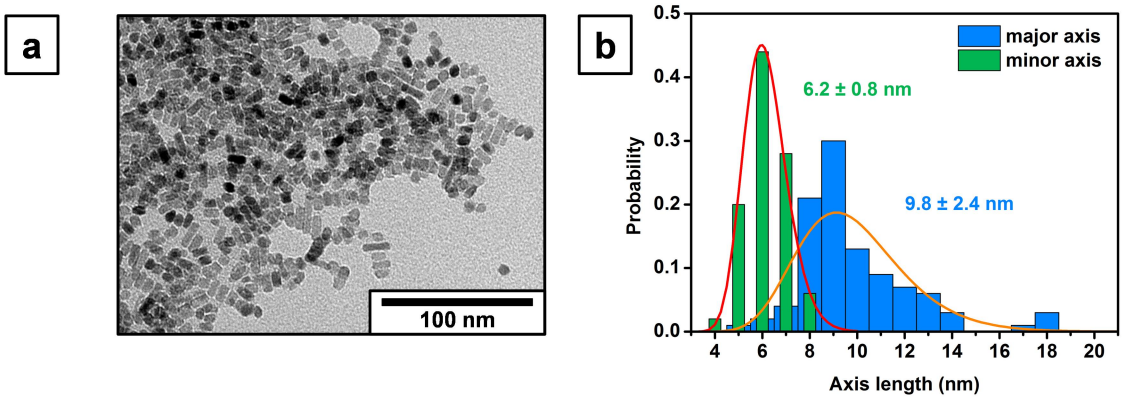

Figure S2.15. Characterization of the second batch of as-synthesized, OA-stabilized TiO_2 NPs. (a) Typical TEM overview image, revealing spherical to elongated morphology. (b) Size histogram over 100 individual particles, fitted as ellipses with major and minor axes, confirming the elongated shape of the TiO_2 NPs. The solid lines (red and orange) were obtained by fitting the size distribution histograms to the log-normal distribution. The values given are the mean values of the corresponding histograms.

Table S2.3. Characteristics of the second batch TiO_2–OA NPs.

quantity	value
major axis (nm)[a]	9.8 ± 2.4
minor axis (nm)[a]	6.2 ± 0.8
volume (nm^3)[b]	197 ± 70
surface area (nm^2)[b]	170 ± 42
specific surface area ($m^2\ g^{-1}$)	180 ± 78
organic fraction (%)	20.6 ± 1.0
ligands per particle	415 ± 149
ligand density (nm^{-2})	2.4 ± 1.1

[a]Mean values from TEM size evaluation after fitting individual particles as ellipses. [b]Values calculated according to the formulae for prolate (elongated) spheroids.

3

TiO_2 Nanoparticles Functionalized with Non-innocent Ligands Allow Oxidative Photo-cyanation of Amines with Visible/Near-Infrared Photons

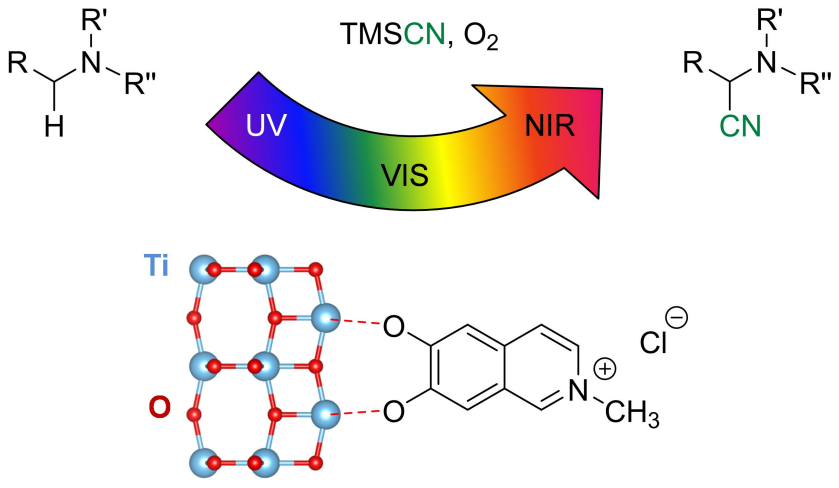

nano anatase TiO_2 + photosensitive surface ligand

This chapter contains an adapted reproduction of *Journal of the American Chemical Society* **2018**, *140*, 14169–14177, reprinted with permission of the American Chemical Society (© 2018).

Authorship Contributions

Study conception and design	E. Schechtel A. M. Nauth W. Tremel T. Opatz
Acquisition of data	E. Schechtel A. M. Nauth R. Dören
Analysis and interpretation of data	E. Schechtel A. M. Nauth R. Dören W. Tremel T. Opatz
Drafting of manuscript	E. Schechtel A. M. Nauth W. Tremel T. Opatz
Critical revision	E. Schechtel A. M. Nauth R. Dören W. Tremel T. Opatz

3.1 Abstract

Photosynthesis is an efficient mechanism for converting solar light energy into chemical energy. We report on a strategy for the aerobic photocyanation of tertiary amines with visible and near-infrared (NIR) light. Panchromatic sensitization was achieved by functionalizing TiO_2 with a 2-methylisoquinolinium chromophore, which captures essential features of the extended π-system of 2,7-diazapyrenium (DAP^{2+}) dications or graphitic carbon nitride. Two phenolic hydroxy groups make this ligand highly redox-active and allow for efficient surface binding and enhanced electron transfer to the TiO_2 surface. Non-innocent ligands have energetically accessible levels that allow redox reactions to change their charge state. Thus, the conduction band is sufficiently high to allow photochemical reduction of molecular oxygen, even with NIR light. The catalytic performance (up to 90% chemical yield for NIR excitation) of this panchromatic photocatalyst is superior to that of all photocatalysts known thus far, enabling oxidative cyanation reactions to the corresponding α-cyanated amines to proceed with high efficiency. The discovery that the surface-binding of redox-active ligands exhibits enhanced light harvesting in the red and NIR region opens up the way to improve the overall yields in heterogeneous photocatalytic reactions. Thus, this class of functionalized semiconductors provides the basis for the design of new photocatalysts containing non-innocent donor ligands. This should increase the molar extinction coefficient, permitting a reduction of nanoparticle catalyst concentration and an increase of the chemical yields in photocatalytic reactions.

3.2 Introduction

Sunlight is an abundant source of energy which can drive chemical reactions in an eco-friendly fashion and is most likely to play a key role in the global energy supply of the future. Catalytic systems using visible (vis) or infrared (IR) light are highly attractive because ultraviolet (UV) radiation accounts only for a small fraction of the sun's energy spectrum.[342–345] In fact, the maximum photon flux of the sun is centered around 880 nm, while its maximum power output is centered around 500 nm.[346] Most plants depend on sunlight and use the visible portion of the solar spectrum with the aid of photosynthetic pigments (e.g. tetrapyrroles and carotenoids).[347]

Chemists attempt to mimic the photosynthetic conversion of solar to chemical energy with photoredox systems and sensitizers. Irradiation leads to a photoexcited state that serves as a source of electrochemical potential.[345,348,349] The lifetime of the photoexcited state, the quantum efficiency of its formation, and the chemical stabilities of ground and excited states have been exploited in the design of systems for solar energy conversion, either directly into electrical current or for electron-transfer reactions, where substrates can be oxidized or reduced, depending on the conditions.

TiO_2 is a stable, non-toxic, low-cost material for photocatalysis,[263,350] whose photocatalytic efficiency is dictated by the charge separation efficiency, surface area, and exposed reactive facets.[267] Photoreduction with unmodified TiO_2 nanoparticles (NPs) requires UV light, which reduces the efficiency of unmodified TiO_2 in solar applications.[351–353] Therefore, transition metal complexes,[354–356] organic dyes,[357,358] and semiconductor NPs[359] have been used as sensitizers in TiO_2-based solar cells. These surface-bound chromophores not only serve to shift the light absorption of unmodified TiO_2 particles from the UV to the visible region, but also – in the case of "black dyes"[360–362] – achieve a panchromatic sensitization.[363] Among the concepts of TiO_2 sensitization via surface-bound chromophores, one particular approach has become popular in the past few years: photosensitization through ligand-to-metal charge transfer (LMCT) on TiO_2 surfaces,[239] which has also been employed in dye-sensitized solar cells (DSSCs).[270,364]

In inorganic photocatalysis, the semiconductors ZnO,[365] ZnS,[366] CdQ (Q = S, Se, Te) quantum dots,[367,368] carbon nitride,[369] BiOBr,[370] and $PbAO_2X$ (A = Sb, Bi; X = Cl, Br[371]), with absorption in the visible range, have been used to maximize the efficiency of light utilization. Likewise, organic dyes[223,372] and inorganic pigments[360,373] have been

used to stretch the absorption into the visible range. Crucial for the TiO_2 catalyst performance are light-absorbing chromophores, which (i) must be thermo-, photo- and chemically stable. In addition, an efficient photocatalyst should (ii) absorb strongly in the UV−vis region to produce electrons and holes, (iii) separate the electrons and holes in space to prevent their recombination, (iv) carry robust anchor groups for surface binding, (v) have a ground-state potential positive enough to facilitate hole transfer to the catalyst and an excited-state potential more negative than the edge of the semiconductor conduction band to allow interfacial electron transfer.[369] It is difficult to fulfill all criteria (i)−(v) simultaneously.

TiO_2 NPs sensitized with a variety of $Ru(bpy)_3^{2+}$ dyes are prototypical heterogeneous photocatalysts.[361–363,374] Although organic dyes find wide application as pigments, colorants, or photoreceptors, only a few have been utilized in photocatalysis, because they suffer from photodegradation on TiO_2 under visible-light irradiation.[375,376] Perylene bisimides[377] and metalated porphyrins[378] fulfill the stability requirements as well as optical and redox criteria[374] when surface-bound via different anchor groups (e.g., carboxylic acids, phosphonic acids, hydroxamic acids, or silatranes).[379] However, these groups are typically redox-inert and do not allow efficient charge transfer. Polymeric carbon nitride (CN_x)−TiO_2 organic−inorganic heterojunction photocatalysts have shown promising photocatalytic activity for the degradation of organic dyes[380] or the photocatalytic generation of H_2.[381] However, their visible-light-harvesting capabilities are limited because they suffer from a weak interaction and poor electron transfer across the TiO_2−CN_x interface.

Here, we demonstrate that a novel redox-active chromophore bound to TiO_2 NPs through strong electronic coupling fulfills all performance criteria and permits panchromatic TiO_2 sensitization for efficient aerobic photocyanation of tertiary amines. To this end, we synthesized the 6,7-dihydroxy-2-methylisoquinolinium (DHMIQ) ligand containing the 2-methylisoquinolinium chromophore equipped with a redox-active catechol surface anchor group (Figure 3.1a). This new ligand combines the essential features of two known chromophores: (i) quinolinium cations (e.g., *N*-methyl-quinolinium (NMQ^+)) and (ii) 2,7-diazapyrenium dications (DAP^{2+}). NMQ^+ cations are powerful photocatalysts with strongly oxidizing and long-lived excited singlet states,[382,383] but their UV absorption range and their susceptibility to attack by nucleophiles in the 2- and 4-positions render them unsuitable for photocyanation. 2,7-Diazapyrenium dications

(DAP^{2+})[352,384] with an extended isoquinolinium-type π-system absorb in the visible range and do not suffer from nucleophilic attack on the chromophore. The catechol surface anchor makes the ligand highly redox-active ("non-innocent"[178,385,386]) by facilitating efficient electron transfer to/from the metal oxide surface.[259,387]

Nature employs these non-innocent ligands in various metalloenzymes, where the active site contains a redox-active ligand that works in synergy with a metal center.[182,258] These ligands have more energetically accessible levels that allow redox reactions to change their charge state. The functionalized TiO_2 NPs exhibit a substantially improved vis−NIR spectral light-harvesting performance compared to pure CN_x[380] or unfunctionalized naked TiO_2 NPs. Neither unfunctionalized particles nor the sensitizer itself show any appreciable light absorption in the visible spectral range. The surface-functionalized particles, however, allow direct photocatalysis down to the NIR region.[388,389]

The TiO_2−DHMIQ photocatalyst is particularly suited for several reasons: (i) Amines and cyanides do not absorb visible light and therefore cannot be excited directly. (ii) Direct oxidation of organic substrates with molecular oxygen is kinetically unfavored.[390] (iii) The redox potentials of functionalized TiO_2 particles are comparable to or even higher than those of typical photoredox catalysts like $Ru(bpy)_3^{2+}$.[391] This enables the use of oxygen as terminal oxidant and circumvents the use of stronger or kinetically faster oxidants like ClO_2, H_2O_2, *t*-BuOOH, or carbenium ions. (iv) The redox potential of the TiO_2−DHMIQ system is utilized for single-electron oxidations[392] of the amines and the subsequent addition of cyanide to the iminium ion resulting from hydrogen abstraction.

We have applied these new photocatalysts for the synthesis of α-aminonitriles by oxidative cyanation of tertiary amines. α-Aminonitriles are an important class of compounds for the synthesis of nitrogen-containing bioactive compounds like α-amino acids and alkaloids or heterocycles.[393–395] Their various modes of reactivity make them versatile and widely applicable intermediates in organic chemistry[396] since the nitrile function can either be transformed to a carboxy, amide, or aminomethyl function or be completely replaced by alkyl or aryl groups in a single operation.[397] This also makes α-aminonitriles ideal intermediates in the post-functionalization of amines. In this paper, we demonstrate the photocatalytic oxidative cyanation of tertiary amines using TiO_2

NPs functionalized with the novel redox-active chromophore DHMIQ, the scope of the reaction, and the basic reaction mechanism.

3.3 Results and Discussion

First, the 6,7-dihydroxy-2-methylisoquinolinium chloride surface ligand (Figure 3.1a) was synthesized from homoveratrylamine (**1**), which was converted with formaldehyde in a combined Pictet–Spengler/Eschweiler–Clarke reaction to 6,7-dimethoxy-2-methyl-1,2,3,4-tetrahydroisoquinoline (**2**) (Figure 3.1b).[398] After oxidation with 2,3-dichloro-5,6-dicyanobenzoquinone (DDQ) to 6,7-dimethoxy-2-methylisoquinolinium chloride (**3**), DHMIQ was obtained by acidic cleavage of the methyl ethers. In the second step, TiO_2 NPs were prepared hydrothermally from titanium(IV) butoxide with oleic acid and oleylamine in ethanol,[56] yielding NPs of spherical to elongated shape and a typical size on the order of 10 nm (Figure S3.1). Powder X-ray diffraction confirmed that the particle cores consist of the anatase phase of TiO_2 (Figure S3.2). The as-synthesized TiO_2 particles carry oleate capping ligands (TiO_2–OA) and are perfectly soluble in apolar solvents like $CHCl_3$, *n*-hexane, and tetrahydrofuran (THF). The outstanding solubility allows for nuclear magnetic resonance (NMR) investigation of the NP's ligand sphere. Thus, the ^{1}H NMR spectrum of as-synthesized TiO_2–OA NPs (Figure S3.3) confirms the presence of oleic acid as surface ligand. The surface-bound ligands give rise to signal broadening.[274] Re-functionalization of TiO_2–OA with the positively charged DHMIQ ligand rendered the NPs water-soluble, inducing a polarity umpolung of the NP's ligand sphere (Figure 3.1c). The DHMIQ-functionalized TiO_2 NPs were purified by repeated cycles of dissolution, precipitation, and drying to remove displaced OA and excess DHMIQ molecules. No significant change in size, shape, or phase of the particles was observed after the ligand exchange (Figures S3.1 and S3.2). ^{1}H NMR investigation of surface-modified TiO_2–DHMIQ NPs in D_2O (Figure S3.4) revealed a virtually complete displacement of native OA ligands, indicated by the loss of the aliphatic signal in the high-field regime of the spectrum. The spectrum is dominated by two intense and rather broad signals, which can be assigned to the partially coalesced signals of DHMIQ. The NMR data reveal that the ligand spheres of the particles consist predominantly of single-molecule species before and after surface modification. Therefore, it is possible to estimate the surface coverage of the ligands simply by

quantifying the organic fraction of the NPs via thermogravimetric analysis (TGA, Figure S3.5). By combining the TGA data with the particle dimensions (Figure S3.1), ligand densities of 2.4 ± 1.0 nm^{-2} for TiO_2–OA and 2.0 ± 0.9 nm^{-2} for TiO_2–DHMIQ NPs were obtained (Table S3.1). The surface density of the OA ligand is lower than for other oleate-stabilized NPs due to the purification (removal of unbound ligand) of the as-synthesized TiO_2 NPs.[281] The same applies for the DHMIQ-modified NPs since most ligand exchange studies with catechol derivatives have yields usually twice as high.[172]

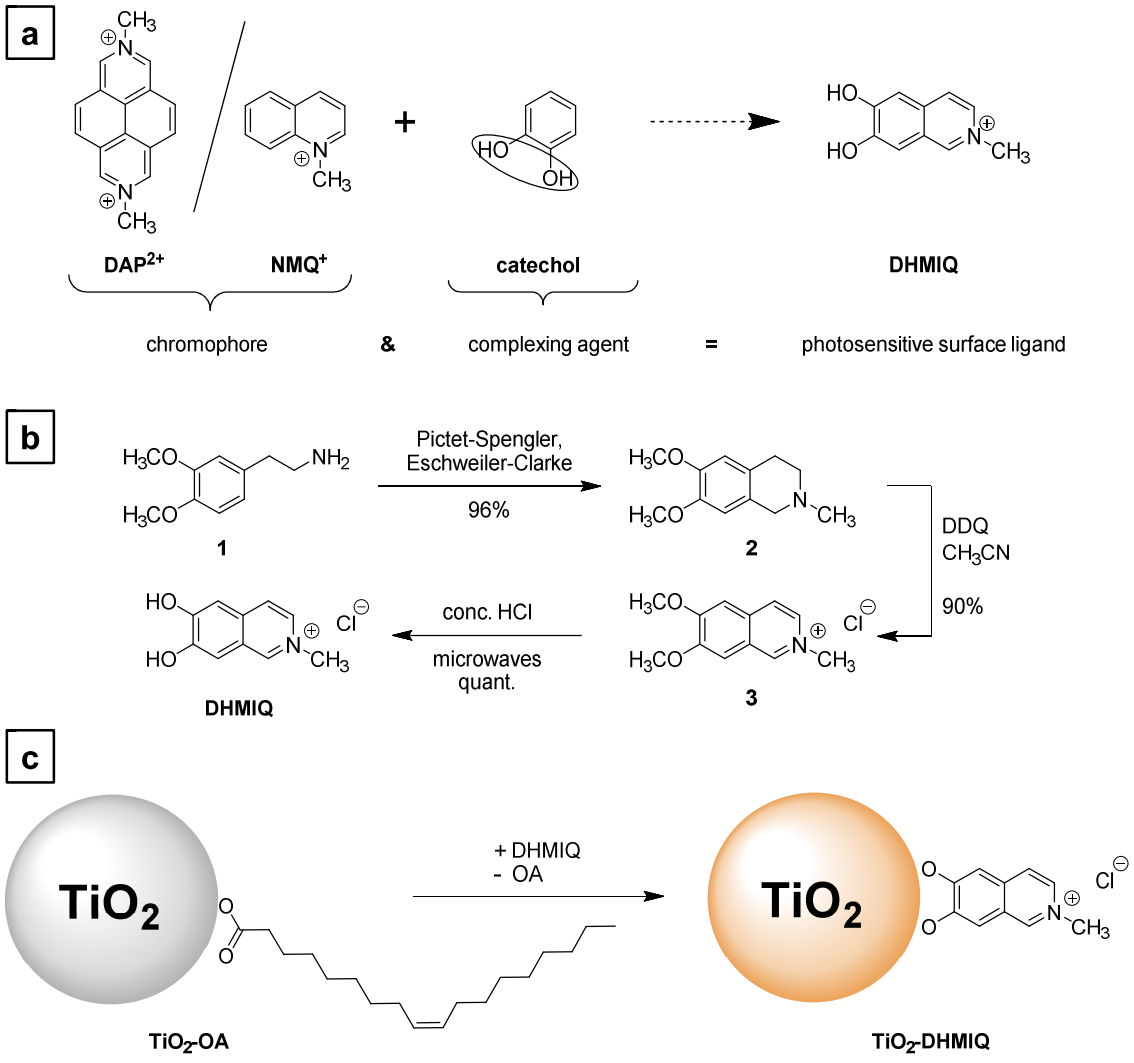

Figure 3.1. Design and synthesis of DHMIQ-sensitized TiO_2 NPs. (a) Combination of the organic photocatalyst (*N*,*N*′-dimethyl-2,7-diazapyrenium (DAP^{2+}) or *N*-methylquinolinium (NMQ^+)) and the complexing agent catechol to yield the photosensitive surface ligand DHMIQ. (b) Synthetic route for the preparation of DHMIQ from homoveratrylamine (**1**). (c) Sensitization of TiO_2 NPs via postsynthetic ligand exchange of oleic acid (OA) with DHMIQ.

The large specific surface area (~150 m^2g^{-1}, Table S3.1) of the anatase NPs aids in the formation of a photocurrent, similar as in DSSCs that operate based on similar principles.[374,375] The functionalized TiO_2 NPs show a substantially enhanced solar light harvesting performance compared to that of "naked" TiO_2 NPs. Band gap excitation of TiO_2 efficiently utilizes the optical spectrum (band gap of 3.2 eV for anatase TiO_2 with the conduction band starting close to the redox potential of the normal hydrogen electrode).[80] A significant portion of the visible and even the NIR spectrum (Figure 3.2a) is utilized with the TiO_2 surface-bound isoquinolinium ligand. Upon photo-excitation of the ligand, electron transfer occurs from the ligand LUMO to the TiO_2 conduction band (Figure 3.2b).

In order to demonstrate that the wide-ranging absorption of TiO_2−DHMIQ NPs arises specifically from the surface complexation, a reference batch of ligand-stripped, water-soluble TiO_2 NPs was prepared by reacting TiO_2−OA NPs with tetramethylammonium hydroxide (TMAH).[399,400] As can be seen by NMR spectroscopy (Figure S3.6), the hydroxide treatment displaced the native oleate ligand quantitatively, leaving a negatively charged TiO_2 NP surface, stabilized electrostatically by the counterion tetramethylammonium (TMA). Due to the non-coordinating nature of the TMA cation, TiO_2−TMA (Figure 3.2a) exhibits no charge-transfer band at ~360 nm, and strong absorption only occurs below 350 nm for TiO_2−TMA, which is a typical feature of non-sensitized TiO_2 NPs.[185] The unbound DHMIQ ligand has two absorption bands centered at 251 and 351 nm. The DHMIQ-functionalized TiO_2 particles show absorption throughout the visible range and tailing into the NIR, while non-sensitized TiO_2 particles and the unbound ligand show no significant absorption in the visible range (Figure 3.2a+c). The catechol group of the DHMIQ ligand acts as the docking site for binding to the TiO_2 surface because the absorption spectrum is red-shifted after the binding of DHMIQ, which indicates the electronic interaction of the chromophore with the TiO_2 NPs. The broad absorption of the TiO_2−DHMIQ NPs is attributed to diverse interactions across the ligand−NP interface: (i) The non-innocent, redox-active nature of DHMIQ allows for a multitude of electronic and associated redox states with diverse electronic transitions. (ii) Multiple facets of the nanocrystals and a non-negligible density of intrinsic surface defects in hydrothermally synthesized TiO_2 NPs[136] lead to a multitude of complexation geometries with different excitation energies.

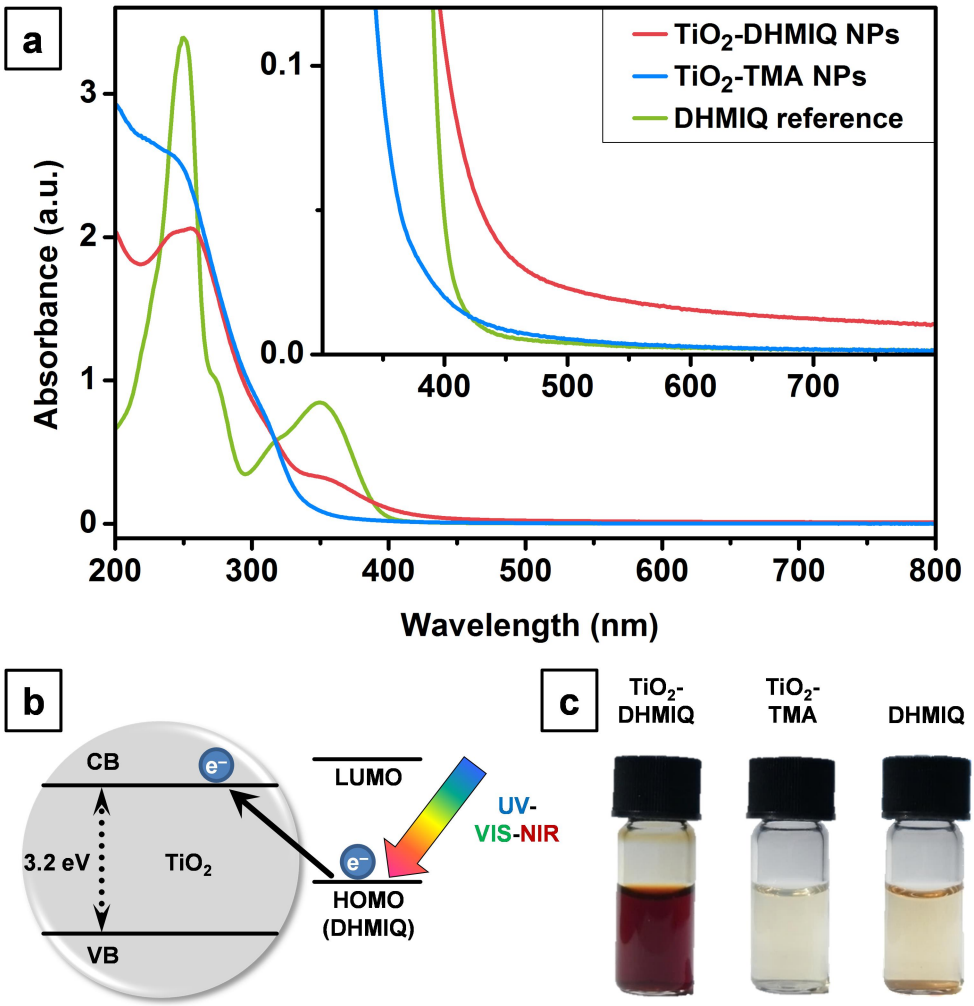

Figure 3.2. Light-absorbing properties of DHMIQ-sensitized TiO_2 NPs. (a) UV−vis absorbance spectrum of TiO_2−DHMIQ NPs (red line) in comparison with ligand-stripped TiO_2 NPs (with tetramethylammonium (TMA) counterions, blue line) and a pure DHMIQ reference (green line). The inset shows the enlarged vis-NIR absorption range where the charge transfer in TiO_2−DHMIQ NPs takes place. (b) Proposed excitation scheme for DHMIQ-sensitized TiO_2 NPs (CB, conduction band; VB, valence band; LUMO, lowest unoccupied molecular orbital; HOMO, highest occupied molecular orbital). (c) Visual appearance of DHMIQ-sensitized TiO_2 NPs (left), ligand-stripped TiO_2 NPs (middle), and DHMIQ reference (right) in aqueous solutions. NP concentrations of TiO_2−DHMIQ and TiO_2−TMA: 100 mg/mL, DHMIQ reference concentration: 12 mg/mL.

The energy conferred by IR light excitation is limited by the energy of the absorbed photons. The energy of NIR photons (800 nm) of 1.6 eV (149 kJ/mol) is the maximum theoretical energy threshold between the photocatalyst and the acceptor. Since a part of this energy is lost due to intersystem crossing or reorganization of the excited states of the photocatalyst by non-radiative pathways, the maximum available

energy of TiO_2−DHMIQ is in the order of 100 kJ/mol and still sufficient for oxidizing tertiary amines. The α-cyanation of tertiary amines reported here is one of the few[223,224] catalytic applications based on photoinduced interfacial electron transfer between a non-innocent ligand covalently bound to a TiO_2 NP surface.

The catalytic activity for the oxidative cyanation of different amines in the presence of trimethylsilyl cyanide (TMSCN) was examined. In a typical reaction, an aliquot of the aqueous catalyst solution was transferred into a reaction vial and freeze-dried. The dried catalyst was suspended in acetonitrile, the amine substrate was added, and the solution was saturated with oxygen. After addition of TMSCN as a cyanide source, the solution was irradiated (Figure S3.7). The crude cyanation product was isolated by extraction and purified by column chromatography. The minimum amount of catalyst required for nearly quantitative yield was determined by successively increasing the catalyst loading in a series of otherwise identical reactions (Figure S3.8). A catalyst loading of 2.5 mg TiO_2−DHMIQ NPs, corresponding to 0.6 mol% of the catalytically active LMCT complex with respect to the standard amount (0.24 mmol) of substrate, was found to be sufficient. Trace amounts of water in the reaction mixture caused considerable losses in yield. A systematic study revealed that increasing amounts of water caused an exponential decay in reaction yield, leveling out at 20% (Figure S3.9). The most plausible explanation for this behavior is the formation of a hydration shell around the polar NPs in the otherwise aprotic environment of acetonitrile which passivates the surface and leads to an energy barrier for the surface reactions.[401] Since the hydration shell has a finite maximum thickness, the conversion is not completely suppressed for higher amounts of water (see section 3.6.4.2 of the Supporting Information for a more thorough discussion).

Different excitation wavelengths were tested to excite the TiO_2−DHMIQ photocatalyst. Nearly quantitative yields were achieved after 3 h reaction upon irradiation with blue and green light (96% and 93%, see Table 3.1). The conversion decreased for excitation with yellow, red, and NIR (730 nm) light. However, this could be compensated by using longer irradiation times (90% yield after 62 h irradiation for NIR). It is unusual and quite extraordinary that even IR radiation at 850 nm from a relatively weak 3.7 W LED module resulted in a conversion of 12% after a 16 h reaction period. This is consistent with the very broad absorption spectrum of the TiO_2−DHMIQ photocatalyst. Controls with free DHMIQ gave much lower yields under identical conditions, and for

Table 3.1. Yields of the photocatalytic oxidative cyanation of tributylamine, using as-synthesized TiO_2−OA NPs, ligand-stripped TiO_2−TMA NPs, DHMIQ-sensitized TiO_2 NPs, and unbound DHMIQ as photocatalysts for different excitation wavelengths (LED source) and excitation powers.[a]

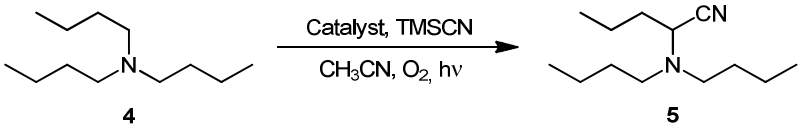

4 5

light source	LED					
	blue	green	yellow	red	IR 1	IR 2
	462 nm	520 nm	592 nm	635 nm	730 nm	850 nm
	100 W	100 W	52 W	67 W	51 W	3.7 W
TiO_2−OA	43%[b]	13%[b]	<1%[b]	×	×	n.t.
TiO_2−TMA	4%[b]	2%[b]	×	×	×	n.t.
TiO_2−DHMIQ	$96\%_{isolated}$	93%[b]	56%[b]	43%[b]	19%[b]/61%[b,c]/90%[e]	2%[b]/12%[b,d]
DHMIQ	84%[b]	22%[b]	2%[b]	<1%[b]	×	×
background	15%[b]	3%[b]	×	×	×	×

[a]Conditions: Bu_3N (0.239 mmol, 1.0 equiv) and TiO_2−DHMIQ NPs (2.5 mg) were dissolved in CH_3CN (4.0 mL), the solution was saturated with O_2, and TMSCN (3.0 equiv) was added. Unless stated otherwise, irradiation time was 3 h. Yield was determined by ^1H NMR using 1,4-bis(trimethylsilyl)benzene as an internal standard. n.t. = not tested, × = no conversion. [b]Incomplete conversion. [c]14 h reaction time. [d]16 h reaction time. [e]62 h reaction time.

ligand-stripped TiO_2−TMA NPs, the yields were almost zero. This demonstrates that covalently functionalized TiO_2 NPs are essential for the oxidative cyanation reaction under visible and NIR light. Finally, recyclability studies revealed that the heterogeneous photocatalyst could be recovered and reused several times, with the yield decreasing only moderately from 95% to 82% after four cycles of photocatalysis (Figure S3.10).

To demonstrate the substrate scope of TiO_2−DHMIQ, the catalyst was applied to a variety of different tertiary amines (Figure 3.3). Besides simple aliphatic amines like tributylamine, complex natural products like nicotine and atropine were also converted into their corresponding *α*-aminonitriles and isolated in remarkable yields. The hydroxyl group of atropine was TMS-protected due to the effect of TMSCN as a silylating agent. Reactions with the TiO_2−DHMIQ catalyst led to different cyanation products compared to those using the organic dye rose bengal as photocatalyst. For nicotine, cyanation occurred in the benzylic position with TiO_2−DHMIQ while rose bengal favors a reaction at the methyl group.[358] For *N*,*N*-dimethyltetradecylamine, the unexpected formation of

2-(dimethlyamino)pentadecannitrile was observed with TiO_2−DHMIQ, and the yield of the cyanation of the *N*-methyl groups of gramine was approximately 4.5 times higher than that with rose bengal (89% vs. 20%).[358] This differential selectivity could prove useful in further synthetic endeavors. In addition, reactions with the TiO_2−DHMIQ catalyst appeared to be milder than those with rose bengal, as the isolated crude products were of superior purity.

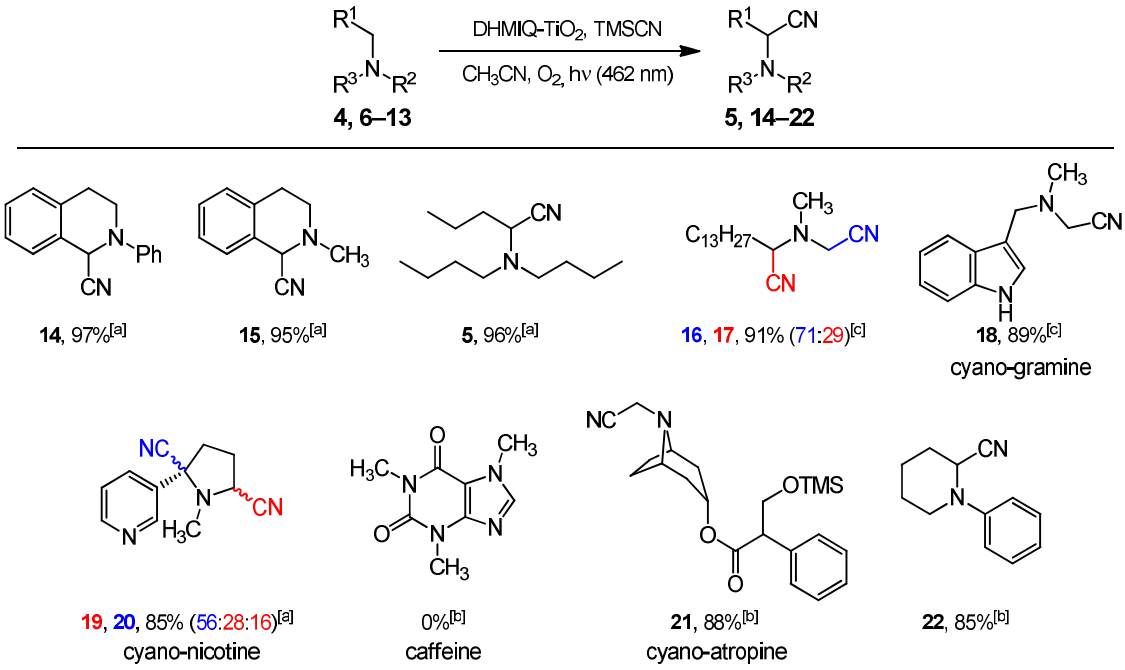

Figure 3.3. Vis−NIR-induced oxidative cyanation of amines into *α*-aminonitriles with O_2 on DHMIQ-sensitized TiO_2 NPs. Yields were isolated. Reaction conditions: [a]3 h. [b]16 h. [c]24 h. Structures verified by ^1H and ^{13}C NMR (Figures A.1−A.33 in Appendix A.1).

With the catalytic activities, the results of the control experiments, and the structure and properties of molecular Ti(IV) complexes[402] and TiO_2 particles functionalized with catechol ligands,[403] a tentative mechanism of visible-NIR light photoredox catalysis with DHMIQ-sensitized TiO_2 NPs is proposed in Figure 3.4. The DHMIQ chromophore is anchored on the TiO_2 particle surface with a catechol group to form a stable LMCT complex. Upon irradiation, DHMIQ is excited and a charge transfer occurs to the TiO_2 NP, which is associated with an injection of an electron into the TiO_2 conduction band. In the next step, the electron reacts with O_2 at the TiO_2 surface to form a hyperoxide radical anion $O_2^{\bullet-}$.[263] The $O_2^{\bullet-}$ radical anion displaces CN^- from TMSCN to form a TMS-peroxo species which then abstracts an H atom from the amine radical cation to generate an iminium ion.[404,405] To elucidate the fate of the TMS-peroxo species, a

reaction mixture was investigated by ^{29}Si NMR spectroscopy after irradiation. The ^{29}Si NMR spectrum (Figure S3.11) revealed the presence of four major Si-containing products, all of them different from TMSCN (Table S3.6). The two most prominent signals can be safely assigned to trimethylsilanol (TMSOH) and its condensation product hexamethyldisiloxane $(TMS)_2O$. The other two species are most probably bis(trimethylsilyl) peroxide $(TMSO)_2$ and trimethylmethoxysilane (Table S3.6). As a mechanistic alternative for iminium formation, α-amino radical intermediates are often discussed in the literature.[406] These might be formed by α-deprotonation of the amine radical cations[407,408] or through H atom transfer[409] from the parent amine. Since neither the addition of diethylsilane (whose Si−H bonds are slightly weaker than the C_α−H bonds of trialkylamines) nor the addition of ethyl acrylate as a known trap for α-amino radicals[410–412] interferes with the clean photocyanation of tributylamine (see section 3.6.5.2 of the Supporting Information for details), both alternatives appear unlikely. Increasing the size of the silyl group from TMS to *tert*-butyldimethylsilyl (TBDMS) slows down the photocyanation, but only leads to minor changes in the regioselectivity (**16**/**17** and **19**/**20**, Table S3.7). Further experimental and theoretical work is needed to obtain a deeper mechanistic insight.

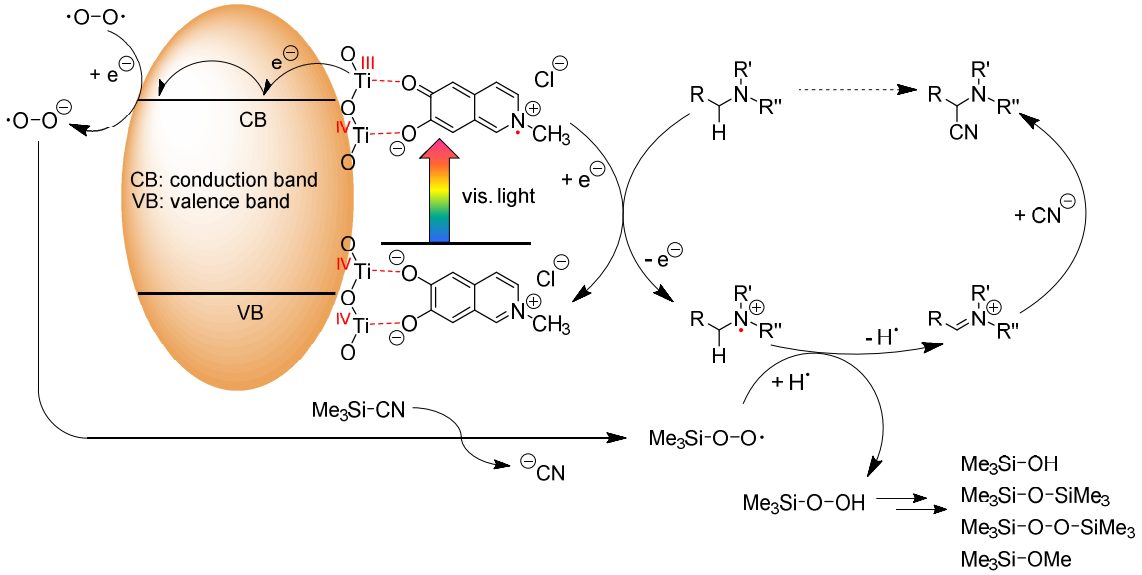

Figure 3.4. Proposed mechanism for the visible-light-induced oxidative cyanation of tertiary amines with O_2, catalyzed by DHMIQ-sensitized TiO_2 NPs.

From a mechanistic point of view, the TiO_2−DHMIQ system is not only responsible for visible light harvesting, but is also driving the oxidative transformation. Compared to similar aerobic oxidation reactions, this double functionality obviates the need for an additional redox mediator such as (2,2,6,6-tetramethylpiperidin-1-yl)oxyl (TEMPO)[223–225] or a radical initiator such as azobis(isobutyronitrile) (AIBN).[395] Furthermore, the heterogeneous nature of the catalyst enables an easy recovery, which makes the TiO_2−DHMIQ system a superior photocatalyst for oxidative cyanation and a promising candidate for other oxidative transformations.

3.4 Conclusion

A redox-active DHMIQ ligand was prepared for surface sensitization of TiO_2 NPs. It allows panchromatic sensitization for photocatalytic oxidative cyanation reactions using molecular oxygen as oxidant. This photo-active DHMIQ ligand was adsorbed onto TiO_2 NPs via postsynthetic quantitative ligand exchange of oleic acid, yielding a DHMIQ ligand density of 2.0 ± 0.9 nm^{-2}. The ligand, when anchored to TiO_2 NPs, achieves very efficient sensitization over the whole visible range extending into the NIR region down to 800 nm. The spectral response in the red and NIR regions is greatly enhanced compared to that of chemically stable standard semiconductors.[232,263,413] On the basis of its catalytic performance (up to 90% chemical yield for NIR excitation), this panchromatic photocatalyst is superior to all photocatalysts known thus far. It enables oxidative cyanation reactions to the corresponding α-aminonitriles to proceed with high efficiency. α-Aminonitriles are useful intermediates for synthesis of a wide variety of compound classes. The reaction formally represents a photoassisted cross-dehydrogenative coupling (CDC)[414] of amines and HCN through sp^3 C−H bond activation adjacent to nitrogen followed by carbon−carbon bond formation under oxidative conditions. The discovery of enhanced light harvesting in the red and NIR regions through surface-binding of redox-active ligands opens up the way to improve the overall yields in photocatalytic reactions. Thus, this class of functionalized semiconductors provides the conceptual basis for the design of new photocatalysts containing non-innocent donor ligands. This increases the molar extinction coefficient, permitting a reduction of NP catalyst concentration and an increase of the overall yields in photocatalytic reactions. Further improvements could be achieved by the use of mi-

croflow technology or through immobilized TiO_2 surfaces in continuous-flow operations.[415]

3.5 Experimental Section

Materials. Unless otherwise stated, all chemicals and solvents were obtained from commercial suppliers and used without further purification. Oleic acid (technical grade, 90%) was obtained from Sigma-Aldrich. Titanium(IV) *n*-butoxide (99%) was purchased from Acros Organics. Oleylamine (>50.0% (GC)) was acquired from TCI. Deionized water (18.2 MΩ·cm) was obtained from a Milli-Q water purification system (Millipore Synergy 185).

Synthesis of Oleic Acid-Stabilized TiO_2 Nanoparticles (TiO_2−OA). TiO_2 NPs were synthesized according to a previously reported procedure.[56] Titanium(IV) butoxide (2.89 g, 2.89 mL, 8.5 mmol, 1.0 equiv) was added to a mixture of oleic acid (14.41 g, 16.24 mL, 51 mmol, 6.0 equiv), oleylamine (9.09 g, 11.19 mL, 34 mmol, 4.0 equiv) and ethanol (7.83 g, 9.93 mL, 170 mmol, 20.0 equiv, absolute grade). The mixture was stirred for 15 min and transferred into a 50 mL Teflon vessel. This vessel was placed into a 250 mL Teflon-lined stainless steel autoclave, already containing 34 mL of the hydrolysis solution of ethanol and water (96:4 v/v). The sealed autoclave was then heated at 180 °C for 18 h. After the cooled autoclave was opened, the content of the inner vessel was decanted into a 50 mL centrifuge tube, and the crude solid product was isolated by centrifugation (9000 rpm, 10 min) and dissolved in *n*-hexane (10 mL). The white solid residue at the bottom of the inner vessel was also dissolved in *n*-hexane (10−15 mL), transferred into a 50 mL centrifuge tube, and precipitated by addition of ethanol (30−35 mL, technical grade). The white precipitate was isolated by centrifugation (9000 rpm, 10 min) and re-dissolved in *n*-hexane (5 mL).The combined NP solutions were further purified by repeated cycles of precipitation and dissolution (3 × 30/5 mL EtOH/*n*-hexane). The last dissolution step was usually carried out in $CHCl_3$ (3 mL) to obtain a concentrated stock solution in a solvent that can be easily displaced for further reactions. The stock solution was stored in a tightly sealed amber glass vial with screw top, protected from sunlight, to extend its shelf life (stable solutions for at least up to a year). The exact concentration of the NP solution was determined from the remaining mass of an evaporated 100 µL aliquot (after several hours of drying at 80 °C).

^{1}H NMR (400 MHz, $CDCl_3$): δ [ppm] = 5.7−5.0 (m, 2H, −CH=CH−), 2.4−0.6 (m, 31H, $-CH_2-$ & $-CH_3$).

Synthesis of 6,7-Dimethoxy-2-methyl-1,2,3,4-tetrahydroisoquinoline (2). Homoveratrylamine (10.0 g, 55.2 mmol, 1.0 equiv), formic acid (16.5 g, 20.8 mL, 552 mmol, 10 equiv), and aqueous formaldehyde solution (37 wt%, 20.5 mL, 5.0 equiv) were combined and heated for 6 h to 100 °C. The solution was made alkaline with sodium hydroxide solution (2 M) and extracted with ethyl acetate (3 × 50 mL). The combined organic layers were dried over sodium sulfate and concentrated in vacuo to yield the crude product. After purification by column chromatography (ethyl acetate/methanol = 2:1) the product was isolated as slightly yellow solid (11.0 g, 52.9 mmol, 96%). Mp: 75.9−78.2 °C. Lit.: 78−90 °C.[398] R_f = 0.23 (ethyl acetate/methanol = 2:1). IR (ATR): ν [cm^{-1}] = 2936 (s), 2834 (m), 2768 (m), 1518 (vs), 1463 (s), 1374 (s), 1258 (vs), 1228 (vs), 1138 (vs), 1104 (s), 1013 (m). ^{1}H NMR, COSY (300 MHz, $CDCl_3$): δ [ppm] = 6.59 (s, 1H, H-5), 6.51 (s, 1H, H-8), 3.84 (s, 3H, OCH_3), 3.83 (s, 3H, OCH_3). 3.50 (s, 2H, H-1), 2.84 (t, $^{3}J_{H\text{-}4,\,H\text{-}3}$ = 5.9 Hz, 2H, H-4), 2.66 (t, $^{3}J_{H\text{-}3,\,H\text{-}4}$ = 5.9 Hz, 2H, H-3), 2.45 (s, 3H, NCH_3). ^{13}C NMR, HMBC, HSQC (75 MHz, $CDCl_3$): δ [ppm] = 147.6, 147.3 (C-6, C-7), 126.7 (C-8a), 125.8 (C-4a), 111.5 (C-5), 109.4 (C-8), 57.7 (C-1), 56.1, 56.0 (2 × OCH_3), 53.1 (C-3), 46.2 (NCH_3), 29.0 (C-4). ESI-MS: *m/z* = 207.0 ([M+H^+], 100%). The spectral data match those reported in the literature.[398,416]

Synthesis of 6,7-Dimethoxy-2-methylisoquinolinium Chloride (3). 6,7-Dimethoxy-2-methyl-1,2,3,4-tetrahydroisoquinoline (1.00 g, 4.83 mmol, 1.0 equiv) was dissolved in acetonitrile (80 mL), and DDQ was added (2.19 g, 9.65 mmol, 2.0 equiv). The reaction mixture was refluxed and every 24 h additional DDQ (2.0 equiv) was added. After 4 d and 8.0 equiv of DDQ added, LC-MS indicated full conversion. The solvent was evaporated in vacuo and the solid residue was dissolved in diluted hydrochloric acid (2 M, 50 mL). The aqueous solution was extracted with diethyl ether in a Kutscher−Steudel apparatus for 2 d (note: ethyl acetate, chloroform, and dichloromethan are not suitable in this case). The organic extract was dried over sodium sulfate and concentrated in vacuo to yield the pure iminium salt (1.04 g, 4.35 mmol, 90%). Mp: 301−311 °C (decomposition). Lit. (iodide salt): 235−238 °C.[417] ^{1}H NMR, COSY (300 MHz, D_2O): δ [ppm] = 9.14 (s, 1H, H-1), 8.21 (dd, $^{3}J_{H\text{-}3,\,H\text{-}4}$ = 6.8 Hz, $^{4}J_{H\text{-}3,\,H\text{-}1}$ = 1.4 Hz, 1H, H-3), 8.03 (d, $^{3}J_{H\text{-}4,\,H\text{-}3}$ = 6.8 Hz, 1H, H-4), 7.48 (s, 1H, H-8), 7.40 (s, 1H, H-5), 4.37

(s, 3H, NCH_3), 4.00 (s, 3H, C-6−OCH_3), 3.97 (s, 3H, C-7−OCH_3). ^{13}C NMR, HMBC, HSQC (75 MHz, D_2O): δ [ppm] = 157.0 (C-6), 152.1 (C-7), 145.1 (C-1), 135.3 (C-4a), 133.7 (C-3), 124.0 (C-8a), 123.5 (C-4), 106.6 (C-8), 105.4 (C-5), 56.6 (C-6−O**C**H_3), 56.2 (C-7−O**C**H_3), 47.1 (NCH_3). ESI-MS: *m/z* = 204.1 ([M^+], 100%). The spectral data match those reported in the literature.[418]

Synthesis of 6,7-Dihydroxy-2-methylisoquinolinium Chloride (DHMIQ). 6,7-Dimethoxy-2-methylisoquinolinium chloride (890 mg, 3.71 mmol, 1.0 equiv) was dissolved in conc. hydrochloric acid (20 mL) and heated in a monomode microwave reactor (8 h, 140 °C, 20 bar, 45 W; ramp: 20 min). The solution was concentrated into dryness in vacuo to yield DHMIQ (786 mg, 3.71 mmol, quant.). Mp: 265−271 °C (decomposition). IR (ATR): ν [cm^{-1}] = 2970 (br w), 1624 (w), 1529 (w), 1483 (m), 1436 (m), 1391 (w), 1371 (w), 1298 (s), 1173 (s), 1156 (s), 871 (s), 628 (m), 576 (m), 471 (vs). ^{1}H NMR, COSY (300 MHz, D_2O): δ [ppm] = 8.96 (s, 1H, H-1), 8.04 (dd, $^3J_{H\text{-}3,\ H\text{-}4}$ = 6.8 Hz, $^4J_{H\text{-}3,\ H\text{-}1}$ = 1.3 Hz, 1H, H-3), 7.84 (d, $^3J_{H\text{-}4,\ H\text{-}3}$ = 6.8 Hz, 1H, H-4), 7.30 (s, 1H, H-8), 7.18 (s, 1H, H-5), 4.30 (s, 3H, NCH_3). ^{13}C NMR, HMBC, HSQC (75 MHz, D_2O): δ [ppm] = 155.2 (C-6), 149.3 (C-7), 144.7 (C-1), 134.5 (C-4a), 132.6 (C-3), 123.6 (C-8a), 122.9 (C-4), 110.5 (C-8), 108.7 (C-5), 46.9 (NCH_3). ESI-HRMS: calcd for $[C_{10}H_{10}NO_2]^+$: *m/z* = 176.0706, found: 176.0711.

Synthesis of TiO_2−DHMIQ Nanoparticles. First, an aliquot of the titania stock solution, corresponding to a NP amount of 100 mg, was transferred into a 2 mL microcentrifuge tube, precipitated with excess acetone, centrifuged (14800 rpm, 3 min), and re-dissolved in THF (1.0 mL). The DHMIQ ligand (50 mg, 0.24 mmol) was dissolved in a ternary solvent mixture of water (1.0 mL), MeOH (0.5 mL), and THF (1.5 mL). The NP solution was added to the ligand solution, forming an opaque suspension, which was then sonicated (280 W) at 40 °C for 1 h. The reaction mixture was centrifuged (9000 rpm, 15 min), the yellow supernatant was discarded, and the brownish-red pellet was dried in rough vacuum (30 mbar, 10 min). The dried NPs were re-dissolved in a minimum amount of water (0.2 mL) with the aid of vortexing and sonication. After precipitation with excess THF (3.0 mL), the NPs were separated by centrifugation (9000 rpm, 10 min) and dried in low vacuum. The DHMIQ-functionalized TiO_2 NPs were further purified by repeated cycles of dissolution, precipitation, and drying as described above (6 iterations in total). To obtain a ^{1}H NMR spectrum of the DHMIQ-functionalized TiO_2 NPs that is not obscured by large residual signals of the undeuterat-

ed solvents, the penultimate dissolution step was performed in D_2O, followed by the ultimate precipitation step with acetone-d_6 and re-dissolution of the dried NPs in D_2O. ^{1}H NMR (400 MHz, D_2O): δ [ppm] = 9.4−5.2 (m, 5H, Ar−H), 5.2−2.5 (m, 3H, NCH_3).

Synthesis of Ligand-Stripped TiO_2 Nanoparticles (TiO_2−TMA). First, an aliquot of the titania stock solution, corresponding to a NP amount of 200 mg, was precipitated with excess acetone, centrifuged (14800 rpm, 3 min), and re-dissolved in THF (1.0 mL). Tetramethylammonium hydroxide pentahydrate (TMAH·$5H_2O$, 1.0 g, 5.5 mmol) was dissolved in 1.0 mL H_2O and added to the NP solution. The combined solution was shaken and sonicated (280 W) at 40 °C for 1 h to afford a biphasic clear mixture. Addition of MeOH (2.0 mL) caused the phases to merge and the NPs were then precipitated with excess THF (15 mL). The mixture was centrifuged (9000 rpm, 10 min), the yellow supernatant was discarded, and the whitish pellet was dried in rough vacuum (30 mbar, 10 min). The dried NPs were re-dissolved in a minimum amount of water (0.2 mL) with the aid of vortexing and sonication. After precipitation with excess THF (3.0 mL), the NPs were again separated by centrifugation (9000 rpm, 10 min) and dried in rough vacuum. The ligand-stripped TiO_2−TMA NPs were further purified by repeated cycles of dissolution, precipitation and drying as described above (4 iterations in total). To obtain a ^{1}H NMR spectrum of the TiO_2−TMA NPs that is not obscured by large residual signals of the undeuterated solvents, the penultimate dissolution step was performed in D_2O, followed by the ultimate precipitation step with acetone-d_6 and re-dissolution of the dried NPs in D_2O. ^{1}H NMR (400 MHz, D_2O): δ [ppm] = 3.6−2.8 (s, 12H, $N(CH_3)_4$).

General Procedure for the Photocyanation of Amines. An aliquot of the TiO_2−DHMIQ solution (2.5 mg catalyst) was transferred in a reaction vial and freeze-dried. The dried catalyst was suspended with acetonitrile (4.0 mL) and the substrate (0.239 mmol, 1.0 equiv) was added. Oxygen was bubbled through the solution for 1 min to saturate the solution. Trimethylsilyl cyanide (3.0 equiv) was added and the vial was closed tightly. The solution was irradiated, if not stated otherwise, for 3 h, poured into concentrated $NaHCO_3$ solution (30 mL), and extracted with CH_2Cl_2 (3 × 20 mL). The combined organic layers were dried over Na_2SO_4 and the solvent was evaporated under reduced pressure to obtain the crude product. The pure product was isolated by filtration through a plug of aluminum oxide (basic) using CH_2Cl_2 as the eluent or by column chromatography.

Further details of the experimental setup and substrate-specific procedures are provided in sections 3.6.2 and 3.6.3 of the Supporting Information.

3.6 Supporting Information

3.6.1 NP Characterization

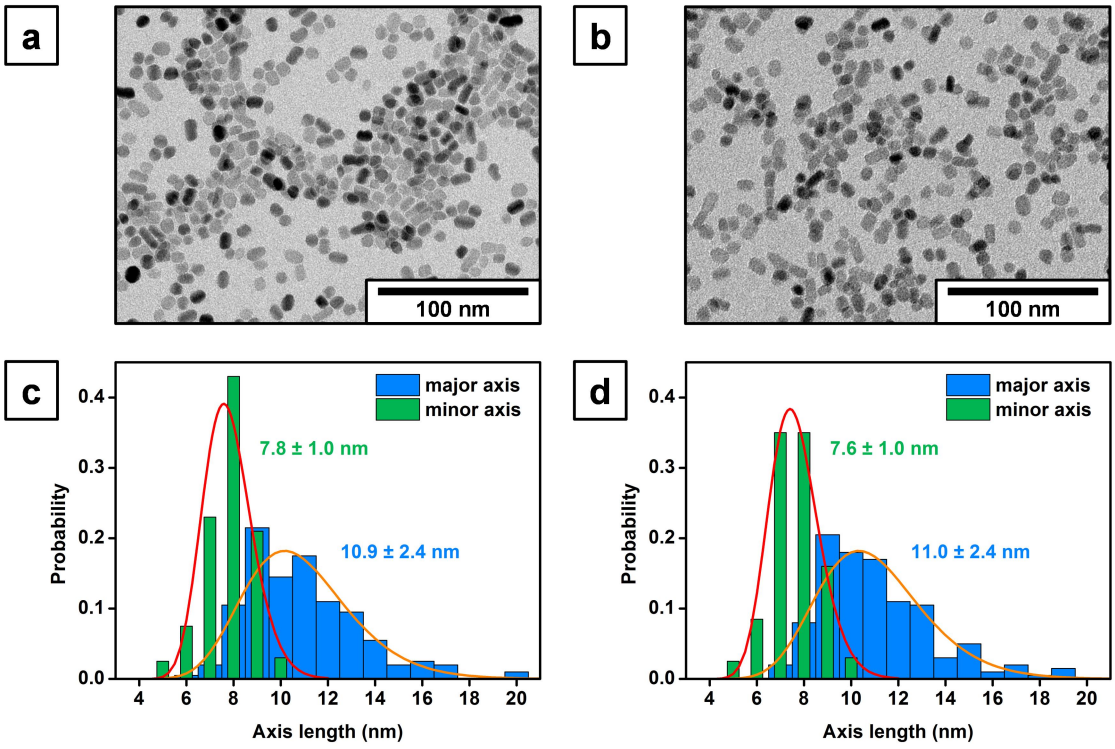

Figure S3.1. TEM images (upper panel) and size distributions (lower panel) of (a, c) as-synthesized oleic acid-stabilized TiO_2 NPs and (b, d) DHMIQ-functionalized TiO_2 NPs. Due to their elongated shape, the NPs were fitted as ellipses with major and minor axes. Size evaluations were performed on 200 single particles before (a, c) and after (b, d) refunctionalization with DHMIQ, respectively. Surface modification with DHMIQ did not cause any changes in size or shape of the NPs.

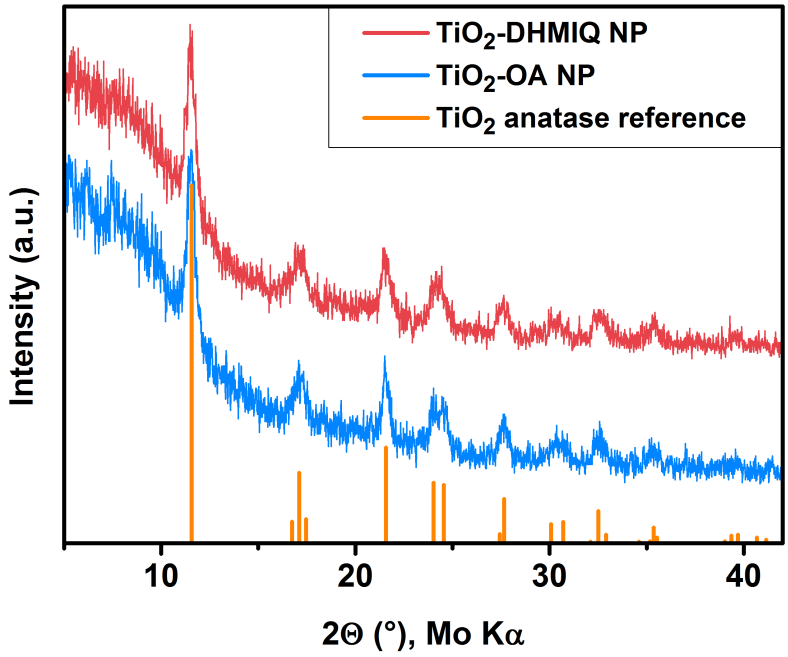

Figure S3.2. Powder X-ray diffractograms of TiO_2 NPs before (blue curve, TiO_2–OA NPs) and after DHMIQ modification (red curve, TiO_2–DHMIQ NPs), both matching the bulk anatase TiO_2 reference pattern (in orange, COD 96-500-0224).

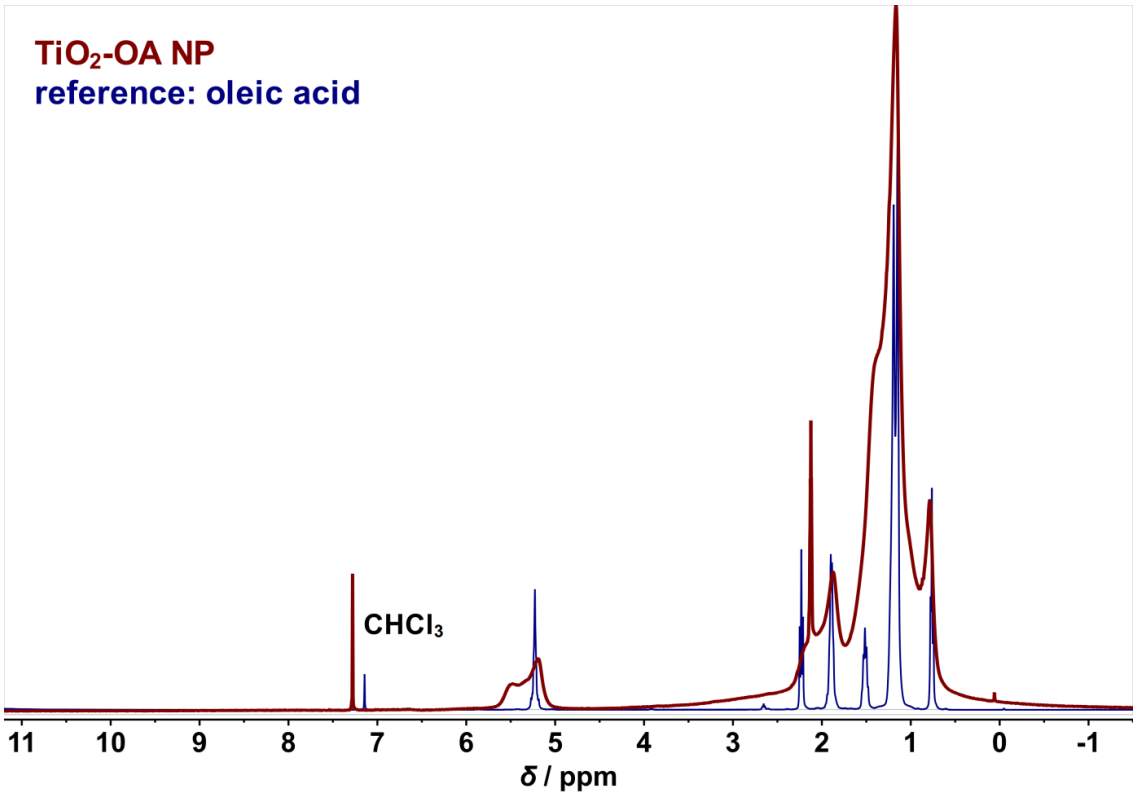

Figure S3.3. ^1H NMR spectra (400 MHz, $CDCl_3$) of TiO_2–OA NPs (maroon) and OA reference (blue).

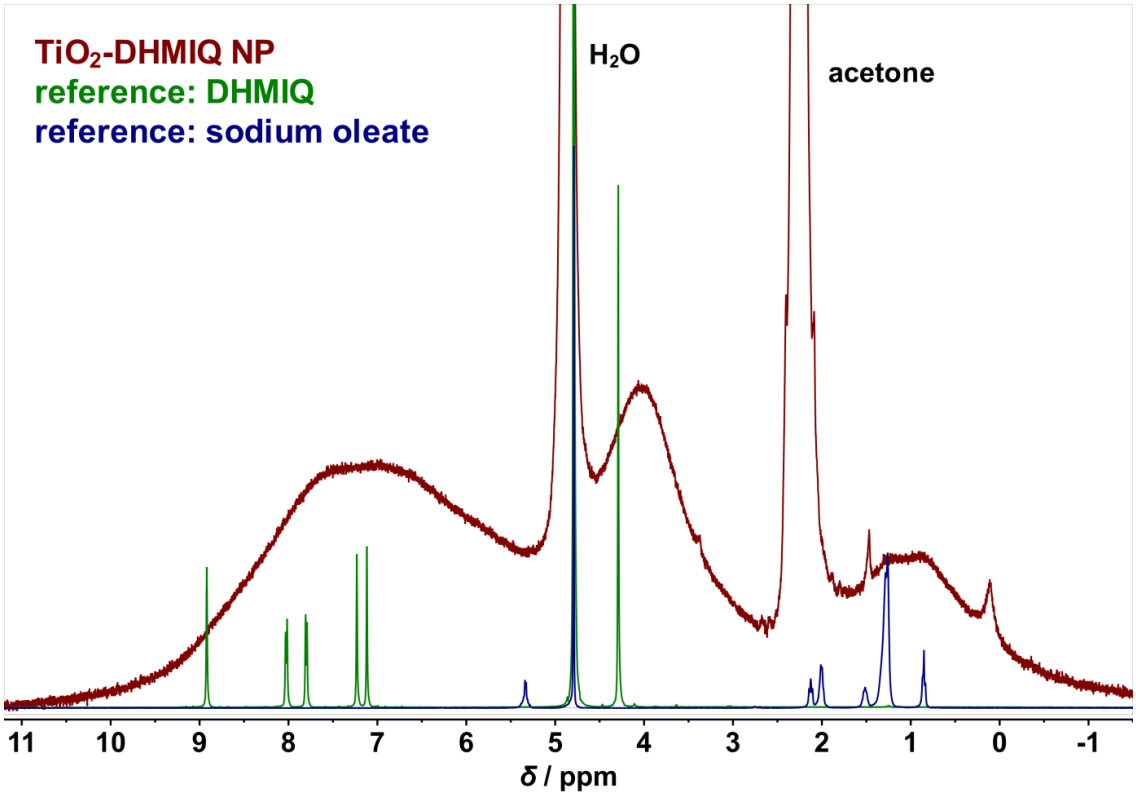

Figure S3.4. ^{1}H NMR spectra (400 MHz, D_2O) of TiO_2–DHMIQ NPs (maroon) and references of DHMIQ (green) and sodium oleate (blue).

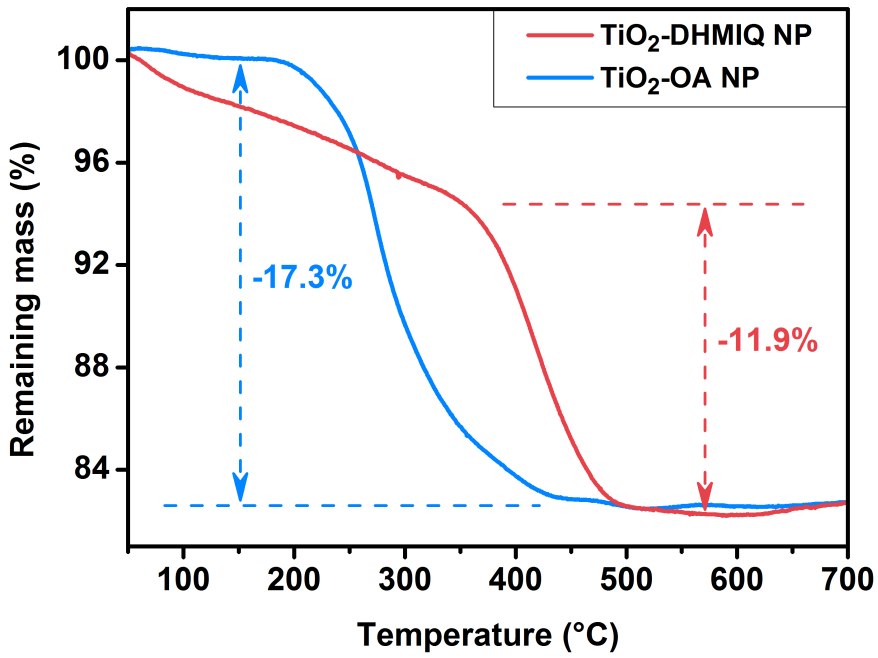

Figure S3.5. TGA profiles of TiO_2 NPs before (blue curve, TiO_2–OA NPs) and after DHMIQ modification (red curve, TiO_2–DHMIQ NPs). The initial drop observed for the TiO_2–DHMIQ sample is presumably due to strongly adsorbed impurity species, such as H_2O.

Table S3.1. Characteristics of as-synthesized and DHMIQ-modified TiO_2 NPs.

NP type	TiO_2–OA	TiO_2–DHMIQ
major axis (nm)[a]	10.9 ± 2.4	11.0 ± 2.4
minor axis (nm)[a]	7.8 ± 1.0	7.6 ± 1.0
volume (nm^3)[b]	347 ± 117	333 ± 114
surface area (nm^2)[b]	243 ± 56	238 ± 56
specific surface area ($m^2\ g^{-1}$)	153 ± 63	166 ± 69
organic fraction (%)	17.3 ± 1.0	11.9 ± 1.0
ligands per particle	588 ± 202	486 ± 171
ligand density (nm^{-2})	2.4 ± 1.0	2.0 ± 0.9

[a]Mean values from TEM size evaluation after fitting individual particles as ellipses. [b]Values calculated according to the formulae for prolate (elongated) spheroids.

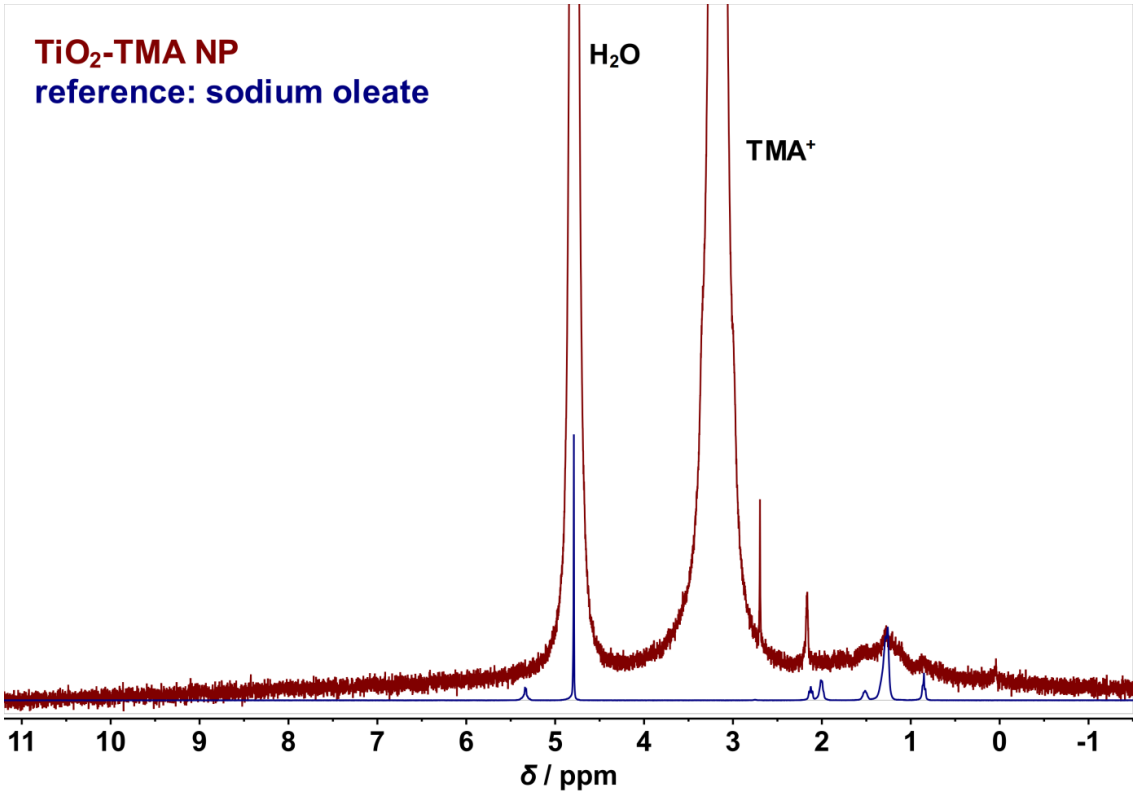

Figure S3.6. ^1H NMR spectra (400 MHz, D_2O) of TiO_2–TMA NPs (maroon) and sodium oleate reference (blue).

3.6.2 Experimental Setup

Light sources used in the photocyanation studies:

- **HPR40E-48K100BG from Huey Jann Electronics Industry Co.:**
  blue LED, power: 100 W, voltage: max. 36 V, light intensity: 2880 lm, λ = 459−465 nm (λ_{max} = 462 nm).
- **HPR40E-43K100G from Huey Jann Electronics Industry Co.:**
  green LED, power: 100 W, voltage: max. 36 V, light intensity: 6200 lm, λ = 515−525 nm (λ_{max} = 520 nm).
- **Flood COB 50 Amber from Deko-Light Elektronik Vertriebs GmbH:**
  yellow LED, power: 52 W, voltage: max. 230 V, light intensity: 1820 lm, light efficiency: 34.85 lm/W, angle of radiation: 120°, λ = 590−595 nm (λ_{max} = 592 nm).
- **RGB LED strips from LED-Konzept:**
  red LED, power: 67 W, voltage: max. 24 V, λ_{max} = 635 nm.
- **730 nm Infrared IR High Power LED Light:**
  NIR-LED, power: 55 W, λ = 720–740 nm (λ_{max} = 730 nm).
  (https://www.ebay.com/itm/690nm-730nm-760nm-790nm-810nm-850nm-940nm-100W-Infrared-IR-High-Power-LED-Light-/362216849137).
  Case: Himanjie 100 W LED Outdoor Flutlicht
  (https://www.amazon.de/gp/product/B06Y4JMGXQ/ref=oh_aui_detailpage_o02_s00?ie=UTF8&psc=1).
- **IR-LED from Sygonix:**
  IR-LED, power: 3.6 W, angle of radiation: 45°, λ_{max} = 850 nm.

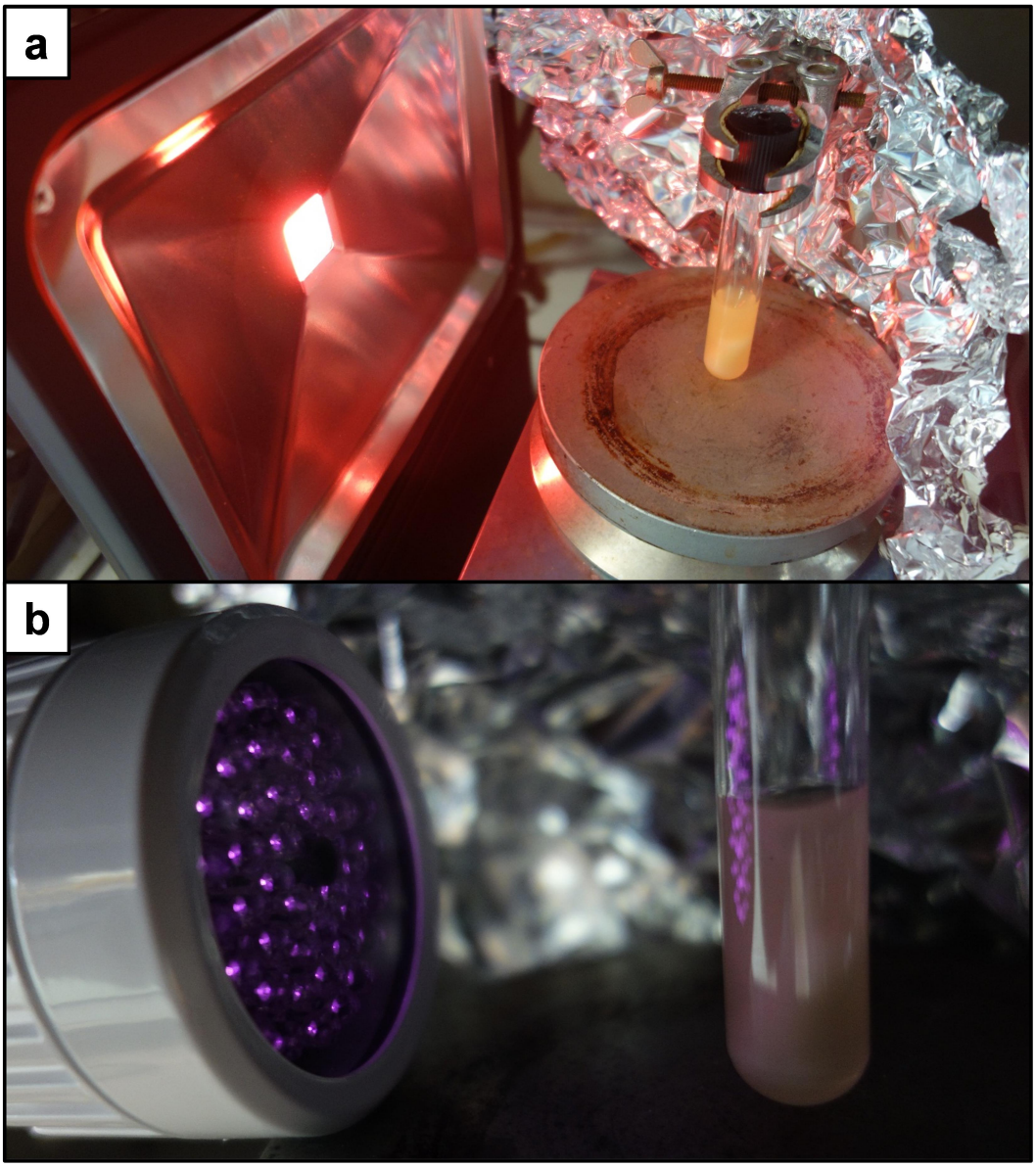

Figure S3.7. Photocyanation reactions with TiO_2–DHMIQ under (a) NIR light (730 nm, ~15 cm distance between radiation source and reaction vessel) and (b) IR light (850 nm, ~7 cm distance between radiation source and reaction vessel).

3.6.3 Substrate-Specific Procedures and Analytical Data

2-(Dibutylamino)-pentanenitrile (5):

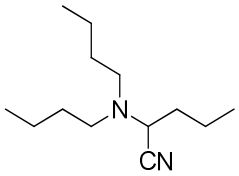

The title compound was prepared according to the general procedure described above from *N*-butylamine (0.239 mmol, 1.0 equiv). After purification by filtration through a plug of aluminum oxide (basic) using CH_2Cl_2 as the eluent, the product (48.2 mg, 0.229 mmol, 96%) was isolated as a colorless oil.

R_f = 0.70 (cyclohexane/ethyl acetate = 7:1).

IR (ATR): ν [cm^{-1}] = 2959 (vs), 2932 (s), 2873 (m), 2221 (w), 1756 (w), 1467 (m), 1379 (w), 1173 (w), 1091 (w), 799 (w), 742 (w).

^{1}H NMR, COSY (300 MHz, $CDCl_3$): δ [ppm] = 3.58 (t, $^3J_{H\text{-}1a,H\text{-}2}$=7.7 Hz, 1H, H-1a), 2.63−2.50 (m, 2H, H-1a′), 2.39−2.28 (m, 2H, H-1b′), 1.77−1.64 (m, 2H, H-2), 1.52−1.23 (m, 10H, H-3, H-2′, H-3′), 0.99−0.82 (m, 9H, H-4, H-4′).

^{13}C NMR, HMBC, HSQC (75 MHz, $CDCl_3$): δ [ppm] = 54.5 (C-1), 51.6 (C-1′), 34.1(C-2), 30.4(C-2′), 20.6(C-3′), 19.5(C-3), 14.1(C-4′), 13.6(C-4).

ESI-MS: *m/z* = 184.3 ([M−CN^-], 18%), 211.2 ([M+H^+], 100%).

The spectral data match those reported in the literature.[419]

2-Phenyl-1,2,3,4-tetrahydroisoquinoline (6):

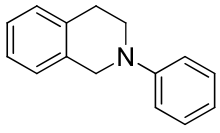

To a stirred suspension of degassed 2-propanol (375 mL), ethylene glycol (42.0 mL, 46.6 g, 75.1 mmol, 4.0 equiv), copper(I) iodide (3.58 g, 18.8 mmol, 0.1 equiv) and tribasic potassium phosphate (79.7 g, 375 mmol, 2.0 equiv), 1,2,3,4-tetrahydroisoquinoline (25.0 g, 188 mmol, 1.0 equiv) and iodobenzene (38.3 g, 188 mmol, 1.0 equiv) were added. The mixture was heated to 90 °C for 24 h. After cooling the suspension to room temperature, the solvent was removed by rotary evaporation. The residue was diluted with water (280 mL) and extracted five times with dichloromethane (50 mL). The combined organic layers were washed with brine, dried over

sodium sulfate and evaporated into dryness. The crude product was purified by column chromatography on silica gel (cyclohexane/ethyl acetate = 50:1) to yield the product (28.9 g, 138 mmol, 73%) as a slightly yellow solid.

Mp: 41.4−42.9 °C. Lit.: 44−46 °C.[420]

R_f = 0.19 (cyclohexane/ethyl acetate = 50:1).

IR (ATR): ν [cm^{-1}] = 3062 (m), 3024 (m), 2901 (m), 2817 (m), 1598 (vs), 1502 (vs), 1463 (m), 1388 (m), 1225 (m), 931 (w), 752 (vs), 692 (s).

^{1}H NMR, COSY (300 MHz, $CDCl_3$): δ [ppm] = 7.51−7.44 (m, 2H, H-3′,5′), 7.38−7.28 (m, 4H, H-5, H-6, H-7, H-8), 7.18−7.13 (m, 2H, H-2′,6′), 7.03 (tt, $^3J_{Ph\text{-}4,\ Ph\text{-}3/5}$ = 7.2 Hz, $^4J_{Ph\text{-}4,\ Ph\text{-}2/6}$ = 1.1 Hz, 1H, H-4′), 4.56 (s, 2H, H-1), 3.70 (t, $^3J_{H\text{-}3,\ H\text{-}4}$ = 5.9 Hz, 2H, H-3), 3.13 (t, $^3J_{H\text{-}4,\ H\text{-}3}$ = 5.9 Hz, 2H, H-4).

^{13}C NMR, HMBC, HSQC (75 MHz, $CDCl_3$): δ [ppm] = 150.4 (C-1′), 134.8, 134.4 (C-4a, C-8a), 129.2 (C-3′,5′), 128.5, 126.5, 126.3, 126.0 (C-5, C-6, C-7, C8), 118.7 (C-4′), 115.1 (C-2′,6′), 50.7 (C-1), 46.5 (C-3), 29.1 (C-4).

ESI-MS: *m/z* = 210.1 ([M+H^+], 100%), 208.1 ([M−H^-], 39%).

The spectral data match those reported in the literature.[420]

2-Phenyl-1,2,3,4-tetrahydroisoquinoline-1-carbonitrile (14):

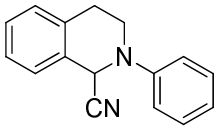

The title compound was prepared according to the general procedure described above from 2-phenyl-1,2,3,4-tetrahydroisoquinoline (44 mg, 0.21 mmol, 1.0 equiv). After column chromatography (cyclohexane/ethyl acetate = 20:1) the product (42.8 mg, 0.183 mmol, 87%) was isolated as a colorless solid.

Mp: 98.1−99.5 °C. Lit.: 95−96 °C.[421]

R_f = 0.27 (cyclohexane/ethyl acetate = 20:1).

IR (ATR): ν [cm^{-1}] = 3064 (w), 3028 (w), 2828 (w), 2834 (w), 1598 (s), 1502 (s), 1427 (m), 1222 (m), 1202 (m), 938 (m), 741 (s), 693 (m).

^{1}H NMR, COSY (300 MHz, $CDCl_3$): δ [ppm] = 7.41−7.22 (m, 6H, Ar-H, H-3′, 5′), 7.13−7.07 (m, 2H, H-2′, 6′), 7.06−6.99 (m, 1H, H-4′), 5.53 (s, 1H, H-1), 3.79 (dddd, $^2J_{H\text{-}3a,\ H\text{-}3b}$ = 12.4 Hz, $^3J_{H\text{-}3a,\ H\text{-}4}$ = 5.9, 3.0 Hz, $^4J_{H\text{-}3a,\ H\text{-}1}$ = 1.1 Hz, 1H, H-3a), 3.50 (ddd, $^2J_{H\text{-}3b,\ H\text{-}3a}$ = 12.4 Hz, $^3J_{H\text{-}3b,\ H\text{-}4}$ = 10.6, 4.1 Hz, 1H, H-3$_b$), 3.18 (ddd, $^2J_{H\text{-}4a,\ H\text{-}4b}$ =

16.4 Hz, $^{3}J_{\text{H-4a, H-3}}$ = 10.6, 5.9 Hz, 1H, H-4a), 2.98 (dt, $^{2}J_{\text{H-4b, H-4a}}$ =16.4 Hz, $^{3}J_{\text{H-4b, H-3}}$ = 3.6 Hz, 1H, H-4b).

^{13}C NMR, HMBC, HSQC (75 MHz, $CDCl_3$): δ [ppm] = 148.5 (C-1′), 134.8 (C-4a, C-8a), 129.7 (C-3′, 5′), 129.5 (C-5), 128.9, 127.2, 127.0 (C-6, C-7, C8), 122.0 (C-4′), 117.9 (CN), 117.7 (C-2′, 6′), 53.4 (C-1), 44.3 (C-3), 28.7 (C-4).

ESI-MS: *m/z* = 208.1 ([M−CN^-], 100%), 235.2 ([M+H^+], 52%).

The spectral data match those reported in the literature.[422]

2-Methyl-1,2,3,4-tetrahydroisoquinoline (7):

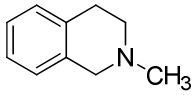

At 0 °C, formic acid (17.28 g, 375 mmol, 14.16 mL, 2.0 equiv), formaldehyde solution (16.77 mL, 207 mmol, 1.1 equiv) and 1,2,3,4-tetrahydroisoquinoline (25.00 g, 188 mmol, 23.81 mL, 1.0 equiv) were combined and heated to 80 °C for 24 h. After cooling to 0 °C, the solution was poured in half concentrated hydrochloric acid (100 mL) and extracted with diethyl ether (3 × 100 mL). The aqueous solution was basified with sodium hydroxide solution (2 M) and extracted with diethyl ether (3 × 100 mL). The combined organic layers were dried over sodium sulfate and concentrated in vacuo to yield the crude product. The purification was performed by Kugelrohr distillation (121 °C, 23 mbar) under vacuum to yield the title product (19.17 g, 130.3 mmol, 69%).

Bp: 121 °C (23 mbar).

R_f = 0.65 (cyclohexane/ethyl acetate/triethylamine = 2:4:1).

IR (ATR): ν [cm^{-1}] = 2919 (m), 2779 (m), 1498 (m), 1427 (m), 1347 (m), 1290 (m), 1099 (m), 936 (m), 738 (vs).

^{1}H NMR, COSY (300 MHz, $CDCl_3$): δ [ppm] = 7.14−7.09 (m, 3H, Ar−H), 7.03−7.01 (m, 1H, Ar−H), 3.60 (s, 2H, H-1), 2.94 (t, $^{3}J_{\text{H-3, H-4}}$ = 5.9 Hz, 2H, H-3), 2.70 (t, $^{3}J_{\text{H-3, H-4}}$ = 5.9 Hz, 2H, H-4), 2.47 (s, 3H, N−CH_3).

^{13}C NMR, HMBC, HSQC (75 MHz, $CDCl_3$): δ [ppm] = 134.7 (C-4a), 133.8 (C-8a), 128.7 (C-5), 126.5 (C-6), 126.2 (C-8), 125.7 (C-7), 58.0 (C-1), 52.99 (C-3), 46.2 (N-CH_3), 26.2 (C-4).

ESI-MS: *m/z* = 148.2 ([M−H^+], 100%).

The spectral data match those reported in the literature.[423]

2-Methyl-1,2,3,4-tetrahydroisoquinoline-1-carbonitrile (15):

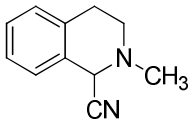

The title compound was prepared according to the general procedure described above from 2-methyl-1,2,3,4-tetrahydroisoquinoline (0.239 mmol, 1.0 equiv). After purification by filtration through a plug of aluminum oxide (basic) using CH_2Cl_2 as the eluent, the product (33.4 mg, 0.227 mmol, 95%) was isolated as a colorless oil.

R_f = 0.56 (cyclohexane/ethyl acetate/triethylamine = 1:3:0.1).

IR (ATR): ν [cm^{-1}] = 2981 (s), 2857 (s), 2809 (s), 2225 (w), 1498 (m), 1455 (m), 1148 (m), 1102 (m), 1067 (w), 945 (w), 853 (m).

^{1}H NMR, COSY (300 MHz, $CDCl_3$): δ [ppm] = 7.29−7.13 (m, 4H, H-5, H-6, H-7, H-8), 4.73 (s, 1H, H-1), 3.12−2.97 (m, 1H, H-4a), 2.94−2.75 (m, 3H, H-3, H-4b), 2.60 (s, 3H, CH_3).

^{13}C NMR, HMBC, HSQC (75 MHz, $CDCl_3$): δ [ppm] = 133.9 (C-4a), 129.6 (C-8a), 129.4, 128.5, 126.5 (C-5, C-6, C-7), 127.1 (C-8), 116.5 (CN), 56.9 (C-1), 48.4 (C-3), 43.7 (CH_3), 27.4 (C-4).

ESI-MS: *m/z* = 173.1 ([M+H^+], 100%), 146.1 ([M−CN^-], 78%).

The spectral data match those reported in the literature.[424]

[Tetradecyl(methyl)amino]acetonitrile and 2-(dimethylamino)pentadecanenitrile (16, 17):

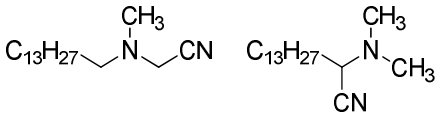

The title compound was prepared according to the general procedure described above from *N*,*N*-dimethyl-tetradecylamine (0.239 mmol, 1.0 equiv). After purification by filtration through a plug of aluminum oxide (basic) using CH_2Cl_2 as the eluent, the product (48.2 mg, 0.229 mmol, 96%) was isolated as a colorless oil as a mixture of [tetradecyl(methyl)amino]acetonitrile and 2-(dimethylamino)pentadecanenitrile with a ratio of 29:71.

R_f = 0.81 (CH_2Cl_2/MeOH = 10:1).

IR (ATR): ν [cm^{-1}] = 2923 (s), 2850 (s), 2812 (m), 2213 (w), 1475 (m), 1369 (w), 1326 (m), 1039 (m).

ESI-MS: *m/z* = 267.2 ([M+H^+], 100%), 240.3 ([M−CN^-], 43%).

[Tetradecyl(methyl)amino]acetonitrile:

^{1}H NMR, COSY (300 MHz, $CDCl_3$): δ [ppm] = 3.53 (s, 2H, H-1), 2.43 (t, $^3J_{H\text{-}1', H\text{-}2'}$ = 7.2 Hz, 1H, H-2), 2.34 (s, 3H, H-1″), 1.50−1.36 (m, 2H, H-2′), 1.35−1.19 (m, 22H, H-3′, H-4′, H-5′, H-6′, H-7′, H-8′, H-9′, H-10′, H-11′, H-12′, H-13′), 0.87 (s, 3H, H-14′).

^{13}C NMR, HMBC, HSQC (75 MHz, $CDCl_3$): δ [ppm] = 114.8 (CN), 56.0 (C-1′), 45.3 (C-1), 42.2 (C-1″), 27.6 (C-2′), 31.1, 29.9−29.4, 27.2, 22.8 (C-3′, C-4′, C-5′, C-6′, C-7′, C-8′, C-9′, C-10′, C-11′, C-12′, C-13′), 14.3 (C-14′).

2-(Dimethylamino)pentadecanenitrile:

^{1}H NMR, COSY (300 MHz, $CDCl_3$): δ [ppm] = 3.46 (t, $^3J_{H\text{-}2, H\text{-}3}$ = 7.4 Hz, 1H, H-2), 2.30 (s, 6H, H-1′, H-1″), 1.78−1.66 (m, 2H, H-3), 1.50−1.36 (m, 2H, H-4), 1.35−1.19 (m, 20H, H-5, H-6, H-7, H-8, H-9, H-10, H-11, H-12, H-13, H-14), 0.87 (s, 3H, H-15).

^{13}C NMR, HMBC, HSQC (75 MHz, $CDCl_3$): δ [ppm] = 117.0 (C-1), 58.9 (C-2), 41.9 (C-1′, C-1″), 31.8 (C-3), 26.1 (C-4), 29.9−29.4, 29.1 (C-5, C-6, C-7, C-8, C-9, C-10, C-11, C-12, C-13, C-14), 14.3 (C-15).

The spectral data match those reported in the literature.[358,419]

[(1*H*-indol-3-ylmethyl)(methyl)amino]acetonitrile (18):

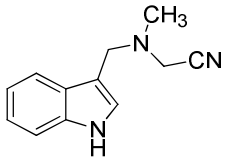

The title compound was prepared according to the general procedure described above from Gramine (0.239 mmol, 1.0 equiv). After column chromatography by flash chromatography on silica gel (CH_2Cl_2/MeOH, 20:1) the product was isolated as a colorless oil (42.4 mg, 0.213 mmol, 89%).

R_f = 0.65 (CH_2Cl_2/MeOH = 10:1).

IR (ATR): ν [cm^{-1}] = 3405 (s), 2951 (s), 2788 (m), 2222 (w), 1670 (m), 1450 (m), 1342 (m), 844 (m), 741 (w).

^{1}H NMR, COSY (300 MHz, $CDCl_3$): δ [ppm] = 8.12 (br s, 1H, NH), 7.74 (d, $^3J_{H\text{-}4, H\text{-}5}$ = 7.7 Hz, 1H, H-4), 7.39 (d, $^3J_{H\text{-}7, H\text{-}6}$ =7.4 Hz, 1H, H-7), 7.25−7.19 (m, 2H, H-2, H-6), 7.14 (m, 1H, H-5) 3.81 (s, 2H, H-8), 3.46 (s, 2H, H-9), 2.50 (s, 3H, H-10).

^{13}C NMR, HMBC, HSQC (75 MHz, $CDCl_3$): δ [ppm] = 136.5 (C-7a), 127.2 (C-3a), 124.0 (C-2), 122.5 (C-6), 119.9 (C-5), 119.5 (C-4), 114.8 (CN), 111.9 (C-3), 111.2 (C-7), 51.2 (C-8), 43.7 (C-9), 42.4 (C-10).

ESI-MS: *m/z* = 173.0 ([M−CN$^-$], 100%).

The spectral data match those reported in the literature.[358]

1-Methyl-5-(pyridin-3-yl)pyrrolidine-2-carbonitrile and 1-methyl-2-(pyridin-3-yl)pyrrolidine-2-carbonitrile (19, 20):

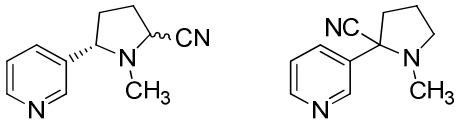

The title compound was prepared according to the general procedure described above from nicotine (0.239 mmol, 1.0 equiv). After purification by filtration through a plug of aluminum oxide (basic) using CH_2Cl_2 as the eluent, the product (38.1 mg, 0.203 mmol, 85%) was isolated as a colorless oil as a mixture of 1-methyl-2-(pyridin-3-yl)pyrrolidine-2-carbonitrile and both diastereomeres of 1-methyl-5-(pyridin-3-yl)pyrrolidine-2-carbonitrile with a ratio of 56:28:16.

R_f = 0.39 (ethyl acetate).

ESI-MS: *m/z* = 188.0 ([M+H$^+$], 100%), 161.1 ([M−CN$^-$], 49%).

1-Methyl-2-(pyridin-3-yl)pyrrolidine-2-carbonitrile:

^{1}H NMR, COSY (300 MHz, $CDCl_3$): δ [ppm] = 8.84 (dd, $^4J_{H\text{-}2',\ H\text{-}4'}$ = 2.5 Hz, $^4J_{H\text{-}2',\ H\text{-}6'}$ = 0.9 Hz, 1H, H-2′), 8.60 (dd, $^3J_{H\text{-}6',\ H\text{-}5'}$ = 4.8 Hz, $^4J_{H\text{-}6',\ H\text{-}4'}$ = 1.6 Hz, 1H, H-6′), 7.88 (ddd, $^3J_{H\text{-}4',\ H\text{-}5'}$ = 8.0 Hz, $^4J_{H\text{-}4',\ H\text{-}2'}$ = 2.5 Hz, $^4J_{H\text{-}4',\ H\text{-}6'}$ = 1.6 Hz, 1H, H-4′), 7.35−7.24 (m, 1H, H-5′), 3.41−3.28 (m, 1H, H-5a), 2.76−2.62 (m, 1H, H-5b), 2.61−2.52 (m, 1H, H-3a), 2.23 (s, 3H, CH_3), 2.14−1.99 (m, 3H, H-3b, H-4).

^{13}C NMR, HMBC, HSQC (75 MHz, $CDCl_3$): δ [ppm] = 150.1 (C-6′), 148.1 (C-2′), 134.1 (C-4′), 133.9 (C-2′), 123.6 (C-5′), 117.0 (CN), 69.8 (C-2), 53.9 (C-5), 43.2 (C-3), 36.3 (CH_3), 21.2 (C-4).

1-Methyl-5-(pyridin-3-yl)pyrrolidine-2-carbonitrile − major diastereomer:

^{1}H NMR, COSY (300 MHz, $CDCl_3$): δ [ppm] = 8.56−8.50 (m, 2H, H-2′, H-6′), 7.64 (dt, $^3J_{H\text{-}4',\ H\text{-}5'}$ = 7.8 Hz, $^4J_{H\text{-}4',\ H\text{-}2'/H\text{-}6'}$ = 2.0 Hz, 1H, H-4′), 7.35−7.24 (m, 1H, H-5′), 4.18−4.10 (m, 1H, H-2), 3.57 (t, $^3J_{H\text{-}5,\ H\text{-}4}$ = 8.0 Hz, 1H, H-5), 2.48−2.43 (m, 1H, H-4a),

2.41−2.27 (m, 1H, H-3a), 2.31 (s, 3H, CH_3), 2.23−2.13 (m, 1H, H-3b), 1.83−1.75 (m, 1H, H-4b).

^{13}C NMR, HMBC, HSQC (75 MHz, $CDCl_3$): δ [ppm] = 149.4 (C-6′), 149.3 (C-2′), 137.5 (C-3′), 134.9 (C-4′), 123.9 (C-5′), 117.5 (CN), 65.2 (C-5), 56.8 (C-2), 39.0 (CH_3), 33.3 (C-4), 28.5 (C-3).

1-Methyl-5-(pyridin-3-yl)pyrrolidine-2-carbonitrile − minor diastereomer:

^{1}H NMR, COSY (300 MHz, $CDCl_3$): δ [ppm] = 8.56−8.50 (m, 2H, H-2′, H-6′), 7.73 (dt, $^3J_{H\text{-}4',\,H\text{-}5'}$ = 7.91 Hz, $^4J_{H\text{-}4',\,H\text{-}2'/H\text{-}6'}$ = 2.0 Hz, 1H, H-4′), 7.35−7.24 (m, 1H, H-5′), 3.41−3.28 (m, 3H, H-2, H-5), 2.41−2.27 (m, 1H, H-3a), 2.30−2.23 (m, 1H, H-4a), 2.29 (s, 3H, CH_3), 2.23−2.13 (m, 1H, H-3b), 1.92−1.80 (m, 1H, H-4b).

^{13}C NMR, HMBC, HSQC (75 MHz, $CDCl_3$): δ [ppm] = 149.5 (C-6′), 149.4 (C-2′), 137.0 (C-3′), 134.7 (C-4′), 123.8 (C-5′), 120.2 (CN), 68.2 (C-5), 55.9 (C-2), 36.6 (CH_3), 34.3 (C-4), 28.7 (C-3).

The spectral data match those reported in the literature.[358]

8-(Cyanomethyl)-8-azabicyclo[3.2.1]oct-3-yl 2-phenyl-3-[(trimethylsilyl)oxy]propanoate (21):

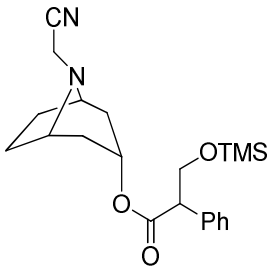

Atropine base was isolated from Atropine sulfate monohydrate as described in the literature.[358] The atropine base (60.8 mg, 0.21 mmol, 1.0 equiv) was cyanated according to the general procedure described above. The crude product was purified by column chromatography on silica gel (chloroform/methanol = 20:1) and the product (51.0 mg, 0.132 mmol, 63%) was isolated as a slightly yellow oil. The product decomposes on the column by deprotection.

R_f = 0.62 (chloroform/methanol = 20:1).

IR (ATR): ν [cm^{-1}] = 2950 (w), 2878 (w), 2245 (w), 1727 (s), 1667 (w), 1251 (s), 1201 (s), 1170 (s), 1155 (s), 1102 (s), 1080 (m), 1065 (s), 1034 (s), 894 (m), 839 (s), 779 (m), 699 (s).

^{1}H NMR, COSY (400 MHz, $CDCl_3$): δ [ppm] = 7.33−7.23 (m, 5H, Ar−H), 4.98 (t, $^3J_{\text{H-3, H-2a \& H-4a}}$ = 5.5 Hz, 1H, H-3), 4.20−4.12 (m, 1H, H-3a′), 3.78−3.70 (m, 2H, H-2′, H-3b′), 3.27−3.13 (m, 2H, H-1, H-5), 3.23 (s, 2H, N−C**H**$_2$−CN), 2.15−1.56 (m, 8H, H-2, H-4, H-6, H-7), 0.07 (s, 9H, TMS).

^{13}C NMR, HMBC, HSQC (100 MHz, $CDCl_3$): δ [ppm] = 171.5 (CO), 135.6 (Ph-1), 128.6, 127.9 (Ph-2, Ph-3, Ph-5, Ph-6), 127.5 (Ph-4), 117.3 (CN), 67.3 (C-3), 64.5 (C-3′), 58.7, 58,6 (C-1, C-5), 54.7 (C-2′), 40.8 (N−**C**H$_2$−CN), 36.7, 36.4 (C-2, C-4), 25.2, 24.9 (C-6, C-7), −0.75 (TMS).

ESI-MS: *m/z* = 387.2 ([M+H$^+$], 100%).

The spectral data match those reported in the literature.[358]

1-Phenylpiperidine-2-carbonitrile (22):

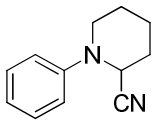

The title compound was prepared according to the general procedure described above from 1-phenylpiperidine (0.239 mmol, 1.0 equiv). After column chromatography on silica gel (cyclohexane/ethyl acetate = 5:1), the product was isolated as a brown oil (37.8 mg, 0.203 mmol, 85%).

R_f = 0.35 (cyclohexane/ethyl acetate = 7:1).

IR (ATR): ν [cm^{-1}] = .

^{1}H NMR, COSY (300 MHz, $CDCl_3$): δ [ppm] = 7.33−7.25 (m, 2H, H-3′, H-5′), 7.01−6.89 (m, 3H, H-2′, H-4′, H-6′), 4.62 (t, $^3J_{\text{H-2, H-3}}$ = 3.5 Hz, 1H, H-2), 3.48−3.38 (m, 1H, H-6a), 3.03−2.93 (m, 1H, H-6b), 2.03−1.89 (m, 2H, H-3), 1.87−1.60 (m, 4H, H-4, H-5).

^{13}C NMR, HMBC, HSQC (75 MHz, $CDCl_3$): δ [ppm] = 149.5 (C-1′), 129.1 (C-3′, C-5), 122.0 (C-4′), 118.3 (C-2′, 5′), 117.2 (CN), 51.7 (C-2), 46.2 (C-6), 29.3 (C-3), 24.9 (C-4), 20.0 (C-5).

ESI-MS: *m/z* = 160.1 ([M−CN$^-$], 100%).

The spectral data match those reported in the literature.[425]

3.6.4 Reaction Screening

Reaction screening with the cyanation of tributylamine:

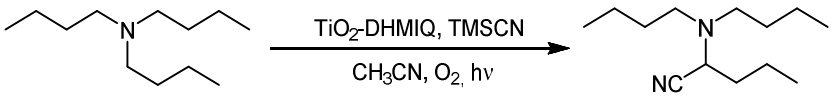

3.6.4.1 Catalyst Loading

Table S3.2. Influence of the catalyst loading on the reaction yield.[a]

catalyst loading (mg)	2.5	1.0	0.5	0.2	0.1	0.05	0.02	0.01	0.00
yield (%)	95	59	51	47	41	30	27	25	14

[a]Reaction conditions: Bu_3N (0.239 mmol, 1.0 equiv) and dry TiO_2–DHMIQ were mixed in acetonitrile (4.0 mL). The suspension was saturated with oxygen and TMSCN (3.0 equiv) was added. The reaction vial was closed and irradiated with blue light for 3 h. The crude product was isolated by extraction and the yield was determined by ^1H NMR spectroscopy with 1,4-bis(trimethylsilyl)benzene as internal standard.

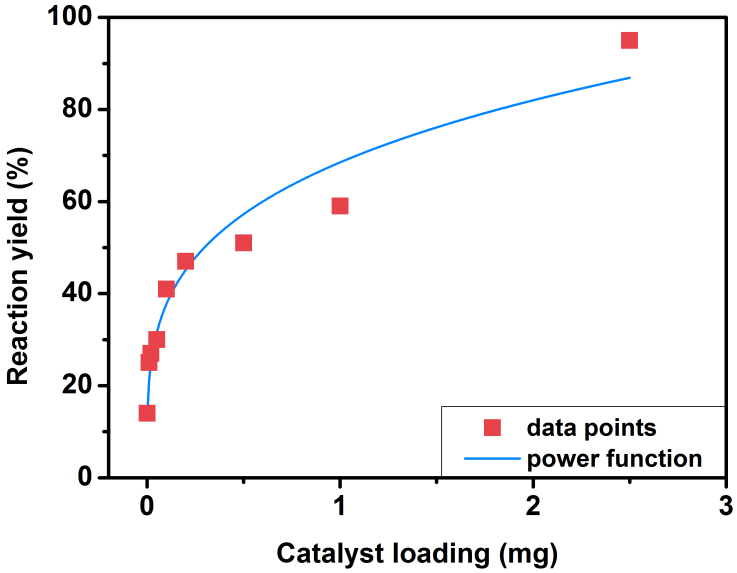

Figure S3.8. Effect of catalyst loading on reaction yield.

The effect of catalyst loading on reaction yield (Figure S3.8) was fitted with a power-type function:

$$\frac{r}{\%} = a\left(\frac{m}{\text{mg}}\right)^{b}$$

where

r = reaction yield (in %),
m = catalyst mass (in mg),
a = 68.51,
b = 0.26.

This type of function is a widely used expression in the field of catalysis to describe adsorption processes on solid surfaces (cf. Freundlich adsorption isotherm).[171] It should be noted, however, that this is only a simplistic mathematical approximation of a complex correlation, which has not been studied in detail.

3.6.4.2 Influence of Water

Table S3.3. Influence of water on the catalysis efficiency of TiO_2–DHMIQ.[a]

water addition (µL)	0	1	5	10	20	40
yield (%)	95	61	27	19	19	20

[a]Reaction conditions: Bu_3N (0.239 mmol, 1.0 equiv), dry TiO_2–DHMIQ (2.5 mg), and water were mixed in acetonitrile (4.0 mL). The suspension was saturated with oxygen and TMSCN (3.0 equiv) was added. The reaction vial was closed and irradiated with blue light for 3 h. The crude product was isolated by extraction and the yield was determined by ^{1}H NMR spectroscopy with 1,4-bis(trimethylsilyl)benzene as internal standard.

The effect of water on reaction yield (Figure S3.9) was fitted with an exponential decay function:

$$\frac{r}{\%} = a \cdot \exp\left(-b\frac{V}{\mu\text{L}}\right) + c$$

where

r = reaction yield (in %),
V = water volume (in µL),
a = 74.52,
b = 0.56,
c = 19.89.

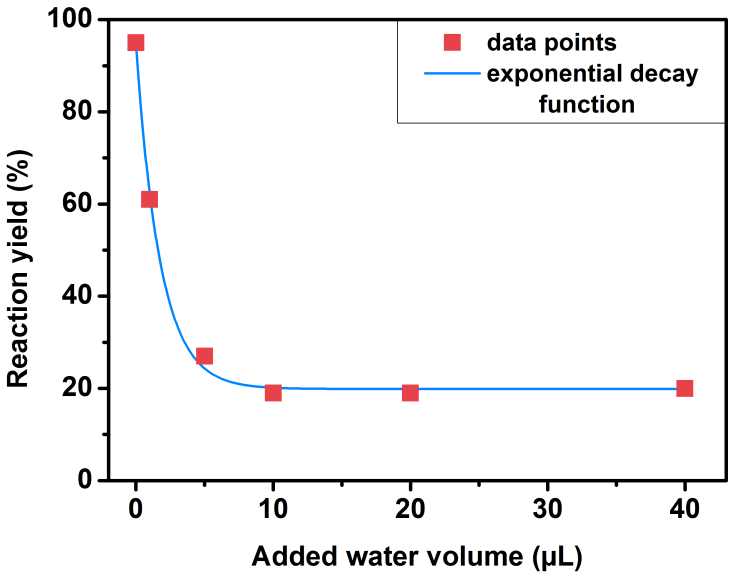

Figure S3.9. Effect of water addition on reaction yield.

The use of an exponential decay function is justified by the observation that the conversion dropped much faster for small amounts of water than for higher amounts. The most plausible explanation for this behavior is the formation of a hydration shell around the polar nanoparticles, thus passivating the surface and preventing the substrate molecules from approaching the reactive sites. Since the hydration shell has a finite maximum thickness, the conversion is not completely suppressed for higher amounts of water, but levels off to a conversion rate of approximately 20%.

This assumption is supported by the fact that 1 µL of added water corresponds to a hydration shell thickness of 2−3 nm (*vide infra* for details on the calculation).* This value is in accordance with experimental results, where hydration layer thicknesses of up to 4 nm were observed on alumina nanoparticles.[426] Given the fact that the uncharged substrate molecules (such as tributylamine) have only a moderate polarity, a hydration layer of several nm thickness constitutes a considerable energy barrier for the molecules to approach the nanoparticle surface. This is why such a small amount as 1 µL of water is sufficient to reduce the reaction yield by 34%. Eventually, the reaction yield levels off at approximately 20% beyond 5 µL of water added. This volume corresponds to a hydration layer of ~12 nm, which is a plausible maximum value for a highly charged surface in the otherwise apolar environment of acetonitrile. Consequently, further addition of water has little effect on reaction yield as it does not add to the hydration shell anymore, but instead mixes with acetonitrile.

Although hydrolysis of TMSCN will certainly occur, it is not likely the main reason for the observed decrease of the reaction yield. Addition of 1 µL of water (0.06 mmol) would only cause 8 mol% of the employed TMSCN (0.72 mmol) to hydrolyze while at the same time the reaction yield drops by 34%.

*The hydration shell thickness was calculated as follows:

$$d = \frac{V}{A} = \frac{V}{A_S \cdot m} = \frac{10^{-9}\ \mathrm{m^3}}{166\ \mathrm{m^2 g^{-1}} \cdot 2.5 \cdot 10^{-3}\ \mathrm{g}} = 2.4 \cdot 10^{-9}\ \mathrm{m} = 2.4\ \mathrm{nm}$$

where

d = hydration shell thickness,
V = water volume (1 µL = 10^{-9} m^3),
A = surface area,
A_S = specific surface area (see Table S3.1: 166 m^2g^{-1}),
m = catalyst mass (2.5 mg).

3.6.4.3 Catalyst Recovery

Table S3.4. Recovery and reuse of the catalyst.[a]

cycle number	1	2	3	4
yield (%)	95	92	87	82

[a]Reaction conditions: Bu_3N (0.239 mmol, 1.0 equiv) and dry TiO_2–DHMIQ (2.5 mg) were mixed in acetonitrile (4.0 mL). The suspension was saturated with oxygen and TMSCN (3.0 equiv) was added. The reaction vial was closed and irradiated with blue light for 3 h. The catalyst was precipitated, isolated by centrifugation (4700 rpm, 10 min, −9 °C) and suspended in acetonitrile (4.0 mL). This washing procedure was repeated twice before the catalyst was reused. The crude product was isolated by extraction from all combined acetonitrile phases and the yield was determined by ^{1}H NMR spectroscopy with 1,4-bis(trimethylsilyl)benzene as internal standard.

The effect of catalyst recycling on reaction yield (Figure S3.10) was fitted with a linear function:

$$\frac{r}{\%} = a \cdot x + b$$

where

r = reaction yield (in %),
x = cycle number,
a = −4.4,
b = 100.

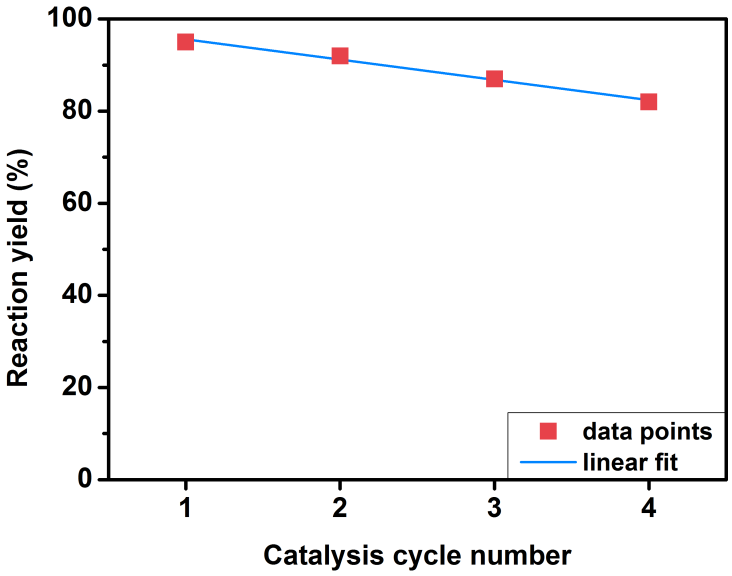

Figure S3.10. Effect of catalyst recycling on reaction yield.

The decrease in catalytic performance follows a linear decay function, presumably due to gradual degradation of the photocatalyst, such as self-oxidation.

3.6.4.4 Additional Screenings

Table S3.5. Addional screening reactions.[a]

entry #	screening conditions	yield
1	no light[b]	<1%
2	no light[b], 16 h	6%
3	no light[b], 50 °C	2%
4	no light[b], 100 °C	9%
5	no light[b] & no catalyst, 50 °C	2%
6	no light[b] & no catalyst, 100 °C	12%
7	2.00 mg DHMIQ (= 4.0 mol%)[c]	53%
8	0.29 mg DHMIQ (= 0.57 mol%)	84%
9	0.06 mg DHMIQ (= 0.12 mol%)	80%
10	0.29 mg DHMIQ (= 0.57 mol%) + TiO_2–TMA (2.2 mg)	62%

[a]General reaction conditions: Bu_3N (0.239 mmol, 1.0 equiv) and dry TiO_2–DHMIQ were mixed in acetonitrile (4.0 mL). The suspension was saturated with oxygen and TMSCN (3.0 equiv) was added. The reaction vial was closed and irradiated with blue light for 3 h. The crude product was isolated by extraction and the yield was determined by ^{1}H NMR spectroscopy with 1,4-bis(trimethylsilyl)benzene as internal standard. [b]The reaction vial was wrapped in aluminum foil and placed in front of the light source. [c]Suspension (DHMIQ not totally dissolved).

3.6.5 Mechanistic Studies

3.6.5.1 ^{29}Si NMR Spectroscopic Investigation

Reaction conditions: Bu_3N (0.239 mmol, 1.0 equiv) and dry TiO_2–DHMIQ (2.5 mg catalyst, 0.6 mol%) were mixed in acetonitrile-d_3 (4.0 mL). The suspension was saturated with oxygen and TMSCN (3.0 equiv) was added. The reaction vial was closed and irradiated with blue light for 3 h. Finally, an aliquot of the irradiated reaction mixture was used for ^{29}Si NMR spectroscopic investigation.

This reaction in deuterated solvent was performed in order to elucidate the fate of the TMS-peroxo species *via* ^{29}Si solution NMR spectroscopy (Figure S3.11). Four major Si-containing products were identified (Table S3.6).

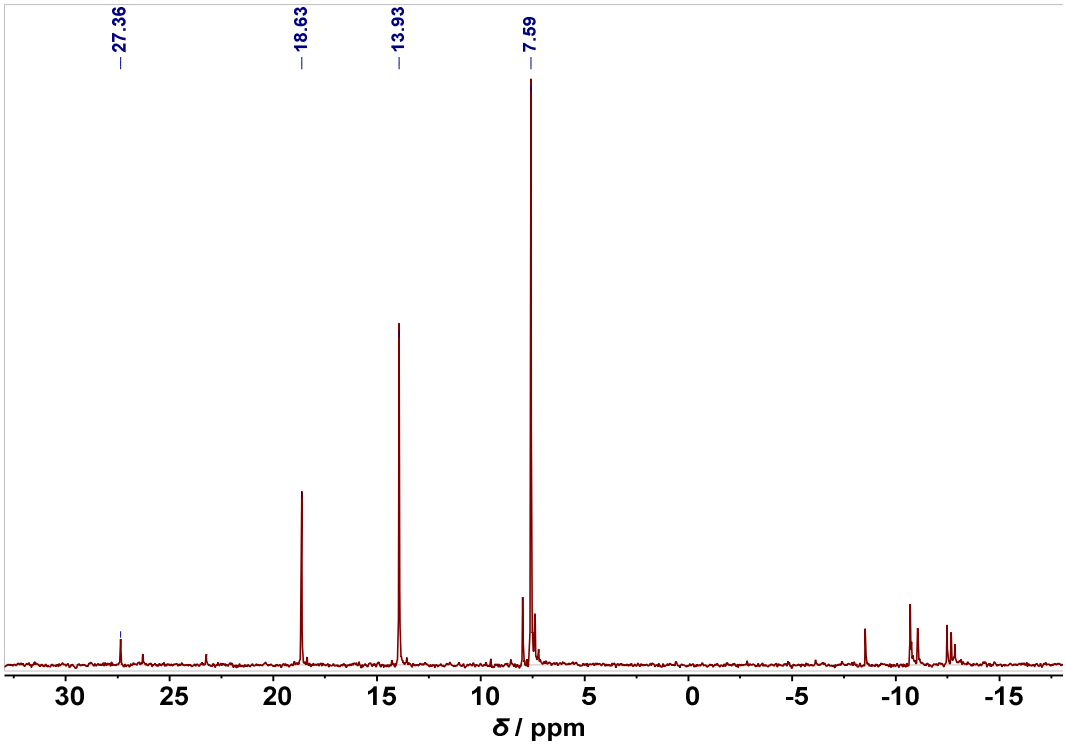

Figure S3.11. ^{29}Si NMR spectrum (80 MHz, CD_3CN) of a reaction mixture after irradiation.

Table S3.6. Assignment of ^{29}Si NMR shifts from Figure S3.11.

assumed Si species	found ^{29}Si NMR shift (80 MHz, CD_3CN)	literature values
Bis(trimethylsilyl) peroxide $Me_3Si–O–O–SiMe_3$ 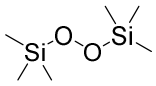	27.36	27.86 (100 MHz, $CDCl_3$)[427] 27.60 (80 MHz, $CDCl_3$)[428]
Trimethylmethoxysilane $Me_3Si–OMe$ 	18.63	18.41 (80 MHz, CD_3CN)[429] 17.64 (80 MHz, C_6D_6)[430]
Trimethylsilanol $Me_3Si–OH$ 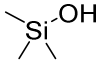	13.93	14.97 (80 MHz, C_6D_6)[431] 12.57 (60 MHz, acetone-d_6)[432]
Hexamethyldisiloxane $Me_3Si–O–SiMe_3$ 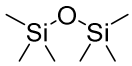	7.59	7.60 (80 MHz, C_6D_6)[433] 7.41 (80 MHz, CD_3CN)[429]

3.6.5.2 Control Experiments

Screening of alternative pathways

Reaction conditions: Bu_3N (0.239 mmol, 1.0 equiv), dry TiO_2−DHMIQ (2.5 mg) and diethylsilane *or* ethyl acrylate (0.239 mmol, 1.0 equiv) were mixed in acetonitrile (4.0 mL). The suspension was saturated with oxygen and TMSCN (3.0 equiv) was added. The reaction vial was closed and irradiated with blue light for 3 h. The crude product was isolated by extraction and the yield was determined by ^{1}H NMR spectroscopy with 1,4-bis(trimethylsilyl)benzene as internal standard.

These control experiments were conceived to investigate the possibility of alternative pathways in the reaction mechanism. Apart from our proposed mechanism, α-amino radical intermediates are often discussed in the literature[406] as a mechanistic alternative for iminium formation (Figure S3.12). The α-amino radical intermediate might be formed in two ways: either by direct H-abstraction from the neutral parent amine (pathway I) or by α-deprotonation of the amine radical cation (pathway II).

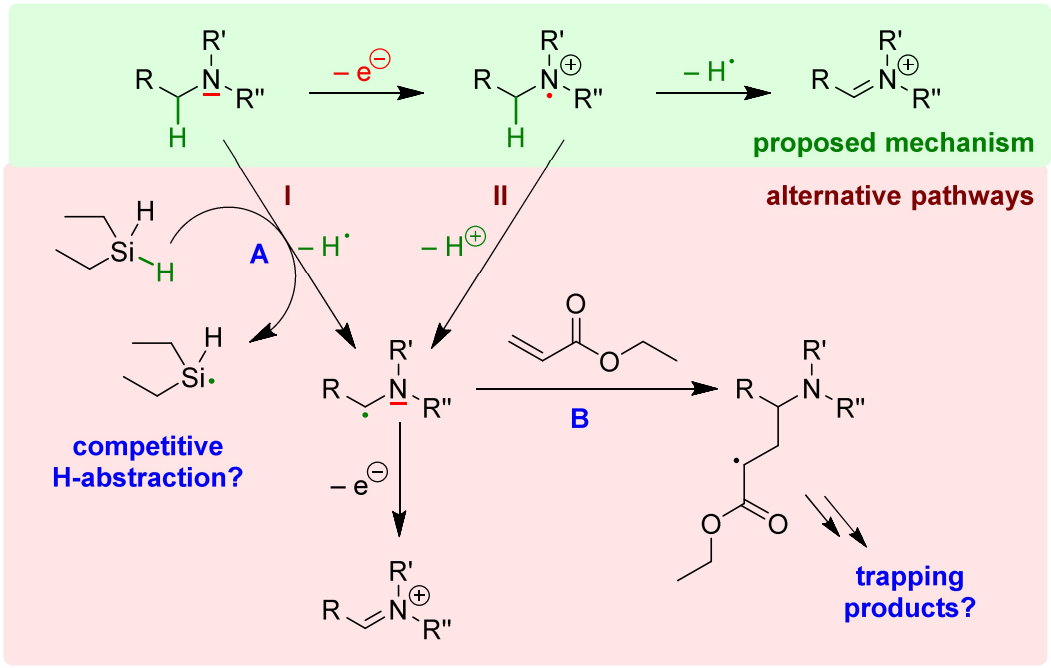

Figure S3.12. Alternative pathways in the reaction mechanism (pathway I: direct H-abstraction from the neutral parent amine; pathway II: α-deprotonation of the amine radical cation) and applied screening reactions (reaction A: addition of diethylsilane for competitive H-abstraction; reaction B: addition of ethyl acrylate for trapping of α-amino radicals).

To investigate pathway I, we performed a control experiment with addition of equimolar amounts of diethylsilane, whose Si–H bond is slightly weaker than the C_α–H-bond of trialkylamines (374 vs. 381 kJ mol^{-1}).[434,435] If pathway I was the main mechanistic route, addition of diethylsilane would induce competitive H-abstraction, resulting in a reduced yield of the α-aminonitrile product. Since, however, the usual quantitative conversion to the desired product was observed, the presence of diethylsilane does not interfere with the photocyanation of tributylamine. Consequently, the direct H-abstraction from the neutral parent amine (as described by pathway I) appears less likely and a prior oxidation is suggested, which weakens the C_α–H-bonds to facilitate the H-abstraction (proposed mechanism).

To investigate pathway II as an alternative route for the generation of α-amino radicals, another control experiment was performed with the addition of ethyl acrylate, an electron-deficient olefin that is known to react with α-amino radicals.[411,412] If α-amino radicals were generated (in any way), addition of ethyl acrylate would produce trapping products which would be easily detectable by NMR. However, no trapping

products were observed in this reaction. Instead, the desired photocyanation product was obtained in quantitative yield.

In sum, *α*-amino radicals appear less likely to be intermediates in the photocyanation reaction. The combined results support the reaction mechanism as proposed in Figure 3.4.

Reactions with *tert*-butyldimethylsilyl cyanide (TBDMSCN)

Reaction conditions: The photocyanation reactions of *N*,*N*-dimethyltetradecylamine (**8**) and nicotine (**10**) were repeated using the same procedures as described above, with the only exception that the cyanide source TMSCN was replaced with equimolar amounts of TBDMSCN.

Table S3.7. Regioselectivity for different cyanide sources TMSCN and TBDMSCN.

cyanated products	TMSCN 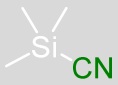	TBDMSCN 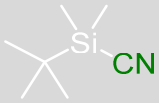
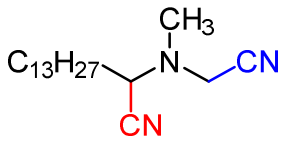 **16**, **17**	71:29	69:31
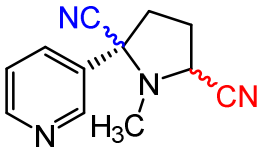 **19**, **20**	56:(28:16)	50:(32:18)

To gain more mechanistic insight into the regioselectivity of the photocyanation, the reactions of *N*,*N*-dimethyl-tetradecylamine (**8**) and nicotine (**10**) were repeated with the altered silyl species TBDMSCN instead of TMSCN.

The photocyanation reactions with TBDMSCN showed somewhat slower conversion rates, while in both cases, the regioselectivity varied only slightly (Table S3.7). We interpret this as a result of an accelerating effect of the silylation of superoxide, which is known to be a less efficient H-abstractor due to its electronic stabilization. With TBDMSCN, the formation of the silylperoxy radical is slowed down due to steric hin-

drance on Si. We did not expect to see a large difference in regioselectivity as the steric bulk for the H-abstraction changes three atoms away from the reaction center, while the nucleophilic substitution at silicon through superoxide should be much more affected.

4

Elastic Modulus and Thermal Conductivity of Thiol–Ene/TiO_2 Nanocomposites

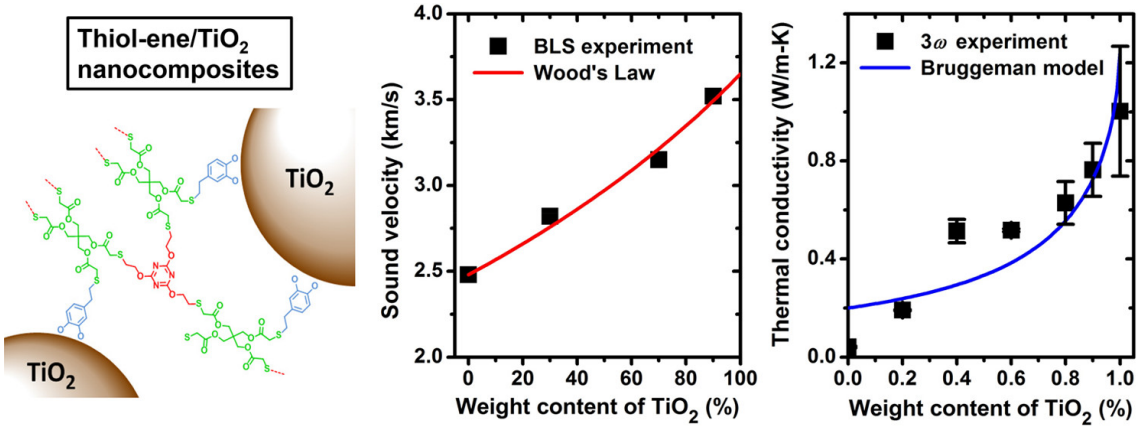

This chapter contains an adapted reproduction of *The Journal of Physical Chemistry C* **2017**, *121*, 25568–25575, reprinted with permission of the American Chemical Society (© 2017).

Authorship Contributions

Study conception and design	E. Schechtel W. Tremel G. Fytas
Acquisition of data	E. Schechtel Y. Yan Y. Cang
Analysis and interpretation of data	E. Schechtel X. Xu Y. Cang Z. Wang G. Fytas
Drafting of manuscript	E. Schechtel X. Xu Y. Cang Z. Wang G. Fytas
Critical revision	E. Schechtel Y. Yan X. Xu Y. Cang W. Tremel Z. Wang B. Li G. Fytas

4.1 Abstract

Metal oxide based polymer nanocomposites find diverse applications as functional materials, and in particular thiol−ene (TE)/TiO_2 nanocomposites are promising candidates for dental restorative materials. The important mechanical and thermal properties of the nanocomposites, however, are still not well understood. In this study, the elastic modulus and thermal conductivity of thiol−ene/TiO_2 nanocomposite thin films with varying weight fractions of TiO_2 nanoparticles (NPs) are investigated by using Brillouin light scattering (BLS) spectroscopy and 3ω measurements, respectively. As the TiO_2 weight fraction increases from 0 to 90%, the effective elastic longitudinal modulus of the films increases from 6.2 to 37.5 GPa, and the effective thermal conductivity from 0.04 to 0.76 W/m·K. The former increase could be attributed to the covalent cross-linking of the nanocomposite constituents. The latter one could be ascribed to the addition of high thermal conductivity TiO_2 NPs and the formation of possible conductive channels at high TiO_2 weight fractions. The linear dependence of the thermal conductivity on the sound velocity, reported for amorphous polymers, is not observed in the present nanocomposite system.

4.2 Introduction

Polymer nanocomposites are hybrid materials that integrate selected properties of both polymers and nanocolloids. It is currently a topic of intensive interest for both fundamental materials science and technology.[436,437] However, polymers and NPs are hardly miscible in the absence of specific interactions due to depletion forces, leading to interesting non-equilibrium morphologies.[438] One strategy to obtain stable dispersions involves polymer grafts that results in matrix-free, one-component hybrid materials with novel mechanical, dielectric, thermal, or phononic properties.[439–441] A similar platform to fabricate homogeneous hybrid materials works by creating strong attachment of the NPs to a network.[442] The elastic modulus and thermal conductivity are two properties of paramount importance for material functions in a range of technologies. Polymers are low modulus (a few gigapascals)[441] and low thermal conductivity (0.1−0.3 W $m^{-1}K^{-1}$)[443] materials compared with the inorganic counterparts. A promising strategy to increase these values is adding NPs into the polymers — the design of polymer nanocomposites. While the elastic modulus depends mainly on the efficient packing and cohesive forces,[444–446] engineering of the thermal conductivity presents major challenges.[447,448] Besides the state of the dispersion, it is essential to have control over interfacial thermal resistance, which involves different characteristic length scales[449] and intermolecular interactions.[450] As for the latter issue, increasing the bonding strength of surfactants to the inorganic surface led to a strong increase of interfacial thermal conductance.[451] A more recent work on thermal conduction in surfactant/semiconductor nanocrystals has further revealed the sensitivity of the effective thermal conductivity to the bonding strength of the molecular ligands.[452] The role of the polymeric tethers on the thermal conductivity has been recently addressed in the case of polymer/particle brush nanocomposites.[453] Favored enthalpic interactions between tethered and matrix polymer chains seem to be more relevant than the conceivable conformational non-uniformity of the tethered chains. However, there is limited literature on the mechanical and thermal properties of hybrid nanocomposites, and solid phenomenology necessary to develop theoretical concepts is also lacking.

In this work, we utilized a system that bridges the few molecular and polymer nanocomposites investigated so far. It is based on titanium dioxide (TiO_2, titania) NPs, dispersed in a cross-linked organic matrix. Titania was chosen for the inorganic phase

because of its use in a wide range of existing and emerging applications. It is not only an industrially important mass product (with numerous applications in health care),[94] but also the subject of current research on photovoltaics[454] and photocatalysis.[263,266] For most applications of NPs in hybrid composites, it is beneficial to avoid particle agglomeration. To account for uniform dispersion and solid anchoring of the TiO_2 NPs, the organic phase requires to be a cross-linked polymer matrix. These requirements can be readily met by thiol−ene (TE) click chemistry, which has proved to be a valuable platform in materials science, owing to its good adaptability and easy practicability.[455,456] Photoinitiated TE polymerizations neither require high curing temperatures, as epoxy resins do, nor suffer from oxygen inhibition or insufficient curing, which are common for photopolymerized acrylate-based resins.[457,458] Photopolymerized TE networks have already been used to fabricate hybrid nanocomposites by incorporating inorganic fillers like silicate clay minerals,[459] gold NPs,[460,461] and TiO_2 particle powders.[462] However, none of these studies investigated nanocomposites with inorganic filler fractions exceeding 7 wt%. Due to the excellent dispersability of the NPs used, the present approach allows fabrication of hybrid nanocomposites with inorganic filler fractions over the entire composition range (i.e., 0−100 wt% TiO_2 NPs).

In this paper, we report on the effective elastic longitudinal moduli and thermal conductivities of TE/TiO_2 nanocomposite films at different NP weight fractions. The former are calculated as $M_{\mathrm{L,\,eff}} = \rho_{\mathrm{eff}}\, c^2_{\mathrm{L,\,eff}}$, where ρ_{eff} is the effective density of the films and $c_{\mathrm{L,\,eff}}$ is the effective longitudinal sound velocity obtained from Brillouin light scattering (BLS)[463–465] measurements; the latter are measured with the 3ω method.[450,466,467] To our knowledge, there are few reports on the relation between the sound velocity and thermal conductivity,[468,469] which are limited to bulk amorphous polymers and have demonstrated a linear dependence of the minimum thermal conductivity on the sound velocity. This work extends this investigation of the relation to polymer nanocomposite thin films. The results suggest that the covalent cross-linking of the nanocomposite constituents had a synergistic effect on sound propagation, yielding effective sound velocities of the nanocomposites that exceeded the value of the soft constituent (i.e., the TE network). The effective elastic longitudinal modulus increased monotonically from 6.2 to 37.5 GPa, as the weight fraction of TiO_2 NPs increased from 0 to 90%. On the other hand, the corresponding effective thermal conductivity increased from 0.04 to 0.76 W/m·K (by a factor of 18), due to the addition of high thermal con-

ductivity TiO_2 NPs and the formation of possible conductive channels at high TiO_2 weight fractions. These findings are potentially applicable for the development of improved dental resin composites, which require high inorganic filler loadings with strong anchoring of the NPs to the polymer matrix to prevent loss of material to the human body. Indeed, both TiO_2 NPs and TE resins have already been discussed as potential dental restorative materials in the literature.[470,471]

4.3 Experimental Section

Materials and Substrates. Unless otherwise stated, all chemicals were obtained from commercial suppliers and used without further purification. Sulfuric acid (H_2SO_4, conc.), hydrogen peroxide solution (H_2O_2, 35 wt%), pentaerythritol tetrakis(3-mercaptopropionate) (PETMP, >95%), 2,4,6-triallyloxy-1,3,5-triazine (TAOTA, 97%), and 2,2-dimethoxy-2-phenylacetophenone (DMPA, 99%) were obtained from Sigma-Aldrich. 4-Allylcatechol[472] and TiO_2 NPs[56] were synthesized according to previously reported procedures with various modifications. The as-synthesized, OA-stabilized TiO_2 NPs were mostly of a spherical shape with a mean diameter of 6.5 ± 1.3 nm (see Figure S4.1a,b in the Supporting Information). The crystallinity of the NPs was confirmed by PXRD, revealing the prominent diffraction lines of the anatase phase (see Figure S4.2 in the Supporting Information). The OA-stabilized TiO_2 NPs were re-functionalized with 4-allylcatechol in a biphasic reaction mixture. Details of the synthetic procedures can be found in section 4.6.3 of the Supporting Information.

Glass substrates of a size 13 × 13 mm^2 were cut from standard-sized microscope slides (75 × 26 mm^2), pre-cleaned with soap and water, and placed vertically into a substrate holder, which was subsequently immersed in Piranha solution (3:1 (v/v) conc. H_2SO_4/35 wt% H_2O_2) at 80 °C for 30 min. After removal, adhering Piranha solution was washed off by dipping the substrates into five consecutive baths of deionized water (Milli-Q, 18.2 MΩ·cm). To minimize salt stains and other evaporation residues, residual water was blown off the substrates by means of controlled blasts of nitrogen gas directed parallel to the substrates. After placing the substrates in a dust-free petri dish, final drying was accomplished in an oven at 120 °C for several hours. The same cleaning procedure was applied to the silicon substrates.

Film Preparation. Nanocomposite films were prepared by repeated spin coating of pre-mixed solutions of TiO_2 NPs and TE monomers. Prior to the spin coating, the allylcatechol-funtionalized TiO_2 NPs were filtered through a series of syringe filters (3.1 μm glass fiber, 0.45 μm PET, and 0.2 μm PTFE) to remove dust particles and large aggregates from the solution. The filtered solution was stored in a dust-free amber glass vial with a screw cap. The exact concentration of the filtered solution was calculated from the remaining mass of an evaporated 100 μL aliquot (after several hours of drying at 80 °C). The concentration was found to be c = 84 mg/mL. A thiol−ene monomer stock solution was prepared by mixing PETMP (2.4433 g, 5.00 mmol, 1.00 equiv), TAOTA (1.6626 g, 6.67 mmol, 1.33 equiv), and DMPA (0.0128 g, 0.05 mmol, 0.01 equiv) with toluene (40.0 mL). This mixture yielded a similar weight concentration as the NP solution ($c \approx$ 90 mg/mL). The TE monomer stock solution was also filtered through a 0.2 μm PTFE syringe filter. TE/TiO_2 nanocomposites with varying TiO_2 contents were realized by mixing the NP and monomer stock solutions in different ratios. For example, for a sample with 70 wt% TiO_2 content, a volume ratio of 7:3 (TiO_2 NP solution/TE monomer solution) was applied. The premixed solutions were then spin-coated to form nanocomposite films. Spin coating was performed using the dynamic dispense technique: first, the substrate was set to spin (acceleration: 5000 rpm/s) and allowed to reach a maximum speed of 5000 rpm; then, 30 μL of pre-mixed solution was quickly dispensed from a 200 μL pipette into the center of the substrate (spinning duration: 40 s). After spin coating, the samples were placed in a dust-free Petri dish and heated in an oven at 150 °C for 20 min to evaporate residual solvent. Subsequently, the Petri dish was placed under a UV lamp (366 nm, 8 W) for 5 min to ensure complete polymerization of the TE monomers. Each sequence of spin coating and post-treatment resulted in a film layer of ~100 nm thickness. The sequence was repeated multiple times to produce films of varying thicknesses to satisfy the requirements of the corresponding characterization techniques. For BLS characterization, which requires a film thickness of about 1 μm on a glass substrate, the nanocomposite films were fabricated by spin coating a total of 8 layers on top of each other. For the 3ω technique, which works fine with thin films on silicon substrates, a pair of samples, consisting of one and two layers, respectively, were fabricated for each composition.

Brillouin Light Spectroscopy. The sound velocities of the nanocomposite films were experimentally characterized by the Brillouin light scattering (BLS) spectroscopy.

BLS is a non-destructive and powerful tool to probe the hypersonic phonon propagation, which utilizes the scattering of an incident probing laser beam by phonons in a specific direction. The phonon wave vector, **q**, is determined by the scattering geometry as $\mathbf{q} = \mathbf{k_s} - \mathbf{k_i}$, where $\mathbf{k_s}$ and $\mathbf{k_i}$ are the wave vectors of the scattered and incident light, respectively. All BLS measurements in this study are conducted in the transmission geometry. In this geometry, the probing phonons propagate in the film plane, and the wavenumber, being independent of the refractive index, can be expressed as $q = \frac{4\pi}{\lambda}\sin\frac{\theta}{2}$,

where λ is the wavelength of the incident beam (i.e., 532 nm) and θ is the scattering angle. The inelastic interactions of the incident light with the activated phonons are represented by the frequency shift, $f(q)$, of the BLS spectra, which are resolved by a six-pass tandem Fabry−Pérot interferometer at the hypersonic frequency range. The longitudinal (VV) and transverse (VH) displacements are selected by the polarizations, where VV and VH represent vertically and horizontally polarized lasers with respect to the scattering plane, respectively.

3ω Method. A thin Cr/Au (5 nm/50 nm) electrode, 50 μm wide and 1 mm long, was deposited onto each TE/TiO_2 film using a metal mask and thermal evaporation. To carry out the 3ω measurement, an alternating current (AC) with a frequency of 1ω was applied to the Cr/Au electrode, which introduces a fluctuation of the temperature and consequently the electrical resistance of the electrode with a frequency of 2ω, when the temperature increase is sufficiently small. The temperature increase of the electrode can be calculated as $T_{2\omega} = 2\frac{\mathrm{d}T}{\mathrm{d}R}\frac{R}{V_{1\omega}}V_{3\omega}$, where R is the average electrical resistance of the Cr/Au electrode, $\mathrm{d}R/\mathrm{d}T$ is the temperature coefficient of the resistance, and $V_{1\omega}$ and $V_{3\omega}$ are the measured 1ω and 3ω voltages on the electrodes, respectively. To measure the out-of-plane thermal conductivity of the TE/TiO_2 film, a differential 3ω measurement was carried out. Two films with different thicknesses were used (see the inset of Figure 4.4a). When the half-width of the electrode is much larger than the thickness of the TE/TiO_2 film, but much smaller than the heat penetration depth, the heat transfer from the electrode, across the sample film, and into the Si substrate can be reasonably approximated as one-dimensional (1D). As a result, the thermal conductivity, k, of the TE/TiO_2 film can be calculated as $k = \frac{P \cdot h}{\Delta T_{2\omega} \cdot A_c}$, where P is the heating power, h is the thickness deference between thin and thick films, A_c is the cross-sectional area of the heat path, and $\Delta T_{2\omega}$ is the temperature difference between the thin and thick films.

4.4 Results and Discussion

4.4.1 Nanocomposite Films

The nanocomposite films were prepared on glass or silicon substrates by repeated spin coating of premixed solutions of TiO_2 NPs and TE monomers in the desired ratios. To chemically link the TiO_2 NPs to the TE polymer matrix, short bifunctional catecholic anchors (derived from eugenol, a natural odorant found in clove oil)[472] were first attached to the TiO_2 NPs, as illustrated in Figure 4.1a. This treatment is similar to the versatile catechol chemistry, which enables marine organisms (e.g., mussels) to adhere to virtually any surface.[473–475] The terminal double bonds at the other ends of the anchor molecules serve as connection points to the cross-linked TE network (see Figure 4.1b).[476] After spin coating and drying, the nanocomposite films were exposed to UV radiation (366 nm, 8 W) for 5 min. As the thermal diffusion time of each spin coating layer can be estimated to be on the order of 10−100 ns, the duration of UV exposure should be sufficient to ensure complete polymerization of the TE monomers.

The nanocomposite films were characterized by using scanning electron microscopy (SEM). Figure 4.1c,d shows two thick films supported on glass substrates and used in the BLS measurements. They contain 30 and 90 wt% of TiO_2 NPs, respectively, and both of them have a thickness around 1 μm. Figure 4.1e,f shows two thin films supported on Si substrates and used in the 3ω measurements. They contain 80 and 100 wt% of TiO_2 NPs, respectively. At a low weight fraction of TiO_2 NPs, the interfaces between consecutive spin-coated layers are discernible (see Figure 4.1c,e). At a large weight fraction of TiO_2 NPs, the interfaces become indistinguishable (see Figure 4.1d,f), leading to a homogeneous film. All nanocomposite films show some degree of surface roughness, especially for the thin films with a low weight fraction of TiO_2 NPs. Additional SEM images can be found in section 4.6.2 of the Supporting Information. Besides being used to check the uniformity and homogeneity of the nanocomposite films, the SEM images were also used to determine the film thicknesses.

We point out that some of the thin nanocomposite films have a relatively high level of roughness (see Figures 4.1e, S4.3b, S4.4c), which could be caused by the evaporation of the solvent in the drying process. Further studies are needed to understand the mechanisms and to optimize the fabrication parameters (e.g., UV light intensity, oven

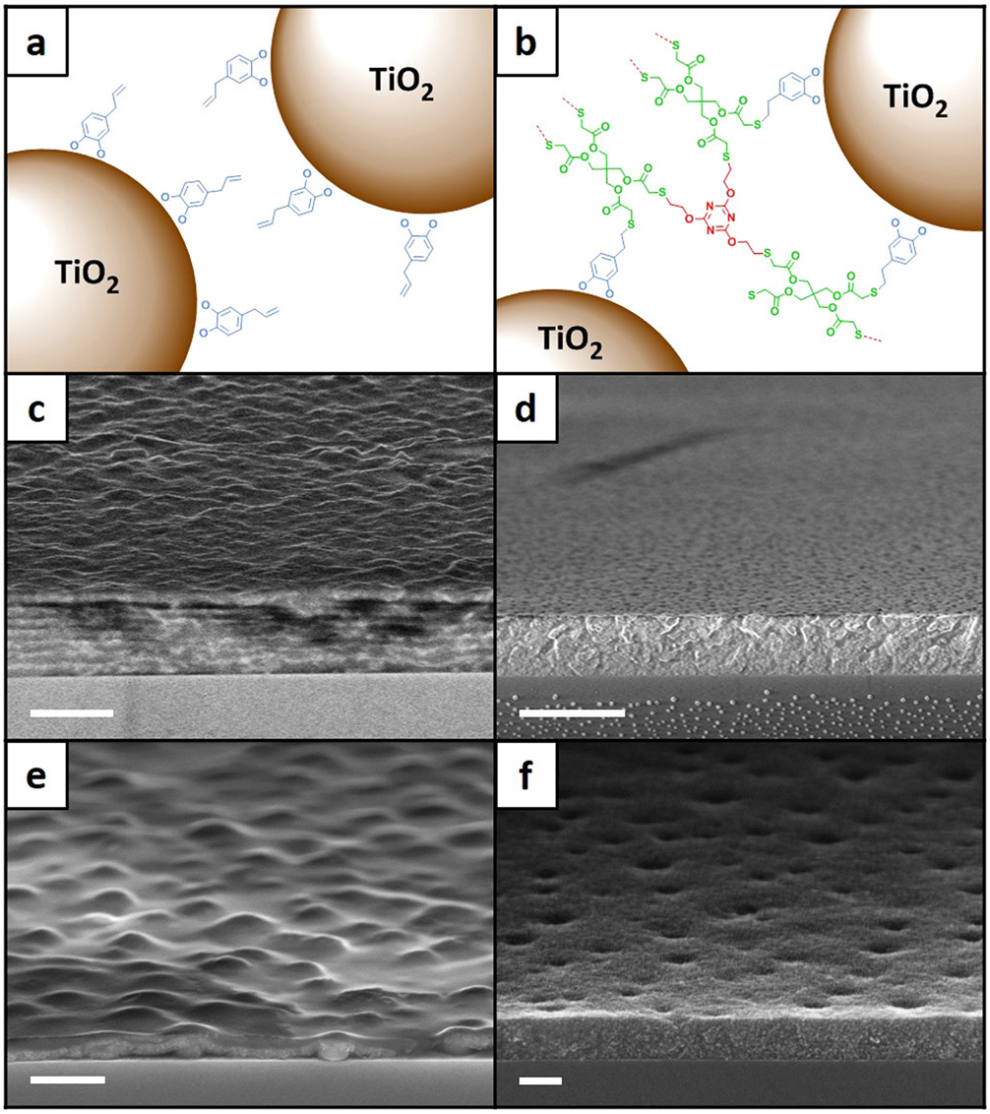

Figure 4.1. (a) Schematic of a pure TiO_2 NP film, where the surface-refunctionalized TiO_2 NPs are not cross-linked. (b) Schematic of a TE/TiO_2 nanocomposite film, where the surface re-functionalized TiO_2 NPs are covalently attached to the TE polymer network. (c) An eight-layer TE/TiO_2 nanocomposite film containing 30 wt% TiO_2 NPs. (d) An eight-layer TE/TiO_2 nanocomposite film containing 90 wt% TiO_2 NPs. (e) A two-layer TE/TiO_2 nanocomposite film containing 40 wt% TiO_2 NPs. (f) A two-layer TiO_2 NP film containing 100 wt% TiO_2 NPs. (c) and (d) are supported on glass substrates and used in the BLS measurements. (e) and (f) are supported on Si substrates and used in the 3ω measurements. The scale bars are (c) 1 μm, (d) 2 μm, (e) 500 nm, and (f) 100 nm.

temperature) to achieve a lower level of roughness. Nevertheless, in the thermal conductivity measurements, the roughness effect should be insignificant, as we always used two films with different thicknesses (see Figure 4.4a); for the BLS experiments, thick films were employed.

4.4.2 Elastic Longitudinal Modulus

All films used in the BLS experiments consisted of 8 consecutive layers to achieve thicknesses about 1 µm, except for the thick bulk TE films used for depolarized BLS measurements. This thickness is required to ensure a linear acoustic behavior[477] for in-plane phonon propagation by fulfilling the condition, $q \cdot h >> 1$, where q is the wavenumber and h is the film thickness. As the elastic properties of the bulk TE and TiO_2 NPs are necessary information for understanding the mechanical behaviors of the nanocomposites, the bulk TE and TiO_2 NP films were first examined. The BLS spectra of these films were recorded at a given q = 0.01355 nm^{-1} in the polarized (for both the bulk TE and TiO_2 NP films) and depolarized light polarizations (for the bulk TE film only), as shown in Figure 4.2a. The single Lorentzian representation of the BLS spectra indicated a homogeneous medium in both the bulk TE and TiO_2 NP films prepared by the spin coating method, as also confirmed by the SEM images in Figure 4.1f for the latter. Note that for spatially inhomogeneous polymer nanocomposites, two acoustic phonons at a given q can be observed.[478] Due to the cross-linked TE network, the bulk TE film displays measurable depolarized BLS spectra, allowing for the measurement of the transverse sound velocity, c_T. This transverse mode in the depolarized spectra is only measured in the thick bulk TE films, as the mode is too weak to be detected in the other thin nanocomposite films. The frequency, f, obtained from the Lorentzian peaks increases linearly with the wavenumber, q, as seen in Figure 4.2b and expected for acoustic phonon propagation.

The sound velocities, $c = \frac{d\omega}{dq} = \frac{2\pi df}{dq}$, obtained from the slope of the linear relations, $f(q) \sim q$, are $c_{L,\,TE}$ = 2480 ± 12 m/s and $c_{T,\,TE}$ = 1000 ± 15 m/s for the pure TE thin film, and $c_{L,\,TiO_2}$ = 3070 ± 30 m/s for the pure TiO_2 NP thin film; the subscripts, L and T, stand for longitudinal and transverse modes, respectively. Based on the $c_{L,\,TE}$ and $c_{T,\,TE}$, the Poisson's ratio, $\nu = \frac{x-2}{2(x-1)}$ with $x = \left(\frac{c_{L,\,TE}}{c_{T,\,TE}}\right)^2$, turns out to be about 0.4, and thus suggests a weakly cross-linked and soften matrix. The relatively low $c_{L,\,TiO_2}$ compared with the value for bulk crystalline anatase TiO_2 film (with a longitudinal sound velocity of around 8880 m/s)[479] could be attributed to the granular structure of the TiO_2 NP film. Similar to the BLS spectra of the bulk TE and TiO_2 NP films, the BLS spectra of the nanocomposite film with 30 wt% of TiO_2 NPs show a single longitudinal mode (see

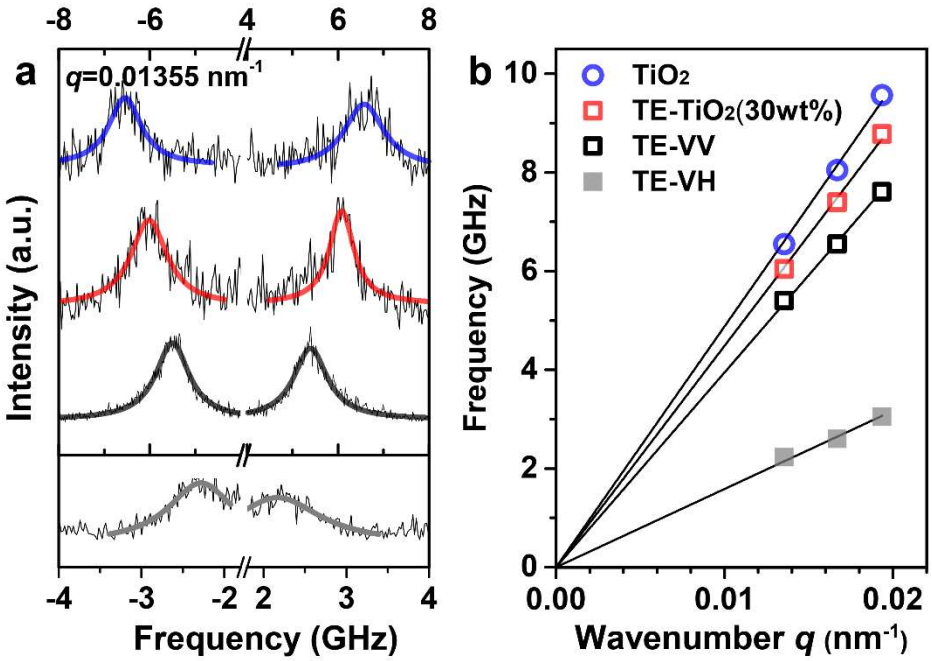

Figure 4.2. (a) Brillouin light scattering (BLS) spectra for in-plane phonon propagation at q = 0.01355 nm^{-1}. The polarized spectra (in the range of −8 to 8 GHz) are represented by single Lorentzian peaks for the bulk TE polymer (black line), a TE/TiO_2 nanocomposite with 30 wt% TiO_2 NPs (red line), and the pure TiO_2 NP film (blue line). The depolarized BLS spectrum of the bulk TE (in the range of −4 to 4 GHz) is also represented by a single Lorentzian peak (gray line), indicating a weak cross-linked structure of the TE matrix. (b) The phonon dispersion relations for these three compositions (shown with the same colors) are linear, $f(q) \sim q$, as indicated by the four black lines.

Figure 4.2a), suggesting a homogeneous medium.[478] The corresponding longitudinal effective medium sound velocity, $c_{L,\,eff}$, estimated from the linear dispersion relation (see Figure 4.2b) of the film, is 2820 ± 20 m/s, which falls between the sound velocities of the pure TE and TiO_2 NP films.

To gain more insights, the sound velocities were represented by Wood's law[480,481] as

$$\frac{1}{M_{L,\,eff}} = \frac{\phi_{TiO_2}}{M_{L,\,TiO_2}} + \frac{1-\phi_{TiO_2}}{M_{L,\,TE}} \tag{4.1}$$

which can be combined with $M_L = \rho c_L^2$, $\rho_{eff} = \rho_{TiO_2}\phi_{TiO_2} + \rho_{TE}\left(1-\phi_{TiO_2}\right)$, and $\phi_{TiO_2} = \left(\rho_{TE} w_{TiO_2}\right) / \left(\rho_{TE} w_{TiO_2} + \rho_{TiO_2}\left(1-w_{TiO_2}\right)\right)$ to give

$$c_{\mathrm{L,\,eff}} = \frac{c_{\mathrm{L,\,TiO_2}}\, c_{\mathrm{L,\,TE}} \left[\rho_{\mathrm{TE}} w_{\mathrm{TiO_2}} + \rho_{\mathrm{TiO_2}}\left(1 - w_{\mathrm{TiO_2}}\right)\right]}{\left[\rho_{\mathrm{TE}}^2\, c_{\mathrm{L,\,TE}}^2\, w_{\mathrm{TiO_2}} + \rho_{\mathrm{TiO_2}}^2\, c_{\mathrm{L,\,TiO_2}}^2\left(1 - w_{\mathrm{TiO_2}}\right)\right]^{0.5}} \tag{4.2}$$

Here, M is the longitudinal modulus, and $\phi_{\mathrm{TiO_2}}$ and $w_{\mathrm{TiO_2}}$ are the volume and weight fractions of the TiO_2 NPs, respectively. In the least-squares fitting with eq 4.2, which expresses $c_{\mathrm{L,\,eff}}$ as a function of $\phi_{\mathrm{TiO_2}}$, the following materials properties were fixed: ρ_{TE} = 1000 kg/m^3 and $c_{\mathrm{L,\,TE}}$ = 2480 m/s, whereas $\rho_{\mathrm{TiO_2}}$ and $c_{\mathrm{L,\,TiO_2}}$ were treated as fitting parameters. The experimental $c_{\mathrm{L,\,eff}}$ data are shown in Figure 4.3a, which also includes the best fit with $\rho_{\mathrm{TiO_2}}$ = 870 kg/m^3 and $c_{\mathrm{L,\,TiO_2}}$ = 3650 m/s, and another fit with the bulk TiO_2 film values, $\rho_{\mathrm{TiO_2}}$ = 3900 kg/m^3 and $c_{\mathrm{L,\,TiO_2}}$ = 8880 m/s. It is surprising that such a low $\rho_{\mathrm{TiO_2}}$ (even lower than ρ_{TE}) is needed to capture the experimental composition dependence of the effective medium sound velocity with Wood's law. To check whether the TiO_2 NPs are porous, XRD measurements were conducted to analyze their crystallinity. The X-ray diffraction pattern shown in Figure S4.2, however, confirms that the TiO_2 NPs are indeed crystalline, without pores inside. We note that in a previous report on the sound velocity of PMMA/$BaTiO_3$ nanocomposites,[444] a $c_{\mathrm{L,\,eff}}$ trend in better agreement with Wood's law was observed. If $\rho_{\mathrm{TiO_2}}$ is fixed at 3900 kg/m^3 and $c_{\mathrm{L,\,TiO_2}}$ at 8880 m/s, the trend of the fitted curve deviates from the experimental data, but shows a similar trend with the results for the PMMA/$BaTiO_3$ nanocomposites.[444] The surprisingly low $\rho_{\mathrm{TiO_2}}$, required to represent the experimental $c_{\mathrm{L,\,eff}}$, could be attributed to the specific interfacial effects (i.e., covalent cross-linking) in this polymer nanocomposite. Figure 4.3b shows the variation of the effective elastic longitudinal modulus with the weight fraction of TiO_2 NPs. It is seen that $M_{\mathrm{L,\,eff}}$ increases monotonically from 6.2 to 37.5 GPa, as the weight fraction of TiO_2 NPs increases from 0 to 90%. Note that $\rho_{\mathrm{TiO_2}}$ = 3900 kg/m^3 was used to calculate ρ_{eff} in the calculations of $M_{\mathrm{L,\,eff}}$.

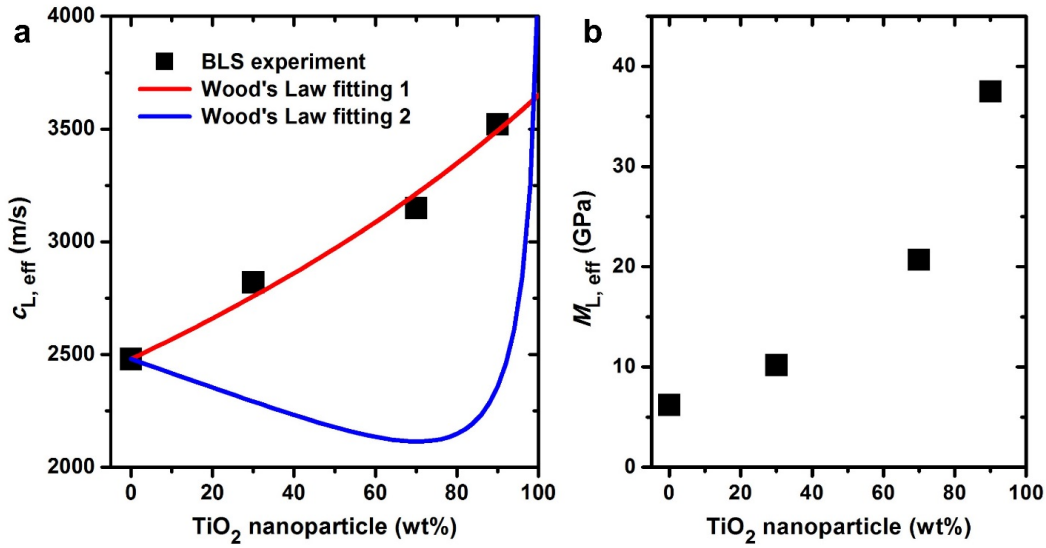

Figure 4.3. (a) Effective longitudinal sound velocity of the TE/TiO_2 nanocomposites at varying weight fractions of TiO_2 NPs. The Wood's law fitting based on eq 4.2 was conducted with two sets of adjustable values of the density and sound velocity of TiO_2 (red line: ρ_{TiO_2} = 870 kg/m^3 and $c_{L,\,TiO_2}$ = 3650 m/s; blue line: ρ_{TiO_2} = 3900 kg/m^3 and $c_{L,\,TiO_2}$ = 8880 m/s). (b) Computed effective elastic longitudinal modulus of the TE/TiO_2 nanocomposites as a function of the weight fraction of TiO_2 NPs (see text).

4.4.3 Thermal Conductivity

The cross-plane thermal conductivities of the TE/TiO_2 nanocomposite films were measured with the differential 3ω method.[466] To eliminate the effects of the interfacial thermal resistances (i.e., between the Cr/Au electrode and TE/TiO_2 film, and between the TE/TiO_2 film and the silicon wafer) and the thermal resistance of the silicon substrate, two TE/TiO_2 samples with different thicknesses (e.g., h_1 and h_2; $h_1 < h_2$) were fabricated (see Figure 4.4a). The temperature vs. AC frequency responses of the two samples can be used to calculate the thermal conductivity corresponding to a film of thickness ($h_2 - h_1$) (refer to the Methods section 4.3 for more details). The experimental thermal conductivities are shown in Figure 4.4b, as a function of the TiO_2 NP weight fraction. For the pure TE film, the measured thermal conductivity (0.04 W/m·K) is lower than the typical values (0.1−0.3 W/m·K)[443] of amorphous polymers. With increasing fraction of the TiO_2 NPs, the thermal conductivity of the nanocomposite increases monotonically and for the 100 wt% TiO_2 NP film, it reaches 1.0 ± 0.3 W/m·K, comparable to that of amorphous TiO_2 thin films and TiO_2 NPs.[482,483]

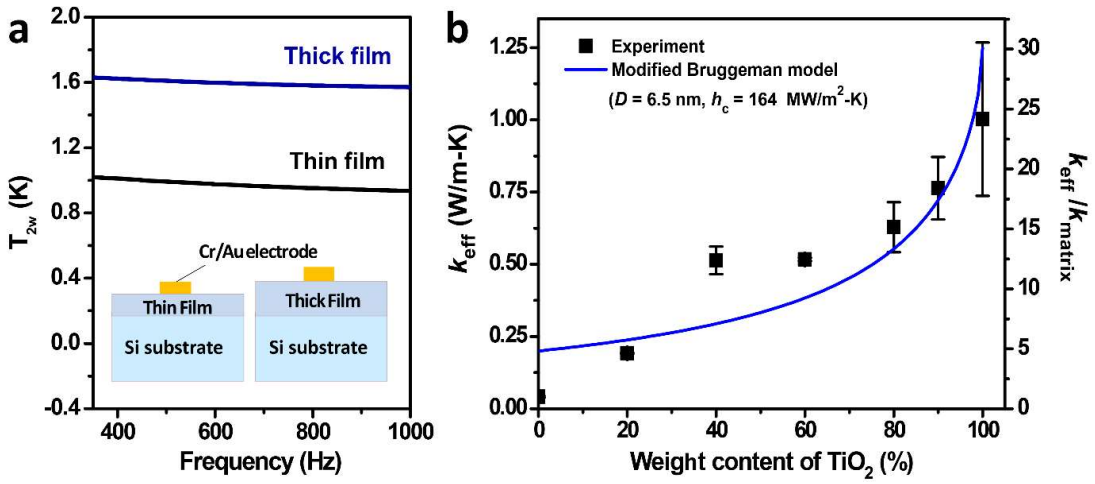

Figure 4.4. Effective thermal conductivity of TE/TiO_2 nanocomposites at varying weight fractions of TiO_2 NPs. The experimental data from the 3ω measurements (solid circles) are represented (blue solid line) by a modified Bruggeman model (eq 4.3).

The thermal conductivities were fitted with a modified Bruggeman model[484,485] as

$$\left(1-\phi_{\mathrm{TiO_2}}\right)^3 = \left(\frac{k_{\mathrm{TE}}}{k_{\mathrm{eff}}}\right)^{(1+2\alpha)/(1-\alpha)} \left(\frac{k_{\mathrm{eff}} - k_{\mathrm{TiO_2}}(1-\alpha)}{k_{\mathrm{TE}} - k_{\mathrm{TiO_2}}(1-\alpha)}\right)^{3/(1-\alpha)} \tag{4.3}$$

where $\alpha = 2k_{\mathrm{TE}}/(Dh_{\mathrm{c}})$ is a parameter depending on the thermal conductivity of the TE matrix (k_{TE}), the diameter of the TiO_2 NPs (D), and the interfacial thermal conductance (h_{c}) between the TiO_2 NPs and the TE matrix. This model by definition takes into account the interactions between the NPs and the matrix, as well as the effect of the interfacial thermal resistance. In the fitting, the following parameters were adopted:[483] D = 6.5 nm, k_{TE} = 0.2 W/m·K, and $k_{\mathrm{TiO_2}}$ = 2.0 W/m·K. Note that the thermal conductivity of the TE matrix is set as that of a typical polymer, instead of the experimentally measured value for the pure TE film. Based on the representation of the experimental data shown in Figure 4.4b, the thermal conductivity trend is well captured, confirming the good predictability of the model for the thermal conductivity of composites with high particle filling fractions.[484,485] From the best fit, the interfacial thermal conductance was determined to be 164 MW/m^2·K, which falls in the range of 10^7–10^8 W/m^2·K for typical interfacial thermal conductances between organic/inorganic interfaces.[449,486] Since the

TiO_2 NPs are covalently linked to the TE polymer matrix, this relatively high interfacial thermal conductance is expected.

By comparing the relative increases of the sound velocities in Figure 4.3a and the thermal conductivities in Figure 4.4b, it is seen that as the weight fraction of the TiO_2 NPs increases from 0 to 90%, the $c_{L,\,eff}$ increases by around 40%, but the k_{eff} increases by a factor of 18. From the kinetic theory of thermal conductivity, it is known that $k_{eff} = \frac{1}{3} C_{eff}\, v_{g,\,eff}\, \Lambda_{eff}$, where C_{eff}, $v_{g,\,eff}$, and Λ_{eff} are the effective specific heat, phonon group velocity, and phonon mean free path, respectively. Since the specific heat of polymers is typically around 1000 J/kg·K[487] and the heat capacity of TiO_2 NPs with a diameter of 6.5 nm is 850 J/kg·K[488] (obtained from extrapolation), the change in the effective specific heat caused by increasing the weight fraction of TiO_2 NPs is expected to be insignificant. For the effective phonon group velocity, it can be reasonably assumed to be equal to the sound velocity and thus increases by 42% as the weight fraction of the TiO_2 NPs increases from 0 to 90%. Therefore, the increase of the thermal conductivity with the increasing TiO_2 NP weight fraction is primarily due to the increase in the effective mean free path. In fact, it has been shown that at high filling fractions, conductive channels could be formed by the NPs to allow for effective thermal transport (the so-called percolation phenomenon).[485,489]

4.5 Conclusion

This study investigates the elastic modulus and thermal conductivity of thiol-ene/TiO_2 nanocomposite thin films with varying weight fractions of TiO_2 NPs by using Brillouin light spectroscopy and 3ω measurements, respectively. The effective elastic longitudinal moduli of the films are found to increase with the weight fraction of the TiO_2 NPs, from 6.2 GPa at 0 wt% of TiO_2 NPs to 37.5 GPa at 90 wt% of TiO_2 NPs. The corresponding effective thermal conductivity shows a much more significant increase, from 0.04 to 0.76 W/m·K (by a factor of 18). The increase of the modulus is not predicted by the effective medium model, probably due to the specific interactions between the components of the nanocomposite. The strong composition dependence of the effective thermal conductivity can be captured by the effective medium model by using a physically meaningful interfacial thermal conductance. However, the relation between

the thermal conductivity and sound velocity is found to be nonlinear, in contrast to the linear relation observed in amorphous polymers. The pronounced enhancement of the effective thermal conductivity could be ascribed to the addition of high thermal conductivity TiO_2 NPs and the formation of possible conductive channels at high TiO_2 NP weight fractions.

4.6 Supporting Information

4.6.1 NP Characterization

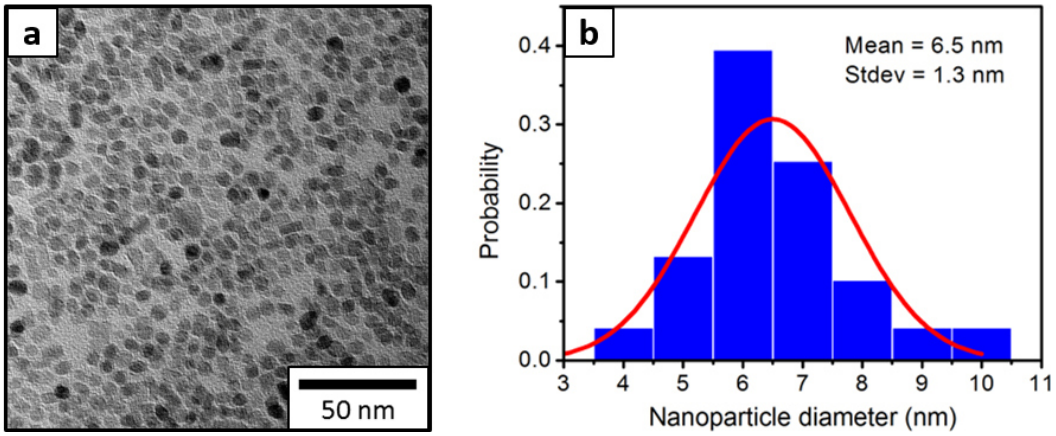

Figure S4.1. (a) A representative TEM image and (b) the corresponding diameter distribution of the as-synthesized TiO_2 NPs.

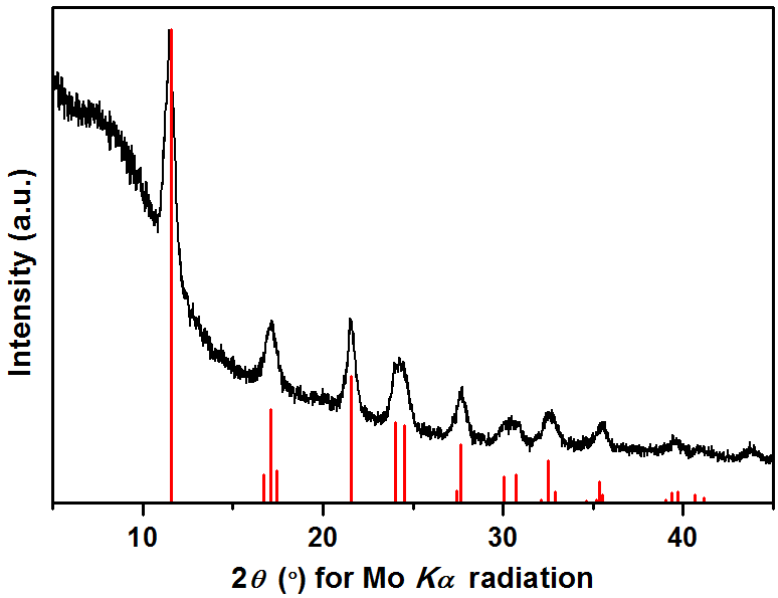

Figure S4.2. X-ray powder diffractogram of TiO_2 NPs (black curve), matching the standard TiO_2 anatase diffraction lines (in red).

4.6.2 Additional SEM Images of Nanocomposite Films

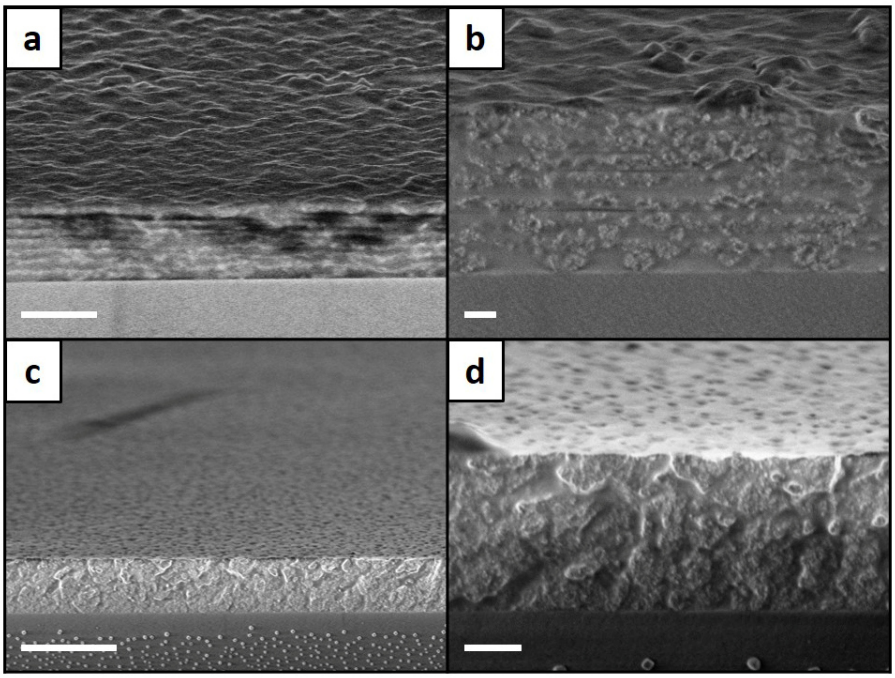

Figure S4.3. (a) An eight-layer TE/TiO_2 nanocomposite film containing 30 wt% TiO_2 NPs. (b) A close-up view of (a). (c) An eight-layer TE/TiO_2 nanocomposite film containing 90 wt% TiO_2 NPs. (d) A close-up view of (c). The films are supported on glass substrates and used in the BLS measurements. The scale bars are (a) 1 μm, (b) 200 nm, (c) 2 μm, and (d) 400 nm.

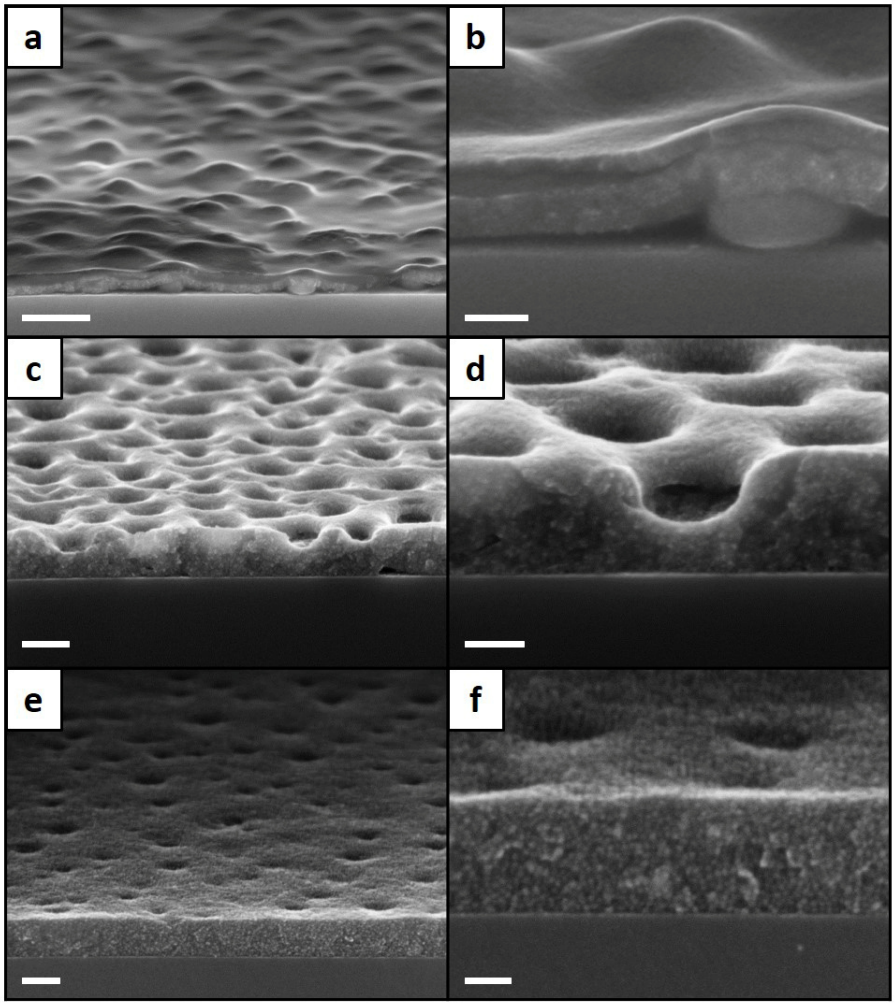

Figure S4.4. (a) A two-layer TE/TiO_2 nanocomposite film containing 40 wt% TiO_2 NPs. (b) A close-up view of (a). (c) A two-layer TE/TiO_2 nanocomposite film containing 80 wt% TiO_2 NPs. (d) A close-up view of (c). (d) A two-layer TiO_2 nanoparticle film containing 100 wt% TiO_2 NPs. (f) A close-up view of (e). The films are supported on Si substrates and used in the 3ω measurements. The scale bars are (a) 500 nm, (b) 100 nm, (c) 200 nm, (d) 100 nm, (e) 100 nm, and (f) 40 nm.

4.6.3 Synthetic Procedures

Materials. Unless otherwise stated, all chemicals were obtained from commercial suppliers and used without further purification. All solvents (*N*,*N*-dimethylformamide (DMF), diethyl ether (Et_2O), methanol (MeOH), *n*-hexane, toluene) and standard reagents (hydrochloric acid (HCl, 37 wt%), sodium chloride (NaCl)) were purchased from Sigma-Aldrich and Fisher Scientific. Eugenol (99%) and lithium chloride (LiCl, 99%) were obtained from Sigma-Aldrich.

Synthesis of 4-Allylcatechol. 4-Allylcatechol was synthesized as previously reported in the literature,[472] but with strongly modified work-up procedure. A 1 L three-necked round-bottom flask, fitted with a reflux condenser and a large magnetic stirring bar, was charged with DMF (400 mL), eugenol (37.0 mL, 39.6 g, 0.24 mol, 1 equiv), and LiCl (30 g, 0.71 mol, 3 equiv). The mixture was heated at reflux, yielding a yellow solution. Reflux was maintained for a total of 39 h, while additional portions of LiCl (30 g, 0.71 mol, 3 equiv) were added after 3 h, 19 h, and 26 h, eventually yielding a brown solution, which solidified upon cooling to room temperature. The crude product was then hydrolyzed by addition of diluted HCl (370 mL of distilled water and 110 mL of concentrated (37 wt%) HCl), while the mixture was cooled in an ice bath and stirred until a homogeneous solution was obtained. The aqueous solution was transferred to a 1 L separatory funnel and extracted with Et_2O (3 × 300 mL). The combined organic layers were concentrated by rotary evaporation to a volume of about 100 mL. Residual DMF was removed by repeated cycles of extraction with half-saturated NaCl solution (4 × 50 mL). The solvent was removed under reduced pressure with a rotary evaporator to afford a crude brown oil. The crude oil was then diluted in a mixture of distilled water (75 mL) and MeOH (25 mL) and extracted many times with *n*-hexane (10 × 50 mL) to remove residual, unreacted eugenol. The solvent was again removed under reduced pressure with a rotary evaporator to afford a crude brown oil. Finally, the crude oil was distilled under high vacuum using a short-path distillation head. The pure colorless product distilled at 80 °C (1×10^{-2} mbar), yielding a total amount of 18.5 g (53%) of 4-allylcatechol. The liquid product crystallized in the receiving flask during distillation (Mp: 48 °C).

Refunctionalization of TiO_2 NPs. To a solution of TiO_2 NPs (370 mg) in *n*-hexane (15 mL, c = 25 mg/mL) was added a solution of 4-allylcatechol (1.0 g,

6.7 mmol) in MeOH (10 mL). The biphasic reaction mixture was sonicated at 40 °C for 15 min. After cooling to room temperature, the allylcatechol-functionalized NPs accumulated in the red-colored upper hexane phase. The lower (methanolic) phase was discarded and the NPs in the hexane phase were precipitated by addition of an excess amount of MeOH. The brown precipitate was isolated by centrifugation (9000 rpm, 10 min) and redissolved in toluene (3 mL). The NPs were further purified by repeated precipitation and dissolution steps (3 × 40:3 mL of MeOH/toluene).

5

Conclusions and Outlook

Showing great potential for sustainable applications, while being readily available and non-toxic, TiO_2 has been one of the most studied oxide nanomaterials in the past few decades. In order to tailor TiO_2 NPs to their potential applications, a thorough understanding and control of their surface chemistry is required. One promiment approach to extend the surface functionality of TiO_2 NPs is their modification with strongly binding and photo-sensitive catechol anchor molecules.

It was the aim of this thesis to use the TiO_2/catechol system to unravel the basic surface chemistry and to exploit this knowledge in applications of photocatalysis and nanocomposites.

The first part of the thesis was fully devoted to the investigation of the surface processes taking place, when hydrophobic oleate-stabilized TiO_2 NPs are reacted with pyrocatechol, the unsubstituted prototype of all catecholic molecules. A broad set of NMR tools (1D and 2D, ^{1}H and ^{13}C, solution and solid state) was utilized in order to gain direct insight into the ligand spheres of native, oleate-stabilized TiO_2 NPs and their catechol-modified counterparts. The main objective of this study was to quantify the surface coverage of the incoming catechol ligand and the displacement of the native oleate ligand. It came as a surprise that catechol was not able to displace more than 20% of the native oleate ligand shell. In sum, the ligand density increased from the native value of 2.3 oleate molecules per nm^2 to 4.8 molecules per nm^2 of a mixed ligand shell. Consequently, incoming catechol must preferably adsorb to unoccupied Ti surface sites before displacing a minor part of the native ligand shell. The adsorption of catechol was successfully described by a Langmuir isotherm, while the desorption of oleate exhibited

Arrhenius-like behavior. An extension of this study to other catecholic ligands with apolar backbones, such as 4-*tert*-butylcatechol and 2,3-dihydroxynaphthalene, revealed very similar pictures of mixed ligand shells. The three catechol species showed only small differences in their adsorption behaviors which correlated well with their Brønsted acidity. Due to the incomplete displacement of the native ligand shell, this kind of surface reaction should not be referred to as ligand exchange, substitution, or replacement, but simply as surface modification. In general, surface modification of hydrophobic TiO_2 NPs with catecholic ligands exhibiting apolar backbones results in the formation of mixed ligand shells. The effect of polar ring substituents (such as the nitro moiety or charged groups) on displacement of oleate remains to be investigated in further quantitative studies.

The second part of the thesis gives a preview on how the displacement characteristics on hydrophobic TiO_2 NPs change when a charged group in introduced into the catecholic anchor molecule. Here, a special molecule, 6,7-dihydroxy-2-methylisoquinolinium chloride (DHMIQ), was specifically designed to incorporate the essential features of a group of powerful homogeneous photocatalysts. These features include (i) an extended aromatic system and (ii) a cationic quaternary ammonium group. The objective of this study was to combine the photocatalytic benefits of organic and inorganic components for synergistic effects in photocatalyzed reactions. Contrary to the formation of mixed ligand shells with apolar catecholic molecules, the cationic species succeeded in displacing the native ligand shell entirely, thus rendering the resulting TiO_2−DHMIQ NPs soluble in water. The ligand density was found to be 2.0 DHMIQ molecules per nm^2. Due to the strong electronic coupling between the catecholic anchor and surface Ti sites, the attachment of DHMIQ causes sensitization of the TiO_2 NPs over the whole visible range and even extending into the NIR region. To exploit this extended spectral response for photocatalysis, TiO_2−DHMIQ NPs were employed as a panchromatic photocatalyst in the oxidative photocyanation of tertiary amines. Using tributylamine as a model substrate, the cyanated product was obtained in nearly quantitative yield upon irradiation with blue light of 462 nm wavelength for a few hours. The conversion decreased with increasing excitation wavelength (green, yellow, red), but the TiO_2−DHMIQ photocatalyst was still able to promote the reaction even under NIR excitation at 730 nm. At such low excitation energies neither the native TiO_2 NPs nor the DHMIQ photosensitizer showed any conversion on their own. The lower conversion

efficiencies at higher excitation wavelengths could be compensated for by using longer irradiation times. The results from the TiO_2−DHMIQ photocatalyst system confirm that catechol sensitization of TiO_2 NPs is a promising way to enhance solar light harvesting capabilities, thus improving the overall yield in photocatalytic reactions. Furthermore, this study may serve as a blueprint for further photocatalyzed oxidative transformations.

In the third part of the thesis, TiO_2 NPs were equipped with 4-allylcatechol, a catecholic anchor bearing a terminal double bond that allowed covalent attachment of the NPs into thiol−ene polymer matrices. The resulting thiol−ene/TiO_2 nanocomposite materials were fabricated as thin films with varying inorganic filler fraction in order to investigate its effect on mechanical and thermal properties of the nanocomposite. These two properties were characterized in terms of the elastic modulus and thermal conductivity of the thin film composites, which in turn were determined by Brillouin light scattering spectroscopy and 3ω measurements, respectively. It was found that both quantities, elastic modulus and thermal conductivity, increased with increasing TiO_2 mass fraction. The effective elastic longitudinal moduli of the films increased from 6.2 GPa at 0 wt% of TiO_2 NPs to 37.5 GPa at 90 wt% of TiO_2 NPs (by a factor of 6). In the same range, the effective thermal conductivity increased even more significantly, from 0.04 to 0.76 W/m·K (by a factor of 18). The increase in elastic modulus is attributed to covalent cross-linking of the nanocomposite constituents, while the increase in thermal conductivity can be rationalized by the addition of a high-conductivity filler in the form of nanoparticulate TiO_2. Unlike blends of amorphous polymers, which show a linear relation between thermal conductivity and sound velocity, thiol−ene/TiO_2 nanocomposites exhibit a nonlinear relation. Hybrid nanocomposites, such as the present thiol−ene/TiO_2 system, find diverse applications as functional materials. By tailoring their mechanical properties, thiol−ene/TiO_2 nanocomposites are promising candidates for dental restorative materials. Due to their tunable thermal conductivity, they might also be useful in thermal applications, e.g. for heat removal purposes.

In conclusion, catechol-functionalized TiO_2 NPs have served as a versatile platform for the study of their fundamental surface chemistry and their benefits in promising applications in the fields of photocatalysis and nanocomposites. The general findings from these studies may also prove valuable in related research topics, such as dye-sensitized solar cells or photocatalytic degradation of pollutants.

A

Appendix

A.1 Additional NMR Spectra

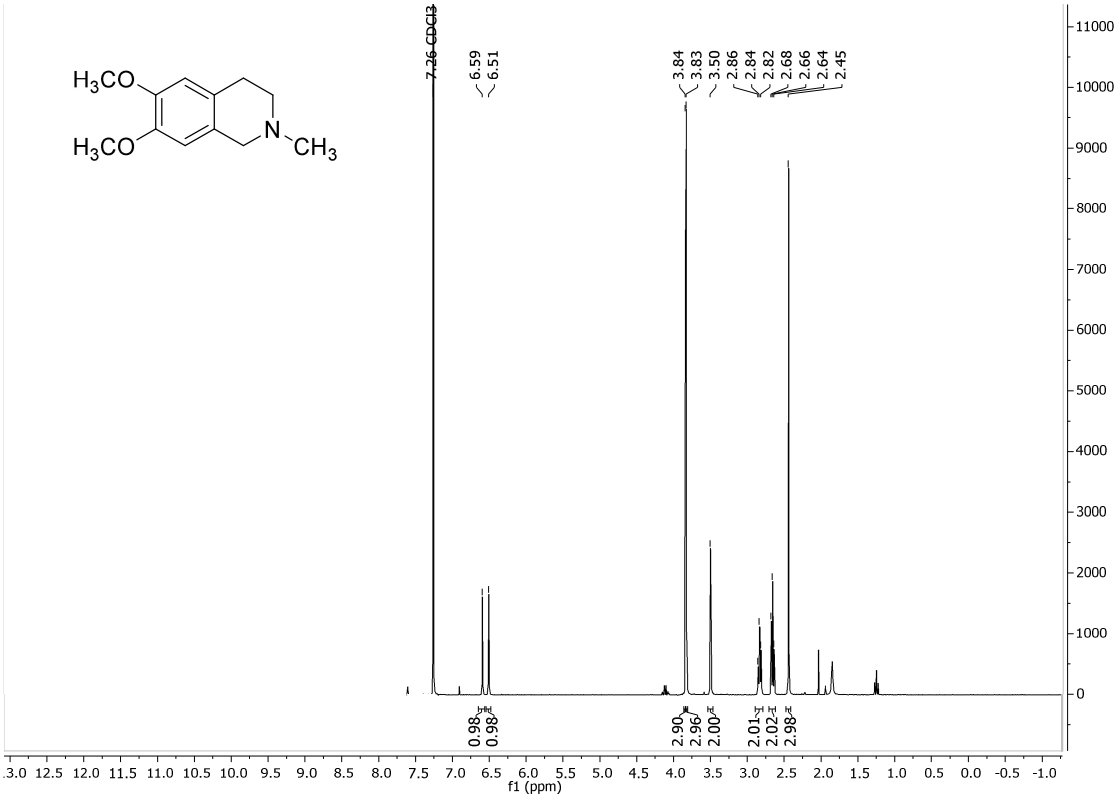

Figure A.1. ^{1}H NMR spectrum (300 MHz, $CDCl_3$) of 6,7-dimethoxy-2-methyl-1,2,3,4-tetrahydroisoquinoline (**2**).

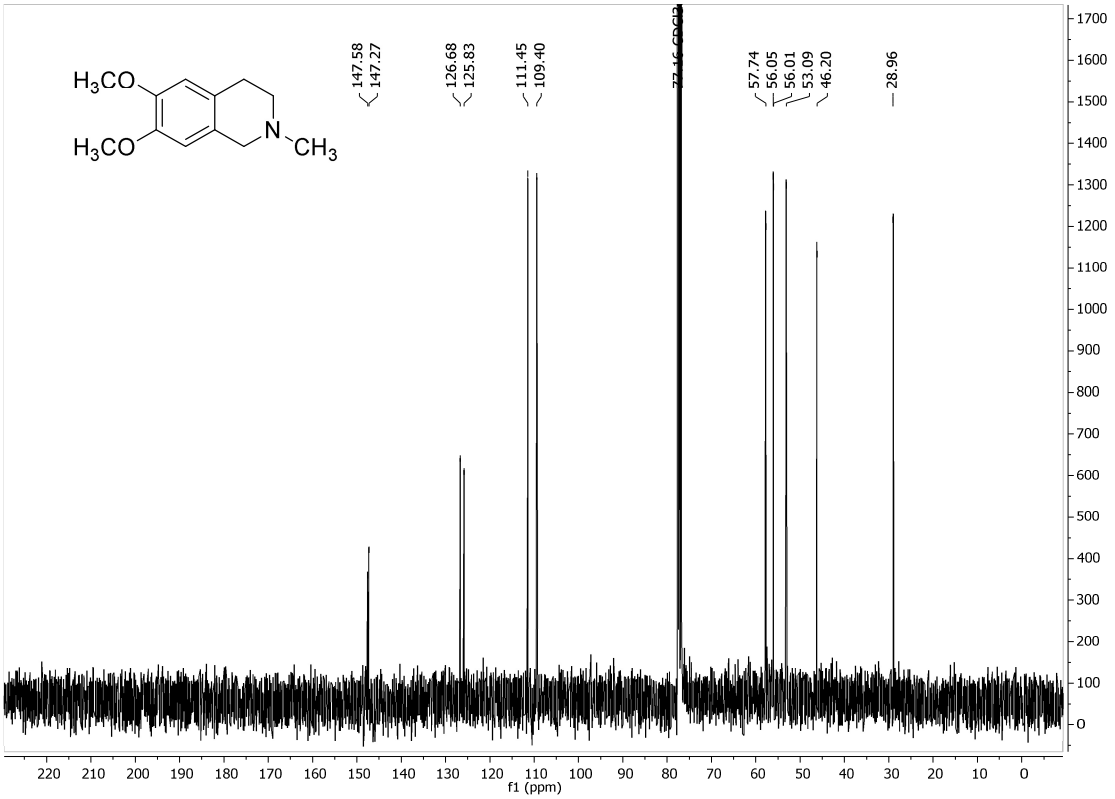

Figure A.2. ^{13}C NMR spectrum (75 MHz, $CDCl_3$) of 6,7-dimethoxy-2-methyl-1,2,3,4-tetrahydroisoquinoline (**2**).

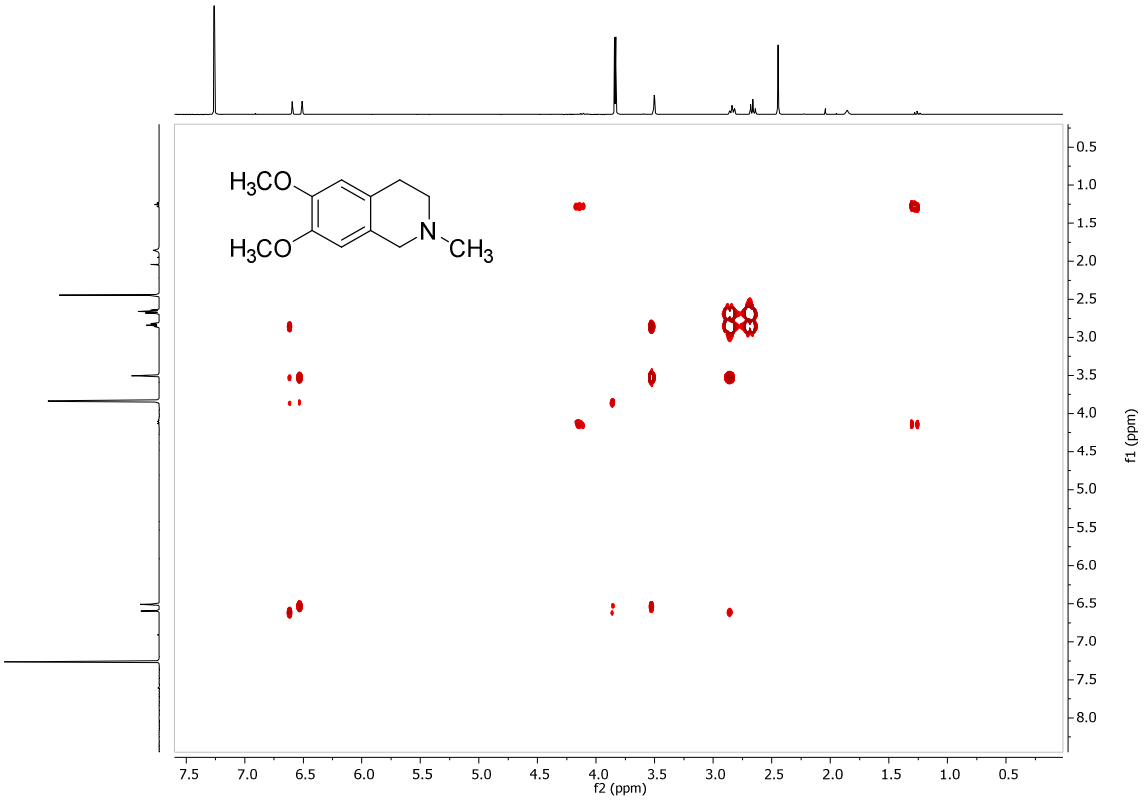

Figure A.3. COSY spectrum ($CDCl_3$) of 6,7-dimethoxy-2-methyl-1,2,3,4-tetrahydroisoquinoline (**2**).

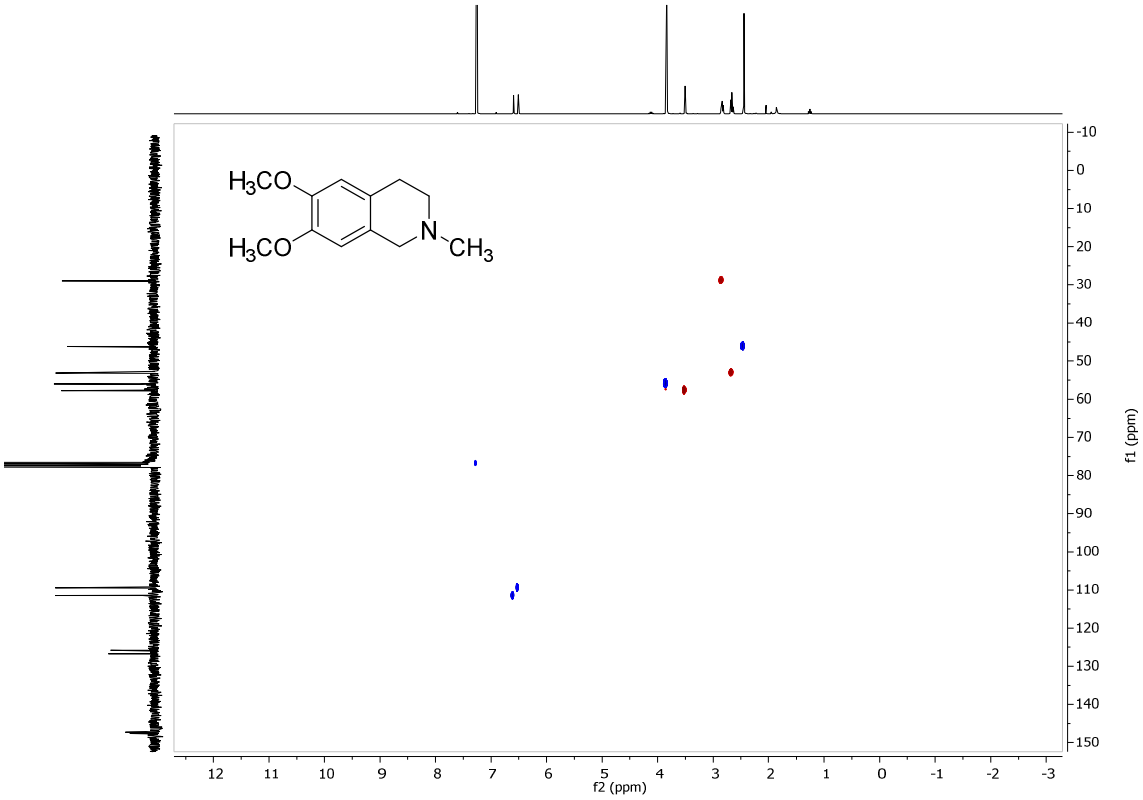

Figure A.4. HSQC spectrum ($CDCl_3$) of 6,7-dimethoxy-2-methyl-1,2,3,4-tetrahydroisoquinoline (**2**).

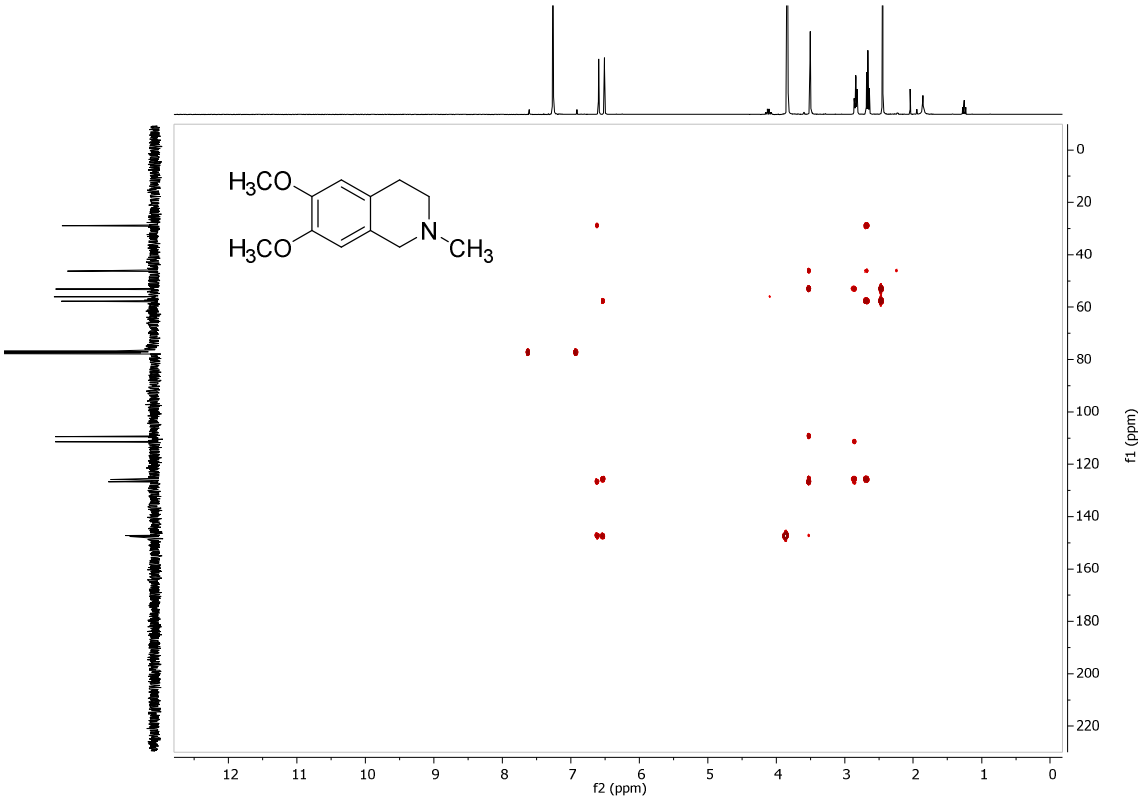

Figure A.5. HMBC spectrum ($CDCl_3$) of 6,7-dimethoxy-2-methyl-1,2,3,4-tetrahydroisoquinoline (**2**).

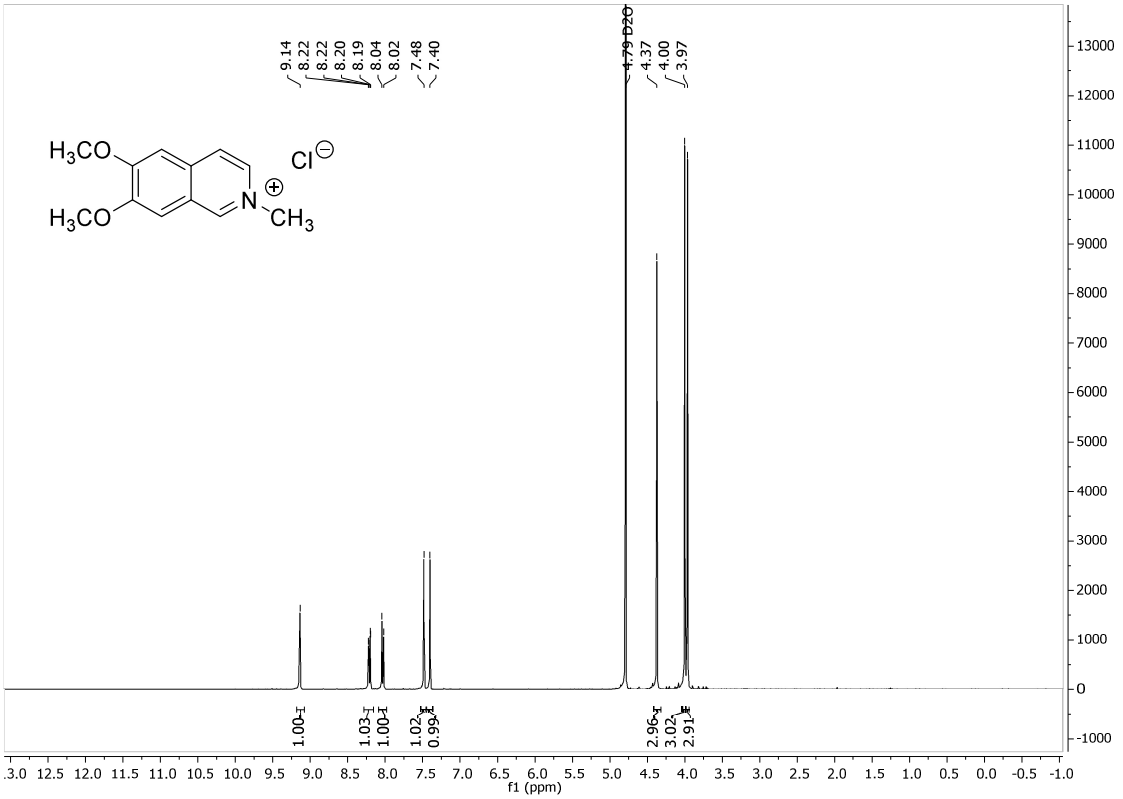

Figure A.6. ^{1}H NMR spectrum (300 MHz, D_2O) of 6,7-dimethoxy-2-methylisoquinolinium chloride (**3**).

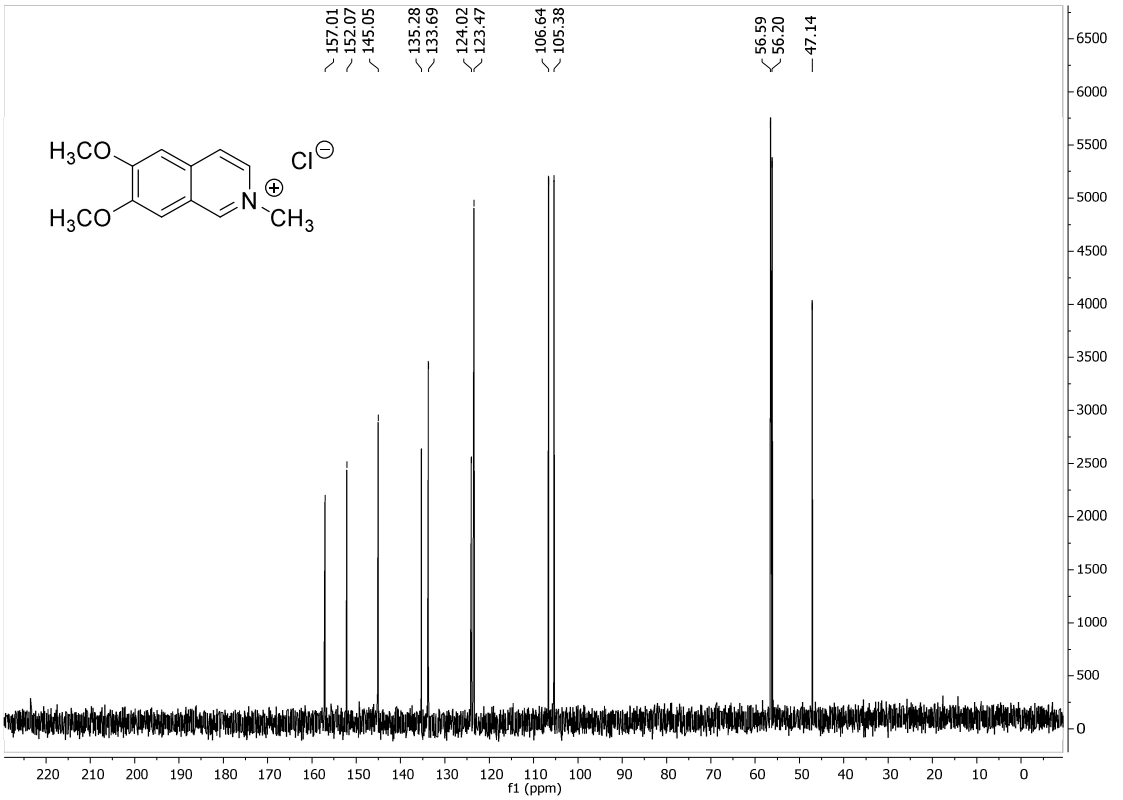

Figure A.7. ^{13}C NMR spectrum (75 MHz, D_2O) of 6,7-dimethoxy-2-methylisoquinolinium chloride (**3**).

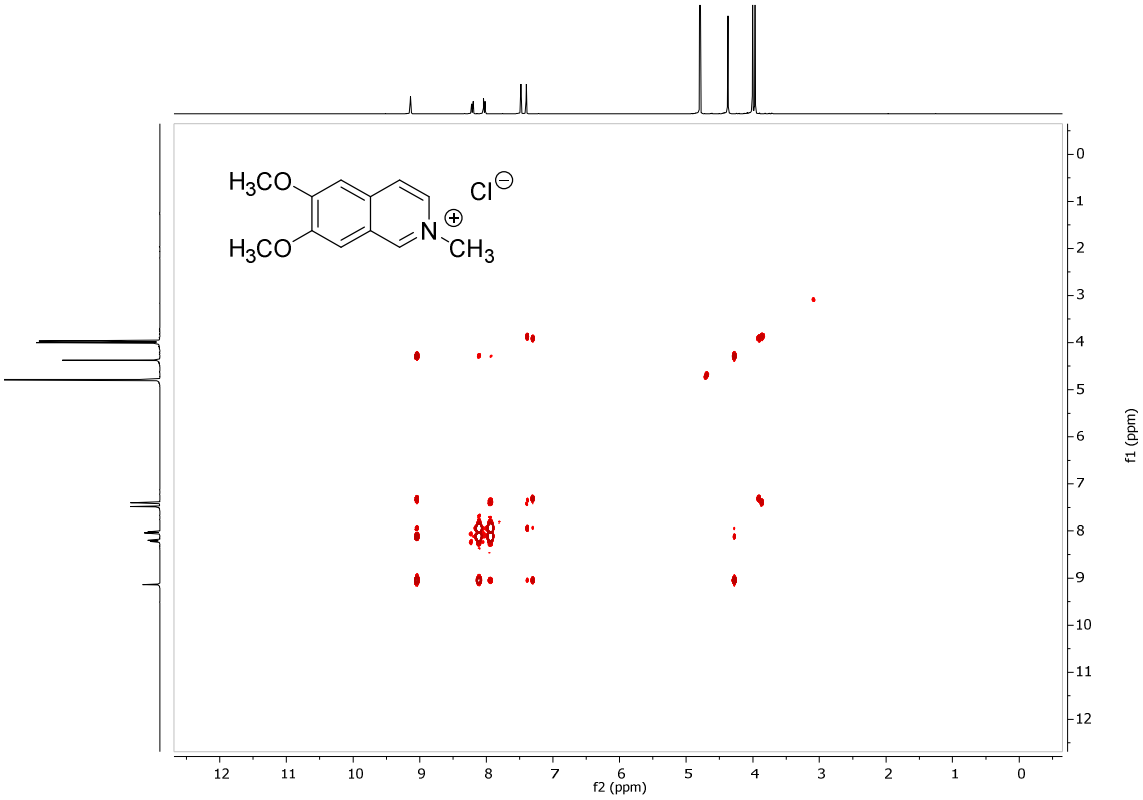

Figure A.8. COSY spectrum (D_2O) of 6,7-dimethoxy-2-methylisoquinolinium chloride (**3**).

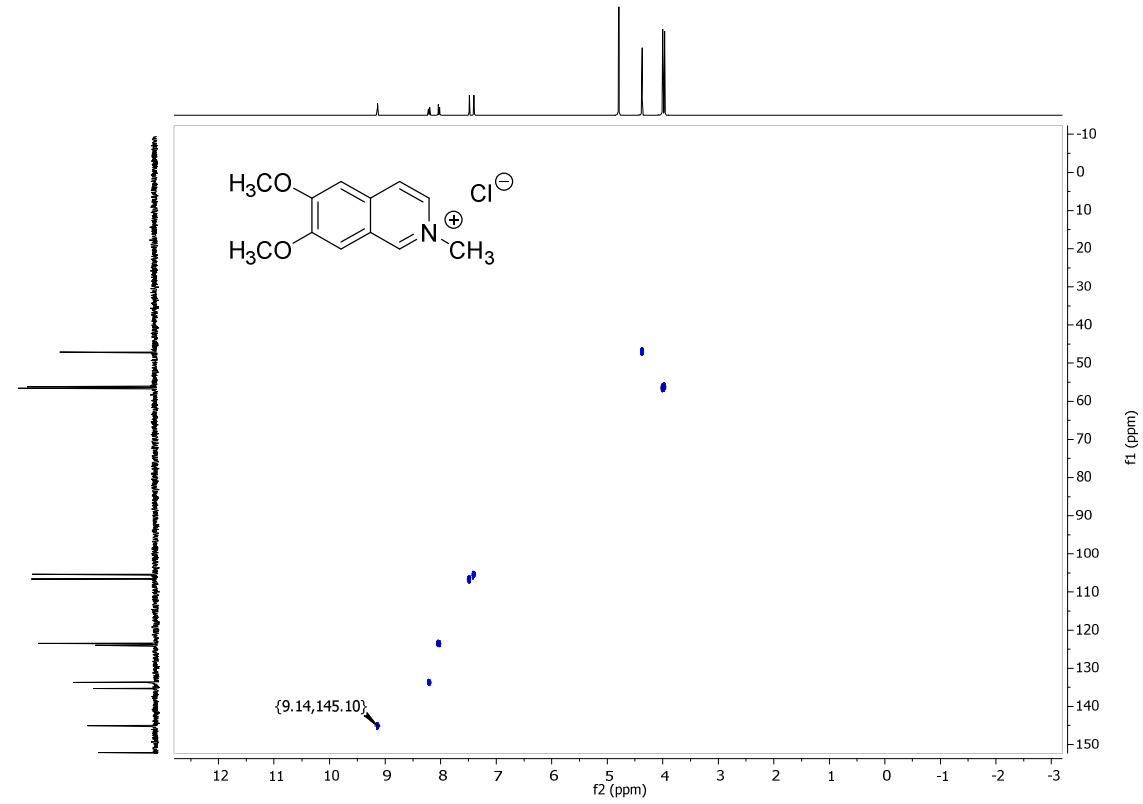

Figure A.9. HSQC spectrum (D_2O) of 6,7-dimethoxy-2-methylisoquinolinium chloride (**3**).

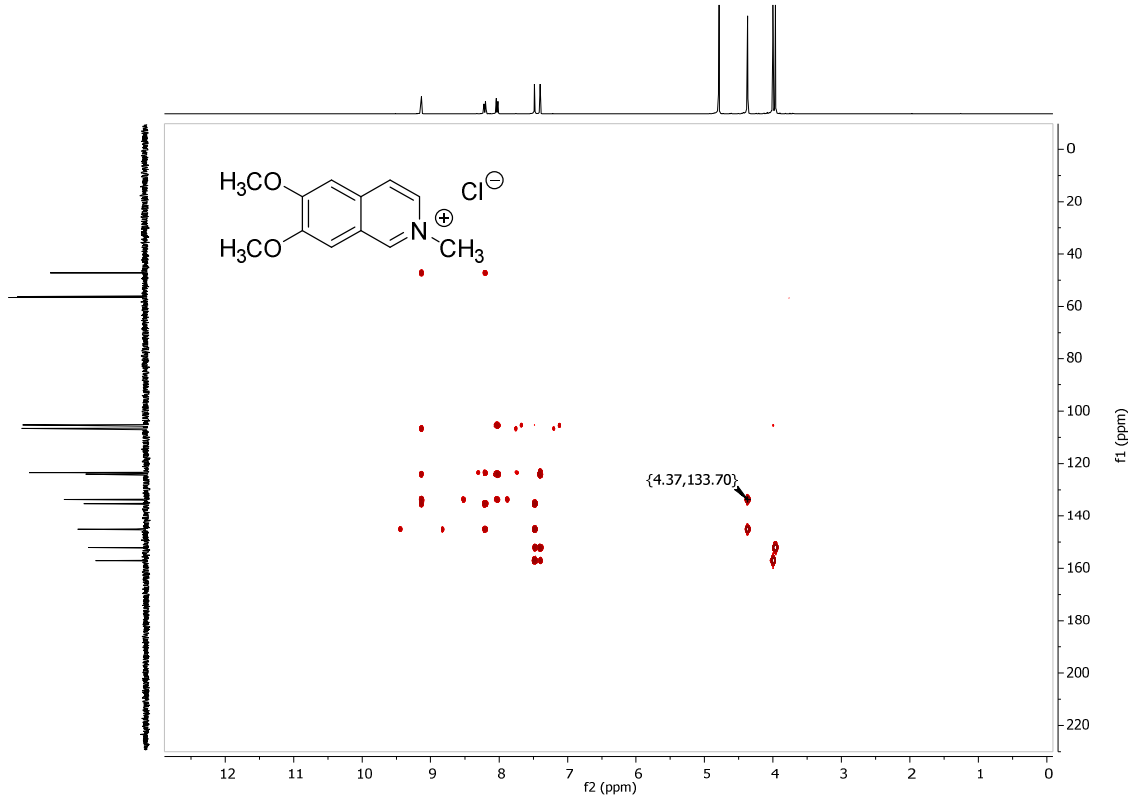

Figure A.10. HMBC spectrum (D_2O) of 6,7-dimethoxy-2-methylisoquinolinium chloride (**3**).

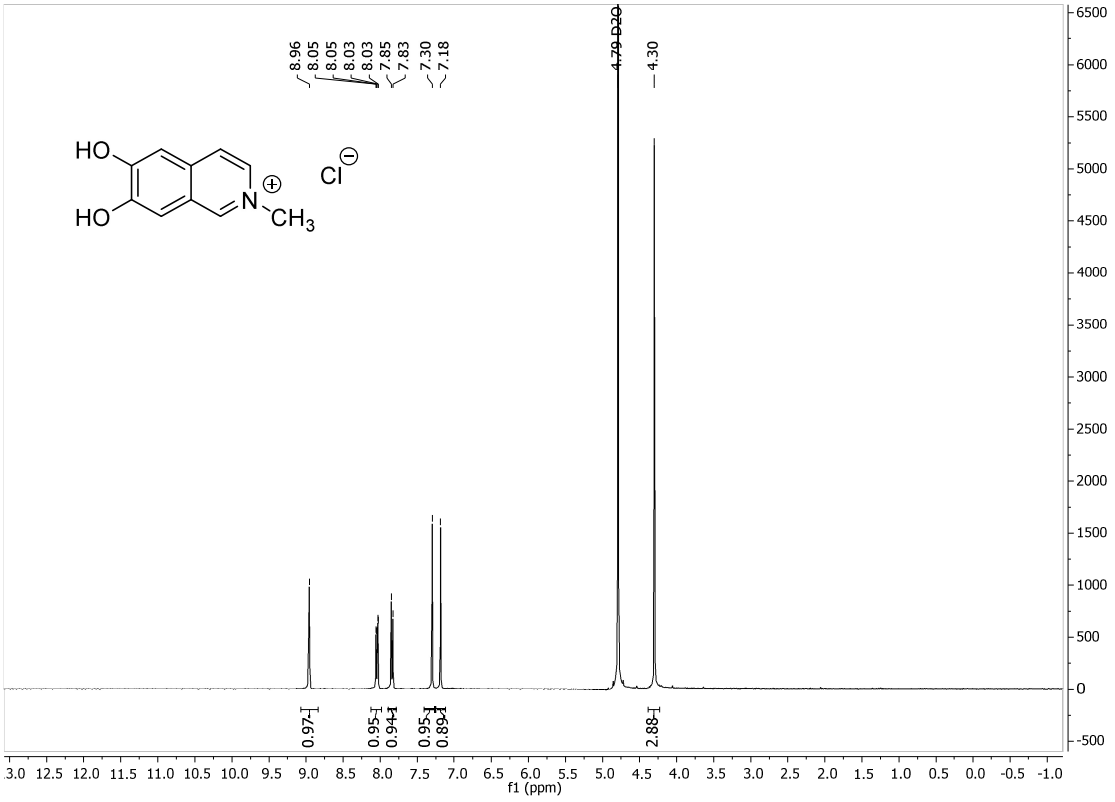

Figure A.11. ^{1}H NMR spectrum (300 MHz, D_2O) of 6,7-dihydroxy-2-methylisoquinolinium chloride (DHMIQ).

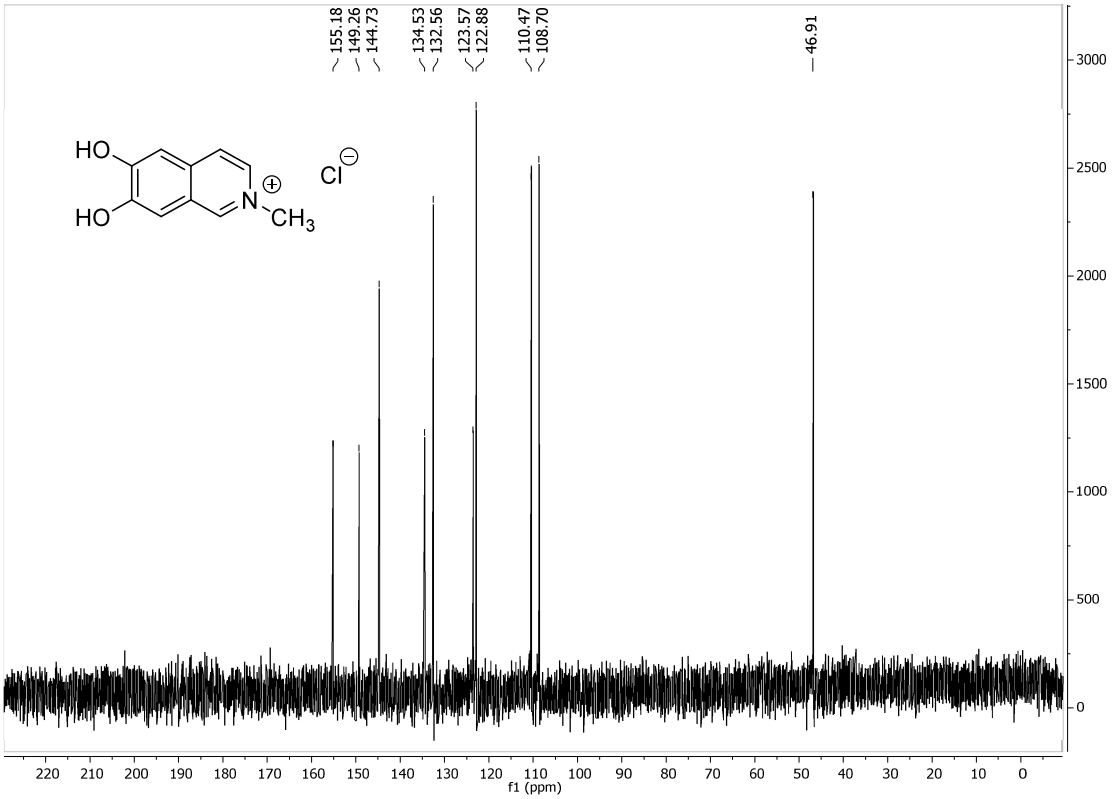

Figure A.12. ^{13}C NMR spectrum (75 MHz, D_2O) of 6,7-dihydroxy-2-methylisoquinolinium chloride (DHMIQ).

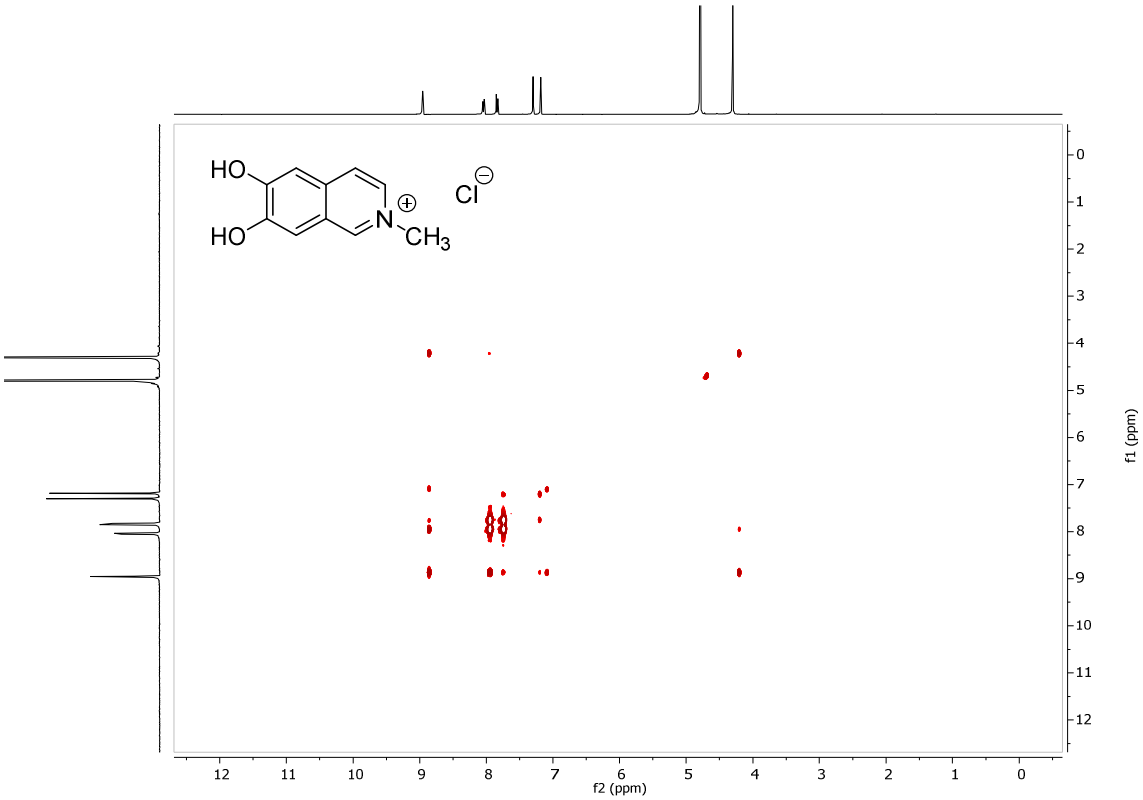

Figure A.13. COSY spectrum (D_2O) of 6,7-dihydroxy-2-methylisoquinolinium chloride (DHMIQ).

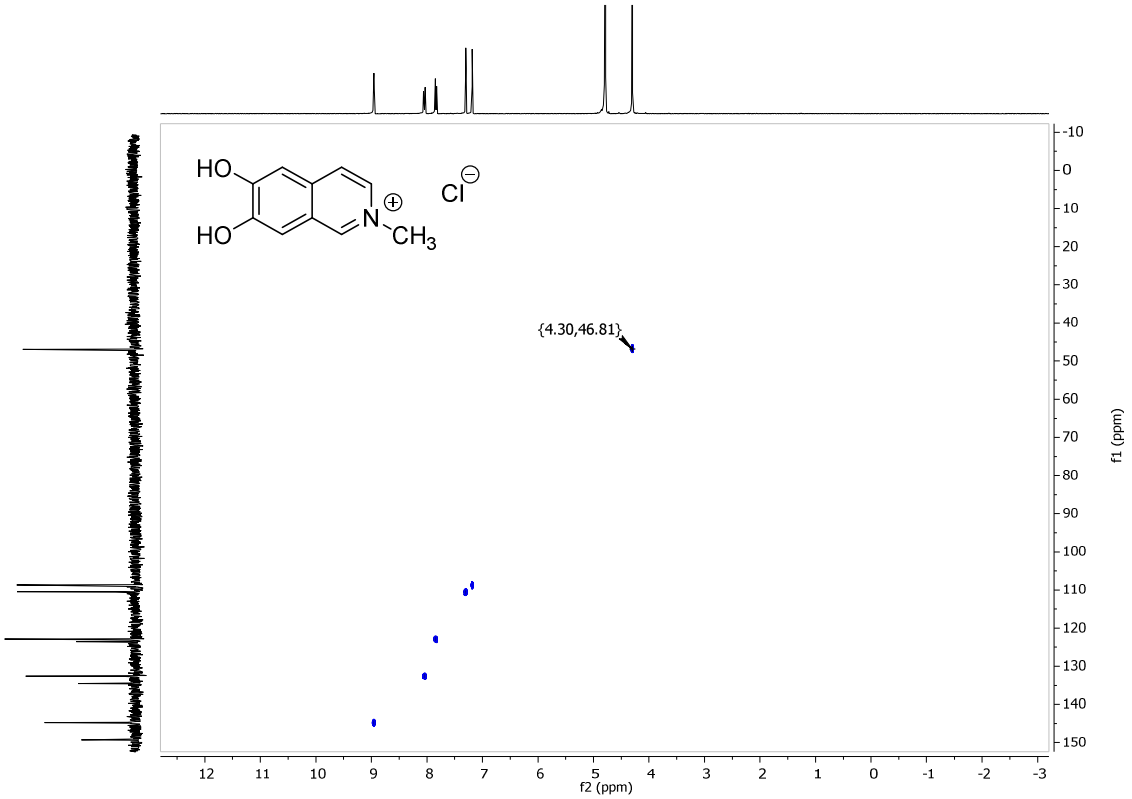

Figure A.14. HSQC spectrum (D_2O) of 6,7-dihydroxy-2-methylisoquinolinium chloride (DHMIQ).

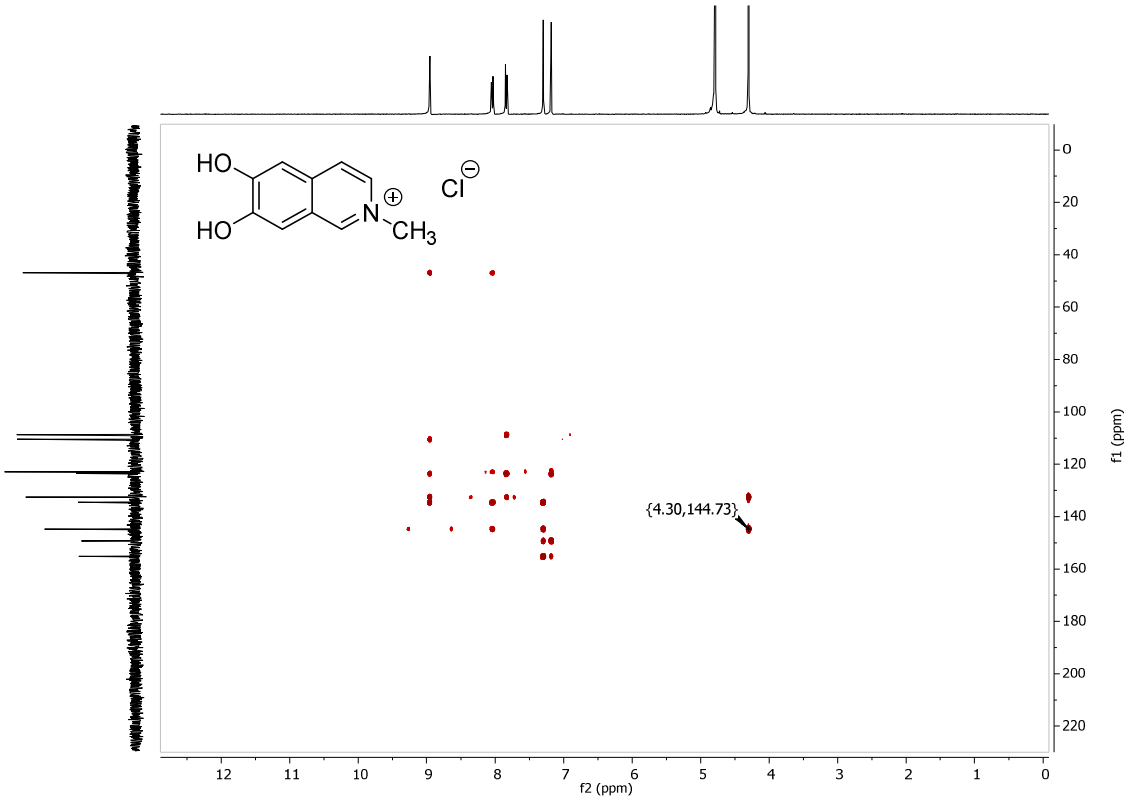

Figure A.15. HMBC spectrum (D_2O) of 6,7-dihydroxy-2-methylisoquinolinium chloride (DHMIQ).

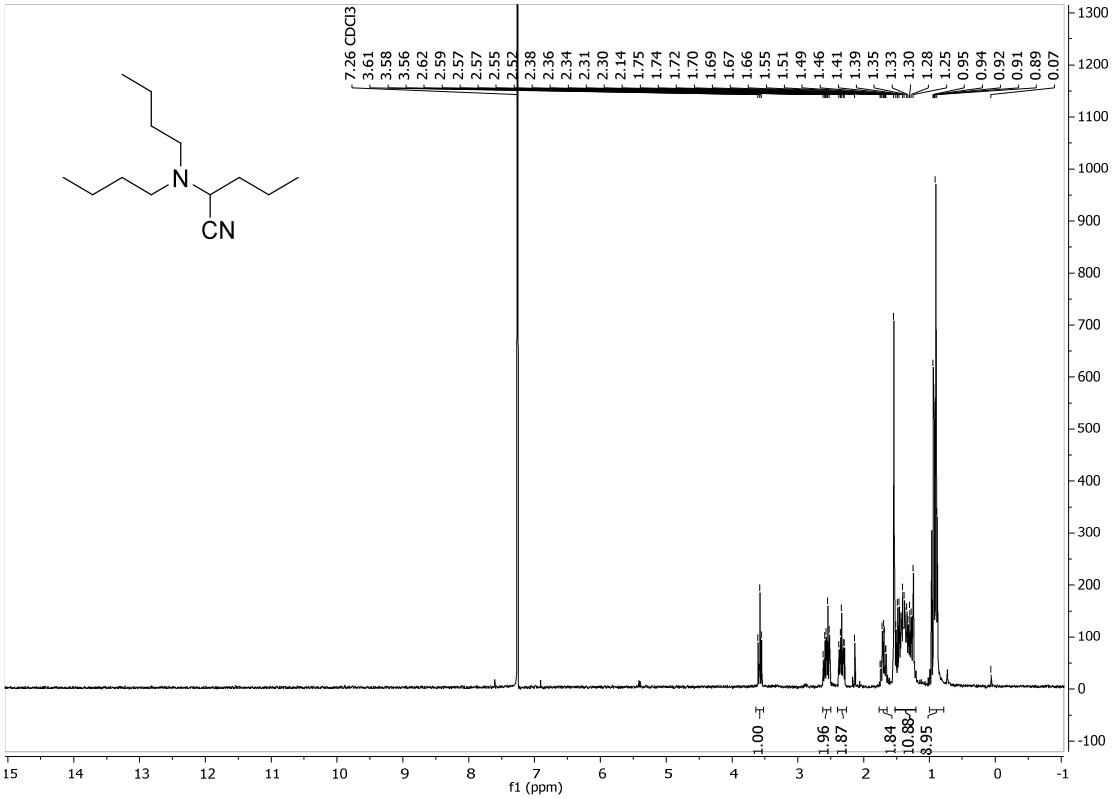

Figure A.16. ^{1}H NMR spectrum (300 MHz, $CDCl_3$) of 2-(dibutylamino)-pentanenitrile (**5**).

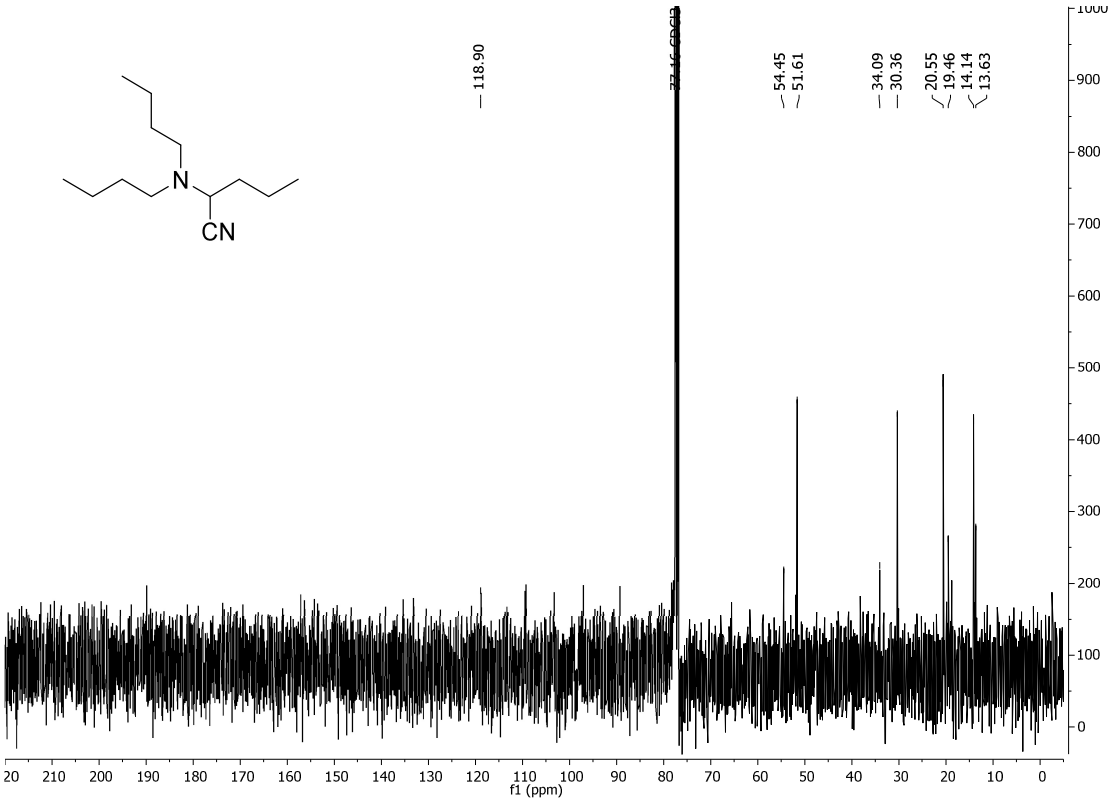

Figure A.17. ^{13}C NMR spectrum (75 MHz, $CDCl_3$) of 2-(dibutylamino)-pentanenitrile (**5**). The CN-signal (118.9 ppm) was determined by HMBC.

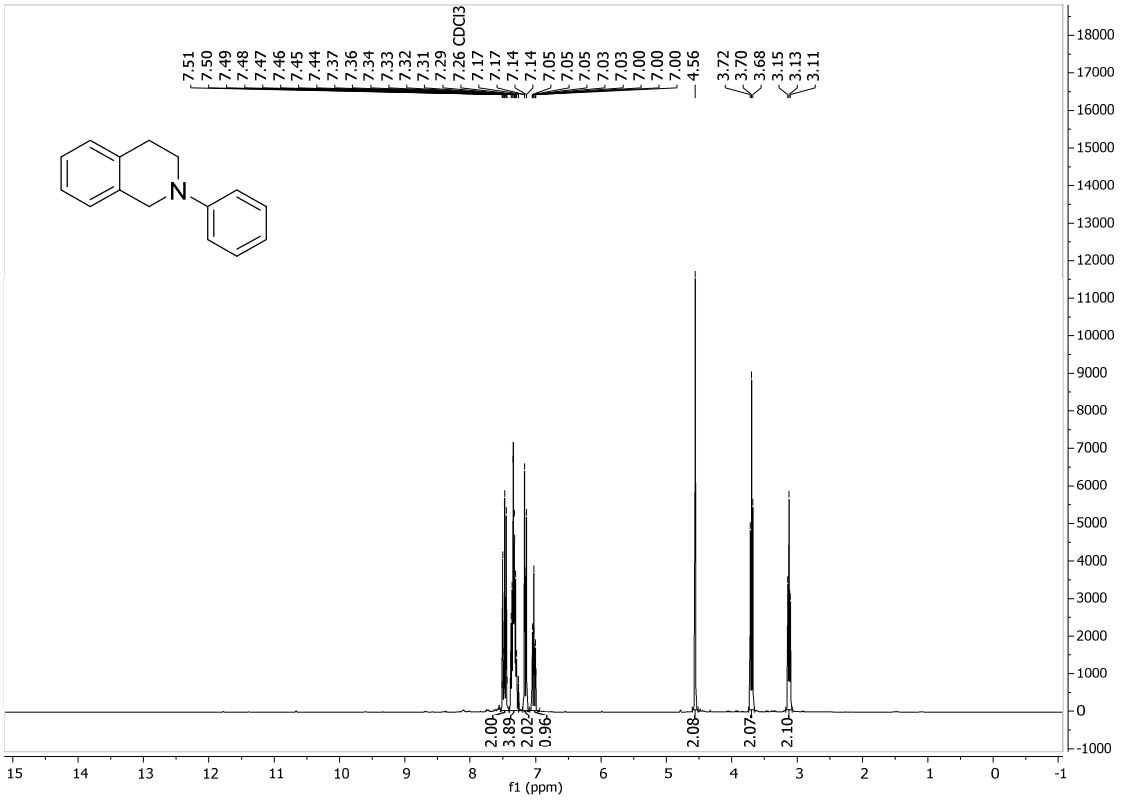

Figure A.18. ^{1}H NMR spectrum (300 MHz, $CDCl_3$) of *N*-phenyl-1,2,3,4-tetrahydroisoquinoline (**6**).

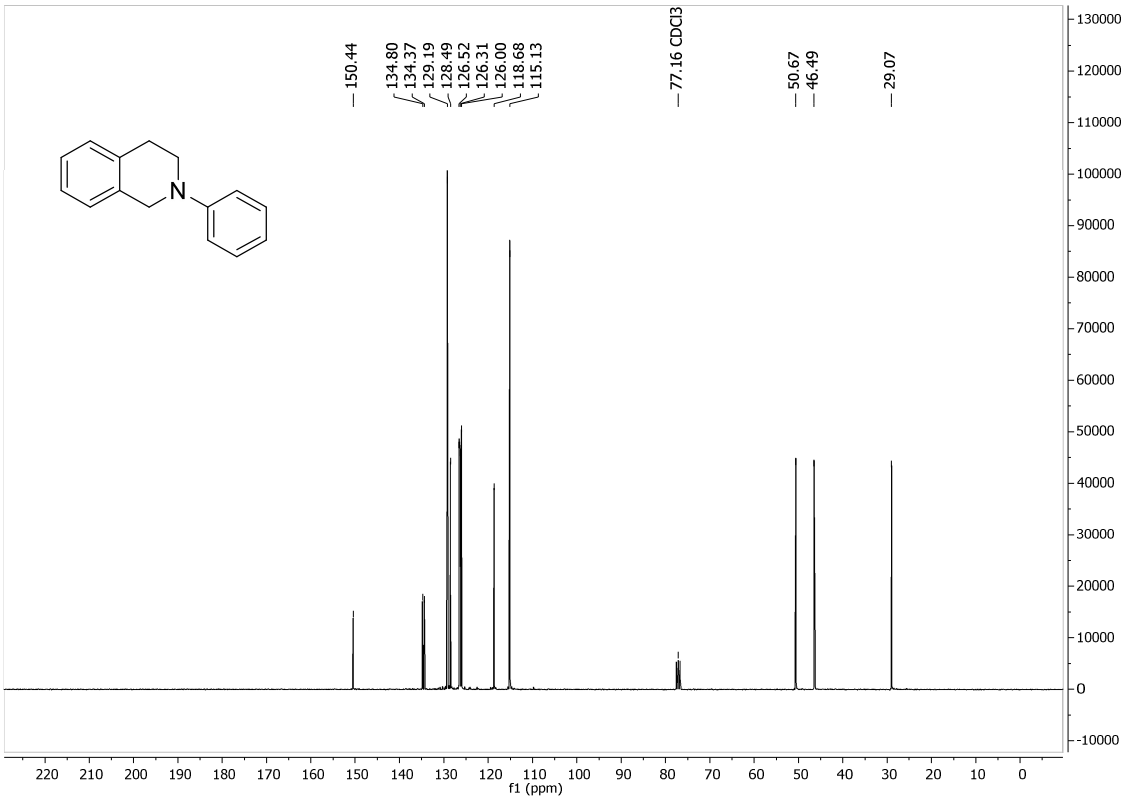

Figure A.19. ^{13}C NMR spectrum (75 MHz, $CDCl_3$) of *N*-phenyl-1,2,3,4-tetrahydroisoquinoline (**6**).

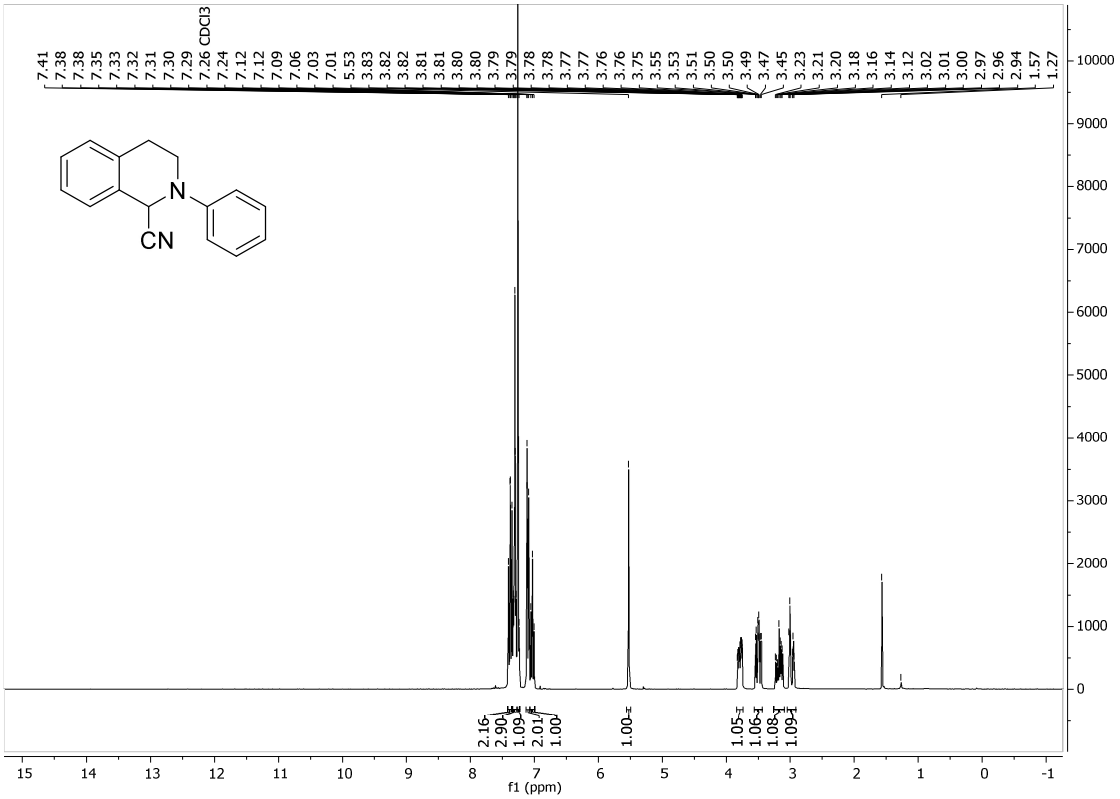

Figure A.20. ^{1}H NMR spectrum (300 MHz, $CDCl_3$) of *N*-phenyl-1,2,3,4-tetrahydroisoquinoline-1-carbonitrile (**14**).

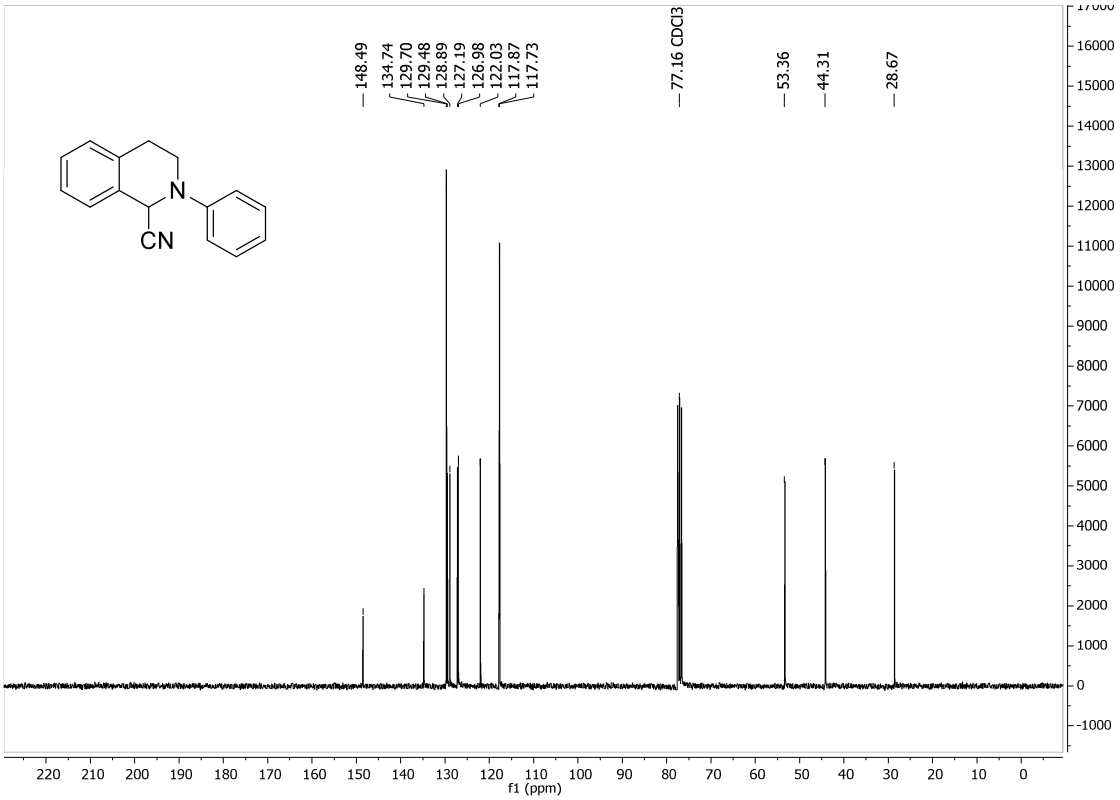

Figure A.21. ^{13}C NMR spectrum (75 MHz, $CDCl_3$) of *N*-phenyl-1,2,3,4-tetrahydroisoquinoline-1-carbonitrile (**14**).

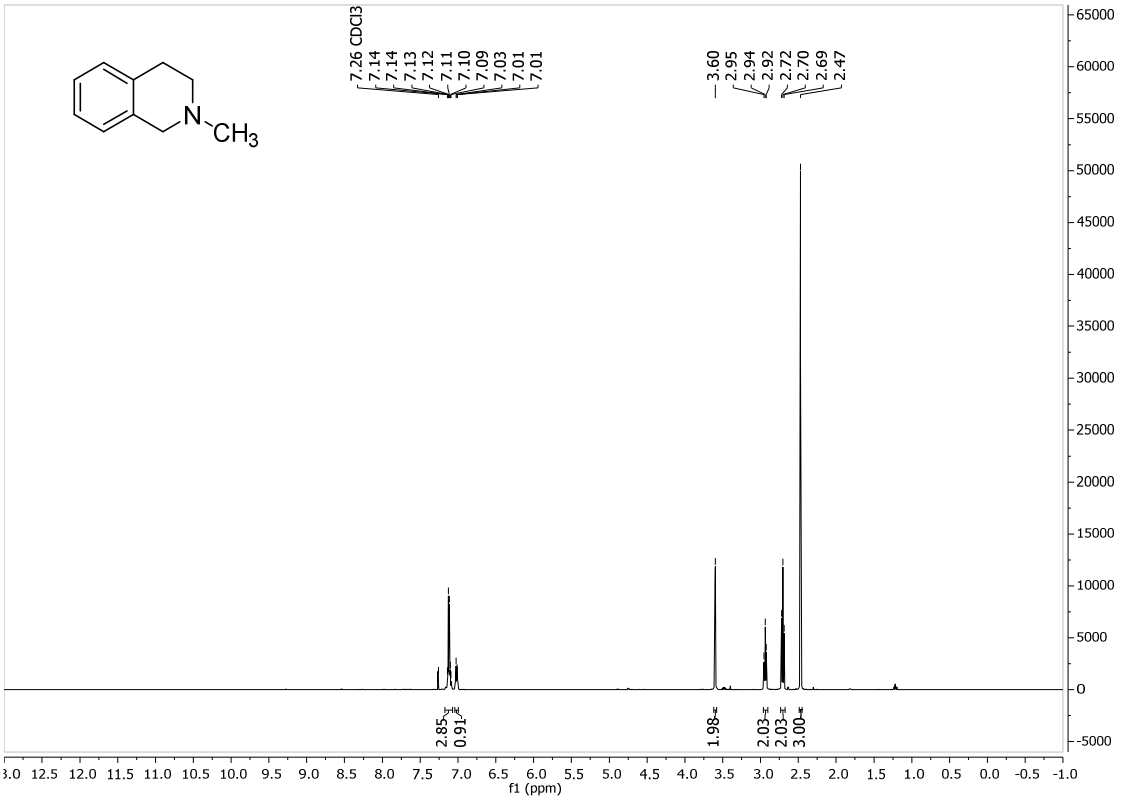

Figure A.22. ^{1}H NMR spectrum (300 MHz, $CDCl_3$) of *N*-methyl-1,2,3,4-tetrahydroisoquinoline (**7**).

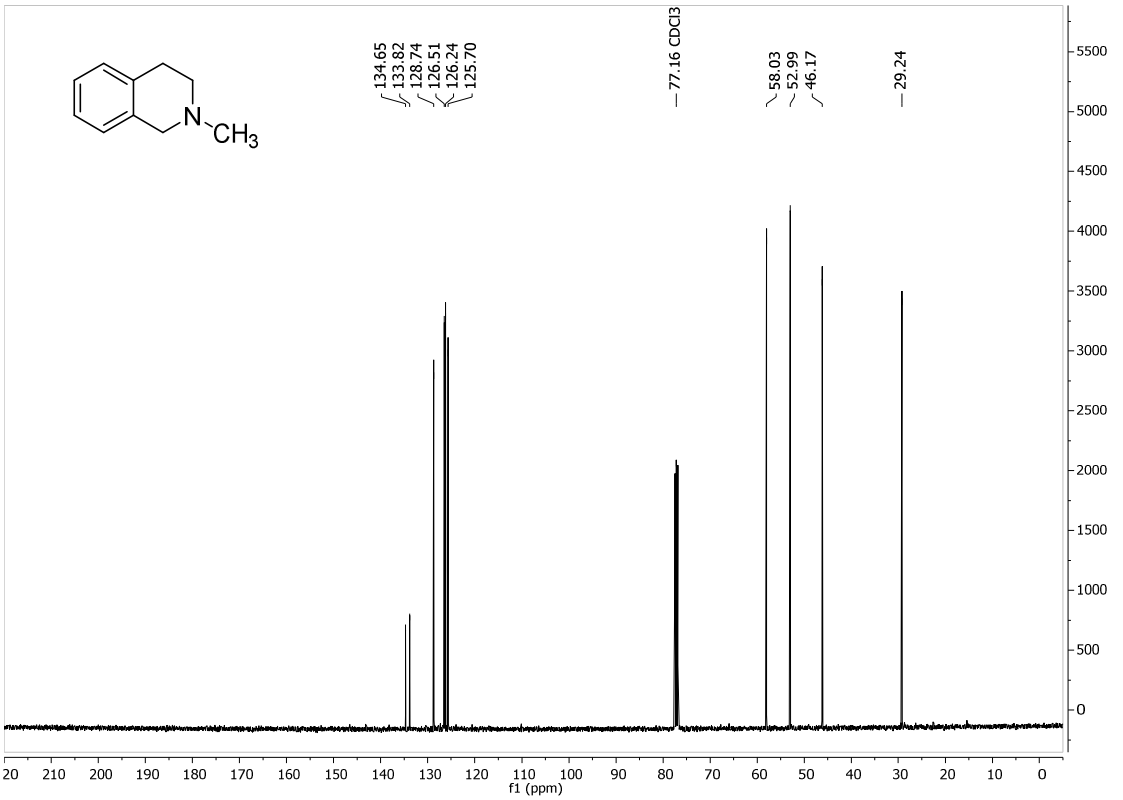

Figure A.23. ^{13}C NMR spectrum (75 MHz, $CDCl_3$) of *N*-methyl-1,2,3,4-tetrahydroisoquinoline (**7**).

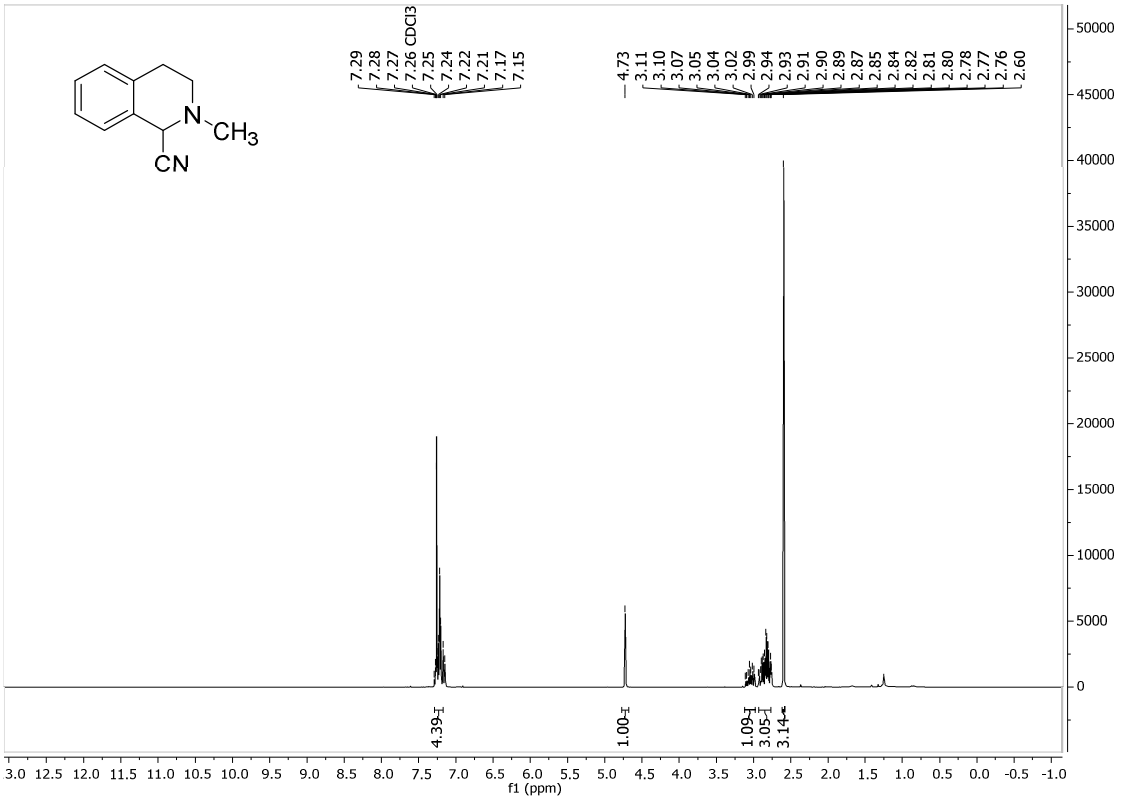

Figure A.24. ^{1}H NMR spectrum (300 MHz, $CDCl_3$) of *N*-methyl-1,2,3,4-tetrahydroisoquinoline-1-carbonitrile (**15**).

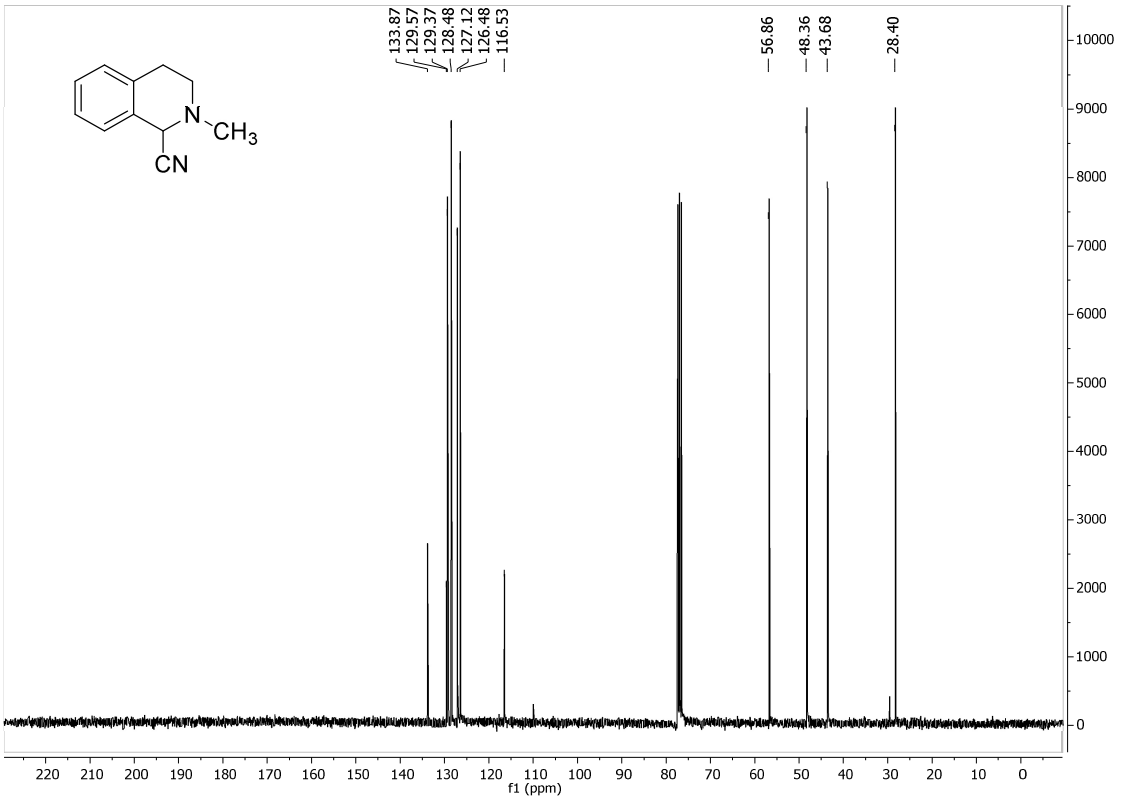

Figure A.25. ^{13}C NMR spectrum (75 MHz, $CDCl_3$) of *N*-methyl-1,2,3,4-tetrahydroisoquinoline-1-carbonitrile (**15**).

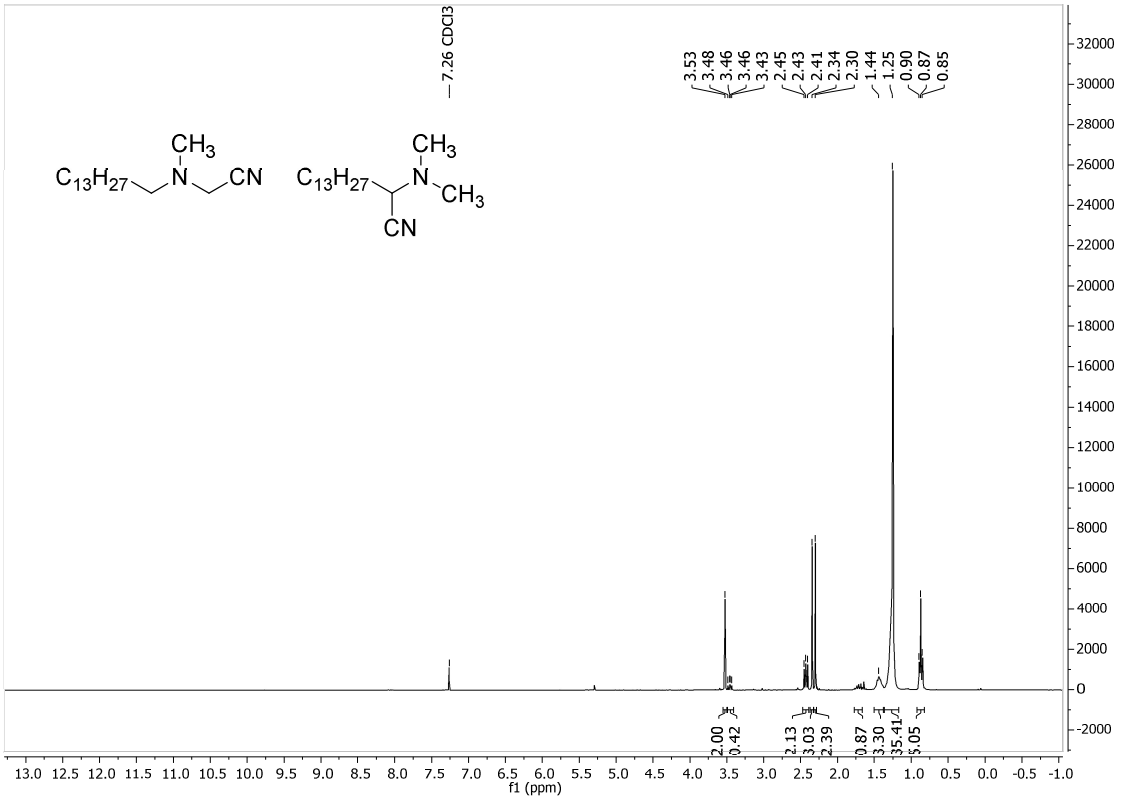

Figure A.26. ^{1}H NMR spectrum (300 MHz, $CDCl_3$) of the mixture of [tetradecyl(methyl)amino]-acetonitrile (**16**) and 2-(dimethylamino)pentadecanenitrile (**17**).

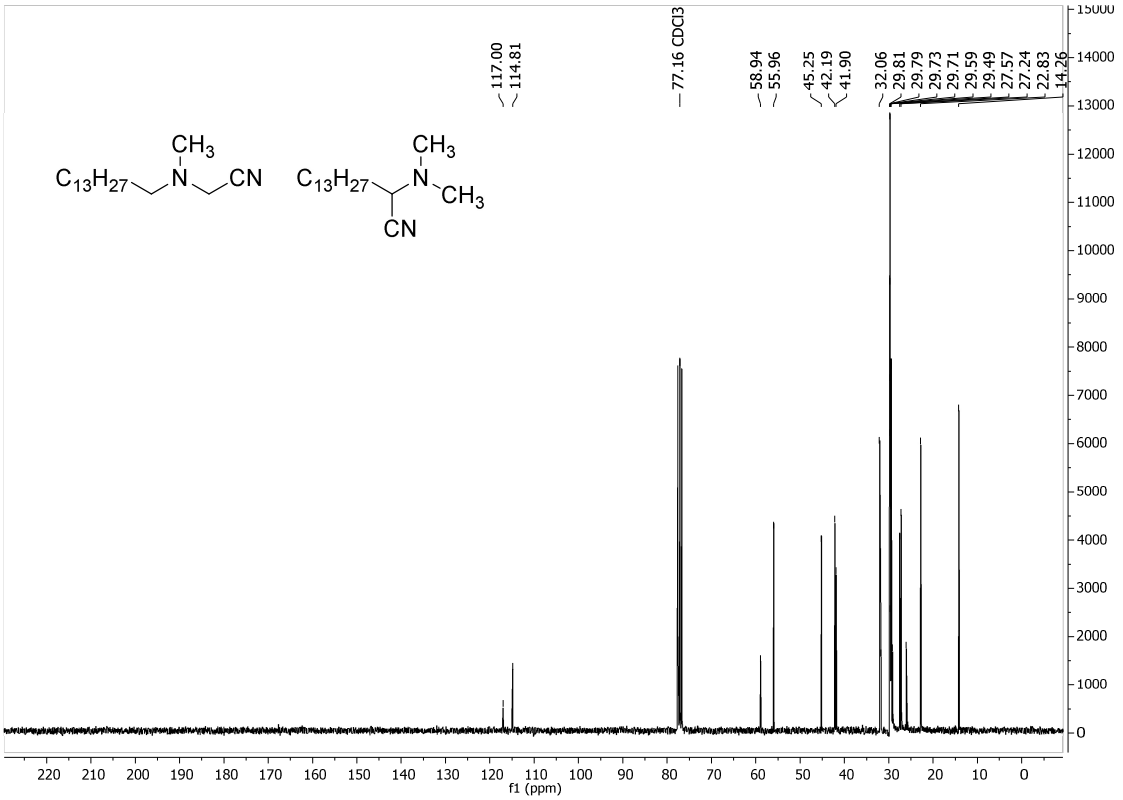

Figure A.27. ^{13}C NMR spectrum (75 MHz, $CDCl_3$) of the mixture of [tetradecyl(methyl)amino]-acetonitrile (**16**) and 2-(dimethylamino)pentadecanenitrile (**17**).

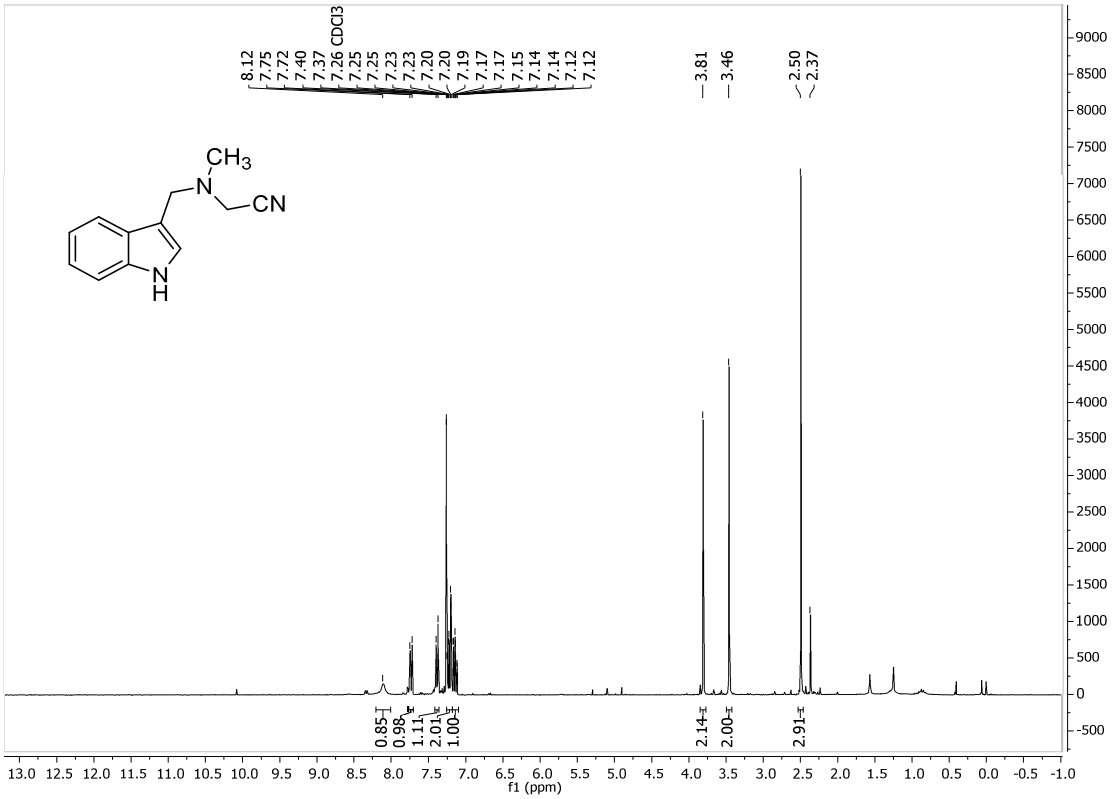

Figure A.28. ^{1}H NMR spectrum (300 MHz, $CDCl_3$) of [(1*H*-indol-3-ylmethyl)(methyl)amino]-acetonitrile (**18**).

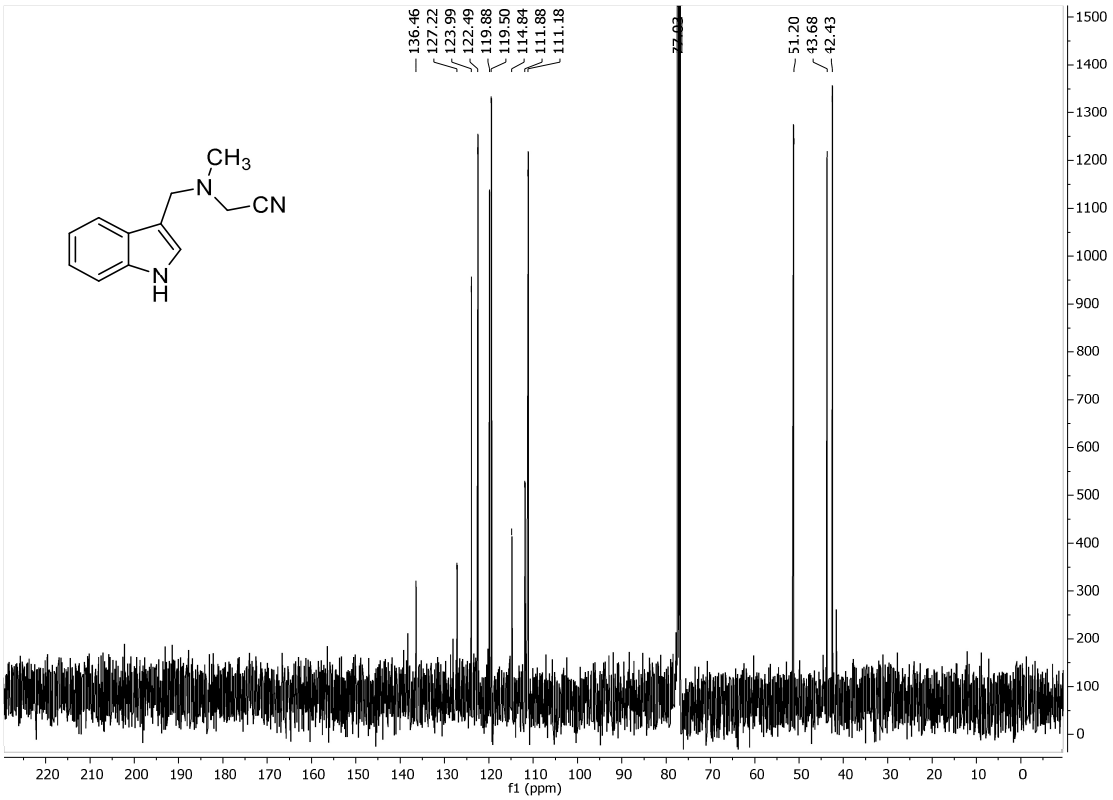

Figure A.29. ^{13}C NMR spectrum (75 MHz, $CDCl_3$) of [(1*H*-indol-3-ylmethyl)(methyl)amino]-acetonitrile (**18**).

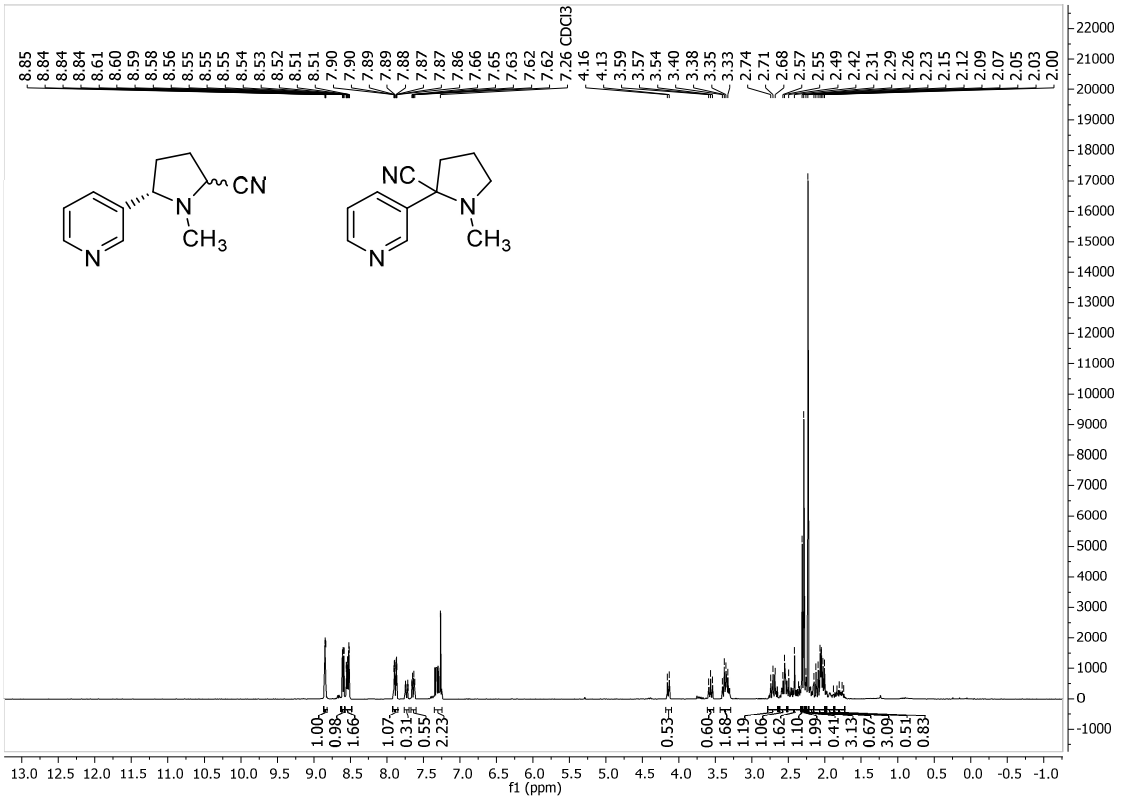

Figure A.30. ^{1}H NMR spectrum (300 MHz, $CDCl_3$) of the mixture of 1-methyl-5-(pyridin-3-yl)pyrrolidine-2-carbonitrile (**19**) and 1-methyl-2-(pyridin-3-yl)pyrrolidine-2-carbonitrile (**20**).

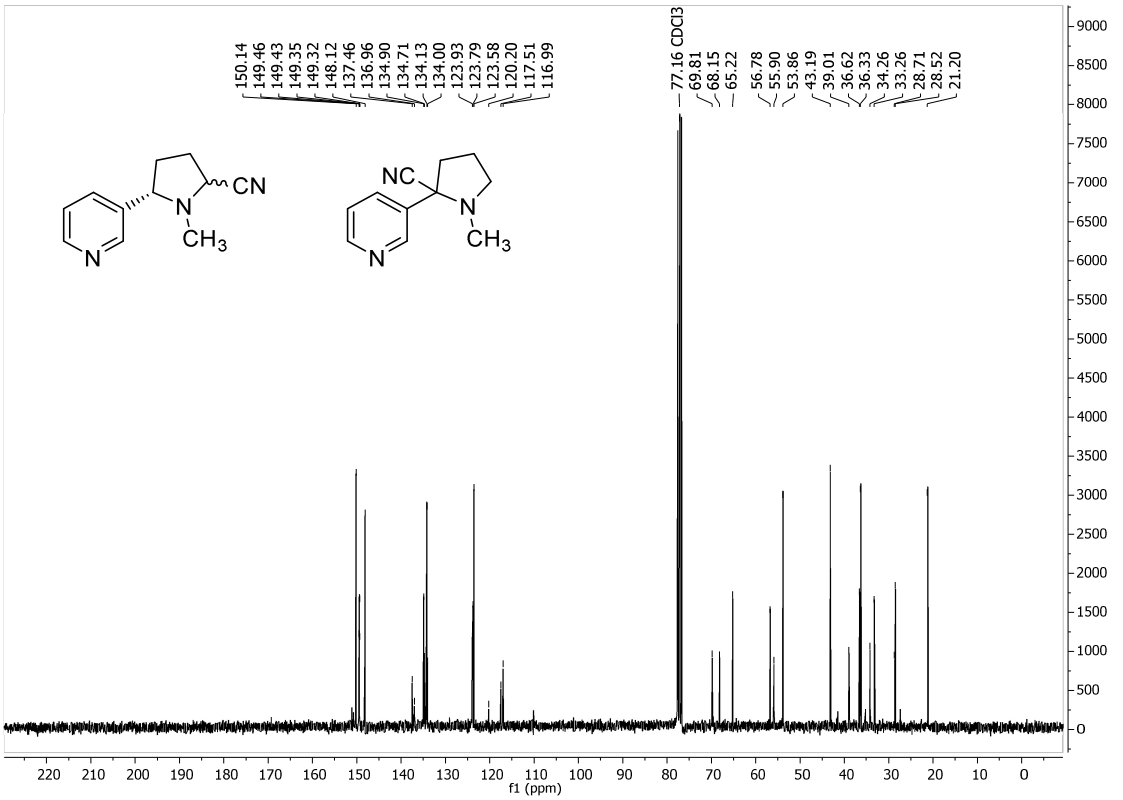

Figure A.31. ^{13}C NMR spectrum (75 MHz, $CDCl_3$) of the mixture of 1-methyl-5-(pyridin-3-yl)pyrrolidine-2-carbonitrile (**19**) and 1-methyl-2-(pyridin-3-yl)pyrrolidine-2-carbonitrile (**20**).

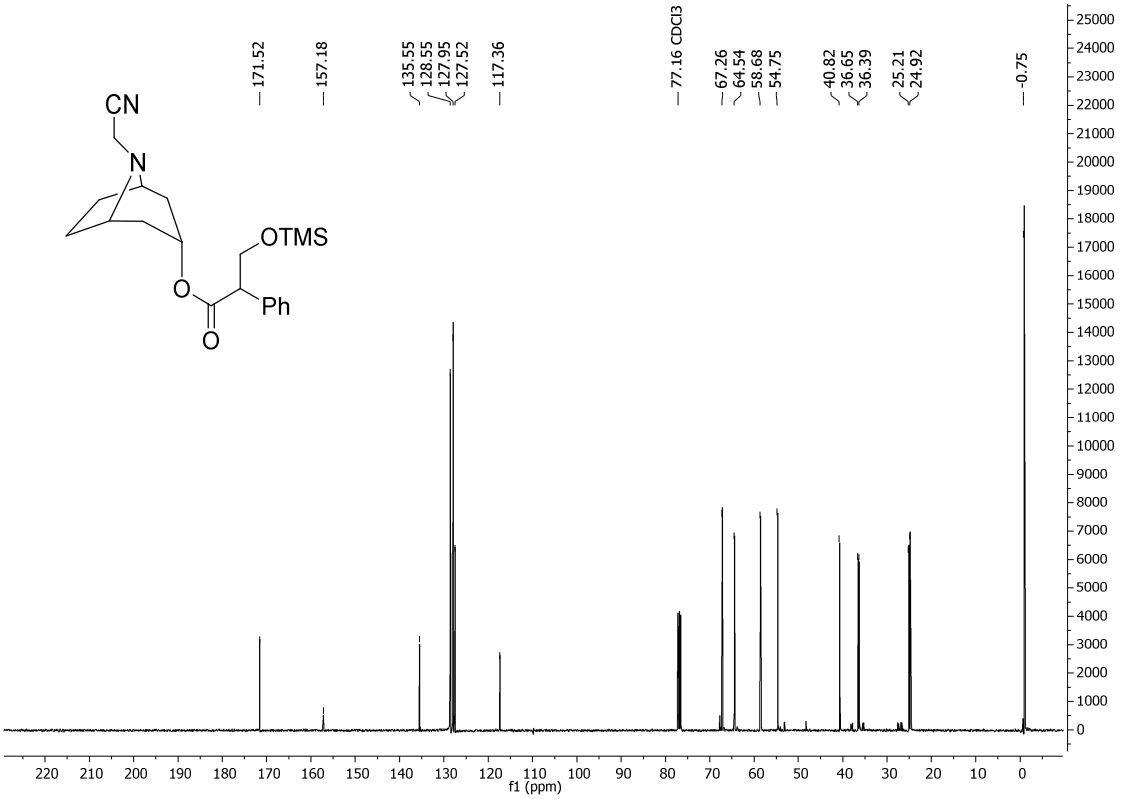

Figure A.32. ^{1}H NMR spectrum (400 MHz, $CDCl_3$) of 8-(cyanomethyl)-8-azabicyclo[3.2.1]oct-3-yl 2-phenyl-3-[(trimethylsilyl)oxy]propanoate (**21**).

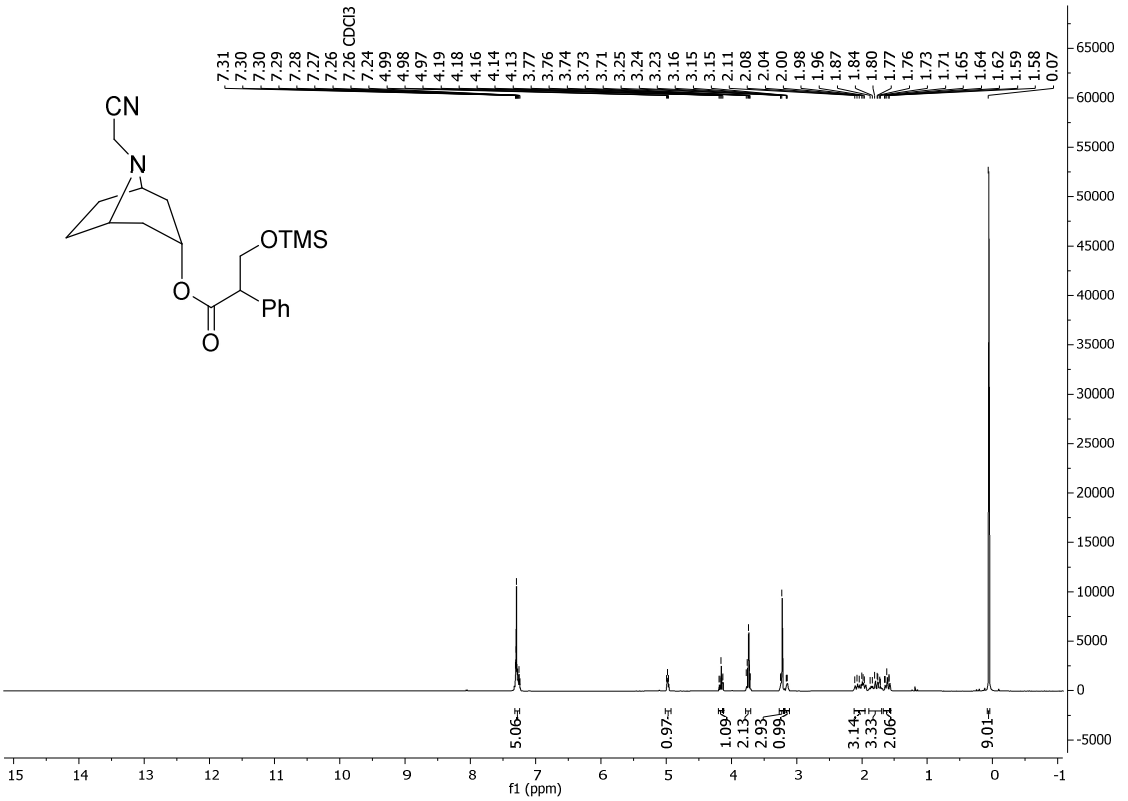

Figure A.33. ^{13}C NMR spectrum (100 MHz, $CDCl_3$) of 8-(cyanomethyl)-8-azabicyclo[3.2.1]oct-3-yl 2-phenyl-3-[(trimethylsilyl)oxy]propanoate (**21**).

List of Abbreviations

A	electron acceptor
AC	alternating current
AIBN	azobis(isobutyronitrile)
AMCSD	American Mineralogist Crystal Structure Database
Ar	aryl
ATR	attenuated total reflection
a.u.	arbitrary unit
BLS	Brillouin light scattering
bpy	2,2′-bipyridine
br	broad signal (both NMR multiplicity and IR intensity)
Cat	catechol
cat	catecholate dianion $(C_6H_4O_2)^{2-}$
cat-H	catecholate monoanion $(C_6H_5O_2)^{-}$
CB	conduction band
CBM	conduction band minimum
CCD	charge-coupled device
CCDC	Cambridge Crystallographic Data Centre
ccp	cubic close-packing
CDC	cross-dehydrogenative coupling
CIF	crystallographic information file
CLN	cluster nuclearity
COD	Crystallography Open Database
COSY	correlation spectroscopy
D	electron donor
d	doublet (NMR multiplicity)
DAP^{2+}	*N*,*N*′-dimethyl-2,7-diazapyrenium dication
dd	doublet of doublets (NMR multiplicity)
DDT	dodecanethiol
DDQ	2,3-dichloro-5,6-dicyanobenzoquinone
DFT	density functional theory

dhcp	double hexagonal close-packing
DHMIQ	6,7-dihydroxy-2-methylisoquinolinium (chloride)
DHN	2,3-dihydroxynaphthalene
DMA	dimethylacetamide
DMF	*N*,*N*-dimethylformamide
DMPA	2,2-dimethoxy-2-phenylacetophenone
DOSY	diffusion-ordered spectroscopy
DSSC	dye-sensitized solar cell
dt	doublet of triplets (NMR multiplicity)
ESI-HRMS	electrospray ionization−high resolution mass spectrometry
ESI-MS	electrospray ionization−mass spectrometry
GC	gas chromatography
hcp	hexagonal close-packing
HMBC	heteronuclear multiple bond correlation (spectroscopy)
HOMO	highest occupied molecular orbital
HRTEM	high-resolution transmission electron microscopy
HSAB	hard and soft acids and bases
HSQC	heteronuclear single quantum correlation (spectroscopy)
IR	infrared
LC-MS	liquid chromatography−mass spectrometry
LED	light-emitting diode
LMCT	ligand-to-metal charge transfer
LUMO	lowest unoccupied molecular orbital
m	multiplet (NMR multiplicity) / medium (IR intensity)
MAS	magic angle spinning
Me	methyl
Mp	melting point
NEXAFS	near-edge X-ray absorption fine structure
NHE	normal hydrogen electrode
NIR	near-infrared
NMQ^+	*N*-methylquinolinium cation
NMR	nuclear magnetic resonance
NOESY	nuclear Overhauser effect spectroscopy

NP(s)	nanoparticle(s)
OA	oleic acid
ODE	1-octadecene
ODT	octadecanethiol
O^iPr	isopropoxide group
OM	oleylamine
OPA	octylphosphonic acid
PCDA	10,12-pentacosadiynoic acid
PES	photoelectron spectroscopy
PET	poly(ethylene terephthalate)
PETMP	pentaerythritol tetrakis(3-mercaptopropionate)
Ph	phenyl
pMBA	*p*-mercaptobenzoic acid
PMMA	poly(methyl methacrylate)
POT	polyoxotitanate
PP	polypropylene
ppm	parts per million
PTFE	poly(tetrafluoroethylene)
PXRD	powder X-ray diffraction
py	pyridine
ref	reference
R_f	retention factor
RM	reaction medium
ROS	reactive oxygen species
rpm	revolutions per minute
s	singlet (NMR multiplicity) / strong (IR intensity)
SEM	scanning electron microscopy
SAM	self-assembled monolayer
SP	synthetic product
STM	scanning tunneling microscopy
t	triplet (NMR multiplicity)
TAOTA	2,4,6-triallyloxy-1,3,5-triazine
TBAC	tetrabutylammonium chloride

TBDMS	*tert*-butyldimethylsilyl
tBuCat	4-*tert*-butylcatechol
TE	thiol−ene
TEM	transmission electron microscopy
TEMPO	(2,2,6,6-tetramethylpiperidin-1-yl)oxyl
TGA	thermogravimetric analysis
THF	tetrahydrofuran
TMA	tetramethylammonium cation
TMAH	tetramethylammonium hydroxide
TMP	trimethylphosphine
TMS	trimethylsilyl
TMSCN	trimethylsilyl cyanide
TOC	titanium oxo cluster
TOPO	trioctylphosphine oxide
tt	triplet of triplets (NMR multiplicity)
UV−vis	ultraviolet−visible
VB	valence band
VBM	valence band maximum
VH	vertical−horizontal (polarization in BLS setup)
vs	very strong (IR intensity)
VV	vertical−vertical (polarization in BLS setup)
w	weak (IR intensity)
XRD	X-ray diffraction

References

(1) Nagarajan, R. Nanoparticles: Building Blocks for Nanotechnology. In *Nanoparticles: Synthesis, Stabilization, Passivation, and Functionalization*; ACS Symposium Series 996; American Chemical Society: Washington, DC, 2008; pp 2–14.

(2) Goesmann, H.; Feldmann, C. Nanoparticulate Functional Materials. *Angew. Chem., Int. Ed.* **2010**, *49*, 1362–1395.

(3) de Mello Donegá, C. The Nanoscience Paradigm: "Size Matters!" In *Nanoparticles: Workhorses of Nanoscience*; de Mello Donegá, C., Ed.; Springer-Verlag: Berlin, Heidelberg, 2014; pp 1–12.

(4) Koole, R.; Groeneveld, E.; Vanmaekelbergh, D.; Meijerink, A.; de Mello Donegá, C. Size Effects on Semiconductor Nanoparticles. In *Nanoparticles: Workhorses of Nanoscience*; de Mello Donegá, C., Ed.; Springer-Verlag: Berlin, Heidelberg, 2014; pp 13–51.

(5) Pietryga, J. M.; Park, Y.-S.; Lim, J.; Fidler, A. F.; Bae, W. K.; Brovelli, S.; Klimov, V. I. Spectroscopic and Device Aspects of Nanocrystal Quantum Dots. *Chem. Rev.* **2016**, *116*, 10513–10622.

(6) Willets, K. A.; Van Duyne, R. P. Localized Surface Plasmon Resonance Spectroscopy and Sensing. *Annu. Rev. Phys. Chem.* **2007**, *58*, 267–297.

(7) Linic, S.; Christopher, P.; Ingram, D. B. Plasmonic-Metal Nanostructures for Efficient Conversion of Solar to Chemical Energy. *Nat. Mater.* **2011**, *10*, 911–921.

(8) Wu, L.; Mendoza-Garcia, A.; Li, Q.; Sun, S. Organic Phase Syntheses of Magnetic Nanoparticles and Their Applications. *Chem. Rev.* **2016**, *116*, 10473–10512.

(9) Klabunde, K. J.; Stark, J.; Koper, O.; Mohs, C.; Park, D. G.; Decker, S.; Jiang, Y.; Lagadic, I.; Zhang, D. Nanocrystals as Stoichiometric Reagents with Unique Surface Chemistry. *J. Phys. Chem.* **1996**, *100*, 12142–12153.

(10) Haines, C.; Morris, L.; Luan, Z.; Doorenbos, Z. Pyrophoric Nanomaterials. In *Energetic Materials*; Shukla, M. K., Boddu, V. M., Steevens, J. A., Damavarapu, R., Leszczynski, J., Eds.; Challenges and Advances in Computational Chemistry and Physics 25; Springer International Publishing: Cham, Switzerland, 2017; pp 135–170.

(11) Rajh, T.; Chen, L. X.; Lukas, K.; Liu, T.; Thurnauer, M. C.; Tiede, D. M. Surface Restructuring of Nanoparticles: An Efficient Route for Ligand−Metal Oxide Crosstalk. *J. Phys. Chem. B* **2002**, *106*, 10543–10552.

(12) Kovalenko, M. V.; Manna, L.; Cabot, A.; Hens, Z.; Talapin, D. V.; Kagan, C. R.; Klimov, V. I.; Rogach, A. L.; Reiss, P.; Milliron, D. J.; Guyot-Sionnnest, P.; Konstantatos, G.; Parak, W. J.; Hyeon, T.; Korgel, B. A.; Murray, C. B.; Heiss, W. Prospects of Nanoscience with Nanocrystals. *ACS Nano* **2015**, *9*, 1012–1057.

(13) Sapsford, K. E.; Algar, W. R.; Berti, L.; Gemmill, K. B.; Casey, B. J.; Oh, E.; Stewart, M. H.; Medintz, I. L. Functionalizing Nanoparticles with Biological Molecules: Developing Chemistries that Facilitate Nanotechnology. *Chem. Rev.* **2013**, *113*, 1904–2074.

(14) Kwon, H. J.; Shin, K.; Soh, M.; Chang, H.; Kim, J.; Lee, J.; Ko, G.; Kim, B. H.;

Kim, D.; Hyeon, T. Large-Scale Synthesis and Medical Applications of Uniform-Sized Metal Oxide Nanoparticles. *Adv. Mater.* **2018**, *30*, 1704290.
(15) *Metal Nanoparticles: Synthesis and Applications in Pharmaceutical Sciences*; Thota, S., Crans, D. C., Eds.; Wiley-VCH Verlag GmbH & Co. KGaA: Weinheim, Germany, 2018.
(16) *Nanoparticles and Catalysis*; Astruc, D., Ed.; Wiley-VCH Verlag GmbH & Co. KGaA: Weinheim, Germany, 2008.
(17) Thakore, S. I.; Rathore, P. S. Nanoparticle-Assisted Organic Transformations. In *Handbook of Nanoparticles*; Aliofkhazraei, M., Ed.; Springer International Publishing: Cham, Switzerland, 2016; pp 769–801.
(18) Liu, J.; Sun, W. Magnetic Nanoparticles in Catalysis. In *Magnetic Nanomaterials: Applications in Catalysis and Life Sciences*; Bossmann, S. H., Wang, H., Eds.; Smart Materials Series No. 26; Royal Society of Chemistry: Cambridge, UK, 2017; pp 59–98.
(19) Talapin, D. V.; Lee, J.-S.; Kovalenko, M. V.; Shevchenko, E. V. Prospects of Colloidal Nanocrystals for Electronic and Optoelectronic Applications. *Chem. Rev.* **2010**, *110*, 389–458.
(20) Kagan, C. R.; Lifshitz, E.; Sargent, E. H.; Talapin, D. V. Building Devices from Colloidal Quantum Dots. *Science* **2016**, *353*, aac5523.
(21) Choi, J.-H.; Wang, H.; Oh, S. J.; Paik, T.; Sung, P.; Sung, J.; Ye, X.; Zhao, T.; Diroll, B. T.; Murray, C. B.; Kagan, C. R. Exploiting the Colloidal Nanocrystal Library to Construct Electronic Devices. *Science* **2016**, *352*, 205–208.
(22) Aricò, A. S.; Bruce, P.; Scrosati, B.; Tarascon, J.-M.; van Schalkwijk, W. Nanostructured Materials for Advanced Energy Conversion and Storage Devices. *Nat. Mater.* **2005**, *4*, 366–377.
(23) Carey, G. H.; Abdelhady, A. L.; Ning, Z.; Thon, S. M.; Bakr, O. M.; Sargent, E. H. Colloidal Quantum Dot Solar Cells. *Chem. Rev.* **2015**, *115*, 12732–12763.
(24) Ortega, S.; Ibáñez, M.; Liu, Y.; Zhang, Y.; Kovalenko, M. V.; Cadavid, D.; Cabot, A. Bottom-Up Engineering of Thermoelectric Nanomaterials and Devices from Solution-Processed Nanoparticle Building Blocks. *Chem. Soc. Rev.* **2017**, *46*, 3510–3528.
(25) Niederberger, M.; Pinna, N. Aqueous and Nonaqueous Sol-Gel Chemistry. In *Metal Oxide Nanoparticles in Organic Solvents*; Engineering Materials and Processes; Springer-Verlag: London, 2009; pp 7–18.
(26) Cargnello, M.; Gordon, T. R.; Murray, C. B. Solution-Phase Synthesis of Titanium Dioxide Nanoparticles and Nanocrystals. *Chem. Rev.* **2014**, *114*, 9319–9345.
(27) Pasquarelli, R. M.; Ginley, D. S.; O'Hayre, R. Solution Processing of Transparent Conductors: From Flask to Film. *Chem. Soc. Rev.* **2011**, *40*, 5406–5441.
(28) Cayado, P.; De Keukeleere, K.; Garzón, A.; Perez-Mirabet, L.; Meledin, A.; De Roo, J.; Vallés, F.; Mundet, B.; Rijckaert, H.; Pollefeyt, G.; Coll, M.; Ricart, S.; Palau, A.; Gázquez, J.; Ros, J.; Van Tendeloo, G.; Van Driessche, I.; Puig, T.; Obradors, X. Epitaxial $YBa_2Cu_3O_{7-x}$ Nanocomposite Thin Films from Colloidal Solutions. *Supercond. Sci. Technol.* **2015**, *28*, 124007.
(29) Saldanha, P. L.; Lesnyak, V.; Manna, L. Large Scale Syntheses of Colloidal Nanomaterials. *Nano Today* **2017**, *12*, 46–63.
(30) Xia, Y.; Xiong, Y.; Lim, B.; Skrabalak, S. E. Shape-Controlled Synthesis of Metal Nanocrystals: Simple Chemistry Meets Complex Physics? *Angew. Chem.,*

Int. Ed. **2009**, *48*, 60–103.
(31) Chang, J.; Waclawik, E. R. Colloidal Semiconductor Nanocrystals: Controlled Synthesis and Surface Chemistry in Organic Media. *RSC Adv.* **2014**, *4*, 23505–23527.
(32) Agrawal, A.; Cho, S. H.; Zandi, O.; Ghosh, S.; Johns, R. W.; Milliron, D. J. Localized Surface Plasmon Resonance in Semiconductor Nanocrystals. *Chem. Rev.* **2018**, *118*, 3121–3207.
(33) Niederberger, M.; Pinna, N. *Metal Oxide Nanoparticles in Organic Solvents*; Engineering Materials and Processes; Springer-Verlag: London, 2009.
(34) Qiao, L.; Swihart, M. T. Solution-Phase Synthesis of Transition Metal Oxide Nanocrystals: Morphologies, Formulae, and Mechanisms. *Adv. Colloid Interface Sci.* **2017**, *244*, 199–266.
(35) de Mello Donega, C. Synthesis and Properties of Colloidal Heteronanocrystals. *Chem. Soc. Rev.* **2011**, *40*, 1512–1546.
(36) Zherebetskyy, D.; Scheele, M.; Zhang, Y.; Bronstein, N.; Thompson, C.; Britt, D.; Salmeron, M.; Alivisatos, P.; Wang, L.-W. Hydroxylation of the Surface of PbS Nanocrystals Passivated with Oleic Acid. *Science* **2014**, *344*, 1380–1384.
(37) Macrae, C. F.; Edgington, P. R.; McCabe, P.; Pidcock, E.; Shields, G. P.; Taylor, R.; Towler, M.; van de Streek, J. *Mercury*: Visualization and Analysis of Crystal Structures. *J. Appl. Crystallogr.* **2006**, *39*, 453–457.
(38) Boles, M. A.; Ling, D.; Hyeon, T.; Talapin, D. V. The Surface Science of Nanocrystals. *Nat. Mater.* **2016**, *15*, 141–153.
(39) Navrotsky, A. Energetics of Nanoparticle Oxides: Interplay between Surface Energy and Polymorphism. *Geochem. Trans.* **2003**, *4*, 34–37.
(40) Norris, D. J.; Efros, A. L.; Erwin, S. C. Doped Nanocrystals. *Science* **2008**, *319*, 1776–1779.
(41) Buonsanti, R.; Milliron, D. J. Chemistry of Doped Colloidal Nanocrystals. *Chem. Mater.* **2013**, *25*, 1305–1317.
(42) Sathya, A.; Guardia, P.; Brescia, R.; Silvestri, N.; Pugliese, G.; Nitti, S.; Manna, L.; Pellegrino, T. $Co_xFe_{3-x}O_4$ Nanocubes for Theranostic Applications: Effect of Cobalt Content and Particle Size. *Chem. Mater.* **2016**, *28*, 1769–1780.
(43) Sharifi Dehsari, H.; Asadi, K. Impact of Stoichiometry and Size on the Magnetic Properties of Cobalt Ferrite Nanoparticles. *J. Phys. Chem. C* **2018**, *122*, 29106–29121.
(44) Sytnyk, M.; Kirchschlager, R.; Bodnarchuk, M. I.; Primetzhofer, D.; Kriegner, D.; Enser, H.; Stangl, J.; Bauer, P.; Voith, M.; Hassel, A. W.; Krumeich, F.; Ludwig, F.; Meingast, A.; Kothleitner, G.; Kovalenko, M. V; Heiss, W. Tuning the Magnetic Properties of Metal Oxide Nanocrystal Heterostructures by Cation Exchange. *Nano Lett.* **2013**, *13*, 586–593.
(45) Shamsi, J.; Urban, A. S.; Imran, M.; De Trizio, L.; Manna, L. Metal Halide Perovskite Nanocrystals: Synthesis, Post-Synthesis Modifications, and Their Optical Properties. *Chem. Rev.* **2019**, *119*, 3296–3348.
(46) Park, J.; Joo, J.; Kwon, S. G.; Jang, Y.; Hyeon, T. Synthesis of Monodisperse Spherical Nanocrystals. *Angew. Chem., Int. Ed.* **2007**, *46*, 4630–4660.
(47) Sharifi Dehsari, H.; Halda Ribeiro, A.; Ersöz, B.; Tremel, W.; Jakob, G.; Asadi, K. Effect of Precursor Concentration on Size Evolution of Iron Oxide Nanoparticles. *CrystEngComm* **2017**, *19*, 6694–6702.
(48) Sharifi Dehsari, H.; Heidari, M.; Halda Ribeiro, A.; Tremel, W.; Jakob, G.; Donadio, D.; Potestio, R.; Asadi, K. Combined Experimental and Theoretical

Investigation of Heating Rate on Growth of Iron Oxide Nanoparticles. *Chem. Mater.* **2017**, *29*, 9648–9656.
(49) Sharifi Dehsari, H.; Harris, R. A.; Ribeiro, A. H.; Tremel, W.; Asadi, K. Optimizing the Binding Energy of the Surfactant to Iron Oxide Yields Truly Monodisperse Nanoparticles. *Langmuir* **2018**, *34*, 6582–6590.
(50) Tao, A. R.; Habas, S.; Yang, P. Shape Control of Colloidal Metal Nanocrystals. *Small* **2008**, *4*, 310–325.
(51) Wu, Z.; Yang, S.; Wu, W. Shape Control of Inorganic Nanoparticles from Solution. *Nanoscale* **2016**, *8*, 1237–1259.
(52) Mourdikoudis, S.; Liz-Marzán, L. M. Oleylamine in Nanoparticle Synthesis. *Chem. Mater.* **2013**, *25*, 1465–1476.
(53) Yu, T.; Joo, J.; Park, Y. Il; Hyeon, T. Large-Scale Nonhydrolytic Sol–Gel Synthesis of Uniform-Sized Ceria Nanocrystals with Spherical, Wire, and Tadpole Shapes. *Angew. Chem., Int. Ed.* **2005**, *44*, 7411–7414.
(54) Hou, Y.; Xu, Z.; Sun, S. Controlled Synthesis and Chemical Conversions of FeO Nanoparticles. *Angew. Chem., Int. Ed.* **2007**, *46*, 6329–6332.
(55) Bu, W.; Chen, Z.; Chen, F.; Shi, J. Oleic Acid/Oleylamine Cooperative-Controlled Crystallization Mechanism for Monodisperse Tetragonal Bipyramid $NaLa(MoO_4)_2$ Nanocrystals. *J. Phys. Chem. C* **2009**, *113*, 12176–12185.
(56) Dinh, C.-T.; Nguyen, T.-D.; Kleitz, F.; Do, T.-O. Shape-Controlled Synthesis of Highly Crystalline Titania Nanocrystals. *ACS Nano* **2009**, *3*, 3737–3743.
(57) Mohamed, M. B.; AbouZeid, K. M.; Abdelsayed, V.; Aljarash, A. A.; El-Shall, M. S. Growth Mechanism of Anisotropic Gold Nanocrystals via Microwave Synthesis: Formation of Dioleamide by Gold Nanocatalysis. *ACS Nano* **2010**, *4*, 2766–2772.
(58) Treadwell, L. J.; Boyle, T. J.; Bell, N. S.; Rodriguez, M. A.; Muntifering, B. R.; Hattar, K. Impact of Oleylamine: Oleic Acid Ratio on the Morphology of Yttria Nanomaterials. *J. Mater. Sci.* **2017**, *52*, 8268–8279.
(59) Costi, R.; Saunders, A. E.; Banin, U. Colloidal Hybrid Nanostructures: A New Type of Functional Materials. *Angew. Chem., Int. Ed.* **2010**, *49*, 4878–4897.
(60) Buck, M. R.; Bondi, J. F.; Schaak, R. E. A Total-Synthesis Framework for the Construction of High-Order Colloidal Hybrid Nanoparticles. *Nat. Chem.* **2012**, *4*, 37–44.
(61) Hodges, J. M.; Morse, J. R.; Fenton, J. L.; Ackerman, J. D.; Alameda, L. T.; Schaak, R. E. Insights into the Seeded-Growth Synthesis of Colloidal Hybrid Nanoparticles. *Chem. Mater.* **2017**, *29*, 106–119.
(62) Yu, H.; Chen, M.; Rice, P. M.; Wang, S. X.; White, R. L.; Sun, S. Dumbbell-like Bifunctional Au−Fe_3O_4 Nanoparticles. *Nano Lett.* **2005**, *5*, 379–382.
(63) Pearson, R. G. Hard and Soft Acids and Bases. *J. Am. Chem. Soc.* **1963**, *85*, 3533–3539.
(64) Pearson, R. G. *Chemical Hardness*; Wiley-VCH Verlag GmbH: Weinheim, Germany, 1997.
(65) Heuer-Jungemann, A.; Feliu, N.; Bakaimi, I.; Hamaly, M.; Alkilany, A.; Chakraborty, I.; Masood, A.; Casula, M. F.; Kostopoulou, A.; Oh, E.; Susumu, K.; Stewart, M. H.; Medintz, I. L.; Stratakis, E.; Parak, W. J.; Kanaras, A. G. The Role of Ligands in the Chemical Synthesis and Applications of Inorganic Nanoparticles. *Chem. Rev.* **2019**, *119*, 4819–4880.
(66) Owen, J. The Coordination Chemistry of Nanocrystal Surfaces. *Science* **2015**, *347*, 615–616.

(67) Liu, P.; Qin, R.; Fu, G.; Zheng, N. Surface Coordination Chemistry of Metal Nanomaterials. *J. Am. Chem. Soc.* **2017**, *139*, 2122–2131.
(68) Jin, R.; Zeng, C.; Zhou, M.; Chen, Y. Atomically Precise Colloidal Metal Nanoclusters and Nanoparticles: Fundamentals and Opportunities. *Chem. Rev.* **2016**, *116*, 10346–10413.
(69) Jadzinsky, P. D.; Calero, G.; Ackerson, C. J.; Bushnell, D. A.; Kornberg, R. D. Structure of a Thiol Monolayer–Protected Gold Nanoparticle at 1.1 Å Resolution. *Science* **2007**, *318*, 430–433.
(70) Whetten, R. L.; Price, R. C. Nano-Golden Order. *Science* **2007**, *318*, 407–408.
(71) Häkkinen, H. The Gold–Sulfur Interface at the Nanoscale. *Nat. Chem.* **2012**, *4*, 443–455.
(72) Zeng, C. Precision at the Nanoscale: On the Structure and Property Evolution of Gold Nanoclusters. *Pure Appl. Chem.* **2018**, *90*, 1409–1427.
(73) Groom, C. R.; Bruno, I. J.; Lightfoot, M. P.; Ward, S. C. The Cambridge Structural Database. *Acta Crystallogr., Sect. B: Struct. Sci. Cryst. Eng. Mater.* **2016**, *72*, 171–179.
(74) Gary, D. C.; Flowers, S. E.; Kaminsky, W.; Petrone, A.; Li, X.; Cossairt, B. M. Single-Crystal and Electronic Structure of a 1.3 nm Indium Phosphide Nanocluster. *J. Am. Chem. Soc.* **2016**, *138*, 1510–1513.
(75) Pujari, S. P.; Scheres, L.; Marcelis, A. T. M.; Zuilhof, H. Covalent Surface Modification of Oxide Surfaces. *Angew. Chem., Int. Ed.* **2014**, *53*, 6322–6356.
(76) Boles, M. A.; Engel, M.; Talapin, D. V. Self-Assembly of Colloidal Nanocrystals: From Intricate Structures to Functional Materials. *Chem. Rev.* **2016**, *116*, 11220–11289.
(77) *CRC Handbook of Chemistry and Physics*, 97th ed.; Haynes, W. M., Ed.; CRC Press, Taylor & Francis Group: Boca Raton, FL, 2016.
(78) Jeitschko, W.; Pottgen, R.; Hoffmann, R.-D. Structural Chemistry of Hard Materials. In *Handbook of Ceramic Hard Materials*; Riedel, R., Ed.; Wiley-VCH Verlag GmbH: Weinheim, Germany, 2000; pp 2–40.
(79) Pauling, L.; Sturdivant, J. H. XV. The Crystal Structure of Brookite. *Zeitschrift für Krist. - Cryst. Mater.* **1928**, *68*, 239–256.
(80) Linsebigler, A. L.; Lu, G.; Yates, J. T. Photocatalysis on TiO_2 Surfaces: Principles, Mechanisms, and Selected Results. *Chem. Rev.* **1995**, *95*, 735–758.
(81) Wells, A. F. The Structures of Crystals. In *Solid State Physics*; Seitz, F., Turnbull, D., Eds.; Academic Press, 1958; Vol. 7, pp 425–503.
(82) Holleman, A. F.; Wiberg, E.; Wiberg, N. *Anorganische Chemie. Band 2: Nebengruppenelemente, Lanthanoide, Actinoide, Transactinoide*, 103rd ed.; Walter de Gruyter GmbH & Co KG: Berlin, 2016.
(83) Vejux, A.; Courtine, P. Interfacial Reactions between V_2O_5 and TiO_2 (Anatase): Role of the Structural Properties. *J. Solid State Chem.* **1978**, *23*, 93–103.
(84) Momma, K.; Izumi, F. *VESTA 3* for Three-Dimensional Visualization of Crystal, Volumetric and Morphology Data. *J. Appl. Crystallogr.* **2011**, *44*, 1272–1276.
(85) Downs, R. T.; Hall-Wallace, M. The *American Mineralogist* Crystal Structure Database. *Am. Mineral.* **2003**, *88*, 247–250.
(86) Baur, W. H.; Khan, A. A. Rutile-Type Compounds. IV. SiO_2, GeO_2 and a Comparison with other Rutile-Type Structures. *Acta Crystallogr. Sect. B Struct. Crystallogr. Cryst. Chem.* **1971**, *27*, 2133–2139.
(87) Horn, M.; Schwerdtfeger, C. F.; Meagher, E. P. Refinement of the Structure of Anatase at Several Temperatures. *Zeitschrift für Krist.* **1972**, *136*, 273–281.

(88) Meagher, E. P.; Lager, G. A. Polyhedral Thermal Expansion in the TiO_2 Polymorphs: Refinement of the Crystal Structures of Rutile and Brookite at High Temperature. *Can. Mineral.* **1979**, *17*, 77–85.
(89) Hanaor, D. A. H.; Sorrell, C. C. Review of the Anatase to Rutile Phase Transformation. *J. Mater. Sci.* **2011**, *46*, 855–874.
(90) Zhang, H.; Banfield, J. F. Structural Characteristics and Mechanical and Thermodynamic Properties of Nanocrystalline TiO_2. *Chem. Rev.* **2014**, *114*, 9613–9644.
(91) Zhang, H.; Banfield, J. F. Understanding Polymorphic Phase Transformation Behavior during Growth of Nanocrystalline Aggregates: Insights from TiO_2. *J. Phys. Chem. B* **2000**, *104*, 3481–3487.
(92) Bøjesen, E. D.; Iversen, B. B. The Chemistry of Nucleation. *CrystEngComm* **2016**, *18*, 8332–8353.
(93) Kränzlin, N.; Staniuk, M.; Heiligtag, F. J.; Luo, L.; Emerich, H.; van Beek, W.; Niederberger, M.; Koziej, D. Rationale for the Crystallization of Titania Polymorphs in Solution. *Nanoscale* **2014**, *6*, 14716–14723.
(94) Chen, X.; Mao, S. S. Titanium Dioxide Nanomaterials: Synthesis, Properties, Modifications, and Applications. *Chem. Rev.* **2007**, *107*, 2891–2959.
(95) Niederberger, M.; Garnweitner, G. Organic Reaction Pathways in the Nonaqueous Synthesis of Metal Oxide Nanoparticles. *Chem. - Eur. J.* **2006**, *12*, 7282–7302.
(96) van Embden, J.; Chesman, A. S. R.; Jasieniak, J. J. The Heat-Up Synthesis of Colloidal Nanocrystals. *Chem. Mater.* **2015**, *27*, 2246–2285.
(97) Niederberger, M.; Bartl, M. H.; Stucky, G. D. Benzyl Alcohol and Titanium Tetrachloride−A Versatile Reaction System for the Nonaqueous and Low-Temperature Preparation of Crystalline and Luminescent Titania Nanoparticles. *Chem. Mater.* **2002**, *14*, 4364–4370.
(98) Niederberger, M.; Bartl, M. H.; Stucky, G. D. Benzyl Alcohol and Transition Metal Chlorides as a Versatile Reaction System for the Nonaqueous and Low-Temperature Synthesis of Crystalline Nano-Objects with Controlled Dimensionality. *J. Am. Chem. Soc.* **2002**, *124*, 13642–13643.
(99) Pan, D.; Zhao, N.; Wang, Q.; Jiang, S.; Ji, X.; An, L. Facile Synthesis and Characterization of Luminescent TiO2 Nanocrystals. *Adv. Mater.* **2005**, *17*, 1991–1995.
(100) Li, J.; Wu, Q.; Wu, J. Synthesis of Nanoparticles via Solvothermal and Hydrothermal Methods. In *Handbook of Nanoparticles*; Springer International Publishing: Cham, Switzerland, 2016; pp 295–328.
(101) Liu, L.; Gu, X.; Ji, Z.; Zou, W.; Tang, C.; Gao, F.; Dong, L. Anion-Assisted Synthesis of TiO_2 Nanocrystals with Tunable Crystal Forms and Crystal Facets and Their Photocatalytic Redox Activities in Organic Reactions. *J. Phys. Chem. C* **2013**, *117*, 18578–18587.
(102) Chae, S. Y.; Park, M. K.; Lee, S. K.; Kim, T. Y.; Kim, S. K.; Lee, W. I. Preparation of Size-Controlled TiO_2 Nanoparticles and Derivation of Optically Transparent Photocatalytic Films. *Chem. Mater.* **2003**, *15*, 3326–3331.
(103) Kim, C.; Moon, B. K.; Park, J.; Choi, B.; Seo, H.-J. Solvothermal Synthesis of Nanocrystalline TiO_2 in Toluene with Surfactant. *J. Cryst. Growth* **2003**, *257*, 309–315.
(104) Trentler, T. J.; Denler, T. E.; Bertone, J. F.; Agrawal, A.; Colvin, V. L. Synthesis of TiO_2 Nanocrystals by Nonhydrolytic Solution-Based Reactions. *J. Am. Chem.*

Soc. **1999**, *121*, 1613–1614.
(105) Zhang, Z.; Zhong, X.; Liu, S.; Li, D.; Han, M. Aminolysis Route to Monodisperse Titania Nanorods with Tunable Aspect Ratio. *Angew. Chem., Int. Ed.* **2005**, *44*, 3466–3470.
(106) Buonsanti, R.; Grillo, V.; Carlino, E.; Giannini, C.; Kipp, T.; Cingolani, R.; Cozzoli, P. D. Nonhydrolytic Synthesis of High-Quality Anisotropically Shaped Brookite TiO_2 Nanocrystals. *J. Am. Chem. Soc.* **2008**, *130*, 11223–11233.
(107) Gordon, T. R.; Cargnello, M.; Paik, T.; Mangolini, F.; Weber, R. T.; Fornasiero, P.; Murray, C. B. Nonaqueous Synthesis of TiO_2 Nanocrystals Using TiF_4 to Engineer Morphology, Oxygen Vacancy Concentration, and Photocatalytic Activity. *J. Am. Chem. Soc.* **2012**, *134*, 6751–6761.
(108) Burrows, N. D.; Vartanian, A. M.; Abadeer, N. S.; Grzincic, E. M.; Jacob, L. M.; Lin, W.; Li, J.; Dennison, J. M.; Hinman, J. G.; Murphy, C. J. Anisotropic Nanoparticles and Anisotropic Surface Chemistry. *J. Phys. Chem. Lett.* **2016**, *7*, 632–641.
(109) Kominami, H.; Takada, Y.; Yamagiwa, H.; Kera, Y.; Inoue, M.; Inui, T. Synthesis of Thermally Stable Nanocrystalline Anatase by High-Temperature Hydrolysis of Titanium Alkoxide with Water Dissolved in Organic Solvent from Gas Phase. *J. Mater. Sci. Lett.* **1996**, *15*, 197–200.
(110) Ruzicka, J.-Y.; Bakar, F. A.; Thomsen, L.; Cowie, B. C.; McNicoll, C.; Kemmitt, T.; Brand, H. E. A.; Ingham, B.; Andersson, G. G.; Golovko, V. B. XPS and NEXAFS Study of Fluorine Modified TiO_2 Nano-Ovoids Reveals Dependence of Ti^{3+} Surface Population on the Modifying Agent. *RSC Adv.* **2014**, *4*, 20649–20658.
(111) Livage, J.; Henry, M.; Sanchez, C. Sol-Gel Chemistry of Transition Metal Oxides. *Prog. Solid State Chem.* **1988**, *18*, 259–341.
(112) Pottier, A.; Chanéac, C.; Tronc, E.; Mazerolles, L.; Jolivet, J.-P. Synthesis of Brookite TiO_2 Nanoparticles by Thermolysis of $TiCl_4$ in Strongly Acidic Aqueous Media. *J. Mater. Chem.* **2001**, *11*, 1116–1121.
(113) Tarasov, A.; Goertz, V.; Goodilin, E.; Nirschl, H. Hydrolytic Stages of Titania Nanoparticles Formation Jointly Studied by SAXS, DLS, and TEM. *J. Phys. Chem. C* **2013**, *117*, 12800–12805.
(114) Jordan, V.; Javornik, U.; Plavec, J.; Podgornik, A.; Rečnik, A. Self-Assembly of Multilevel Branched Rutile-Type TiO_2 Structures via Oriented Lateral and Twin Attachment. *Sci. Rep.* **2016**, *6*, 24216.
(115) Kumar, S. G.; Rao, K. S. R. K. Polymorphic Phase Transition Among the Titania Crystal Structures Using a Solution-Based Approach: From Precursor Chemistry to Nucleation Process. *Nanoscale* **2014**, *6*, 11574–11632.
(116) Rozes, L.; Sanchez, C. Titanium Oxo-Clusters: Precursors for a Lego-like Construction of Nanostructured Hybrid Materials. *Chem. Soc. Rev.* **2011**, *40*, 1006–1030.
(117) Coppens, P.; Chen, Y.; Trzop, E. Crystallography and Properties of Polyoxotitanate Nanoclusters. *Chem. Rev.* **2014**, *114*, 9645–9661.
(118) Fang, W.-H.; Zhang, L.; Zhang, J. Synthetic Strategies, Diverse Structures and Tuneable Properties of Polyoxo-Titanium Clusters. *Chem. Soc. Rev.* **2018**, *47*, 404–421.
(119) Zhang, G.; Hou, J.; Tung, C.-H.; Wang, Y. Small Titanium Oxo Clusters: Primary Structures of Titanium(IV) in Water. *Inorg. Chem.* **2016**, *55*, 3212–3214.

(120) Fang, W.-H.; Zhang, L.; Zhang, J. A 3.6 nm Ti_{52}–Oxo Nanocluster with Precise Atomic Structure. *J. Am. Chem. Soc.* **2016**, *138*, 7480–7483.
(121) Stötzel, J.; Lützenkirchen-Hecht, D.; Frahm, R.; Santilli, C. V.; Pulcinelli, S. H.; Kaminski, R.; Fonda, E.; Villain, F.; Briois, V. QEXAFS and UV/Vis Simultaneous Monitoring of the TiO_2-Nanoparticles Formation by Hydrolytic Sol−Gel Route. *J. Phys. Chem. C* **2010**, *114*, 6228–6236.
(122) Benedict, J. B.; Freindorf, R.; Trzop, E.; Cogswell, J.; Coppens, P. Large Polyoxotitanate Clusters: Well-Defined Models for Pure-Phase TiO_2 Structures and Surfaces. *J. Am. Chem. Soc.* **2010**, *132*, 13669–13671.
(123) Hou, J.; Hu, J.; Sun, Q.; Zhang, G.; Tung, C.-H.; Wang, Y. A Post-Functionalizable *Iso*-Polyoxotitanate Cage Cluster. *Inorg. Chem.* **2016**, *55*, 7075–7078.
(124) Zhang, G.; Hou, J.; Li, M.; Tung, C.-H.; Wang, Y. Counteranion-Stabilized Titanium(IV) Isopolyoxocationic Clusters Isolated from Water. *Inorg. Chem.* **2016**, *55*, 4704–4709.
(125) Zhang, G.; Liu, C.; Long, D.-L.; Cronin, L.; Tung, C.-H.; Wang, Y. Water-Soluble Pentagonal-Prismatic Titanium-Oxo Clusters. *J. Am. Chem. Soc.* **2016**, *138*, 11097–11100.
(126) Sun, Q.; Liu, C.; Zhang, G.; Zhang, J.; Tung, C.-H.; Wang, Y. Aqueous Isolation of 17-Nuclear Zr/Hf Oxide Clusters during the Hydrothermal Synthesis of ZrO_2/HfO_2. *Chem. - Eur. J.* **2018**, *24*, 14701–14706.
(127) Ruther, R. E.; Baker, B. M.; Son, J.; Casey, W. H.; Nyman, M. Hafnium Sulfate Prenucleation Clusters and the Hf_{18} Polyoxometalate Red Herring. *Inorg. Chem.* **2014**, *53*, 4234–4242.
(128) Sadeghi, O.; Zakharov, L. N.; Nyman, M. Aqueous Formation and Manipulation of the Iron-Oxo Keggin Ion. *Science* **2015**, *347*, 1359–1362.
(129) Steunou, N.; Kickelbick, G.; Boubekeur, K.; Sanchez, C. A New Polyoxo–Alkoxo Titanium Cluster of the Keggin Family: Synthesis and Characterization by X-Ray Diffraction and NMR Spectroscopy. *J. Chem. Soc., Dalton Trans.* **1999**, No. 21, 3653–3655.
(130) Hong, Z.-F.; Xu, S.-H.; Yan, Z.-H.; Lu, D.-F.; Kong, X.-J.; Long, L.-S.; Zheng, L.-S. A Large Titanium Oxo Cluster Featuring a Well-Defined Structural Unit of Rutile. *Cryst. Growth Des.* **2018**, *18*, 4864–4868.
(131) Tomita, K.; Petrykin, V.; Kobayashi, M.; Shiro, M.; Yoshimura, M.; Kakihana, M. A Water-Soluble Titanium Complex for the Selective Synthesis of Nanocrystalline Brookite, Rutile, and Anatase by a Hydrothermal Method. *Angew. Chem., Int. Ed.* **2006**, *45*, 2378–2381.
(132) Benedict, J. B.; Coppens, P. The Crystalline Nanocluster Phase as a Medium for Structural and Spectroscopic Studies of Light Absorption of Photosensitizer Dyes on Semiconductor Surfaces. *J. Am. Chem. Soc.* **2010**, *132*, 2938–2944.
(133) Testino, A.; Canevali, C.; D'Arienzo, M.; Scotti, R.; Morazzoni, F.; Bellobono, I. R.; Buscaglia, V.; Polizzi, S. Optimizing the Photocatalytic Properties of Hydrothermal TiO_2 by the Control of Phase Composition and Particle Morphology. A Systematic Approach. *J. Am. Chem. Soc.* **2007**, *129*, 3564–3575.
(134) Reyes-Coronado, D.; Rodríguez-Gattorno, G.; Espinosa-Pesqueira, M. E.; Cab, C.; de Coss, R.; Oskam, G. Phase-Pure TiO_2 Nanoparticles: Anatase, Brookite and Rutile. *Nanotechnology* **2008**, *19*, 145605.
(135) Mi, J.-L.; Clausen, C.; Bremholm, M.; Lock, N.; Jensen, K. M. Ø.; Christensen, M.; Iversen, B. B. Rapid Hydrothermal Preparation of Rutile TiO_2 Nanoparticles

by Simultaneous Transformation of Primary Brookite and Anatase: An in Situ Synchrotron PXRD Study. *Cryst. Growth Des.* **2012**, *12*, 6092–6097.

(136) Mi, J.-L.; Jensen, K. M. Ø.; Tyrsted, C.; Bremholm, M.; Iversen, B. B. *In Situ* Total X-Ray Scattering Study of the Formation Mechanism and Structural Defects in Anatase TiO_2 Nanoparticles under Hydrothermal Conditions. *CrystEngComm* **2015**, *17*, 6868–6877.

(137) Day, V. W.; Eberspacher, T. A.; Klemperer, W. G.; Park, C. W. Dodecatitanates: A New Family of Stable Polyoxotitanates. *J. Am. Chem. Soc.* **1993**, *115*, 8469–8470.

(138) Joo, J.; Kwon, S. G.; Yu, T.; Cho, M.; Lee, J.; Yoon, J.; Hyeon, T. Large-Scale Synthesis of TiO_2 Nanorods via Nonhydrolytic Sol−Gel Ester Elimination Reaction and Their Application to Photocatalytic Inactivation of *E. coli*. *J. Phys. Chem. B* **2005**, *109*, 15297–15302.

(139) Barrow, H.; Brown, D. A.; Alcock, N. W.; Errington, W.; Wallbridge, M. G. H. Titanium Oxo Carboxylate Compounds. Crystal and Molecular Structures of [{TiCl2(O2CEt)(EtCO2H)}2O] and [Ti3Cl3O2(O2CEt)5] and an Unusual Quantitative Conversion of a Ti_2O to a Ti_3O_2 Oxo Derivative. *J. Chem. Soc., Dalton Trans.* **1994**, *12*, 3533–3538.

(140) Boyle, T. J.; Alam, T. M.; Tafoya, C. J.; Scott, B. L. Formic Acid Modified $Ti(OCHMe_2)_4$. Syntheses, Characterization, and X-ray Structures of $Ti_4(\mu4\text{-}O)(\mu\text{-}O)(OFc)_2(\mu\text{-}OR)_4(OR)_6$ and $Ti_6(\mu3\text{-}O)_6(OFc)_6(OR)_6$. *Inorg. Chem.* **1998**, *37*, 5588–5594.

(141) Lazzeri, M.; Vittadini, A.; Selloni, A. Structure and Energetics of Stoichiometric TiO_2 Anatase Surfaces. *Phys. Rev. B* **2001**, *63*, 155409.

(142) Diebold, U.; Ruzycki, N.; Herman, G. S.; Selloni, A. One Step Towards Bridging the Materials Gap: Surface Studies of TiO_2 Anatase. *Catal. Today* **2003**, *85*, 93–100.

(143) Selloni, A. Anatase Shows Its Reactive Side. *Nat. Mater.* **2008**, *7*, 613–615.

(144) Wu, B.; Guo, C.; Zheng, N.; Xie, Z.; Stucky, G. D. Nonaqueous Production of Nanostructured Anatase with High-Energy Facets. *J. Am. Chem. Soc.* **2008**, *130*, 17563–17567.

(145) Bourikas, K.; Kordulis, C.; Lycourghiotis, A. Titanium Dioxide (Anatase and Rutile): Surface Chemistry, Liquid–Solid Interface Chemistry, and Scientific Synthesis of Supported Catalysts. *Chem. Rev.* **2014**, *114*, 9754–9823.

(146) Diebold, U. The Surface Science of Titanium Dioxide. *Surf. Sci. Rep.* **2003**, *48*, 53–229.

(147) Chen, W.; Kuang, Q.; Wang, Q.; Xie, Z. Engineering a High Energy Surface of Anatase TiO_2 Crystals Towards Enhanced Performance for Energy Conversion and Environmental Applications. *RSC Adv.* **2015**, *5*, 20396–20409.

(148) Fang, W. Q.; Gong, X.-Q.; Yang, H. G. On the Unusual Properties of Anatase TiO_2 Exposed by Highly Reactive Facets. *J. Phys. Chem. Lett.* **2011**, *2*, 725–734.

(149) Chen, H. Y.; Zahraa, O.; Bouchy, M. Inhibition of the Adsorption and Photocatalytic Degradation of an Organic Contaminant in an Aqueous Suspension of TiO_2 by Inorganic Ions. *J. Photochem. Photobiol. A Chem.* **1997**, *108*, 37–44.

(150) Zhang, H.; Yu, H.; Zheng, A.; Li, S.; Shen, W.; Deng, F. Reactivity Enhancement of 2-Propanol Photocatalysis on SO_4^{2-}/TiO_2: Insights from Solid-State NMR Spectroscopy. *Environ. Sci. Technol.* **2008**, *42*, 5316–5321.

(151) Cornejo, J.; Steinle, J.; Boehm, H. P. Über die Chemie der Oberfläche des

Titandioxids, V Die Oberflächenacidität von Titandioxid und von mit Phosphationen belegtem Titandioxid. *Zeitschrift für Naturforsch. B* **1978**, *33*, 1238–1241.

(152) Tielens, F.; Gervais, C.; Deroy, G.; Jaber, M.; Stievano, L.; Coelho Diogo, C.; Lambert, J.-F. Characterization of Phosphate Species on Hydrated Anatase TiO_2 Surfaces. *Langmuir* **2016**, *32*, 997–1008.

(153) Farner Budarz, J.; Turolla, A.; Piasecki, A. F.; Bottero, J.-Y.; Antonelli, M.; Wiesner, M. R. Influence of Aqueous Inorganic Anions on the Reactivity of Nanoparticles in TiO_2 Photocatalysis. *Langmuir* **2017**, *33*, 2770–2779.

(154) Ghosh, S.; Manna, L. The Many "Facets" of Halide Ions in the Chemistry of Colloidal Inorganic Nanocrystals. *Chem. Rev.* **2018**, *118*, 7804–7864.

(155) Yang, H. G.; Sun, C. H.; Qiao, S. Z.; Zou, J.; Liu, G.; Smith, S. C.; Cheng, H. M.; Lu, G. Q. Anatase TiO_2 Single Crystals with a Large Percentage of Reactive Facets. *Nature* **2008**, *453*, 638–641.

(156) Wu, X.; Chen, Z.; Lu, G. Q. M.; Wang, L. Nanosized Anatase TiO_2 Single Crystals with Tunable Exposed (001) Facets for Enhanced Energy Conversion Efficiency of Dye-Sensitized Solar Cells. *Adv. Funct. Mater.* **2011**, *21*, 4167–4172.

(157) Liu, G.; Yang, H. G.; Pan, J.; Yang, Y. Q.; Lu, G. Q. M.; Cheng, H.-M. Titanium Dioxide Crystals with Tailored Facets. *Chem. Rev.* **2014**, *114*, 9559–9612.

(158) Wang, Q.; Chen, C.; Zhao, D.; Ma, W.; Zhao, J. Change of Adsorption Modes of Dyes on Fluorinated TiO_2 and Its Effect on Photocatalytic Degradation of Dyes under Visible Irradiation. *Langmuir* **2008**, *24*, 7338–7345.

(159) Han, X.; Kuang, Q.; Jin, M.; Xie, Z.; Zheng, L. Synthesis of Titania Nanosheets with a High Percentage of Exposed (001) Facets and Related Photocatalytic Properties. *J. Am. Chem. Soc.* **2009**, *131*, 3152–3153.

(160) Thomas, A. G.; Jackman, M. J.; Wagstaffe, M.; Radtke, H.; Syres, K.; Adell, J.; Lévy, A.; Martsinovich, N. Adsorption Studies of *p*-Aminobenzoic Acid on the Anatase TiO_2 (101) Surface. *Langmuir* **2014**, *30*, 12306–12314.

(161) Zhang, L.; Cole, J. M.; Dai, C. Variation in Optoelectronic Properties of Azo Dye-Sensitized TiO_2 Semiconductor Interfaces with Different Adsorption Anchors: Carboxylate, Sulfonate, Hydroxyl and Pyridyl Groups. *ACS Appl. Mater. Interfaces* **2014**, *6*, 7535–7546.

(162) Wagstaffe, M.; Thomas, A. G.; Jackman, M. J.; Torres-Molina, M.; Syres, K. L.; Handrup, K. An Experimental Investigation of the Adsorption of a Phosphonic Acid on the Anatase TiO_2 (101) Surface. *J. Phys. Chem. C* **2016**, *120*, 1693–1700.

(163) Etschel, S. H.; Tykwinski, R. R.; Halik, M. Enhancing the Dispersibility of TiO_2 Nanorods and Gaining Control over Region-Selective Layer Formation. *Langmuir* **2016**, *32*, 10604–10609.

(164) Zeininger, L.; Stiegler, L. M. S.; Portilla, L.; Halik, M.; Hirsch, A. Manufacturing Nanoparticles with Orthogonally Adjustable Dispersibility in Hydrocarbons, Fluorocarbons, and Water. *ChemistryOpen* **2018**, *7*, 282–287.

(165) Ganbold, E.-O.; Lee, Y.; Lee, K.; Kwon, O.; Joo, S.-W. Interfacial Behavior of Benzoic Acid and Phenylphosphonic Acid on Nanocrystalline TiO_2 Surfaces. *Chem. - An Asian J.* **2010**, *5*, 852–858.

(166) Raza, M.; Bachinger, A.; Zahn, N.; Kickelbick, G. Interaction and UV-Stability of Various Organic Capping Agents on the Surface of Anatase Nanoparticles. *Materials (Basel).* **2014**, *7*, 2890–2912.

(167) Lamiel-Garcia, O.; Fernandez-Hevia, D.; Caballero, A. C.; Illas, F. Adsorption Properties of Trifluoroacetic Acid on Anatase (101) and (001) Surfaces: A Density Functional Theory Study. *Phys. Chem. Chem. Phys.* **2015**, *17*, 23627–23633.
(168) Le, N. Q.; Ekuma, C. E.; Dunlap, B. I.; Gunlycke, D. First-Principles Calculations of Sarin Adsorption on Anatase Surfaces. *J. Phys. Chem. C* **2018**, *122*, 2832–2839.
(169) Peng, Y.-K.; Hu, Y.; Chou, H.-L.; Fu, Y.; Teixeira, I. F.; Zhang, L.; He, H.; Tsang, S. C. E. Mapping Surface-Modified Titania Nanoparticles with Implications for Activity and Facet Control. *Nat. Commun.* **2017**, *8*, 675.
(170) Peng, Y.-K.; Chou, H.-L.; Edman Tsang, S. C. Differentiating Surface Titanium Chemical States of Anatase TiO_2 Functionalized with Various Groups. *Chem. Sci.* **2018**, *9*, 2493–2500.
(171) Limousin, G.; Gaudet, J.-P.; Charlet, L.; Szenknect, S.; Barthès, V.; Krimissa, M. Sorption Isotherms: A Review on Physical Bases, Modeling and Measurement. *Appl. Geochemistry* **2007**, *22*, 249–275.
(172) Zeininger, L.; Portilla, L.; Halik, M.; Hirsch, A. Quantitative Determination and Comparison of the Surface Binding of Phosphonic Acid, Carboxylic Acid, and Catechol Ligands on TiO_2 Nanoparticles. *Chem. - Eur. J.* **2016**, *22*, 13506–13512.
(173) Saiz-Poseu, J.; Mancebo-Aracil, J.; Nador, F.; Busqué, F.; Ruiz-Molina, D. The Chemistry behind Catechol-Based Adhesion. *Angew. Chem., Int. Ed.* **2018**, *58*, 696–714.
(174) Avdeef, A.; Sofen, S. R.; Bregante, T. L.; Raymond, K. N. Coordination Chemistry of Microbial Iron Transport Compounds. 9. Stability Constants for Catechol Models of Enterobactin. *J. Am. Chem. Soc.* **1978**, *100*, 5362–5370.
(175) Sever, M. J.; Wilker, J. J. Absorption Spectroscopy and Binding Constants for First-Row Transition Metal Complexes of a DOPA-Containing Peptide. *Dalton Trans.* **2006**, 813–822.
(176) Shultz, M. D.; Reveles, J. U.; Khanna, S. N.; Carpenter, E. E. Reactive Nature of Dopamine as a Surface Functionalization Agent in Iron Oxide Nanoparticles. *J. Am. Chem. Soc.* **2007**, *129*, 2482–2487.
(177) Hocking, R. K.; DeBeer George, S.; Raymond, K. N.; Hodgson, K. O.; Hedman, B.; Solomon, E. I. Fe L-Edge X-ray Absorption Spectroscopy Determination of Differential Orbital Covalency of Siderophore Model Compounds: Electronic Structure Contributions to High Stability Constants. *J. Am. Chem. Soc.* **2010**, *132*, 4006–4015.
(178) Pierpont, C. G.; Lange, C. W. The Chemistry of Transition Metal Complexes Containing Catechol and Semiquinone Ligands. *Prog. Inorg. Chem.* **1994**, *41*, 331–442.
(179) Hendrickson, D. N.; Pierpont, C. G. Valence Tautomeric Transition Metal Complexes. *Top. Curr. Chem.* **2004**, *234*, 63–95.
(180) Moser, J.; Punchihewa, S.; Infelta, P. P.; Graetzel, M. Surface Complexation of Colloidal Semiconductors Strongly Enhances Interfacial Electron-Transfer Rates. *Langmuir* **1991**, *7*, 3012–3018.
(181) Kaim, W.; Schwederski, B. Non-Innocent Ligands in Bioinorganic Chemistry—An Overview. *Coord. Chem. Rev.* **2010**, *254*, 1580–1588.
(182) Praneeth, V. K. K.; Ringenberg, M. R.; Ward, T. R. Redox-Active Ligands in Catalysis. *Angew. Chem., Int. Ed.* **2012**, *51*, 10228–10234.

(183) Patil, N.; Jérôme, C.; Detrembleur, C. Recent Advances in the Synthesis of Catechol-Derived (Bio)Polymers for Applications in Energy Storage and Environment. *Prog. Polym. Sci.* **2018**, *82*, 34–91.
(184) Rodríguez, R.; Blesa, M. A.; Regazzoni, A. E. Surface Complexation at the TiO_2 (Anatase)/Aqueous Solution Interface: Chemisorption of Catechol. *J. Colloid Interface Sci.* **1996**, *177*, 122–131.
(185) Creutz, C.; Chou, M. H. Binding of Catechols to Mononuclear Titanium(IV) and to 1- and 5-nm TiO_2 Nanoparticles. *Inorg. Chem.* **2008**, *47*, 3509–3514.
(186) Savić, T. D.; Čomor, M. I.; Nedeljković, J. M.; Veljković, D. Ž.; Zarić, S. D.; Rakić, V. M.; Janković, I. A. The Effect of Substituents on the Surface Modification of Anatase Nanoparticles with Catecholate-Type Ligands: A Combined DFT and Experimental Study. *Phys. Chem. Chem. Phys.* **2014**, *16*, 20796–20805.
(187) Li, S.-C.; Chu, L.-N.; Gong, X.-Q.; Diebold, U. Hydrogen Bonding Controls the Dynamics of Catechol Adsorbed on a TiO_2(110) Surface. *Science* **2010**, *328*, 882–884.
(188) Liu, L.-M.; Li, S.-C.; Cheng, H.; Diebold, U.; Selloni, A. Growth and Organization of an Organic Molecular Monolayer on TiO_2: Catechol on Anatase (101). *J. Am. Chem. Soc.* **2011**, *133*, 7816–7823.
(189) Li, S.-C.; Wang, J.; Jacobson, P.; Gong, X.-Q.; Selloni, A.; Diebold, U. Correlation between Bonding Geometry and Band Gap States at Organic−Inorganic Interfaces: Catechol on Rutile TiO_2(110). *J. Am. Chem. Soc.* **2009**, *131*, 980–984.
(190) Syres, K. L.; Thomas, A. G.; Flavell, W. R.; Spencer, B. F.; Bondino, F.; Malvestuto, M.; Preobrajenski, A.; Grätzel, M. Adsorbate-Induced Modification of Surface Electronic Structure: Pyrocatechol Adsorption on the Anatase TiO_2 (101) and Rutile TiO_2 (110) Surfaces. *J. Phys. Chem. C* **2012**, *116*, 23515–23525.
(191) Kristoffersen, H. H.; Shea, J.-E.; Metiu, H. Catechol and HCl Adsorption on TiO_2(110) in Vacuum and at the Water–TiO_2 Interface. *J. Phys. Chem. Lett.* **2015**, *6*, 2277–2281.
(192) Gigant, K.; Rammal, A.; Henry, M. Synthesis and Molecular Structures of Some New Titanium(IV) Aryloxides. *J. Am. Chem. Soc.* **2001**, *123*, 11632–11637.
(193) Assi, H.; Mouchaham, G.; Steunou, N.; Devic, T.; Serre, C. Titanium Coordination Compounds: From Discrete Metal Complexes to Metal–Organic Frameworks. *Chem. Soc. Rev.* **2017**, *46*, 3431–3452.
(194) Bazhenova, T. A.; Kovaleva, N. V.; Shilov, G. V.; Petrova, G. N.; Kuznetsov, D. A. A Family of Titanium Complexes with Catechol Ligands: Structural Investigation and Catalytic Application. *Eur. J. Inorg. Chem.* **2016**, *2016*, 5215–5221.
(195) Boyle, T. J.; Tribby, L. J.; Alam, T. M.; Bunge, S. D.; Holland, G. P. Catechol Derivatives of Group 4 and 5 Compounds. *Polyhedron* **2005**, *24*, 1143–1152.
(196) Davidson, M. G.; Jones, M. D.; Lunn, M. D.; Mahon, M. F. Synthesis and X-ray Structures of New Titanium(IV) Aryloxides and Their Exploitation for the Ring Opening Polymerization of ε-Caprolactone. *Inorg. Chem.* **2006**, *45*, 2282–2287.
(197) Chaumont, C.; Mobian, P.; Henry, M. An Unprecedented High Nuclearity Catecholato-Based Ti(IV)-Architecture Bearing Labile Pyridine Ligands. *Dalton Trans.* **2014**, *43*, 3416–3419.
(198) Chaumont, C.; Huen, E.; Huguenard, C.; Mobian, P.; Henry, M. Toward Colored Reticular Titanium-Based Hybrid Networks: Evaluation of the Reactivity of the

$[Ti_8O_8(OOCCH_2Bu^t)_{16}]$ Wheel with Phenol, Resorcinol and Catechol. *Polyhedron* **2013**, *57*, 70–76.
(199) Sokolow, J. D.; Trzop, E.; Chen, Y.; Tang, J.; Allen, L. J.; Crabtree, R. H.; Benedict, J. B.; Coppens, P. Binding Modes of Carboxylate- and Acetylacetonate-Linked Chromophores to Homodisperse Polyoxotitanate Nanoclusters. *J. Am. Chem. Soc.* **2012**, *134*, 11695–11700.
(200) Habisreutinger, S. N.; Schmidt-Mende, L.; Stolarczyk, J. K. Photocatalytic Reduction of CO_2 on TiO_2 and Other Semiconductors. *Angew. Chem., Int. Ed.* **2013**, *52*, 7372–7408.
(201) Asahi, R.; Morikawa, T.; Irie, H.; Ohwaki, T. Nitrogen-Doped Titanium Dioxide as Visible-Light-Sensitive Photocatalyst: Designs, Developments, and Prospects. *Chem. Rev.* **2014**, *114*, 9824–9852.
(202) Hu, W.; Li, L.; Li, G.; Tang, C.; Sun, L. High-Quality Brookite TiO_2 Flowers: Synthesis, Characterization, and Dielectric Performance. *Cryst. Growth Des.* **2009**, *9*, 3676–3682.
(203) Yan, X.; Chen, X. Titanium Dioxide Nanomaterials. In *Encyclopedia of Inorganic and Bioinorganic Chemistry*; John Wiley & Sons, Ltd: Chichester, UK, 2015; Vol. 107, pp 1–38.
(204) Dahl, M.; Liu, Y.; Yin, Y. Composite Titanium Dioxide Nanomaterials. *Chem. Rev.* **2014**, *114*, 9853–9889.
(205) Beranek, R. (Photo)electrochemical Methods for the Determination of the Band Edge Positions of TiO_2-Based Nanomaterials. *Adv. Phys. Chem.* **2011**, *2011*, 1–20.
(206) Chen, S.; Wang, L.-W. Thermodynamic Oxidation and Reduction Potentials of Photocatalytic Semiconductors in Aqueous Solution. *Chem. Mater.* **2012**, *24*, 3659–3666.
(207) Duonghong, D.; Ramsden, J.; Grätzel, M. Dynamics of Interfacial Electron-Transfer Processes in Colloidal Semiconductor Systems. *J. Am. Chem. Soc.* **1982**, *104*, 2977–2985.
(208) Maeda, K. Photocatalytic Water Splitting Using Semiconductor Particles: History and Recent Developments. *J. Photochem. Photobiol. C Photochem. Rev.* **2011**, *12*, 237–268.
(209) Ma, Y.; Wang, X.; Jia, Y.; Chen, X.; Han, H.; Li, C. Titanium Dioxide-Based Nanomaterials for Photocatalytic Fuel Generations. *Chem. Rev.* **2014**, *114*, 9987–10043.
(210) Shwetharani, R.; Sakar, M.; Fernando, C. A. N.; Binas, V.; Balakrishna, R. G. Recent Advances and Strategies to Tailor the Energy Levels, Active Sites and Electron Mobility in Titania and Its Doped/Composite Analogues for Hydrogen Evolution in Sunlight. *Catal. Sci. Technol.* **2019**, *9*, 12–46.
(211) Hayyan, M.; Hashim, M. A.; AlNashef, I. M. Superoxide Ion: Generation and Chemical Implications. *Chem. Rev.* **2016**, *116*, 3029–3085.
(212) Nosaka, Y.; Nosaka, A. Y. Generation and Detection of Reactive Oxygen Species in Photocatalysis. *Chem. Rev.* **2017**, *117*, 11302–11336.
(213) Hoffmann, M. R.; Martin, S. T.; Choi, W.; Bahnemann, D. W. Environmental Applications of Semiconductor Photocatalysis. *Chem. Rev.* **1995**, *95*, 69–96.
(214) Chen, C.; Ma, W.; Zhao, J. Semiconductor-Mediated Photodegradation of Pollutants under Visible-Light Irradiation. *Chem. Soc. Rev.* **2010**, *39*, 4206–4219.
(215) Ong, W.; Tan, L.; Chai, S.; Yong, S.; Mohamed, A. R. Facet-Dependent Photocatalytic Properties of TiO_2-Based Composites for Energy Conversion and

Environmental Remediation. *ChemSusChem* **2014**, *7*, 690–719.
(216) Li, X.; Yu, J.; Jaroniec, M.; Chen, X. Cocatalysts for Selective Photoreduction of CO_2 into Solar Fuels. *Chem. Rev.* **2019**, *119*, 3962–4179.
(217) Shiraishi, Y.; Hirai, T. Selective Organic Transformations on Titanium Oxide-Based Photocatalysts. *J. Photochem. Photobiol. C Photochem. Rev.* **2008**, *9*, 157–170.
(218) Augugliaro, V.; Caronna, T.; Di Paola, A.; Marcì, G.; Pagliaro, M.; Palmisano, G.; Palmisano, L. TiO_2-Based Photocatalysis for Organic Synthesis. In *Environmentally Benign Photocatalysts*; Anpo, M., Kamat, P. V., Eds.; Nanostructure Science and Technology; Springer: New York, NY, 2010; pp 623–645.
(219) Bloh, J. Z.; Marschall, R. Heterogeneous Photoredox Catalysis: Reactions, Materials, and Reaction Engineering. *Eur. J. Org. Chem.* **2017**, *2017*, 2085–2094.
(220) Riente, P.; Noël, T. Application of Metal Oxide Semiconductors in Light-Driven Organic Transformations. *Catal. Sci. Technol.* **2019**, *9*, 5186–5232.
(221) Wang, H.; Yan, J.; Chang, W.; Zhang, Z. Practical Synthesis of Aromatic Amines by Photocatalytic Reduction of Aromatic Nitro Compounds on Nanoparticles N-Doped TiO_2. *Catal. Commun.* **2009**, *10*, 989–994.
(222) Shiraishi, Y.; Togawa, Y.; Tsukamoto, D.; Tanaka, S.; Hirai, T. Highly Efficient and Selective Hydrogenation of Nitroaromatics on Photoactivated Rutile Titanium Dioxide. *ACS Catal.* **2012**, *2*, 2475–2481.
(223) Zhang, M.; Chen, C.; Ma, W.; Zhao, J. Visible-Light-Induced Aerobic Oxidation of Alcohols in a Coupled Photocatalytic System of Dye-Sensitized TiO_2 and TEMPO. *Angew. Chem., Int. Ed.* **2008**, *47*, 9730–9733.
(224) Lang, X.; Zhao, J.; Chen, X. Visible-Light-Induced Photoredox Catalysis of Dye-Sensitized Titanium Dioxide: Selective Aerobic Oxidation of Organic Sulfides. *Angew. Chem., Int. Ed.* **2016**, *55*, 4697–4700.
(225) Wang, Z.; Lang, X. Visible Light Photocatalysis of Dye-Sensitized TiO_2: The Selective Aerobic Oxidation of Amines to Imines. *Appl. Catal. B Environ.* **2018**, *224*, 404–409.
(226) Zoller, J.; Fabry, D. C.; Rueping, M. Unexpected Dual Role of Titanium Dioxide in the Visible Light Heterogeneous Catalyzed C–H Arylation of Heteroarenes. *ACS Catal.* **2015**, *5*, 3900–3904.
(227) Ma, D.; Liu, A.; Li, S.; Lu, C.; Chen, C. TiO_2 Photocatalysis for C–C Bond Formation. *Catal. Sci. Technol.* **2018**, *8*, 2030–2045.
(228) Vanýsek, P. Electrochemical Series. In *CRC Handbook of Chemistry and Physics*; Haynes, W. M., Ed.; CRC Press, Taylor & Francis Group: Boca Raton, FL, 2016; pp 5-78−5-84.
(229) Wardman, P. Reduction Potentials of One Electron Couples Involving Free Radicals in Aqueous Solution. *J. Phys. Chem. Ref. Data* **1989**, *18*, 1637–1755.
(230) O'Regan, B.; Grätzel, M. A Low-Cost, High-Efficiency Solar Cell Based on Dye-Sensitized Colloidal TiO_2 Films. *Nature* **1991**, *353*, 737–740.
(231) Hagfeldt, A.; Boschloo, G.; Sun, L.; Kloo, L.; Pettersson, H. Dye-Sensitized Solar Cells. *Chem. Rev.* **2010**, *110*, 6595–6663.
(232) Duncan, W. R.; Prezhdo, O. V. Theoretical Studies of Photoinduced Electron Transfer in Dye-Sensitized TiO_2. *Annu. Rev. Phys. Chem.* **2007**, *58*, 143–184.
(233) Ooyama, Y.; Harima, Y. Photophysical and Electrochemical Properties, and Molecular Structures of Organic Dyes for Dye-Sensitized Solar Cells.

ChemPhysChem **2012**, *13*, 4032–4080.
(234) Zhang, L.; Cole, J. M. Anchoring Groups for Dye-Sensitized Solar Cells. *ACS Appl. Mater. Interfaces* **2015**, *7*, 3427–3455.
(235) Persson, P.; Bergström, R.; Lunell, S. Quantum Chemical Study of Photoinjection Processes in Dye-Sensitized TiO_2 Nanoparticles. *J. Phys. Chem. B* **2000**, *104*, 10348–10351.
(236) Tachan, Z.; Hod, I.; Zaban, A. The TiO_2-Catechol Complex: Coupling Type II Sensitization with Efficient Catalysis of Water Oxidation. *Adv. Energy Mater.* **2014**, *4*, 1301249.
(237) Sánchez-de-Armas, R.; San-Miguel, M. A.; Oviedo, J.; Sanz, J. F. Direct vs. Indirect Mechanisms for Electron Injection in DSSC: Catechol and Alizarin. *Comput. Theor. Chem.* **2011**, *975*, 99–105.
(238) Sánchez-de-Armas, R.; Oviedo, J.; San Miguel, M. Á.; Sanz, J. F. Direct vs Indirect Mechanisms for Electron Injection in Dye-Sensitized Solar Cells. *J. Phys. Chem. C* **2011**, *115*, 11293–11301.
(239) Zhang, G.; Kim, G.; Choi, W. Visible Light Driven Photocatalysis Mediated *via* Ligand-to-Metal Charge Transfer (LMCT): An Alternative Approach to Solar Activation of Titania. *Energy Environ. Sci.* **2014**, *7*, 954–966.
(240) Kamegawa, T.; Seto, H.; Matsuura, S.; Yamashita, H. Preparation of Hydroxynaphthalene-Modified TiO_2 via Formation of Surface Complexes and their Applications in the Photocatalytic Reduction of Nitrobenzene under Visible-Light Irradiation. *ACS Appl. Mater. Interfaces* **2012**, *4*, 6635–6639.
(241) Kominami, H.; Kitagawa, S.; Okubo, Y.; Fukui, M.; Hashimoto, K.; Imamura, K. Organically Modified Titania Having a Metal Catalyst: A New Type of Liquid-Phase Hydrogen-Transfer Photocatalyst Working under Visible Light Irradiation and H_2-Free Conditions. *Phys. Chem. Chem. Phys.* **2016**, *18*, 16076–16079.
(242) Fukui, M.; Tanaka, A.; Hashimoto, K.; Kominami, H. Visible Light-Induced Heterogeneous Meerwein–Ponndorf–Verley-Type Reduction of an Aldehyde Group over an Organically Modified Ttitanium Dioxide Photocatalyst. *Chem. Commun.* **2017**, *53*, 4215–4218.
(243) Cao, Y.; Denny, M. S.; Caspar, J. V.; Farneth, W. E.; Guo, Q.; Ionkin, A. S.; Johnson, L. K.; Lu, M.; Malajovich, I.; Radu, D.; Rosenfeld, H. D.; Choudhury, K. R.; Wu, W. High-Efficiency Solution-Processed $Cu_2ZnSn(S,Se)_4$ Thin-Film Solar Cells Prepared from Binary and Ternary Nanoparticles. *J. Am. Chem. Soc.* **2012**, *134*, 15644–15647.
(244) Liaqat, F.; Tahir, M. N.; Schechtel, E.; Kappl, M.; Auernhammer, G. K.; Char, K.; Zentel, R.; Butt, H.-J.; Tremel, W. High-Performance TiO_2 Nanoparticle/DOPA-Polymer Composites. *Macromol. Rapid Commun.* **2015**, *36*, 1129–1137.
(245) Schechtel, E.; Yan, Y.; Xu, X.; Cang, Y.; Tremel, W.; Wang, Z.; Li, B.; Fytas, G. Elastic Modulus and Thermal Conductivity of Thiol-Ene/TiO_2 Nanocomposites. *J. Phys. Chem. C* **2017**, *121*, 25568–25575.
(246) Kharisov, B. I.; Dias, H. V. R.; Kharissova, O. V.; Vázquez, A.; Peña, Y.; Gómez, I. Solubilization, Dispersion and Stabilization of Magnetic Nanoparticles in Water and Non-Aqueous Solvents: Recent Trends. *RSC Adv.* **2014**, *4*, 45354–45381.
(247) Ling, D.; Lee, N.; Hyeon, T. Chemical Synthesis and Assembly of Uniformly Sized Iron Oxide Nanoparticles for Medical Applications. *Acc. Chem. Res.* **2015**, *48*, 1276–1285.

(248) Harrington, M. J.; Masic, A.; Holten-Andersen, N.; Waite, J. H.; Fratzl, P. Iron-Clad Fibers: A Metal-Based Biological Strategy for Hard Flexible Coatings. *Science* **2010**, *328*, 216–220.
(249) Tang, W.; Policastro, G. M.; Hua, G.; Guo, K.; Zhou, J.; Wesdemiotis, C.; Doll, G. L.; Becker, M. L. Bioactive Surface Modification of Metal Oxides via Catechol-Bearing Modular Peptides: Multivalent-Binding, Surface Retention, and Peptide Bioactivity. *J. Am. Chem. Soc.* **2014**, *136*, 16357–16367.
(250) Lin, W.; Walter, J.; Burger, A.; Maid, H.; Hirsch, A.; Peukert, W.; Segets, D. A General Approach To Study the Thermodynamics of Ligand Adsorption to Colloidal Surfaces Demonstrated by Means of Catechols Binding to Zinc Oxide Quantum Dots. *Chem. Mater.* **2015**, *27*, 358–369.
(251) Lin, W.; Schmidt, J.; Mahler, M.; Schindler, T.; Unruh, T.; Meyer, B.; Peukert, W.; Segets, D. Influence of Tail Groups during Functionalization of ZnO Nanoparticles on Binding Enthalpies and Photoluminescence. *Langmuir* **2017**, *33*, 13581–13589.
(252) Xu, C.; Xu, K.; Gu, H.; Zheng, R.; Liu, H.; Zhang, X.; Guo, Z.; Xu, B. Dopamine as a Robust Anchor to Immobilize Functional Molecules on the Iron Oxide Shell of Magnetic Nanoparticles. *J. Am. Chem. Soc.* **2004**, *126*, 9938–9939.
(253) Yuen, A. K. L.; Hutton, G. a.; Masters, A. F.; Maschmeyer, T. The Interplay of Catechol Ligands with Nanoparticulate Iron Oxides. *Dalton Trans.* **2012**, *41*, 2545–2559.
(254) Becker, G.; Ackermann, L.-M.; Schechtel, E.; Klapper, M.; Tremel, W.; Wurm, F. R. Joining Two Natural Motifs: Catechol-Containing Poly(phosphoester)s. *Biomacromolecules* **2017**, *18*, 767–777.
(255) Niederberger, M.; Garnweitner, G.; Krumeich, F.; Nesper, R.; Cölfen, H.; Antonietti, M. Tailoring the Surface and Solubility Properties of Nanocrystalline Titania by a Nonaqueous In Situ Functionalization Process. *Chem. Mater.* **2004**, *16*, 1202–1208.
(256) Tahir, M. N.; Eberhardt, M.; Theato, P.; Faiß, S.; Janshoff, A.; Gorelik, T.; Kolb, U.; Tremel, W. Reactive Polymers: A Versatile Toolbox for the Immobilization of Functional Molecules on TiO_2 Nanoparticles. *Angew. Chem., Int. Ed.* **2006**, *45*, 908–912.
(257) Ward, M. D.; McCleverty, J. A. Non-Innocent Behaviour in Mononuclear and Polynuclear Complexes: Consequences for Redox and Electronic Spectroscopic Properties. *J. Chem. Soc., Dalton Trans.* **2002**, 275–288.
(258) Kaim, W. Manifestations of Noninnocent Ligand Behavior. *Inorg. Chem.* **2011**, *50*, 9752–9765.
(259) Lyaskovskyy, V.; de Bruin, B. Redox Non-Innocent Ligands: Versatile New Tools to Control Catalytic Reactions. *ACS Catal.* **2012**, *2*, 270–279.
(260) Daniel, P.; Shylin, S. I.; Lu, H.; Tahir, M. N.; Panthöfer, M.; Weidner, T.; Möller, A.; Ksenofontov, V.; Tremel, W. The Surface Chemistry of Iron Oxide Nanocrystals: Surface Reduction of γ-Fe_2O_3 to Fe_3O_4 by Redox-Active Catechol Surface Ligands. *J. Mater. Chem. C* **2018**, *6*, 326–333.
(261) Nauth, A. M.; Schechtel, E.; Dören, R.; Tremel, W.; Opatz, T. TiO_2 Nanoparticles Functionalized with Non-innocent Ligands Allow Oxidative Photocyanation of Amines with Visible/Near-Infrared Photons. *J. Am. Chem. Soc.* **2018**, *140*, 14169–14177.
(262) Carp, O.; Huisman, C. L.; Reller, A. Photoinduced Reactivity of Titanium Dioxide. *Prog. Solid State Chem.* **2004**, *32*, 33–177.

(263) Schneider, J.; Matsuoka, M.; Takeuchi, M.; Zhang, J.; Horiuchi, Y.; Anpo, M.; Bahnemann, D. W. Understanding TiO_2 Photocatalysis: Mechanisms and Materials. *Chem. Rev.* **2014**, *114*, 9919–9986.
(264) Rajh, T.; Dimitrijevic, N. M.; Bissonnette, M.; Koritarov, T.; Konda, V. Titanium Dioxide in the Service of the Biomedical Revolution. *Chem. Rev.* **2014**, *114*, 10177–10216.
(265) Daghrir, R.; Drogui, P.; Robert, D. Modified TiO_2 for Environmental Photocatalytic Applications: A Review. *Ind. Eng. Chem. Res.* **2013**, *52*, 3581–3599.
(266) Zhang, Y.; Jiang, Z.; Huang, J.; Lim, L. Y.; Li, W.; Deng, J.; Gong, D.; Tang, Y.; Lai, Y.; Chen, Z. Titanate and Titania Nanostructured Materials for Environmental and Energy Applications: A Review. *RSC Adv.* **2015**, *5*, 79479–79510.
(267) Su, R.; Dimitratos, N.; Liu, J.; Carter, E.; Althahban, S.; Wang, X.; Shen, Y.; Wendt, S.; Wen, X.; Niemantsverdriet, J. W.; Iversen, B. B.; Kiely, C. J.; Hutchings, G. J.; Besenbacher, F. Mechanistic Insight into the Interaction Between a Titanium Dioxide Photocatalyst and Pd Cocatalyst for Improved Photocatalytic Performance. *ACS Catal.* **2016**, *6*, 4239–4247.
(268) Ye, M.; Jia, J.; Wu, Z.; Qian, C.; Chen, R.; O'Brien, P. G.; Sun, W.; Dong, Y.; Ozin, G. A. Synthesis of Black TiO_x Nanoparticles by Mg Reduction of TiO_2 Nanocrystals and their Application for Solar Water Evaporation. *Adv. Energy Mater.* **2017**, *7*, 1601811.
(269) Macyk, W.; Szaciłowski, K.; Stochel, G.; Buchalska, M.; Kuncewicz, J.; Łabuz, P. Titanium(IV) Complexes as Direct TiO_2 Photosensitizers. *Coord. Chem. Rev.* **2010**, *254*, 2687–2701.
(270) Ooyama, Y.; Kanda, M.; Uenaka, K.; Ohshita, J. Effect of Substituents in Catechol Dye Sensitizers on Photovoltaic Performance of Type II Dye-Sensitized Solar Cells. *ChemPhysChem* **2015**, *16*, 3049–3057.
(271) Moreels, I.; Fritzinger, B.; Martins, J. C.; Hens, Z. Surface Chemistry of Colloidal PbSe Nanocrystals. *J. Am. Chem. Soc.* **2008**, *130*, 15081–15086.
(272) Liu, X.; Yu, M.; Kim, H.; Mameli, M.; Stellacci, F. Determination of Monolayer-Protected Gold Nanoparticle Ligand–Shell Morphology Using NMR. *Nat. Commun.* **2012**, *3*, 1182.
(273) De Roo, J.; Van Driessche, I.; Martins, J. C.; Hens, Z. Colloidal Metal Oxide Nanocrystal Catalysis by Sustained Chemically Driven Ligand Displacement. *Nat. Mater.* **2016**, *15*, 517–521.
(274) Hens, Z.; Martins, J. C. A Solution NMR Toolbox for Characterizing the Surface Chemistry of Colloidal Nanocrystals. *Chem. Mater.* **2013**, *25*, 1211–1221.
(275) Marbella, L. E.; Millstone, J. E. NMR Techniques for Noble Metal Nanoparticles. *Chem. Mater.* **2015**, *27*, 2721–2739.
(276) Vroman, L. Effect of Adsorbed Proteins on the Wettability of Hydrophilic and Hydrophobic Solids. *Nature* **1962**, *196*, 476–477.
(277) Casals, E.; Pfaller, T.; Duschl, A.; Oostingh, G. J.; Puntes, V. Time Evolution of the Nanoparticle Protein Corona. *ACS Nano* **2010**, *4*, 3623–3632.
(278) Schladt, T. D.; Schneider, K.; Shukoor, M. I.; Natalio, F.; Bauer, H.; Tahir, M. N.; Weber, S.; Schreiber, L. M.; Schröder, H. C.; Müller, W. E. G.; Tremel, W. Highly Soluble Multifunctional MnO Nanoparticles for Simultaneous Optical and MRI Imaging and Cancer Treatment Using Photodynamic Therapy. *J. Mater. Chem.* **2010**, *20*, 8297–8304.

(279) Smith, A. M.; Johnston, K. A.; Crawford, S. E.; Marbella, L. E.; Millstone, J. E. Ligand Density Quantification on Colloidal Inorganic Nanoparticles. *Analyst* **2017**, *142*, 11–29.
(280) Anderson, N. C.; Hendricks, M. P.; Choi, J. J.; Owen, J. S. Ligand Exchange and the Stoichiometry of Metal Chalcogenide Nanocrystals: Spectroscopic Observation of Facile Metal-Carboxylate Displacement and Binding. *J. Am. Chem. Soc.* **2013**, *135*, 18536–18548.
(281) Tong, L.; Lu, E.; Pichaandi, J.; Cao, P.; Nitz, M.; Winnik, M. A. Quantification of Surface Ligands on $NaYF_4$ Nanoparticles by Three Independent Analytical Techniques. *Chem. Mater.* **2015**, *27*, 4899–4910.
(282) Arita, T.; Yoo, J.; Adschiri, T. Relation between the Solution-State Behavior of Self-Assembled Monolayers on Nanoparticles and Dispersion of Nanoparticles in Organic Solvents. *J. Phys. Chem. C* **2011**, *115*, 3899–3909.
(283) Fritzinger, B.; Capek, R. K.; Lambert, K.; Martins, J. C.; Hens, Z. Utilizing Self-Exchange to Address the Binding of Carboxylic Acid Ligands to CdSe Quantum Dots. *J. Am. Chem. Soc.* **2010**, *132*, 10195–10201.
(284) De Roo, J.; Van den Broeck, F.; De Keukeleere, K.; Martins, J. C.; Van Driessche, I.; Hens, Z. Unravelling the Surface Chemistry of Metal Oxide Nanocrystals, the Role of Acids and Bases. *J. Am. Chem. Soc.* **2014**, *136*, 9650–9657.
(285) De Roo, J.; Justo, Y.; De Keukeleere, K.; Van den Broeck, F.; Martins, J. C.; Van Driessche, I.; Hens, Z. Carboxylic-Acid-Passivated Metal Oxide Nanocrystals: Ligand Exchange Characteristics of a New Binding Motif. *Angew. Chem., Int. Ed.* **2015**, *54*, 6488–6491.
(286) Hwang, E. T.; Sheikh, K.; Orchard, K. L.; Hojo, D.; Radu, V.; Lee, C.-Y.; Ainsworth, E.; Lockwood, C.; Gross, M. A.; Adschiri, T.; Reisner, E.; Butt, J. N.; Jeuken, L. J. C. A Decaheme Cytochrome as a Molecular Electron Conduit in Dye-Sensitized Photoanodes. *Adv. Funct. Mater.* **2015**, *25*, 2308–2315.
(287) Thermo Fisher Scientific Inc. Centrifuge Ware Chemical Resistance Table https://assets.thermofisher.com/TFS-Assets/LSG/brochures/CentrifugeWare-Chemical-Resistance-Table-SSLSPCWCHEMTBL-EN.pdf (accessed Nov 16, 2018).
(288) Wolf, R.; Kaul, B. L. Plastics, Additives. In *Ullmann's Encyclopedia of Industrial Chemistry*; Wiley-VCH Verlag GmbH & Co. KGaA: Weinheim, Germany, 2000.
(289) Lewis, L.; Robson, M.; Vecherkina, Y.; Ji, C.; Beall, G. Interference with Spectrophotometric Analysis of Nucleic Acids and Proteins by Leaching of Chemicals from Plastic Tubes. *Biotechniques* **2010**, *48*, 297–302.
(290) McDonald, G. R.; Hudson, A. L.; Dunn, S. M. J.; You, H.; Baker, G. B.; Whittal, R. M.; Martin, J. W.; Jha, A.; Edmondson, D. E.; Holt, A. Bioactive Contaminants Leach from Disposable Laboratory Plasticware. *Science* **2008**, *322*, 917.
(291) Olivieri, A.; Degenhardt, O. S.; McDonald, G. R.; Narang, D.; Paulsen, I. M.; Kozuska, J. L.; Holt, A. On the Disruption of Biochemical and Biological Assays by Chemicals Leaching from Disposable Laboratory Plasticware. *Can. J. Physiol. Pharmacol.* **2012**, *90*, 697–703.
(292) Cuhra, M.; Bøhn, T.; Cuhra, P. *In Plastico*: Laboratory Material Newness Affects Growth and Reproduction of *Daphnia Magna* Reared in 50-ml Polypropylene Tubes. *Sci. Rep.* **2017**, *7*, 46442.

(293) Singh, S.; Tomar, R.; ten Brinck, S.; De Roo, J.; Geiregat, P.; Martins, J. C.; Infante, I.; Hens, Z. Colloidal CdSe Nanoplatelets, A Model for Surface Chemistry/Optoelectronic Property Relations in Semiconductor Nanocrystals. *J. Am. Chem. Soc.* **2018**, *140*, 13292–13300.
(294) Fritzinger, B.; Moreels, I.; Lommens, P.; Koole, R.; Hens, Z.; Martins, J. C. In Situ Observation of Rapid Ligand Exchange in Colloidal Nanocrystal Suspensions Using Transfer NOE Nuclear Magnetic Resonance Spectroscopy. *J. Am. Chem. Soc.* **2009**, *131*, 3024–3032.
(295) Davis, K.; Qi, B.; Witmer, M.; Kitchens, C. L.; Powell, B. A.; Mefford, O. T. Quantitative Measurement of Ligand Exchange on Iron Oxides via Radiolabeled Oleic Acid. *Langmuir* **2014**, *30*, 10918–10925.
(296) Davis, K.; Cole, B.; Ghelardini, M.; Powell, B. A.; Mefford, O. T. Quantitative Measurement of Ligand Exchange with Small-Molecule Ligands on Iron Oxide Nanoparticles via Radioanalytical Techniques. *Langmuir* **2016**, *32*, 13716–13727.
(297) Bixner, O.; Lassenberger, A.; Baurecht, D.; Reimhult, E. Complete Exchange of the Hydrophobic Dispersant Shell on Monodisperse Superparamagnetic Iron Oxide Nanoparticles. *Langmuir* **2015**, *31*, 9198–9204.
(298) Nernst, W. Verteilung eines Stoffes zwischen zwei Lösungsmitteln und zwischen Lösungsmittel und Dampfraum. *Z. Phys. Chem.* **1891**, *8U*, 110–139.
(299) Langmuir, I. The Adsorption of Gases on Plane Surfaces of Glass, Mica and Platinum. *J. Am. Chem. Soc.* **1918**, *40*, 1361–1403.
(300) Arrhenius, S. Über die Reaktionsgeschwindigkeit bei der Inversion von Rohrzucker durch Säuren. *Z. Phys. Chem.* **1889**, *4U*, 226–248.
(301) Polanyi, M.; Wigner, E. Über die Interferenz von Eigenschwingungen als Ursache von Energieschwankungen und chemischer Umsetzungen. *Z. Phys. Chem.* **1928**, *139A*, 439–452.
(302) Fitzgerald, S. A.; Shinbrough, K.; Rigdon, K. H.; Rowsell, J. L. C.; Kapelewski, M. T.; Pang, S. H.; Lawler, K. V.; Forster, P. M. Temperature-Programmed Desorption for Isotope Separation in Nanoporous Materials. *J. Phys. Chem. C* **2018**, *122*, 1995–2001.
(303) Slabbert, N. P. Ionisation of Some Flavanols and Dihydroflavonols. *Tetrahedron* **1977**, *33*, 821–824.
(304) Bartušek, M. Komplexe des Uranyls mit phenolischen Liganden VIII. Potentiometrische Untersuchung der Uranylkomplexe mit *p*-Nitrophenol, 4-Nitrobenzcatechin, 2,3-Dihydroxynaphthalin, Alizarin S, Pyrogallolcarbonsäure, Pyrogallolsulfonsäure und mit dem Gemisch von. *Collect. Czechoslov. Chem. Commun.* **1967**, *32*, 757–773.
(305) Hostetler, M. J.; Templeton, A. C.; Murray, R. W. Dynamics of Place-Exchange Reactions on Monolayer-Protected Gold Cluster Molecules. *Langmuir* **1999**, *15*, 3782–3789.
(306) Atkins, P. W.; Overton, T. L.; Rourke, J. P.; Weller, M. T.; Armstrong, F. A. *Shriver and Atkins' Inorganic Chemistry*, 5th ed.; Oxford University Press: Oxford, U.K., 2010.
(307) Heinecke, C. L.; Ni, T. W.; Malola, S.; Mäkinen, V.; Wong, O. A.; Häkkinen, H.; Ackerson, C. J. Structural and Theoretical Basis for Ligand Exchange on Thiolate Monolayer Protected Gold Nanoclusters. *J. Am. Chem. Soc.* **2012**, *134*, 13316–13322.
(308) Fernando, A.; Aikens, C. M. Ligand Exchange Mechanism on Thiolate

Monolayer Protected $Au_{25}(SR)_{18}$ Nanoclusters. *J. Phys. Chem. C* **2015**, *119*, 20179–20187.
(309) Saniepay, M.; Mi, C.; Liu, Z.; Abel, E. P.; Beaulac, R. Insights into the Structural Complexity of Colloidal CdSe Nanocrystal Surfaces: Correlating the Efficiency of Nonradiative Excited-State Processes to Specific Defects. *J. Am. Chem. Soc.* **2018**, *140*, 1725–1736.
(310) Drijvers, E.; De Roo, J.; Martins, J. C.; Infante, I.; Hens, Z. Ligand Displacement Exposes Binding Site Heterogeneity on CdSe Nanocrystal Surfaces. *Chem. Mater.* **2018**, *30*, 1178–1186.
(311) Dong, A.; Ye, X.; Chen, J.; Kang, Y.; Gordon, T.; Kikkawa, J. M.; Murray, C. B. A Generalized Ligand-Exchange Strategy Enabling Sequential Surface Functionalization of Colloidal Nanocrystals. *J. Am. Chem. Soc.* **2011**, *133*, 998–1006.
(312) Rosen, E. L.; Buonsanti, R.; Llordes, A.; Sawvel, A. M.; Milliron, D. J.; Helms, B. A. Exceptionally Mild Reactive Stripping of Native Ligands from Nanocrystal Surfaces by Using Meerwein's Salt. *Angew. Chem., Int. Ed.* **2012**, *51*, 684–689.
(313) Doris, S. E.; Lynch, J. J.; Li, C.; Wills, A. W.; Urban, J. J.; Helms, B. A. Mechanistic Insight into the Formation of Cationic Naked Nanocrystals Generated under Equilibrium Control. *J. Am. Chem. Soc.* **2014**, *136*, 15702–15710.
(314) Röcker, C.; Pötzl, M.; Zhang, F.; Parak, W. J.; Nienhaus, G. U. A Quantitative Fluorescence Study of Protein Monolayer Formation on Colloidal Nanoparticles. *Nat. Nanotechnol.* **2009**, *4*, 577–580.
(315) Monopoli, M. P.; Åberg, C.; Salvati, A.; Dawson, K. A. Biomolecular Coronas Provide the Biological Identity of Nanosized Materials. *Nat. Nanotechnol.* **2012**, *7*, 779–786.
(316) Wu, H.; Yang, Y.; Cao, Y. C. Synthesis of Colloidal Uranium−Dioxide Nanocrystals. *J. Am. Chem. Soc.* **2006**, *128*, 16522–16523.
(317) Cara, C.; Musinu, A.; Mameli, V.; Ardu, A.; Niznansky, D.; Bursik, J.; Scorciapino, M. A.; Manzo, G.; Cannas, C. Dialkylamide as Both Capping Agent and Surfactant in a Direct Solvothermal Synthesis of Magnetite and Titania Nanoparticles. *Cryst. Growth Des.* **2015**, *15*, 2364–2372.
(318) Dalu, F.; Scorciapino, M. A.; Cara, C.; Luridiana, A.; Musinu, A.; Casu, M.; Secci, F.; Cannas, C. A Catalyst-Free, Waste-Less Ethanol-Based Solvothermal Synthesis of Amides. *Green Chem.* **2018**, *20*, 375–381.
(319) Matthijs, D.; Jamtvedt, S.; Härkönen, M.; Øysaed, H. Process of Injection Moulding a Syringe from Polyethylene Wax Containing Polypropylenne, Syringe Obtained Thereby and Particulate Composition Therefor. U.S. Patent 7,182,987, February 27, 2007.
(320) Karpuz, M.; Özer, A. Y. Syringes as Medical Devices. *Fabad J. Pharm. Sci.* **2016**, *41*, 27–37.
(321) Heggs, T. G. Polypropylene. In *Ullmann's Encyclopedia of Industrial Chemistry*; Wiley-VCH Verlag GmbH & Co. KGaA: Weinheim, Germany, 2011.
(322) Lammerting, H. Release Agents. In *Ullmann's Encyclopedia of Industrial Chemistry*; Wiley-VCH Verlag GmbH & Co. KGaA: Weinheim, Germany, 2000.
(323) Ferguson, R. C. 220-MHz Proton Magnetic Resonance Spectra of Polymers. II. Polypropylene and Ethylene-Propylene Copolymers. *Macromolecules* **1971**, *4*, 324–329.
(324) Tonelli, A. E.; Schilling, F. C. ^{13}C NMR Chemical Shifts and the Microstructure

of Polymers. *Acc. Chem. Res.* **1981**, *14*, 233–238.
(325) Tonelli, A. E.; White, J. L. NMR Spectroscopy of Polymers. In *Physical Properties of Polymers Handbook*; Springer: New York, NY, 2007; pp 359–383.
(326) Cheng, H. N.; Lee, G. H. Two-Dimensional NMR Spectroscopy and Automated ^{1}H NMR Analysis of Ethylene-Propylene Copolymers. *Polym. Bull.* **1984**, *12*, 463–470.
(327) Cheng, H. N. ^{13}C NMR Analysis of Ethylene−Propylene Rubbers. *Macromolecules* **1984**, *17*, 1950–1955.
(328) Crain, W. O.; Zambelli, A.; Roberts, J. D. Carbon-13 Magnetic Resonance Spectra of Some Polypropylenes and Ethylene-Propylene Copolymers. *Macromolecules* **1971**, *4*, 330–332.
(329) Mirabella, F. M. Impact Polypropylene Copolymers: Fractionation and Structural Characterization. *Polymer* **1993**, *34*, 1729–1735.
(330) McKeen, L. W. Plastics Used in Medical Devices. In *Handbook of Polymer Applications in Medicine and Medical Devices*; Modjarrad, K., Ebnesajjad, S., Eds.; Plastics Design Library; William Andrew Publishing: Oxford, 2014; pp 21–53.
(331) Santonja-Blasco, L.; Rungswang, W.; Alamo, R. G. Characterization and Morphological Distribution of Ethylene Content in Impact Propylene Copolymers. *Macromol. Symp.* **2018**, *377*, 1700046.
(332) Carman, C. J.; Harrington, R. A.; Wilkes, C. E. Monomer Sequence Distribution in Ethylene–Propylene Rubber Measured by ^{13}C NMR. 3. Use of Reaction Probability Model. *Macromolecules* **1977**, *10*, 536–544.
(333) Lai, W.-C. The Effect of Self-Assembled Nanofibrils on the Morphology and Microstructure of Poly(L-Lactic Acid). *Soft Matter* **2011**, *7*, 3844–3851.
(334) Okesola, B. O.; Vieira, V. M. P.; Cornwell, D. J.; Whitelaw, N. K.; Smith, D. K. 1,3:2,4-Dibenzylidene-D-Sorbitol (DBS) and Its Derivatives – Efficient, Versatile and Industrially-Relevant Low-Molecular-Weight Gelators with over 100 Years of History and a Bright Future. *Soft Matter* **2015**, *11*, 4768–4787.
(335) Rossi, A.; Odian, G.; Zhang, J. End Groups in 1-Butene Polymerization via Methylaluminoxane and Zirconocene Catalyst. *Macromolecules* **1995**, *28*, 1739–1749.
(336) Sasaki, D.; Suzuki, Y.; Hagiwara, T.; Yano, S.; Sawaguchi, T. Synthesis and Applications of Triblock and Multiblock Copolymers Using Telechelic Oligopropylene. *Polymer* **2008**, *49*, 4094–4100.
(337) Shiono, T.; Soga, K. Synthesis of Terminally Aluminum-Functionalized Polypropylene. *Macromolecules* **1992**, *25*, 3356–3361.
(338) Polito, L.; Colombo, M.; Monti, D.; Melato, S.; Caneva, E.; Prosperi, D. Resolving the Structure of Ligands Bound to the Surface of Superparamagnetic Iron Oxide Nanoparticles by High-Resolution Magic-Angle Spinning NMR Spectroscopy. *J. Am. Chem. Soc.* **2008**, *130*, 12712–12724.
(339) De Roo, J.; De Keukeleere, K.; Hens, Z.; Van Driessche, I. From Ligands to Binding Motifs and Beyond; the Enhanced Versatility of Nanocrystal Surfaces. *Dalton Trans.* **2016**, *45*, 13277–13283.
(340) Sun, S.; Gebauer, D.; Cölfen, H. A General Strategy for Colloidal Stable Ultrasmall Amorphous Mineral Clusters in Organic Solvents. *Chem. Sci.* **2017**, *8*, 1400–1405.
(341) Kluenker, M.; Mondeshki, M.; Nawaz Tahir, M.; Tremel, W. Monitoring Thiol–Ligand Exchange on Au Nanoparticle Surfaces. *Langmuir* **2018**, *34*, 1700–1710.

(342) Kisch, H. Semiconductor Photocatalysis − Mechanistic and Synthetic Aspects. *Angew. Chem., Int. Ed.* **2013**, *52*, 812–847.
(343) Kisch, H. Semiconductor Photocatalysis for Chemoselective Radical Coupling Reactions. *Acc. Chem. Res.* **2017**, *50*, 1002–1010.
(344) Rusina, O.; Linnik, O.; Eremenko, A.; Kisch, H. Nitrogen Photofixation on Nanostructured Iron Titanate Films. *Chem. - Eur. J.* **2003**, *9*, 561–565.
(345) Balzani, V.; Bergamini, G.; Ceroni, P. Light: A Very Peculiar Reactant and Product. *Angew. Chem., Int. Ed.* **2015**, *54*, 11320–11337.
(346) Soffer, B. H.; Lynch, D. K. Some Paradoxes, Errors, and Resolutions Concerning the Spectral Optimization of Human Vision. *Am. J. Phys.* **1999**, *67*, 946–953.
(347) Taiz, L.; Zeiger, E.; Møller, I. M.; Murphy, A. *Plant Physiology and Development*, 6th ed.; Oxford University Press, Inc.: Oxford, 2018.
(348) Prier, C. K.; Rankic, D. A.; MacMillan, D. W. C. Visible Light Photoredox Catalysis with Transition Metal Complexes: Applications in Organic Synthesis. *Chem. Rev.* **2013**, *113*, 5322–5363.
(349) Senaweera, S.; Weaver, J. D. Dual C–F, C–H Functionalization via Photocatalysis: Access to Multifluorinated Biaryls. *J. Am. Chem. Soc.* **2016**, *138*, 2520–2523.
(350) Sang, L.; Zhao, Y.; Burda, C. TiO_2 Nanoparticles as Functional Building Blocks. *Chem. Rev.* **2014**, *114*, 9283–9318.
(351) Caronna, T.; Gambarotti, C.; Palmisano, L.; Punta, C.; Recupero, F. Sunlight Induced Functionalisation of Some Heterocyclic Bases in the Presence of Polycrystalline TiO_2. *Chem. Commun.* **2003**, 2350–2351.
(352) Fagnoni, M.; Dondi, D.; Ravelli, D.; Albini, A. Photocatalysis for the Formation of the C−C Bond. *Chem. Rev.* **2007**, *107*, 2725–2756.
(353) Ravelli, D.; Dondi, D.; Fagnoni, M.; Albini, A. Photocatalysis. A Multi-Faceted Concept for Green Chemistry. *Chem. Soc. Rev.* **2009**, *38*, 1999–2011.
(354) Yoon, T. P.; Ischay, M. A.; Du, J. Visible Light Photocatalysis as a Greener Approach to Photochemical Synthesis. *Nat. Chem.* **2010**, *2*, 527–532.
(355) Jin, J.; MacMillan, D. W. C. Alcohols as Alkylating Agents in Heteroarene C–H Functionalization. *Nature* **2015**, *525*, 87–90.
(356) Jin, H.; Huang, L.; Xie, J.; Rudolph, M.; Rominger, F.; Hashmi, A. S. K. Gold-Catalyzed C–H Annulation of Anthranils with Alkynes: A Facile, Flexible, and Atom-Economical Synthesis of Unprotected 7-Acylindoles. *Angew. Chem., Int. Ed.* **2016**, *55*, 794–797.
(357) Ushakov, D. B.; Gilmore, K.; Kopetzki, D.; McQuade, D. T.; Seeberger, P. H. Continuous-Flow Oxidative Cyanation of Primary and Secondary Amines Using Singlet Oxygen. *Angew. Chem., Int. Ed.* **2014**, *53*, 557–561.
(358) Orejarena Pacheco, J. C.; Lipp, A.; Nauth, A. M.; Acke, F.; Dietz, J.-P.; Opatz, T. A Highly Active System for the Metal-Free Aerobic Photocyanation of Tertiary Amines with Visible Light: Application to the Synthesis of Tetraponerines and Crispine A. *Chem. - Eur. J.* **2016**, *22*, 5409–5415.
(359) Hernández-Alonso, M. D.; Fresno, F.; Suárez, S.; Coronado, J. M. Development of Alternative Photocatalysts to TiO_2: Challenges and Opportunities. *Energy Environ. Sci.* **2009**, *2*, 1231–1257.
(360) Yoon, H.-S.; Ho, X.-H.; Jang, J.; Lee, H.-J.; Kim, S.-J.; Jang, H.-Y. N719 Dye-Sensitized Organophotocatalysis: Enantioselective Tandem Michael Addition/Oxyamination of Aldehydes. *Org. Lett.* **2012**, *14*, 3272–3275.
(361) Nazeeruddin, M. K.; Péchy, P.; Renouard, T.; Zakeeruddin, S. M.; Humphry-

Baker, R.; Comte, P.; Liska, P.; Cevey, L.; Costa, E.; Shklover, V.; Spiccia, L.; Deacon, G. B.; Bignozzi, C. A.; Grätzel, M. Engineering of Efficient Panchromatic Sensitizers for Nanocrystalline TiO_2-Based Solar Cells. *J. Am. Chem. Soc.* **2001**, *123*, 1613–1624.

(362) Tian, H.; Yang, X.; Chen, R.; Hagfeldt, A.; Sun, L. A Metal-Free "Black Dye" for Panchromatic Dye-Sensitized Solar Cells. *Energy Environ. Sci.* **2009**, *2*, 674–677.

(363) Cid, J.-J.; Yum, J.-H.; Jang, S.-R.; Nazeeruddin, M. K.; Martínez-Ferrero, E.; Palomares, E.; Ko, J.; Grätzel, M.; Torres, T. Molecular Cosensitization for Efficient Panchromatic Dye-Sensitized Solar Cells. *Angew. Chem., Int. Ed.* **2007**, *46*, 8358–8362.

(364) Ooyama, Y.; Yamaji, K.; Ohshita, J. Photovoltaic Performances of Type-II Dye-Sensitized Solar Sells Based on Catechol Dye Sensitizers: Retardation of Back-Electron Transfer by PET (Photo-Induced Electron Transfer). *Mater. Chem. Front.* **2017**, *1*, 2243–2255.

(365) Wada, K.; Yoshida, K.; Takatani, T.; Watanabe, Y. Selective Photo-Oxidation of Light Alkanes Using Solid Metal Oxide Semiconductors. *Appl. Catal., A* **1993**, *99*, 21–36.

(366) Zeug, N.; Bücheler, J.; Kisch, H. Catalytic Formation of Hydrogen and Carbon-Carbon Bonds on Illuminated Zinc Sulfide Generated from Zinc Dithiolenes. *J. Am. Chem. Soc.* **1985**, *107*, 1459–1465.

(367) Zhang, Y.; Zhang, N.; Tang, Z.-R.; Xu, Y.-J. Transforming CdS into an Efficient Visible Light Photocatalyst for Selective Oxidation of Saturated Primary C–H bonds under Ambient Conditions. *Chem. Sci.* **2012**, *3*, 2812–2822.

(368) Pal, A.; Ghosh, I.; Sapra, S.; König, B. Quantum Dots in Visible-Light Photoredox Catalysis: Reductive Dehalogenations and C–H Arylation Reactions Using Aryl Bromides. *Chem. Mater.* **2017**, *29*, 5225–5231.

(369) Su, F.; Mathew, S. C.; Möhlmann, L.; Antonietti, M.; Wang, X.; Blechert, S. Aerobic Oxidative Coupling of Amines by Carbon Nitride Photocatalysis with Visible Light. *Angew. Chem., Int. Ed.* **2011**, *50*, 657–660.

(370) Yuan, R.; Fan, S.; Zhou, H.; Ding, Z.; Lin, S.; Li, Z.; Zhang, Z.; Xu, C.; Wu, L.; Wang, X.; Fu, X. Chlorine-Radical-Mediated Photocatalytic Activation of C–H Bonds with Visible Light. *Angew. Chem., Int. Ed.* **2013**, *52*, 1035–1039.

(371) Füldner, S.; Pohla, P.; Bartling, H.; Dankesreiter, S.; Stadler, R.; Gruber, M.; Pfitzner, A.; König, B. Selective Photocatalytic Reductions of Nitrobenzene Derivatives Using $PbBiO_2X$ and Blue Light. *Green Chem.* **2011**, *13*, 640–643.

(372) Füldner, S.; Mild, R.; Siegmund, H. I.; Schroeder, J. A.; Gruber, M.; König, B. Green-Light Photocatalytic Reduction Using Dye-Sensitized TiO_2 and Transition Metal Nanoparticles. *Green Chem.* **2010**, *12*, 400–406.

(373) Füldner, S.; Mitkina, T.; Trottmann, T.; Frimberger, A.; Gruber, M.; König, B. Urea Derivatives Enhance the Photocatalytic Activity of Dye-Modified Titanium Dioxide. *Photochem. Photobiol. Sci.* **2011**, *10*, 623–625.

(374) Peter, L. "Sticky Electrons" Transport and Interfacial Transfer of Electrons in the Dye-Sensitized Solar Cell. *Acc. Chem. Res.* **2009**, *42*, 1839–1847.

(375) Grätzel, M. Recent Advances in Sensitized Mesoscopic Solar Cells. *Acc. Chem. Res.* **2009**, *42*, 1788–1798.

(376) Nour-Mohhamadi, F.; Nguyen, S. D.; Boschloo, G.; Hagfeldt, A.; Lund, T. Determination of the Light-Induced Degradation Rate of the Solar Cell Sensitizer N719 on TiO_2 Nanocrystalline Particles. *J. Phys. Chem. B* **2005**, *109*, 22413–

22419.
(377) Li, C.; Yum, J.-H.; Moon, S.-J.; Herrmann, A.; Eickemeyer, F.; Pschirer, N. G.; Erk, P.; Schöneboom, J.; Müllen, K.; Grätzel, M.; Nazeeruddin, M. K. An Improved Perylene Sensitizer for Solar Cell Applications. *ChemSusChem* **2008**, *1*, 615–618.
(378) Ye, S.; Kathiravan, A.; Hayashi, H.; Tong, Y.; Infahsaeng, Y.; Chabera, P.; Pascher, T.; Yartsev, A. P.; Isoda, S.; Imahori, H.; Sundström, V. Role of Adsorption Structures of Zn-Porphyrin on TiO_2 in Dye-Sensitized Solar Cells Studied by Sum Frequency Generation Vibrational Spectroscopy and Ultrafast Spectroscopy. *J. Phys. Chem. C* **2013**, *117*, 6066–6080.
(379) Materna, K. L.; Crabtree, R. H.; Brudvig, G. W. Anchoring Groups for Photocatalytic Water Oxidation on Metal Oxide Surfaces. *Chem. Soc. Rev.* **2017**, *46*, 6099–6110.
(380) Ma, W.; Han, D.; Zhou, M.; Sun, H.; Wang, L.; Dong, X.; Niu, L. Ultrathin g-C_3N_4/TiO_2 Composites as Photoelectrochemical Elements for the Real-Time Evaluation of Global Antioxidant Capacity. *Chem. Sci.* **2014**, *5*, 3946–3951.
(381) Caputo, C. A.; Wang, L.; Beranek, R.; Reisner, E. Carbon Nitride–TiO_2 Hybrid Modified with Hydrogenase for Visible Light Driven Hydrogen Production. *Chem. Sci.* **2015**, *6*, 5690–5694.
(382) Baciocchi, E.; Del Giacco, T.; Elisei, F.; Gerini, M. F.; Guerra, M.; Lapi, A.; Liberali, P. Electron Transfer and Singlet Oxygen Mechanisms in the Photooxygenation of Dibutyl Sulfide and Thioanisole in MeCN Sensitized by *N*-Methylquinolinium Tetrafluoborate and 9,10-Dicyanoanthracene. The Probable Involvement of a Thiadioxirane Intermediat. *J. Am. Chem. Soc.* **2003**, *125*, 16444–16454.
(383) Baciocchi, E.; Del Giacco, T.; Lanzalunga, O.; Mencarelli, P.; Procacci, B. Photosensitized Oxidation of Alkyl Phenyl Sulfoxides. C−S Bond Cleavage in Alkyl Phenyl Sulfoxide Radical Cations. *J. Org. Chem.* **2008**, *73*, 5675–5682.
(384) Santamaria, J.; Kaddachi, M. T.; Rigaudy, J. Electron-Transfer Activation. Photocyanation of Tertiary Amines. *Tetrahedron Lett.* **1990**, *31*, 4735–4738.
(385) Jørgensen, C. K. Differences between the Four Halide Ligands, and Discussion Remarks on Trigonal-Bipyramidal Complexes, on Oxidation States, and on Diagonal Elements of One-Electron Energy. *Coord. Chem. Rev.* **1966**, *1*, 164–178.
(386) Chirik, P. J.; Wieghardt, K. Radical Ligands Confer Nobility on Base-Metal Catalysts. *Science* **2010**, *327*, 794–795.
(387) Zorn, M.; Weber, S. A. L.; Tahir, M. N.; Tremel, W.; Butt, H.-J.; Berger, R.; Zentel, R. Light Induced Charging of Polymer Functionalized Nanorods. *Nano Lett.* **2010**, *10*, 2812–2816.
(388) Sang, Y.; Liu, H.; Umar, A. Photocatalysis from UV/Vis to Near-Infrared Light: Towards Full Solar-Light Spectrum Activity. *ChemCatChem* **2015**, *7*, 559–573.
(389) Tahir, M. N.; Natalio, F.; Cambaz, M. A.; Panthöfer, M.; Branscheid, R.; Kolb, U.; Tremel, W. Controlled Synthesis of Linear and Branched Au@ZnO Hybrid Nanocrystals and Their Photocatalytic Properties. *Nanoscale* **2013**, *5*, 9944–9949.
(390) Piera, J.; Bäckvall, J.-E. Catalytic Oxidation of Organic Substrates by Molecular Oxygen and Hydrogen Peroxide by Multistep Electron Transfer—A Biomimetic Approach. *Angew. Chem., Int. Ed.* **2008**, *47*, 3506–3523.
(391) Zeitler, K. Photoredox Catalysis with Visible Light. *Angew. Chem., Int. Ed.*

2009, *48*, 9785–9789.
(392) Wang, Y.; Hang, K.; Anderson, N. A.; Lian, T. Comparison of Electron Transfer Dynamics in Molecule-to-Nanoparticle and Intramolecular Charge Transfer Complexes. *J. Phys. Chem. B* **2003**, *107*, 9434–9440.
(393) Duthaler, R. O. Recent Developments in the Stereoselective Synthesis of α-Aminoacids. *Tetrahedron* **1994**, *50*, 1539–1650.
(394) North, M. Oxidative Synthesis of α-Amino Nitriles from Tertiary Amines. *Angew. Chem., Int. Ed.* **2004**, *43*, 4126–4128.
(395) Liu, L.; Wang, Z.; Fu, X.; Yan, C.-H. Azobisisobutyronitrile Initiated Aerobic Oxidative Transformation of Amines: Coupling of Primary Amines and Cyanation of Tertiary Amines. *Org. Lett.* **2012**, *14*, 5692–5695.
(396) Otto, N.; Opatz, T. Heterocycles from α-Aminonitriles. *Chem. - Eur. J.* **2014**, *20*, 13064–13077.
(397) Murahashi, S.-I.; Zhang, D. Ruthenium Catalyzed Biomimetic Oxidation in Organic Synthesis Inspired by Cytochrome P-450. *Chem. Soc. Rev.* **2008**, *37*, 1490–1501.
(398) Ruchirawat, S.; Chaisupakitsin, M.; Patranuwatana, N.; Cashaw, J. L.; Davis, V. E. A Convenient Synthesis of Simple Tetrahydroisoquinolines. *Synth. Commun.* **1984**, *14*, 1221–1228.
(399) Euliss, L. E.; Grancharov, S. G.; O'Brien, S.; Deming, T. J.; Stucky, G. D.; Murray, C. B.; Held, G. A. Cooperative Assembly of Magnetic Nanoparticles and Block Copolypeptides in Aqueous Media. *Nano Lett.* **2003**, *3*, 1489–1493.
(400) Salgueiriño-Maceira, V.; Liz-Marzán, L. M.; Farle, M. Water-Based Ferrofluids from Fe_xPt_{1-x} Nanoparticles Synthesized in Organic Media. *Langmuir* **2004**, *20*, 6946–6950.
(401) Smith, J. G.; Jain, P. K. The Ligand Shell as an Energy Barrier in Surface Reactions on Transition Metal Nanoparticles. *J. Am. Chem. Soc.* **2016**, *138*, 6765–6773.
(402) Borgias, B. A.; Cooper, S. R.; Koh, Y. B.; Raymond, K. N. Synthetic, Structural, and Physical Studies of Titanium Complexes of Catechol and 3,5-Di-*tert*-butylcatechol. *Inorg. Chem.* **1984**, *23*, 1009–1016.
(403) Wang, J.; Tahir, M. N.; Kappl, M.; Tremel, W.; Metz, N.; Barz, M.; Theato, P.; Butt, H.-J. Influence of Binding-Site Density in Wet Bioadhesion. *Adv. Mater.* **2008**, *20*, 3872–3876.
(404) Dondi, D.; Buttafava, A.; Zeffiro, A.; Bracco, S.; Sozzani, P.; Faucitano, A. Reaction Mechanisms in Irradiated, Precipitated, and Mesoporous Silica. *J. Phys. Chem. A* **2013**, *117*, 3304–3318.
(405) Estévez, C. M.; Dmitrenko, O.; Winter, J. E.; Bach, R. D. Reactivity of Alkyl versus Silyl Peroxides. The Consequences of 1,2-Silicon Bridging on the Epoxidation of Alkenes with Silyl Hydroperoxides and Bis(trialkylsilyl)peroxides. *J. Org. Chem.* **2000**, *65*, 8629–8639.
(406) Hu, J.; Wang, J.; Nguyen, T. H.; Zheng, N. The Chemistry of Amine Radical Cations Produced by Visible Light Photoredox Catalysis. *Beilstein J. Org. Chem.* **2013**, *9*, 1977–2001.
(407) Nelsen, S. F.; Ippoliti, J. T. On the Deprotonation of Trialkylamine Cation Radicals by Amines. *J. Am. Chem. Soc.* **1986**, *108*, 4879–4881.
(408) Dombrowski, G. W.; Dinnocenzo, J. P.; Zielinski, P. A.; Farid, S.; Wosinska, Z. M.; Gould, I. R. Efficient Unimolecular Deprotonation of Aniline Radical Cations. *J. Org. Chem.* **2005**, *70*, 3791–3800.

(409) Nazran, A. S.; Griller, D. Hydrogen Abstraction from Amines: Formation of Aminyl vs. α-Aminoalkyl Radicals. *J. Am. Chem. Soc.* **1983**, *105*, 1970–1971.
(410) Lal, J.; Green, R. Effect of Amine Accelerators on the Polymerization of Methyl Methacrylate with Benzoyl Peroxide. *J. Polym. Sci.* **1955**, *17*, 403–409.
(411) Kohls, P.; Jadhav, D.; Pandey, G.; Reiser, O. Visible Light Photoredox Catalysis: Generation and Addition of *N*-Aryltetrahydroisoquinoline-Derived α-Amino Radicals to Michael Acceptors. *Org. Lett.* **2012**, *14*, 672–675.
(412) Cai, S.; Zhao, X.; Wang, X.; Liu, Q.; Li, Z.; Wang, D. Z. Visible-Light-Promoted C–C Bond Cleavage: Photocatalytic Generation of Iminium Ions and Amino Radicals. *Angew. Chem., Int. Ed.* **2012**, *51*, 8050–8053.
(413) Molet, P.; Garcia-Pomar, J. L.; Matricardi, C.; Garriga, M.; Alonso, M. I.; Mihi, A. Ultrathin Semiconductor Superabsorbers from the Visible to the Near-Infrared. *Adv. Mater.* **2018**, *30*, 1705876.
(414) Girard, S. A.; Knauber, T.; Li, C.-J. The Cross-Dehydrogenative Coupling of C_{sp3}–H Bonds: A Versatile Strategy for C–C Bond Formations. *Angew. Chem., Int. Ed.* **2014**, *53*, 74–100.
(415) Su, Y.; Straathof, N. J. W.; Hessel, V.; Noël, T. Photochemical Transformations Accelerated in Continuous-Flow Reactors: Basic Concepts and Applications. *Chem. - Eur. J.* **2014**, *20*, 10562–10589.
(416) Katritzky, A. R.; He, H.-Y.; Jiang, R.; Long, Q. 2-Substituted-1,2,3,4-tetrahydroisoquinolines and Chiral 3-Carboxyl Analogues from *N*-Benzotriazolylmethyl-*N*-phenethylamines. *Tetrahedron: Asymmetry* **2001**, *12*, 2427–2434.
(417) Knabe, J.; Roloff, H. Dehydrierung von tertiären Aminen mit Hg^{II}-ÄDTA, IX. 1-Alkyl-2-methyl-1.2.3.4-tetrahydro-isochinoline. *Chem. Ber.* **1964**, *97*, 3452–3455.
(418) Janssen, R. H. A. M.; Ch. Lousberg, R. J. J.; Wijkens, P.; Kruk, C.; Theuns, H. G. Assignment of ^{1}H and ^{13}C NMR Resonances of Some Isoquinoline Alkaloids. *Phytochemistry* **1989**, *28*, 2833–2839.
(419) Wagner, A.; Han, W.; Mayer, P.; Ofial, A. R. Iron-Catalyzed Generation of α-Amino Nitriles from Tertiary Amines. *Adv. Synth. Catal.* **2013**, *355*, 3058–3070.
(420) Alagiri, K.; Devadig, P.; Prabhu, K. R. Molybdenum Trioxide Catalyzed Oxidative Cross-Dehydrogenative Coupling of Benzylic sp^3 C–H Bonds: Synthesis of α-Aminophosphonates under Aerobic Conditions. *Tetrahedron Lett.* **2012**, *53*, 1456–1459.
(421) Yang, R.; Ruan, Q.; Zhang, B.-Y.; Zheng, Z.-L.; Miao, F.; Zhou, L.; Geng, H.-L. A Class of Promising Acaricidal Tetrahydroisoquinoline Derivatives: Synthesis, Biological Evaluation and Structure-Activity Relationships. *Molecules* **2014**, *19*, 8051–8066.
(422) Zhang, C.; Liu, C.; Shao, Y.; Bao, X.; Wan, X. Nucleophilic Attack of α-Aminoalkyl Radicals on Carbon–Nitrogen Triple Bonds to Construct α-Amino Nitriles: An Experimental and Computational Study. *Chem. - Eur. J.* **2013**, *19*, 17917–17925.
(423) Ebden, M. R.; Simpkins, N. S.; Fox, D. N. A. Metallation of Benzylic Amines via Amine-Borane Complexes. *Tetrahedron* **1998**, *54*, 12923–12952.
(424) Allen, J. M.; Lambert, T. H. Tropylium Ion Mediated α-Cyanation of Amines. *J. Am. Chem. Soc.* **2011**, *133*, 1260–1262.
(425) Nauth, A. M.; Otto, N.; Opatz, T. α-Cyanation of Aromatic Tertiary Amines using Ferricyanide as a Non-Toxic Cyanide Source. *Adv. Synth. Catal.* **2015**, *357*,

3424–3428.
(426) Firlar, E.; Çınar, S.; Kashyap, S.; Akinc, M.; Prozorov, T. Direct Visualization of the Hydration Layer on Alumina Nanoparticles with the Fluid Cell STEM *in situ*. *Sci. Rep.* **2015**, *5*, 9830.
(427) Sakamoto, R.; Sakurai, S.; Maruoka, K. Bis(trialkylsilyl) Peroxides as Alkylating Agents in the Copper-Catalyzed Selective Mono-*N*-Alkylation of Primary Amides. *Chem. Commun.* **2017**, *53*, 6484–6487.
(428) Berchadsky, Y.; Bernard-Henriet, C.; Finet, J.-P.; Lauricella, R.; Marque, S. R. A.; Tordo, P. Persilylated Phosphoranyl Radicals: The First Persistent Noncyclic Phosphoranyl Radicals. *Chem. - Eur. J.* **2006**, *12*, 7084–7094.
(429) Zhang, Q.; Yuan, H.-Y.; Fukaya, N.; Yasuda, H.; Choi, J.-C. Direct Synthesis of Carbamate from CO_2 Using a Task-Specific Ionic Liquid Catalyst. *Green Chem.* **2017**, *19*, 5614–5624.
(430) Tsuji, Y.; Taniguchi, M.; Yasuda, T.; Kawamura, T.; Obora, Y. Palladium-Catalyzed Cyanation of Propargylic Carbonates with Trimethylsilyl Cyanide. *Org. Lett.* **2000**, *2*, 2635–2637.
(431) Ji, P.; Solomon, J. B.; Lin, Z.; Johnson, A.; Jordan, R. F.; Lin, W. Transformation of Metal–Organic Framework Secondary Building Units into Hexanuclear Zr-Alkyl Catalysts for Ethylene Polymerization. *J. Am. Chem. Soc.* **2017**, *139*, 11325–11328.
(432) Cerkovnik, J.; Tuttle, T.; Kraka, E.; Lendero, N.; Plesničar, B.; Cremer, D. The Ozonation of Silanes and Germanes: An Experimental and Theoretical Investigation. *J. Am. Chem. Soc.* **2006**, *128*, 4090–4100.
(433) Tobisu, M.; Kita, Y.; Ano, Y.; Chatani, N. Rhodium-Catalyzed Silylation and Intramolecular Arylation of Nitriles via the Silicon-Assisted Cleavage of Carbon−Cyano Bonds. *J. Am. Chem. Soc.* **2008**, *130*, 15982–15989.
(434) Walsh, R. Thermochemistry. In *The Chemistry of Organic Silicon Compounds*; Patai, S., Rappoport, Z., Eds.; John Wiley & Sons, Ltd: Chichester, UK, 1989; pp 371–391.
(435) Wayner, D. D. M.; Clark, K. B.; Rauk, A.; Yu, D.; Armstrong, D. A. C−H Bond Dissociation Energies of Alkyl Amines: Radical Structures and Stabilization Energies. *J. Am. Chem. Soc.* **1997**, *119*, 8925–8932.
(436) Kumar, S. K.; Krishnamoorti, R. Nanocomposites: Structure, Phase Behavior, and Properties. *Annu. Rev. Chem. Biomol. Eng.* **2010**, *1*, 37–58.
(437) Varol, H. S.; Meng, F.; Hosseinkhani, B.; Malm, C.; Bonn, D.; Bonn, M.; Zaccone, A.; Parekh, S. H. Nanoparticle Amount, and Not Size, Determines Chain Alignment and Nonlinear Hardening in Polymer Nanocomposites. *Proc. Natl. Acad. Sci. U. S. A.* **2017**, *114*, E3170–E3177.
(438) Akcora, P.; Liu, H.; Kumar, S. K.; Moll, J.; Li, Y.; Benicewicz, B. C.; Schadler, L. S.; Acehan, D.; Panagiotopoulos, A. Z.; Pryamitsyn, V.; Ganesan, V.; Ilavsky, J.; Thiyagarajan, P.; Colby, R. H.; Douglas, J. F. Anisotropic Self-Assembly of Spherical Polymer-Grafted Nanoparticles. *Nat. Mater.* **2009**, *8*, 354–359.
(439) Grabowski, C. A.; Koerner, H.; Meth, J. S.; Dang, A.; Hui, C. M.; Matyjaszewski, K.; Bockstaller, M. R.; Durstock, M. F.; Vaia, R. A. Performance of Dielectric Nanocomposites: Matrix-Free, Hairy Nanoparticle Assemblies and Amorphous Polymer–Nanoparticle Blends. *ACS Appl. Mater. Interfaces* **2014**, *6*, 21500–21509.
(440) Kim, S. A.; Mangal, R.; Archer, L. A. Relaxation Dynamics of Nanoparticle-Tethered Polymer Chains. *Macromolecules* **2015**, *48*, 6280–6293.

(441) Alonso-Redondo, E.; Schmitt, M.; Urbach, Z.; Hui, C. M.; Sainidou, R.; Rembert, P.; Matyjaszewski, K.; Bockstaller, M. R.; Fytas, G. A New Class of Tunable Hypersonic Phononic Crystals Based on Polymer-Tethered Colloids. *Nat. Commun.* **2015**, *6*, 8309.
(442) Fuhrer, R.; Athanassiou, E. K.; Luechinger, N. A.; Stark, W. J. Crosslinking Metal Nanoparticles into the Polymer Backbone of Hydrogels Enables Preparation of Soft, Magnetic Field-Driven Actuators with Muscle-Like Flexibility. *Small* **2009**, *5*, 383–388.
(443) Yang, Y. Thermal Conductivity. In *Physical Properties of Polymers Handbook*; Mark, J. E., Ed.; Springer: New York, 2007; pp 155–163.
(444) Alonso-Redondo, E.; Gueddida, A.; Huesmann, H.; El Abouti, O.; Tremel, W.; El Boudouti, E. H.; Djafari-Rouhani, B.; Fytas, G. Direction-Dependent Elastic Properties and Phononic Behavior of PMMA/$BaTiO_3$ Nanocomposite Thin Films. *J. Chem. Phys.* **2017**, *146*, 203325.
(445) Mirigian, S.; Schweizer, K. S. Elastically Cooperative Activated Barrier Hopping Theory of Relaxation in Viscous Fluids. II. Thermal Liquids. *J. Chem. Phys.* **2014**, *140*, 194507.
(446) Mbanga, B. L.; Iyer, B. V. S.; Yashin, V. V.; Balazs, A. C. Tuning the Mechanical Properties of Polymer-Grafted Nanoparticle Networks through the Use of Biomimetic Catch Bonds. *Macromolecules* **2016**, *49*, 1353–1361.
(447) Neogi, S.; Reparaz, J. S.; Pereira, L. F. C.; Graczykowski, B.; Wagner, M. R.; Sledzinska, M.; Shchepetov, A.; Prunnila, M.; Ahopelto, J.; Sotomayor-Torres, C. M.; Donadio, D. Tuning Thermal Transport in Ultrathin Silicon Membranes by Surface Nanoscale Engineering. *ACS Nano* **2015**, *9*, 3820–3828.
(448) Volz, S.; Ordonez-Miranda, J.; Shchepetov, A.; Prunnila, M.; Ahopelto, J.; Pezeril, T.; Vaudel, G.; Gusev, V.; Ruello, P.; Weig, E. M.; Schubert, M.; Hettich, M.; Grossman, M.; Dekorsy, T.; Alzina, F.; Graczykowski, B.; Chavez-Angel, E.; Sebastian Reparaz, J.; Wagner, M. R.; et al. Nanophononics: State of the Art and Perspectives. *Eur. Phys. J. B* **2016**, *89*, 15.
(449) Putnam, S. A.; Cahill, D. G.; Ash, B. J.; Schadler, L. S. High-Precision Thermal Conductivity Measurements as a Probe of Polymer/Nanoparticle Interfaces. *J. Appl. Phys.* **2003**, *94*, 6785–6788.
(450) Kim, G.-H.; Lee, D.; Shanker, A.; Shao, L.; Kwon, M. S.; Gidley, D.; Kim, J.; Pipe, K. P. High Thermal Conductivity in Amorphous Polymer Blends by Engineered Interchain Interactions. *Nat. Mater.* **2015**, *14*, 295–300.
(451) Losego, M. D.; Grady, M. E.; Sottos, N. R.; Cahill, D. G.; Braun, P. V. Effects of Chemical Bonding on Heat Transport Across Interfaces. *Nat. Mater.* **2012**, *11*, 502–506.
(452) Ong, W.-L.; Rupich, S. M.; Talapin, D. V.; McGaughey, A. J. H.; Malen, J. A. Surface Chemistry Mediates Thermal Transport in Three-Dimensional Nanocrystal Arrays. *Nat. Mater.* **2013**, *12*, 410–415.
(453) Mahoney, C.; Hui, C. M.; Majumdar, S.; Wang, Z.; Malen, J. A.; N. Tchoul, M.; Matyjaszewski, K.; Bockstaller, M. R. Enhancing Thermal Transport in Nanocomposites by Polymer-Graft Modification of Particle Fillers. *Polymer* **2016**, *93*, 72–77.
(454) Shakeel Ahmad, M.; Pandey, A. K.; Abd Rahim, N. Advancements in the Development of TiO_2 Photoanodes and Its Fabrication Methods for Dye Sensitized Solar Cell (DSSC) Applications. A Review. *Renew. Sustain. Energy Rev.* **2017**, *77*, 89–108.

(455) Hoyle, C. E.; Lowe, A. B.; Bowman, C. N. Thiol-Click Chemistry: A Multifaceted Toolbox for Small Molecule and Polymer Synthesis. *Chem. Soc. Rev.* **2010**, *39*, 1355–1387.
(456) Hoyle, C. E.; Bowman, C. N. Thiol-Ene Click Chemistry. *Angew. Chem., Int. Ed.* **2010**, *49*, 1540–1573.
(457) Hoyle, C. E.; Lee, T. Y.; Roper, T. Thiol–Enes: Chemistry of the Past with Promise for the Future. *J. Polym. Sci. Part A: Polym. Chem.* **2004**, *42*, 5301–5338.
(458) Li, Q.; Zhou, H.; Hoyle, C. E. The Effect of Thiol and Ene Structures on Thiol–Ene Networks: Photopolymerization, Physical, Mechanical and Optical Properties. *Polymer* **2009**, *50*, 2237–2245.
(459) Colucci, G.; Mana, S.; Conzatti, L.; Sangermano, M. Hybrid Organic–Inorganic Silicate/Thiol–Ene Photocured Coatings. *Surf. Coat. Technol.* **2012**, *206*, 2719–2724.
(460) Phillips, J. P.; Mackey, N. M.; Confait, B. S.; Heaps, D. T.; Deng, X.; Todd, M. L.; Stevenson, S.; Zhou, H.; Hoyle, C. E. Dispersion of Gold Nanoparticles in UV-Cured, Thiol−Ene Films by Precomplexation of Gold−Thiol. *Chem. Mater.* **2008**, *20*, 5240–5245.
(461) Boyd, D. A.; Naciri, J.; Fontana, J.; Pacardo, D. B.; Shields, A. R.; Verbarg, J.; Spillmann, C. M.; Ligler, F. S. Facile Fabrication of Color Tunable Film and Fiber Nanocomposites via Thiol Click Chemistry. *Macromolecules* **2014**, *47*, 695–704.
(462) Jefferson, L. U.; Netchaev, A. D.; Jefcoat, J. A.; Windham, A. D.; McFarland, F. M.; Guo, S.; Buchanan, R. K.; Buchanan, J. P. Preparation and Characterization of Polyhedral Oligomeric Silsesquioxane-Containing, Titania-Thiol-Ene Composite Photocatalytic Coatings, Emphasizing the Hydrophobic–Hydrophilic Transition. *ACS Appl. Mater. Interfaces* **2015**, *7*, 12639–12648.
(463) Gomopoulos, N.; Maschke, D.; Koh, C. Y.; Thomas, E. L.; Tremel, W.; Butt, H.-J.; Fytas, G. One-Dimensional Hypersonic Phononic Crystals. *Nano Lett.* **2010**, *10*, 980–984.
(464) Schneider, D.; Liaqat, F.; El Boudouti, E. H.; El Hassouani, Y.; Djafari-Rouhani, B.; Tremel, W.; Butt, H.-J.; Fytas, G. Engineering the Hypersonic Phononic Band Gap of Hybrid Bragg Stacks. *Nano Lett.* **2012**, *12*, 3101–3108.
(465) Alonso-Redondo, E.; Huesmann, H.; El Boudouti, E.-H.; Tremel, W.; Djafari-Rouhani, B.; Butt, H.-J.; Fytas, G. Phoxonic Hybrid Superlattice. *ACS Appl. Mater. Interfaces* **2015**, *7*, 12488–12495.
(466) Cahill, D. G. Thermal Conductivity Measurement from 30 to 750 K: The 3ω Method. *Rev. Sci. Instrum.* **1990**, *61*, 802–808.
(467) Lee, S.-M.; Cahill, D. G. Heat Transport in Thin Dielectric Films. *J. Appl. Phys.* **1997**, *81*, 2590–2595.
(468) Xie, X.; Li, D.; Tsai, T.-H.; Liu, J.; Braun, P. V.; Cahill, D. G. Thermal Conductivity, Heat Capacity, and Elastic Constants of Water-Soluble Polymers and Polymer Blends. *Macromolecules* **2016**, *49*, 972–978.
(469) Xie, X.; Yang, K.; Li, D.; Tsai, T.-H.; Shin, J.; Braun, P. V.; Cahill, D. G. High and Low Thermal Conductivity of Amorphous Macromolecules. *Phys. Rev. B* **2017**, *95*, 035406.
(470) Habib, E.; Wang, R.; Wang, Y.; Zhu, M.; Zhu, X. X. Inorganic Fillers for Dental Resin Composites: Present and Future. *ACS Biomater. Sci. Eng.* **2016**, *2*, 1–11.
(471) Podgórski, M.; Becka, E.; Claudino, M.; Flores, A.; Shah, P. K.; Stansbury, J.

W.; Bowman, C. N. Ester-Free Thiol–Ene Dental Restoratives—Part A: Resin Development. *Dent. Mater.* **2015**, *31*, 1255–1262.
(472) Kraft, P.; Eichenberger, W. Conception, Characterization and Correlation of New Marine Odorants. *Eur. J. Org. Chem.* **2003**, *2003*, 3735–3743.
(473) Waite, J. H. Adhesion à la Moule. *Integr. Comp. Biol.* **2002**, *42*, 1172–1180.
(474) Lee, H.; Scherer, N. F.; Messersmith, P. B. Single-Molecule Mechanics of Mussel Adhesion. *Proc. Natl. Acad. Sci. U. S. A.* **2006**, *103*, 12999–13003.
(475) Danner, E. W.; Kan, Y.; Hammer, M. U.; Israelachvili, J. N.; Waite, J. H. Adhesion of Mussel Foot Protein Mefp-5 to Mica: An Underwater Superglue. *Biochemistry* **2012**, *51*, 6511–6518.
(476) Sparks, B. J.; Hoff, E. F. T.; Hayes, L. P.; Patton, D. L. Mussel-Inspired Thiol–Ene Polymer Networks: Influencing Network Properties and Adhesion with Catechol Functionality. *Chem. Mater.* **2012**, *24*, 3633–3642.
(477) Cheng, W.; Sainidou, R.; Burgardt, P.; Stefanou, N.; Kiyanova, A.; Efremov, M.; Fytas, G.; Nealey, P. F. Elastic Properties and Glass Transition of Supported Polymer Thin Films. *Macromolecules* **2007**, *40*, 7283–7290.
(478) Zhao, D.; Schneider, D.; Fytas, G.; Kumar, S. K. Controlling the Thermomechanical Behavior of Nanoparticle/Polymer Films. *ACS Nano* **2014**, *8*, 8163–8173.
(479) Ivanda, M.; Furić, K.; Musić, S.; Ristić, M.; Gotić, M.; Ristić, D.; Tonejc, A. M.; Djerdj, I.; Mattarelli, M.; Montagna, M.; Rossi, F.; Ferrari, M.; Chiasera, A.; Jestin, Y.; Righini, G. C.; Kiefer, W.; Gonçalves, R. R. Low Wavenumber Raman Scattering of Nanoparticles and Nanocomposite Materials. *J. Raman Spectrosc.* **2007**, *38*, 647–659.
(480) Wood, A. B. *A Textbook of Sound: Being an Account of the Physics of Vibrations with Special Reference to Recent Theoretical and Technical Developments*; Macmillan: New York, 1930.
(481) Torrent, D.; Sánchez-Dehesa, J. Acoustic Metamaterials for New Two-Dimensional Sonic Devices. *New J. Phys.* **2007**, *9*, 323–323.
(482) Kim, D. J.; Kim, D. S.; Cho, S.; Kim, S. W.; Lee, S. H.; Kim, J. C. Measurement of Thermal Conductivity of TiO_2 Thin Films Using 3ω Method. *Int. J. Thermophys.* **2004**, *25*, 281–289.
(483) Lee, S.-M.; Cahill, D. G.; Allen, T. H. Thermal Conductivity of Sputtered Oxide Films. *Phys. Rev. B* **1995**, *52*, 253–257.
(484) Every, A. G.; Tzou, Y.; Hasselman, D. P. H.; Raj, R. The Effect of Particle Size on the Thermal Conductivity of ZnS/Diamond Composites. *Acta Metall. Mater.* **1992**, *40*, 123–129.
(485) Pietrak, K.; Winiewski, T. S. A Review of Models for Effective Thermal Conductivity of Composite Materials. *J. Power Technol.* **2015**, *95*, 14–24.
(486) Losego, M. D.; Moh, L.; Arpin, K. A.; Cahill, D. G.; Braun, P. V. Interfacial Thermal Conductance in Spun-Cast Polymer Films and Polymer Brushes. *Appl. Phys. Lett.* **2010**, *97*, 011908.
(487) Wen, J. Heat Capacities of Polymers. In *Physical Properties of Polymers Handbook*; Mark, J. E., Ed.; Springer: New York, 2007; pp 145–154.
(488) Saeedian, M.; Mahjour-Shafiei, M.; Shojaee, E.; Mohammadizadeh, M. R. Specific Heat Capacity of TiO_2 Nanoparticles. *J. Comput. Theor. Nanosci.* **2012**, *9*, 616–620.
(489) Prasher, R. Thermal Interface Materials: Historical Perspective, Status, and Future Directions. *Proc. IEEE* **2006**, *94*, 1571–1586.

Publications

08/2019 **E. Schechtel**, R. Dören, H. Frerichs, M. Panthöfer, M. Mondeshki, W. Tremel, "Mixed Ligand Shell Formation upon Catechol Ligand Adsorption on Hydrophobic TiO_2 Nanoparticles", *Langmuir* **2019**, *35*, 12518–12531.

05/2019 H. Huesmann, **E. Schechtel**, I. Lieberwirth, M. Panthöfer, W. Tremel, "Surface Chemistry Directs the Tunable Assembly of TiO_2 Anatase Nanocubes into Three-Dimensional Mesocrystals", *European Journal of Inorganic Chemistry* **2019**, 3165–3170.

09/2018 **E. Schechtel**, A. M. Nauth, R. Dören, T. Opatz, W. Tremel, "TiO_2 Nanoparticles Functionalized with Non-Innocent Ligands Allow Oxidative Photocyanation of Amines with Visible/Near-Infrared Photons", *Journal of the American Chemical Society* **2018**, *140*, 14169–14177.

10/2017 **E. Schechtel**, Y. Yan, X. Xu, Y. Cang, W. Tremel, Z. Wang, B. Li, G. Fytas, "Elastic Modulus and Thermal Conductivity of Thiol-Ene/TiO_2 Nanocomposites", *The Journal of Physical Chemistry C* **2017**, *121*, 25568–25575.

01/2017 G. Becker, L.-M. Ackermann, **E. Schechtel**, M. Klapper, W. Tremel, F. R. Wurm, "Joining Two Natural Motifs: Catechol-Containing Poly(phosphoester)s", *Biomacromolecules* **2017**, *18*, 767–777.

04/2015 F. Liaqat, M. N. Tahir, **E. Schechtel**, M. Kappl, G. K. Auernhammer, K. Char, R. Zentel, H.-J. Butt, W. Tremel, "High-Performance TiO_2 Nanoparticle/DOPA-Polymer Composites", *Macromolecular Rapid Communications* **2015**, *36*, 1129–1137.

08/2013 W. G. Zeier, T. Day, **E. Schechtel**, G. J. Snyder, W. Tremel, "Influence of the chemical potential on the carrier effective mass in the thermoelectric solid solution $Cu_2Zn_{1-x}Fe_xGeSe_4$", *Functional Materials Letters* **2013**, *6*, 1340010.

11/2012 H. Wang, **E. Schechtel**, Y. Pei, G. J. Snyder, "High Thermoelectric Efficiency of n-type PbS", *Advanced Energy Materials* **2013**, *3*, 488–495.

09/2012 A. Zevalkink, W. G. Zeier, G. Pomrehn, **E. Schechtel**, W. Tremel, G. J. Snyder, "Thermoelectric properties of Sr_3GaSb_3 – a chain-forming Zintl compound", *Energy & Environmental Science* **2012**, *5*, 9121–9128.

03/2012 W. G. Zeier, A. Zevalkink, **E. Schechtel**, W. Tremel, G. J. Snyder, "Thermoelectric properties of Zn-doped Ca_3AlSb_3", *Journal of Materials Chemistry* **2012**, *22*, 9826–9830.